Polymerisation-Induced Self-Assembly in Non-Polar Media

Matthew John Derry

Department of Chemistry

The University of Sheffield

Submitted to the University of Sheffield

In fulfilment of the requirements for the award of

Doctor of Philosophy

March 2016

Declaration

The work described in this Thesis was carried out at the University of Sheffield under the supervision of Professor Steven P. Armes FRS between October 2012 and March 2016 and has not been submitted, either wholly or in part, for this or any other degree. All the work is the original work of the author, except where acknowledged by references.

Signature: _____

Matthew John Derry March 2016

Abstract

This Thesis describes the reversible addition-fragmentation chain transfer (RAFT) dispersion polymerisation of benzyl methacrylate (BzMA) in non-polar solvents. Firstly, oil-soluble poly(lauryl methacrylate) (PLMA), poly(stearyl methacrylate) (PSMA) and poly(behenyl methacrylate) (PBhMA) macromolecular chain transfer agents (macro-CTAs) are synthesised via RAFT solution polymerisation in toluene. These macro-CTAs are then chain-extended in turn with varying amounts of BzMA in industrially-sourced mineral oil or a poly(α-olefin). Polymerisation-induced self-assembly (PISA) occurs under these conditions, where the soluble BzMA monomer polymerises to form an insoluble poly(benzyl methacrylate) (PBzMA) block, thus driving the *in situ* formation of spheres, worms or vesicles. Subtle differences in the phase diagrams constructed for PLMA-PBzMA diblock copolymer nano-objects are observed in different solvents. In such PISA formulations, the stabiliser block DP is an important parameter, because only kinetically-trapped spheres are accessible when sufficiently long stabilisers (e.g. $PLMA_{39}$, $PSMA_{18}$ or $PBhMA_{37}$) are used. $PLMA_{47}$-$PBzMA_{100}$ spheres could be prepared at copolymer concentrations up to 50% w/w solids. Importantly, a highly convenient 'one-pot' synthetic protocol was developed, whereby 39 nm $PLMA_{50}$-$PBzMA_{100}$ spheres were prepared at 30% w/w solids within 9 h starting from LMA monomer. The phase diagram for $PSMA_{13}$-$PBzMA_x$ diblock copolymer nanoparticles in mineral oil indicates that the final copolymer morphologies are only weakly dependent on copolymer concentration, which enables the synthesis of pure spheres, worms or vesicles at just 5.0% w/w solids. This facilitated *in situ* small-angle X-ray scattering (SAXS) studies during the PISA synthesis. When targeting $PSMA_{31}$-$PBzMA_{2000}$ spheres, the PBzMA core diameter and aggregation number per sphere (N_s) increased monotonically during the polymerisation. When targeting $PSMA_{13}$-$PBzMA_{150}$ vesicles, the full range of morphologies is observed, from soluble copolymer chains to the final vesicles via intermediate spheres and worms. Transmission electron microscopy (TEM) studies indicated that vesicles are formed from worms via transient octopi and jellyfish morphologies, which is consistent with observations previously reported for aqueous PISA formulations. A combination of dynamic light scattering (DLS), TEM and both *in situ* and *post mortem* SAXS analyses confirmed that the overall vesicle dimensions are conserved as the membrane thickens, which indicates an 'inward growth' mechanism. This is consistent with observations recently reported for an aqueous PISA formulation and hence suggests a universal vesicle growth mechanism for all PISA formulations. $PSMA_{13}$-$PBzMA_{96}$ vesicles undergo a vesicle-to-worm transition, which is attributed to surface plasticisation of the core-forming PBzMA block via solvent ingress. This morphological transition was analysed using DLS, TEM, SAXS, ^{1}H NMR spectroscopy and rheology. Dispersions of $PSMA_{13}$-$PBzMA_{65}$ worms form free-standing gels at 20 °C due to multiple inter-worm contacts, but heating leads to surface plasticisation. This induces a worm-to-sphere transition and concomitant degelation, since isotropic spheres cannot form inter-particle contacts at this copolymer concentration. The worm-to-sphere transition was characterised using TEM, DLS and rheology. In addition, shear-induced polarised light imaging (SIPLI) indicated that the highly anisotropic worms become aligned under shear, with birefringence giving rise to a Maltese cross pattern. Conversely, isotropic spheres do not display birefringence.

Publications

S. P. Armes; L. A. Fielding; **M. J. Derry**, Block Copolymer Synthesis, **2014** (filed 2013), Patent number WO2014049363-A1.

L. A. Fielding; **M. J. Derry**; V. Ladmiral; J. Rosselgong; A. M. Rodrigues; L. P. D. Ratcliffe; S. Sugihara; S. P. Armes, RAFT Dispersion Polymerization in Non-Polar Solvents: Facile Production of Block Copolymer Spheres, Worms and Vesicles in *n*-Alkanes, *Chemical Science*, **2013**, 4, 2081-2087.

L. A. Fielding; J. A. Lane; **M. J. Derry**; O. O. Mykhaylyk; S. P. Armes, Thermo-Responsive Diblock Copolymer Worm Gels in Non-Polar Solvents, *Journal of the American Chemical Society*, **2014**, 136, 5790-5798.

M. J. Derry; L. A. Fielding; S. P. Armes, Industrially-Relevant Polymerization-Induced Self-Assembly Formulations in Non-Polar Solvents: RAFT Dispersion Polymerization of Benzyl Methacrylate, *Polymer Chemistry*, **2015**, 6, 3054-3062.

A. P. Lopez-Oliva; N. J. Warren; A. Rajkumar; O. O. Mykhaylyk; **M. J. Derry**; K. Doncom; M. J. Rymaruk; S. P. Armes, Polydimethylsiloxane-Based Diblock Copolymer Nano-Objects Prepared in Non-Polar Media via RAFT-Mediated Polymerization-Induced Self-Assembly, *Macromolecules*, **2015**, 48, 3547-3555.

K. L. Thompson; C. J. Mable; J. A. Lane; **M. J. Derry**; L. A. Fielding; S. P. Armes, Preparation of Pickering Double Emulsions Using Block Copolymer Worms, *Langmuir*, **2015**, 31, 4137-4144.

K. L. Thompson; L. A. Fielding; O. O. Mykhaylyk; J. A. Lane; **M. J. Derry**; S. P. Armes, Vermicious Thermo-Responsive Pickering Emulsifiers, *Chemical Science*, **2015**, 6, 4207-4214.

K. L. Thompson; J. A. Lane; **M. J. Derry**; S. P. Armes, Non-Aqueous Isorefractive Pickering Emulsions, *Langmuir*, **2015**, 31, 4373-4376.

D. J. Growney; P. W. Fowler; O. O. Mykhaylyk; L. A. Fielding; **M. J. Derry**; N. Aragrag; G. D. Lamb; S. P. Armes, Determination of Effective Particle Density for Sterically Stabilized Carbon Black Particles: Effect of Diblock Copolymer Stabilizer Composition, *Langmuir*, **2015**, 31, 8764-8773.

D. J. Growney; O. O. Mykhaylyk; L. A. Middlemiss; L. A. Fielding; **M. J. Derry**; N. Aragrag; G. D. Lamb; S. P. Armes, Is Carbon Black a Suitable Model Colloidal Substrate for Diesel Soot?, *Langmuir*, **2015**, 31, 10358-10369.

M. J. Derry; L. A. Fielding; S. P. Armes, Polymerization-Induced Self-Assembly of Block Copolymer Nanoparticles via RAFT Non-Aqueous Dispersion Polymerization, *Progress in Polymer Science*, **2016**, 52, 1-18.

M. J. Derry; L. A. Fielding; N. J. Warren; C. J. Mable; A. J. Smith; O. O. Mykhaylyk; S. P. Armes, *In situ* Small-Angle X-ray Scattering Studies of Sterically-Stabilized Diblock Copolymer Nanoparticles Formed During Polymerization-Induced Self-Assembly in Non-Polar Media, *Chemical Science*, **2016**, Advance Article, DOI:10.1039/C6SC01243D.

V. J. Cunningham; **M. J. Derry**; L. A. Fielding; S. P. Armes; O. M. Musa, RAFT Aqueous Dispersion Polymerization of *N*-2-(methacryloyloxy)ethyl pyrrolidone: A Convenient Low-Viscosity Route to High Molecular Weight Water-Soluble Copolymers, *Macromolecules*, **2016**, 49, 4520-4533.

M. J. Rymaruk; K. L. Thompson; **M. J. Derry**; N. J. Warren; L. P. D. Ratcliffe; C. N. Williams; S. L. Brown; S. P. Armes, Bespoke Contrast-Matched Diblock Copolymer Nanoparticles Enable the Rational Design of Highly Transparent Pickering Double Emulsions, submitted manuscript, **2016**.

M. J. Derry; O. O. Mykhaylyk; S. P. Armes, A Vesicle-to-Worm Transition for Block Copolymer Vesicles Prepared by RAFT Dispersion Polymerization Enables High-Temperature Thickening of Automotive Engine Oils, manuscript in preparation.

M. J. Derry; O. O. Mykhaylyk; S. P. Armes, Shear-Induced Alignment of Worm Gels, manuscript in preparation.

M. J. Derry; S. P. Armes, Temperature-Dependent Properties of Poly(behenyl methacrylate)-Stabilized Diblock Copolymer Nanoparticles Prepared by Polymerization-Induced Self-Assembly, manuscript in preparation.

Conferences

March 2013	S4SAS Workshop and Meeting, organised by Diamond Light Source, Sheffield, UK
July 2013	Poster presentation at Macro Group Young Researcher's Meeting, Nottingham, UK
August 2013	Poster presentation at 10th IUPAC International Conference on Advanced Polymers via Macromolecular Engineering, Durham, UK
May 2014	Sheffield University GRAD School, Sheffield, UK
July 2014	Poster presentation at UK Colloids 2014, London, UK
July 2014	Oral presentation at Macro Group Young Researcher's Meeting, Durham, UK
August 2014	Poster presentation at 248th ACS National Meeting, San Francisco, USA
September 2014	Poster presentation at Northern University Postgraduate Symposium, Sheffield, UK
March 2015	Arrested Gels: Dynamics, Structure and Applications, Cambridge, UK
June 2015	Oral presentation at European Polymer Federation 2015 Meeting, Dresden, Germany
August 2015	Two oral presentations at 250th ACS National Meeting, Boston, USA
September 2015	Oral presentation at 29th European Colloid and Interface Society Conference, Bordeaux, France

Acknowledgements

I am extremely lucky to have received the support of so many people over the past few years. Firstly, I am immensely indebted to Prof. Steve Armes FRS for giving me the opportunity to carry out my PhD studies in his great research group. Your advice, support, encouragement and meticulous proof reading have been greatly appreciated. I must also thank you for providing me with the opportunity to travel to several national and international conferences. A massive thank you goes to Dr. Oleksandr Mykhaylyk (Sasha, the SAXS man) for your thorough explanations of all things SAXS, rheology and general polymer physics, regardless of how many times I asked. I also owe a lot to Dr. Lee Fielding for helping me find my feet in the lab and for throwing me into the first of many football matches on my very first day in the group. I also thank the amazing SAXS team, without who those long, long night shifts would not have been bearable: Sasha, Lee, Dr. Nick Warren, Charlotte Morse, Dr. Pengcheng Yang and Dr. Liam Ratcliffe.

My industrial sponsors, Lubrizol Corporation Ltd., are of course thanked for their generous funding and also for their enthusiasm whenever discussing my project. My thanks go to Dr. Tim Smith and Dr. Paul O'Hora as my direct industry supervisors, as well as the many other people within the organisation who have conducted experiments or taken time to discuss my research. I must also thank the people who have helped with various techniques during my studies: Dr. Svetomir Tzokov (TEM), Sue Bradshaw and Dr. Geoff Akien (NMR), Dr. Andy Smith (SAXS at I22, Diamond Light Source) and Dr. Sylvain Prevost (SAXS at ID02, ESRF).

Of course, every member of the Armes group past and present have played their part. As well as those already mentioned, thanks go to Dr. Mark Williams, Dr. Andrew Morse, Dr. Kate Kirkham, Dr. Jeppe Madsen, Dr. David Growney, Dr. Lizzy Jones, Dr. Andreas Hanisch, Dr. Carlo Gonzato, Dr. Greg Smith, Dr. Sarah Canning, Dr. Beulah McKenzie, Dr. Joe Lovett, Vicki Cunningham, Nick Penfold, Yin Ning, Amy Cockram, Matt Rymaruk, Jake Lane and Erik Jan Cornel. I would also like to thank all of the staff in the Accounts office and Stores for their help throughout my project and also the common room staff for providing the necessary tea breaks!

Sport plays a massive role in keeping me going, so I must thank all of those who have played football with me for the Panthers, Armes Animals, various ChemSoc teams as well as the Wednesday football crew and also the squash team (Lee, Andrew, Penfold, Rymaruk, Carlo, Liam R and Greg).

I would like to thank my entire family for supporting me over the years. In particular Mom and Dad for your unconditional love, support and encouragement, and for always asking how things were going in the lab regardless of whether you were going to understand, as well as Nan for your support, but also for the impeccable tactical analysis after each and every Liverpool match or England football or cricket game. The Arnold clan have always been enthusiastic about my studies and I am extremely grateful for that. My great friends from home, particularly Pricey, are thanked for making it seem like I had never left when I visit. Also to my friends from my time in York, especially Tom and Heppel, for the regular catch ups filled with moments where we can't speak due to laughter, often caused by Tom's clumsy antics or Heppel's Geordie tendencies.

Finally, I am unbelievably grateful to Lucy. You have been at my side every step of the way and coming home and being generally silly with you provides the perfect remedy to those long days in the lab. You are my best friend and I know I can always rely on your love and support for whatever the future holds.

Nomenclature

η	-	Viscosity
η_{sp}	-	Specific viscosity
φ_{BzMA}	-	Volume fraction of BzMA monomer within the core domain
ω	-	Angular frequency
AGO	-	Automotive gear oil
AIBN	-	2,2'-azobisisobutyronitrile
ATRP	-	Atom transfer radical polymerisation
BzMA	-	Benzyl methacrylate
CDB	-	Cumyl dithiobenzoate
CGC	-	Critical gelation concentration
CGT	-	Critical gelation temperature
CTA	-	Chain transfer agent
D_{in}	-	Inner vesicle core diameter
d_{int}	-	Distance between adjacent copolymer chains at the core-shell interface
D_{out}	-	Outer vesicle core diameter
D_s	-	Spherical core diameter
DLS	-	Dynamic light scattering
DP	-	Degree of polymerisation
EGDMA	-	Ethylene glycol dimethacrylate
FRP	-	Free-radical polymerisation
G'	-	storage modulus
G''	-	Loss modulus
GMA	-	Glycerol monomethacrylate
GMO	-	Glyceryl monooleate
GPC	-	Gel permeation chromatography
HPMA	-	2-Hydroxypropyl methacrylate
L_w	-	Worm contour length
LAP	-	Living anionic polymerisation
LMA	-	Lauryl methacrylate

M_n	-	Number-average molecular weight
M_w	-	Weight-average molecular weight
MAA	-	Methacrylic acid
Macro-CTA	-	Macromolecular chain transfer agent
MMA	-	Methyl methacrylate
MWD	-	Molecular weight distribution
N_s	-	Number of copolymer chains per sphere
N_v	-	Number of copolymer chains per vesicle
NMP	-	Nitroxide-mediated polymerisation
NMR	-	Nuclear magnetic resonance
PAO	-	Poly(α-olefin)
PETTC	-	4-Cyano-4-(2-phenylethane sulfanylthiocarbonyl)sulfanylpentanoic acid
PISA	-	Polymerisation-induced self-assembly
PMA	-	Poly(methacrylate)
PPD	-	Pour point depressant
PRE	-	Persistent radical effect
q	-	Scattering vector
R_g	-	Radius of gyration
R_{in}	-	Vesicle inner core radius
R_{out}	-	Vesicle outer core radius
R_s	-	Spherical core radius
RAFT	-	Reversible addition-fragmentation chain transfer
RDRP	-	Reversible deactivation radical polymerisation
RI	-	Refractive index
S_{agg}	-	Number of copolymer chains per unit surface area
SAXS	-	Small-angle X-ray scattering
SIPLI	-	Shear-induced polarised light imaging
SMA	-	Stearyl methacrylate
SRR	-	Slide-to-roll ratio
T21s	-	*Tert*-butyl peroxy-2-ethylhexanoate
T_m	-	Vesicle membrane thickness

T_w	-	Worm thickness
TEM	-	Transmission electron microscopy
THF	-	Tetrahydrofuran
UCST	-	Upper critical solution temperature
V_m	-	Molecular volume of a single PBzMA core-forming block within the vesicle membrane
V_s	-	Molecular volume of a single PBzMA core-forming block within the spherical core
VM	-	Viscosity modifier
x_{sol}	-	Volume fraction of solvent within the core domain

Contents

1. Introduction

1.1. Polymers

A polymer is a long-chain molecule formed from many smaller repeat units, or monomers. The simplest polymer is a homopolymer, which is synthesised from a single monomer. The general nomenclature of the resulting homopolymer is usually poly(monomer), for example methyl methacrylate (MMA) is polymerised to form poly(methyl methacrylate) (PMMA).

Unlike small molecules, polymers do not have a single unique molecular weight. Instead, polymers possess a molecular weight distribution (MWD). The MWD can be represented by polydispersity index (PDI), or simply dispersity (*Đ*) as recommended by the International Union of Pure and Applied Chemistry (IUPAC) in 2009,[1] which is defined as the weight-average molecular weight (M_w) divided by the number-average molecular weight (M_n).

$$\text{PDI or Đ} = \frac{M_w}{M_n} \qquad 1.1$$

A polymer chain comprises an *average* number of repeat units, known as the mean degree of polymerisation (DP). Two common terms used to describe the molecular weight of a polymer are M_n and M_w. The M_n is defined as:

$$M_n = \frac{\sum n_i M_i}{\sum n_i} \qquad 1.2$$

where n_i is the number of chains containing *i* repeat units, and M_i is the molecular weight of these chains. Statistically, the M_n value tells us the average molecular weight of a polymer chain if we were to select a single chain at random. The M_w is defined as:

$$M_w = \frac{\sum w_i M_i}{\sum w_i} = \frac{\sum n_i M_i^2}{\sum n_i M_i} \qquad 1.3$$

where w_i is the weight fraction of chains with *i* repeat units, which is equal to the product of $n_i M_i$. M_w differs from M_n since it represents the average molecular weight of an individual chain upon randomly selecting one monomer unit. Considering both the M_w and M_n values provides information on the MWDs (see Equation 1.1).

If every polymer chain within a sample has the same DP and therefore the same M_n and M_w values, then M_w/M_n is equal to unity and such samples are said to be monodisperse (e.g. proteins).[2] Typically, a MWD is considered to be narrow if M_w/M_n is less than 1.5, whereas it is regarded as broad if the PDI exceeds 2.0, as suggested by Hiemenz and Lodge.[3]

1.2. Polymer Characterisation

1.2.1. Gel Permeation Chromatography (GPC)

Various characterisation techniques have been developed to measure the molecular weight of polymers including end-group analysis, osmometry, light scattering, mass spectroscopy and viscometry.[3] However, by far the most commonly utilised technique is size exclusion chromatography (SEC), otherwise known as GPC. GPC differentiates between polymer chains of varying molecular weight based on their hydrodynamic volume (V_h). This is achieved using columns packed with porous beads, through which polymer chains with a smaller V_h flow more slowly, so the characteristic elution time for smaller chains is longer than those of larger chains. GPC is a comparative technique that requires the use of calibration standards such as PMMA or polystyrene (PS). Such standards are polymers of known molecular weight and narrow MWD, which elute at various retention times based on their V_h. Upon elution, the polymer chains are detected using a refractive index (RI), ultraviolet (UV) spectroscopy, viscosity or light scattering detector.[3] Cross-referencing the specific elution time with the calibration curve yields the molecular weight of the polymer chains relative to the specific calibration standards used. Since the unknown sample is rarely the same polymer type as that used for the calibration curve, the molecular weights obtained by this method are merely relative to that of the calibrant polymer. In order to determine absolute molecular weights, a 'universal' calibration method can be employed, where the Mark-Houwink equation is used to obtain the intrinsic viscosity ($[\eta]$):

$$[\eta] = KM^{\alpha} \qquad 1.4$$

where K and α are known values for a particular solvent-polymer pair at a given temperature. If the K and α values are known for the calibrant, the measured $[\eta]$ for

the unknown polymer can be used to determine its molecular weight. This is because the V_h can be represented as $\log([\eta]M)$, and:

$$\log([\eta]_c M_c) = \log([\eta]_s M_s) \qquad 1.5$$

where the subscripts 'c' and 's' are used to represent the calibrant and sample, respectively.[4] This allows the absolute molecular weight of the polymer to be calculated when a concentration detector (e.g. RI) and a viscosity detector are connected in parallel. If the K and α values are known for both the selected calibrant and sample of unknown molecular weight in a particular solvent, then the absolute molecular weight of the unknown polymer can be determined using:

$$M_s = \left(\frac{\left(K_c {M_c}^{1+\alpha_c}\right)}{K_s}\right)^{\frac{1}{1+\alpha_s}} \qquad 1.6$$

Since this latter method requires knowledge of the K and α parameters for both the calibrant and the unknown polymer in the eluent, the absolute molecular weight must be determined by an independent method such as light scattering.[3, 4]

1.2.2. Dynamic Light Scattering (DLS)

DLS is a technique commonly used to determine the hydrodynamic diameter (D_h) of particles. DLS must be measured for highly dilute dispersions, since inter-particle interactions should be negligible. The translational diffusion coefficient (D) of the particles is measured by monitoring the decay of a correlation function over time by following fluctuations in the scattered light intensity due to particles undergoing Brownian motion. D_h is then calculated according to the Stokes-Einstein equation:

$$D_h = \frac{k_B T}{3\pi\eta D} \qquad 1.7$$

where k_B is Boltzmann's constant, T is the absolute temperature and η is the solution viscosity.[5] Smaller particles diffuse faster than larger particles, so display a larger D value in a given solvent. Equation 1.7 assumes that the particles are spherical, so the

D_h reported by DLS is a sphere-equivalent diameter. DLS is highly biased towards larger particles, since the scattered light intensity scales as the sixth power of the particle diameter. This makes DLS highly sensitive to the onset of particle aggregation, but rather insensitive to particle dissociation.

1.2.3. Rheology of viscoelastic materials

Rheology is the study of the flow and/or deformation of a material upon the application of an external force.[6, 7] The force per unit area is known as the stress (σ). Shear deformation is the application of stress in one direction, and can be simply illustrated by considering the response of a cuboid to such an external force (see Figure 1.1). On the application of a shear stress (σ) to a solid or liquid, a flow or deformation is produced, defined as the displacement per unit length or strain (γ).

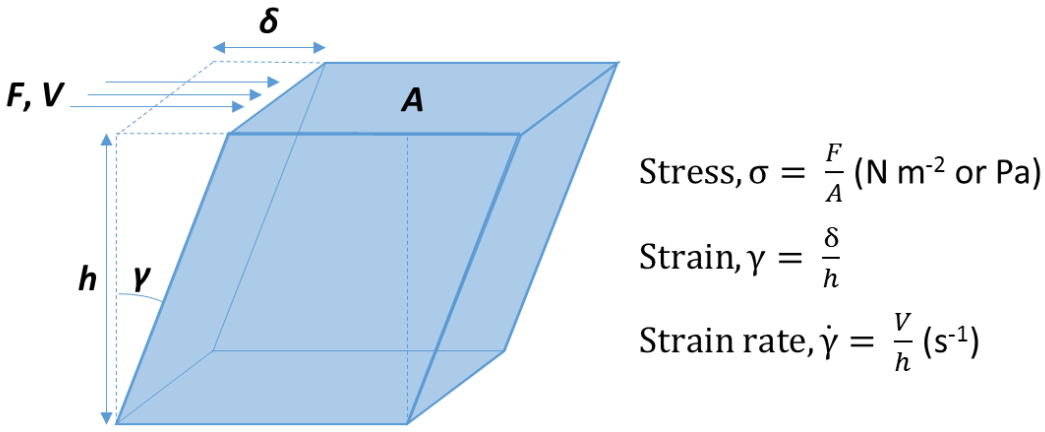

Figure 1.1. Shear deformation of a cuboid on the application of stress (σ) to one face with an area (A). F is the force applied, V is the velocity, h is the height and δ is the displacement. Equations for the stress (σ), strain (γ) and strain rate ($\dot{\gamma}$) are also given.

For a Newtonian liquid, which is defined as a liquid that exhibits shear rate-independent viscosity,[6-8] the stress (σ) can be defined as the viscosity (η) of the fluid multiplied by the strain rate ($\dot{\gamma}$), i.e. $\sigma = \eta\dot{\gamma}$, hence σ is dependent on $\dot{\gamma}$. For a Hookean (elastic) solid, σ can be defined as the elastic modulus (G) multiplied by the strain (γ), $\sigma = G\gamma$, and so σ is dependent on the magnitude of G. These definitions indicate that a Newtonian liquid immediately deforms upon the application of stress, and continues to deform until the strain rate ($\dot{\gamma}$) is zero. Conversely, a Hookean solid deforms to a discrete extent and returns to its original state upon removal of the applied stress. However, for the purpose of this Thesis, it is appropriate to consider a combination of

these responses rather than a purely viscous or elastic response. Therefore, the *viscoelastic* and, more specifically, *linear viscoelastic* behaviour of a material is considered. In the linear viscoelastic region, a linear dependence of stress and strain is observed (i.e. on doubling the applied stress, the resulting strain is doubled). For the following discussion, it is useful to consider a Newtonian fluid as a dashpot (a cup filled with a viscous, Newtonian fluid with a plunger moving through it) and a Hookean solid as a spring (see Figure 1.2). The Maxwell model is the simplest model of a viscoelastic *liquid*, where a spring and dashpot are arranged in series. The Kelvin-Voigt model considers the spring and dashpot arranged in parallel and is the simplest model for a viscoelastic *solid* (Figure 1.2).[8]

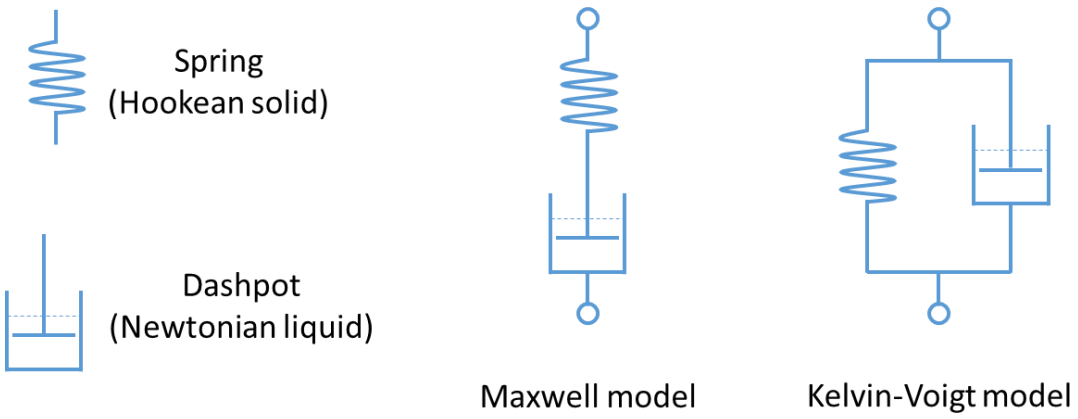

Figure 1.2. Illustrated examples for the mechanical analogues of a Hookean solid or spring, Newtonian fluid or liquid and the Maxwell and Kelvin-Voigt models for viscoelastic materials.[7, 8]

The response of viscoelastic materials to an applied stress is determined by the relative amounts of viscous and elastic behaviour exhibited by the material. The relaxation time (τ) is the time taken for the material to return to its original state, and is represented by:[8]

$$\tau = \frac{\eta}{G} \qquad 1.8$$

Thus the characteristic relaxation time for a viscoelastic solid is shorter than that for a viscoelastic liquid. There are various experimental methods to evaluate the viscoelastic properties of a material, including creep, stress relaxation, start-up and oscillatory measurements. In creep measurements, a constant stress is applied and the resulting strain is monitored as a function of time. In some cases, the deformation

under constant stress can be very slow (months to years, e.g. glass) and such behaviour is termed creep. Stress-relaxation measurements involve the sudden application of strain and the monitoring of the resulting stress, whereas start-up experiments involves the application of a constant strain rate and measurement of the resulting stress. Oscillatory measurements will be used in this Thesis, where a typical cone-and-plate geometry (see Figure 1.3) is utilised.

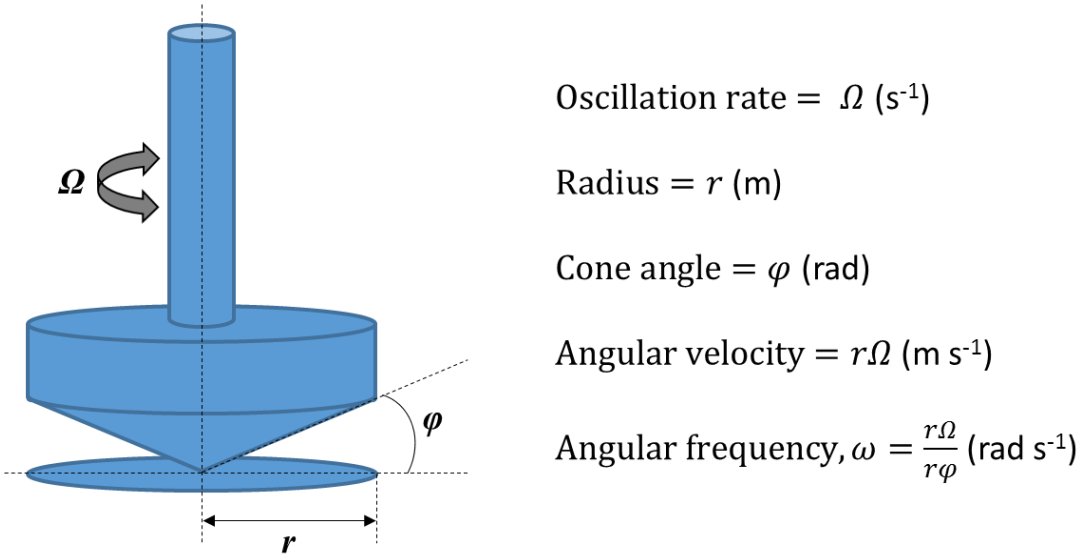

Figure 1.3. Cone-and-plate geometry used for oscillatory measurements of viscoelastic materials.

For oscillatory rheology, the input strain is applied in a sinusoidal fashion and the resulting sinusoidal stress is resolved. When a fixed strain is applied the amplitude of the wave represents the maximum strain and the frequency of the wave indicates the oscillation rate (Ω). The phase difference (δ) between the input strain and output stress indicates the physical properties of the material. For a material with a solely elastic response, the input stress and output strain will be in phase with one another ($\delta = 0°$). Conversely, a material with a solely viscous response will display an output stress which is out of phase with the input strain ($\delta = 90°$).[6] In reality, the phase difference for a viscoelastic material lies between that for an ideal solid and an ideal liquid. A more useful measure of this ratio between viscous and elastic behaviour at a given angular frequency is tan δ, which is equal to the loss modulus (G") divided by the storage modulus (G'), i.e. tan $\delta = G"/G'$.[8] Thus, if a Hookean solid is oscillated, $G' = \sigma/\gamma$ and $G" = 0$, whereas for a Newtonian fluid, $G' = 0$ and $G" = \eta\omega$. Importantly, in

the linear viscoelastic region, the values of G' and G'' for a viscoelastic material depend only on the angular frequency (ω) and are independent of the strain (i.e. the amplitude of oscillation). This linear region is often quite narrow, so it must be determined experimentally before performing additional measurements. A viscoelastic material exhibits varying behaviour over a wide range of angular frequencies (see Figure 1.4).

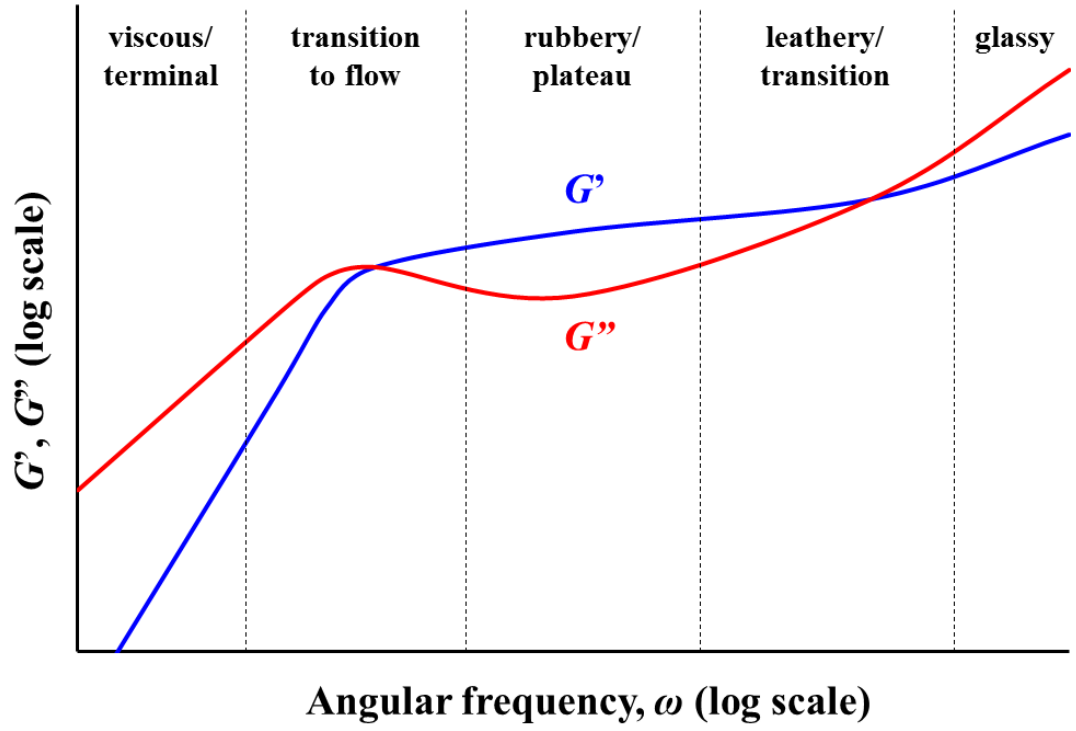

Figure 1.4. Typical dependence of the storage modulus (G') and loss modulus (G'') with angular frequency (ω) of a viscoelastic material during oscillatory measurements using a cone-and-plate geometry.[8]

Five distinct regions are shown in the frequency sweep (see Figure 1.4). The viscous or terminal region is observed at low frequencies, where viscous (G'') behaviour prevails. Crossover in the G' and G'' curves occurs in the transition to flow region, where elastic behaviour begins to dominate (when $G' > G''$). The crossover point corresponds to the relaxation time (τ) of the material, where $\tau = 1/\omega$. Elastic behaviour dominates throughout the rubbery or plateau region. Ideal viscoelastic materials possess a frequency-independent G' in this regime, with G'' being much (often more than an order of magnitude) smaller than G'. G'' becomes more significant in the leathery or transition region and another crossover point is observed. Again, the ω

value at which $G' = G''$ indicates τ. At very high frequencies, the glassy region is reached. Here, G'' again exceeds G' and increases at a faster rate than G' at higher ω.[8] For most commercial rheometers, typically only one or two of the five regions shown in Figure 1.4 are experimentally accessible, depending on the properties of the material. Varying the temperature at which such measurements are performed enables a broader viscoelastic range to be monitored.[8] Other geometries such as parallel plates are also commonly utilised for various measurements, which will be discussed in Chapter 5.

For the purpose of this Thesis, it is important to consider the viscoelastic properties of gels. It is generally accepted that a gel should exhibit a pronounced G' plateau over an appreciable frequency range with G'' being considerably smaller than G'.[6] Although there are many classes of gels, including well-ordered structures, highly disordered covalent networks and physical networks, all gels arise from the formation of an extended 3D structure. Gels can also be formed when polymer particles are dispersed in a continuous phase. In particular, worm-like nanoparticles formed by block copolymers can form free-standing gels at relatively low copolymer concentrations.[9] This phenomenon will be discussed in detail in this Chapters 2 and 5.

1.3. Chain Polymerisation

Two major classes of polymerisation are step-growth (or condensation) and chain-growth (or addition) polymerisation.[3] For the purpose of this Thesis, only chain-growth polymerisation will be discussed in detail. Chain polymerisation usually involves the reaction of vinyl monomers to yield single σ bonds, which is triggered by a reactive initiating species such as a radical, cation or anion.[10]

1.3.1. Free Radical Polymerisation (FRP)

FRP is an example of a chain polymerisation that provides an effective and convenient method of polymerising a wide range of vinyl monomers with various functionalities and under many different reaction conditions.[10] In the case of FRP, radicals ($I^{\bullet}$) are usually produced via homolytic cleavage of an initiator (I_2) at a characteristic rate described by the rate constant for initiator decomposition, k_d.

$$I_2 \xrightarrow{k_d} 2\,I^{\bullet}$$

These reactive radicals immediately react with monomer (M), at a rate constant for initiation, k_i (where $k_d << k_i$). This forms a new active radical centre (I-M$^{\bullet}$ or $P_1^{\bullet}$).

$$I^{\bullet} + M \xrightarrow{k_i} I\text{-}M^{\bullet}\ (= P_1^{\bullet})$$

Further addition of monomer to this active radical centre is termed propagation, which proceeds at a rate constant k_p. Since $k_d << k_p$, the decomposition of initiator is the rate-limiting step determined by the initiator half-life, $t_{1/2} = \ln(2)/k_d$. Also, the initiator efficiency (f) can be reduced due to the cage effect, where primary recombination ($I^{\bullet} + I^{\bullet} \rightarrow I_2$) can occur within the solvent cage. Successive monomer addition occurs at essentially the same rate of propagation (k_p) since k_p is independent of the length of the polymer chain. These propagation events can be generalised as the addition of a single monomer unit to a polymer radical with a mean DP of n ($P_n^{\bullet}$) to form a new polymer radical that is larger by one monomer residue ($P_{n+1}^{\bullet}$).

$$P_n^{\bullet} + M \xrightarrow{k_p} P_{n+1}^{\bullet}$$

Propagation of monomers occurs mostly via a head-to-tail mechanism, whereby X groups of the initial vinyl monomers ($H_2C{=}CHX$) are found on alternate carbon atoms within the polymer backbone. This scenario is generally favoured on both steric and electronic grounds. Such propagation proceeds until termination occurs, where one active species ($P_n^{\bullet}$) reacts with another ($P_m^{\bullet}$) to form an inactive or 'dead' polymer chain. This can occur via combination (with a rate constant k_{tc}) or via disproportionation (with a rate constant k_{td}). Termination by combination is simply the coupling of two radical species to form a 'dead' polymer chain with a DP equal to the sum of the two initial reactive species (P_{n+m}).

$$P_n^{\bullet} + P_m^{\bullet} \xrightarrow{k_{tc}} P_{n+m}$$

In contrast, termination by disproportionation involves abstraction of a hydrogen atom from one polymer radical by another to produce a polymer with an unsaturated terminus ($P_n{=}$) and another 'dead' polymer with a saturated terminus (P_m-H).

$$P_n^{\bullet} + P_m^{\bullet} \xrightarrow{k_{td}} P_n{=} + P_m\text{-}H$$

The overall rate constant for termination (k_t) can therefore be described as the sum of k_{tc} and k_{td}.

Although initiation, propagation and termination are the three most important steps during FRP, a number of side reactions may also occur. The first side reaction to consider is transfer to initiator, whereby an active polymer chain reacts with an initiator molecule that has not yet undergone homolytic cleavage (I_2) to form an initiator-capped 'dead' polymer chain (P_n-I) and an active initiator species ($I^{\bullet}$) with a rate constant k_{trI}.

$$P_n^{\bullet} + I_2 \xrightarrow{k_{trI}} P_n\text{-}I + I^{\bullet}$$

Similarly, transfer to monomer or solvent can occur, where $P_n^{\bullet}$ abstracts a hydrogen atom from a monomer (M) or solvent (S) molecule with a characteristic rate constant k_{trM} or k_{trS}, respectively.

$$P_n^{\bullet} + M \xrightarrow{k_{trM}} P_n + M^{\bullet}$$

$$P_n^{\bullet} + S \xrightarrow{k_{trS}} P_n + S^{\bullet}$$

Also, transfer to another polymer chain (with rate constant k_{trPol}) may also occur via hydrogen abstraction, resulting in one 'dead' polymer chain and one active polymer chain with the radical being located at some point along the main chain, which can lead to chain branching.

$$P_n^{\bullet} + P_x \xrightarrow{k_{trPol}} P_n + P_x^{\bullet}$$

Since these four chain transfer side reactions do not consume radical species, they should not adversely affect the overall polymerisation kinetics. In fact, the radical species formed from each chain transfer step ($I^{\bullet}$, $M^{\bullet}$, $S^{\bullet}$ or $P_x^{\bullet}$) is capable of reinitiation, thus forming new $P_n^{\bullet}$ species.

Each of the polymerisation steps described above have an associated rate equation, as summarised in Table 1.1.

Table 1.1. Rate equations for the main steps and chain transfer side reactions during free radical polymerisation.

Rate of decomposition	$R_{\mathrm{d}} = -\frac{\mathrm{d}[\mathrm{I}_2]}{\mathrm{dt}} = k_{\mathrm{d}}[\mathrm{I}_2]$
Rate of initiation	$R_{\mathrm{i}} = \frac{\mathrm{d}[P_1^{\bullet}]}{\mathrm{dt}} = 2fR_{\mathrm{d}} = 2fk_{\mathrm{d}}[\mathrm{I}_2]$
Rate of propagation	$R_{\mathrm{p}} = -\frac{\mathrm{d}[\mathrm{M}]}{\mathrm{dt}} = k_{\mathrm{p}}[\mathrm{M}][\mathrm{P_n}^{\bullet}]$
Rate of termination by combination	$R_{\mathrm{tc}} = -k_{\mathrm{tc}}[\mathrm{P_n}^{\bullet}]^2$
Rate of termination by disproportionation	$R_{\mathrm{td}} = -k_{\mathrm{td}}[\mathrm{P_n}^{\bullet}]^2$
Rate of termination	$R_{\mathrm{t}} = 2(k_{\mathrm{tc}} + k_{\mathrm{td}})[\mathrm{P_n}^{\bullet}]^2 = 2k_{\mathrm{t}}[\mathrm{P_n}^{\bullet}]^2$
Rate of chain transfer to initiator	$R_{\mathrm{trI}} = k_{\mathrm{trI}}[\mathrm{P_n}^{\bullet}][\mathrm{I}_2]$
Rate of chain transfer to monomer	$R_{\mathrm{trM}} = k_{\mathrm{trM}}[\mathrm{P_n}^{\bullet}][\mathrm{M}]$
Rate of chain transfer to solvent	$R_{\mathrm{trS}} = k_{\mathrm{trS}}[\mathrm{P_n}^{\bullet}][\mathrm{S}]$
Rate of chain transfer to polymer	$R_{\mathrm{trPol}} = k_{\mathrm{trPol}}[\mathrm{P_n}^{\bullet}][\mathrm{P_x}]$

Assuming that the chain transfer side reactions do not affect the polymerisation kinetics, the overall rate of polymerisation (R_{polym}) can be described using the following equation:

$$R_{\mathrm{polym}} = k_{\mathrm{p}}[\mathrm{M}]\sqrt{\frac{fk_{\mathrm{d}}[\mathrm{I}_2]}{k_{\mathrm{t}}}} \qquad 1.9$$

The derivation of this equation involves invoking the 'steady-state' approximation, which assumes that the rates of initiation and termination are equivalent ($R_i = R_t$). Also, it is assumed that the number of monomer molecules consumed during initiation is negligible compared to those consumed during propagation. Thus, it is shown that increasing both the monomer ([M]) and initiator ([I_2]) concentrations would result in a faster rate of polymerisation. Since initiators with relatively long $t_{1/2}$ values are used, the rate of initiation is much slower than that for propagation ($R_i << R_p$).[11] This, along with chain termination, results in the characteristically broad MWDs associated with FRP. The rate of any polymerisation can be monitored as a function of time by comparing the instantaneous monomer concentration ([M]) with the initial monomer concentration ([M_0]). Specifically, a plot of ln([M]/[M_0]) vs. time should be linear if the rate of polymerisation is first-order with respect to monomer.[3] The kinetic chain

length (D_k), which is defined as the mean number of monomer molecules consumed per radical active centre, can be calculated using the relative rates of propagation and termination as shown below, given that $R_i = R_t$ (and hence $[P_n^\bullet] = (f.k_d.[I_2]/k_t)^{0.5}$):

$$D_k = \frac{R_p}{R_t} = \frac{k_p[M][P_n^\bullet]}{2k_t[P_n^\bullet]^2} = \frac{k_p[M]}{2\sqrt{fk_dk_t[I_2]}} \qquad 1.10$$

Thus D_k (and hence the polymer molecular weight) is dictated by [M] and $[I_2]^{-0.5}$, with higher molecular weights being achieved when the monomer concentration is increased or the initiator concentration is reduced. Given that the rate of polymerisation is proportional to [M] and $[I_2]^{0.5}$, it is self-evident that it is difficult to efficiently synthesise high molecular weight polymers. The mean DP for polymers synthesised by FRP is influenced by the termination mechanism. For example, if termination occurs purely by combination, DP = $2D_k$, whereas if only termination by disproportionation occurs, DP = D_k. Since termination of polymer chains to form 'dead' species is prevalent in FRP, the production of sophisticated, well-defined block copolymer architectures via sequential monomer addition is not possible by this technique.[11]

1.3.2. Living Anionic Polymerisation (LAP)

LAP is an example of chain polymerisation developed by Szwarc in the 1950s where the reactive species is an anion.[12] Thus there is a mutual electrostatic repulsion between the growing polymer chain-ends and hence no intrinsic termination is possible. This results in a so-called 'living' polymerisation under ideal conditions ($k_i >> k_p$) when conducted using a suitable monomer in a dry, inert solvent. For such polymerisations, the molecular weight increases linearly with monomer conversion (see Figure 1.5) and polymers with very narrow MWDs can be achieved ($M_w/M_n \lesssim 1.10$).

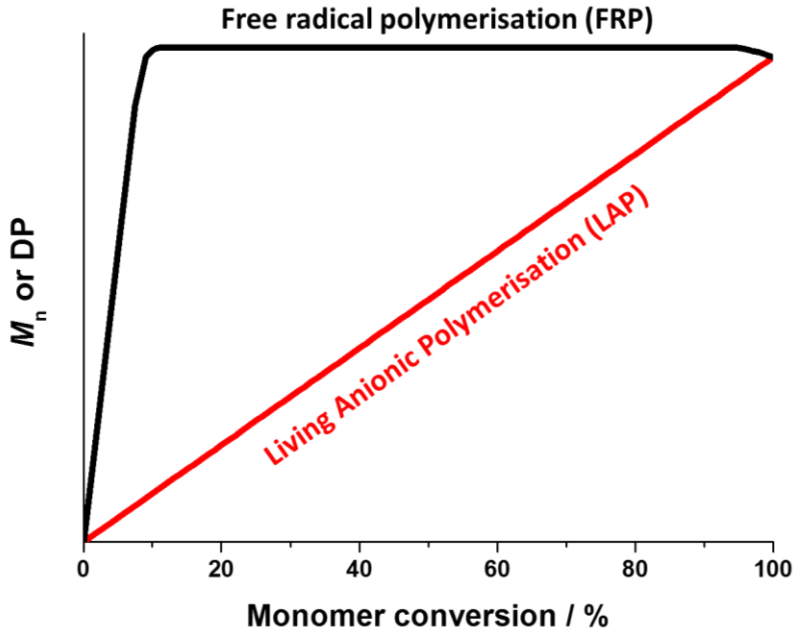

Figure 1.5. Variation of number-average molecular weight (M_n) or mean degree of polymerisation (DP) with monomer conversion for conventional free radical polymerisation (FRP, black data) and living anionic polymerisation (LAP, red data).

Suitable monomers for LAP include vinyl monomers (H_2C=CHX) with suitable electron-withdrawing X groups (e.g. phenyl, cyano or ester functionalities). The choice of solvent is also important, since protic solvents such as water react rapidly with the active anion species via proton transfer. For the same reason, any protic impurities in the monomer must be completely removed prior to polymerisation. The rate of propagation (and therefore the rate of the overall polymerisation if $k_i >> k_p$) is related to the concentration of propagating anionic polymer chains ($[P_n^-]$) and unreacted monomer molecules ([M]):[10]

$$R_p = k_p[P_n^-][M] \qquad 1.11$$

A general reaction scheme for LAP is shown in Scheme 1.1, where *n*-butyl lithium is used as a typical initiator.

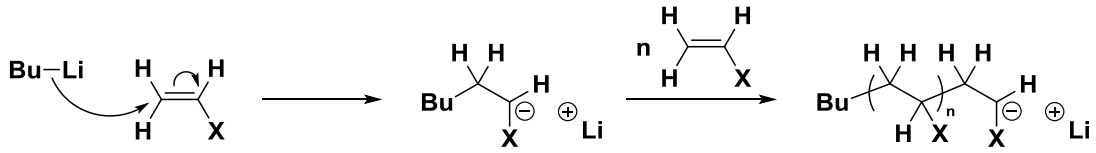

Scheme 1.1. General reaction scheme for the living anionic polymerisation (LAP) of a functional vinyl monomer such as styrene with an electron-withdrawing X group, where *n*-butyl lithium is used as an initiator.[10]

If it is assumed that each initiator molecule produces a propagating polymer chain, the DP of a polymer synthesised via LAP can be varied simply by adjusting the monomer/initiator molar ratio.[10] Moreover, well-defined block copolymers can be synthesised via sequential monomer addition due to the 'living' character of LAP. However, given the extreme sensitivity of LAP to protic solvents and impurities, there are only a few examples of polymers prepared via LAP on an industrial scale.

1.3.3. Reversible Deactivation Radical Polymerisation (RDRP)

RDRP is the IUPAC approved term for techniques commonly referred to as controlled radical polymerisation (CRP) or living radical polymerisation (LRP).[13] Generally, RDRP techniques involve the equilibrium between active and dormant polymer chains (after radical species are generated via the homolytic cleavage of an initiator as for conventional FRP), allowing control over the targeted molecular weight and polymers with a narrow MWD to be synthesised.[14] RDRP is particularly attractive since it combines the advantages of FRP and LAP whilst also eliminating some of their respective disadvantages. For example, FRP can be utilised to polymerise a wide range of monomers in a range of solvents with high tolerance to the functionality of each component, whereas LAP is limited to aprotic environments and monomers with electron withdrawing groups. However, FRP does not allow polymers with a targeted molecular weight and with a narrow MWD to be synthesised. Thus, RDRP enables a wide range of functional vinyl monomers to be polymerised in various solvents via a less synthetically demanding protocol whilst producing well-defined polymers with control over the molecular weight. As with LAP, sequential monomer addition enables the synthesis of sophisticated copolymer architectures (see Figure 1.6).

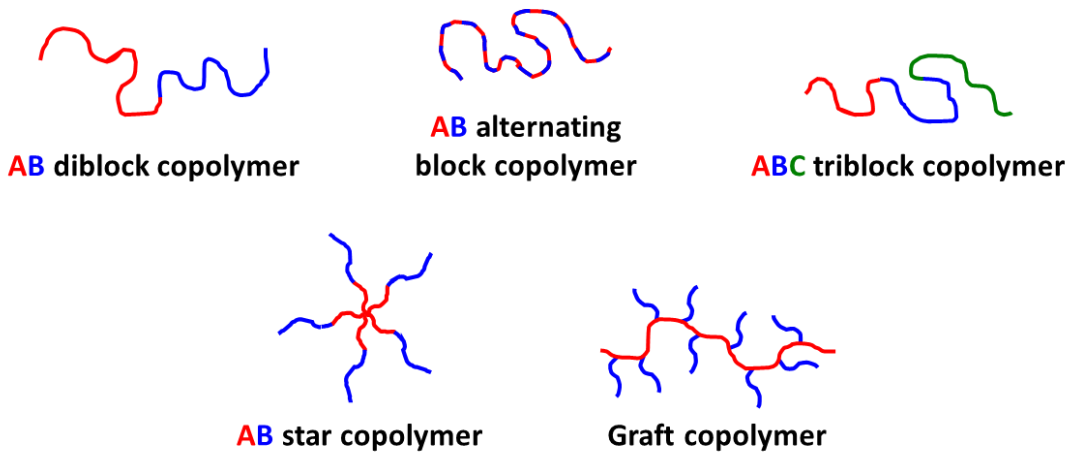

Figure 1.6. Examples of copolymer architectures accessible via reversible deactivation radical polymerisation (RDRP) techniques.[3, 15]

There are various examples of RDRP,[11, 14] but the most commonly used techniques are nitroxide-mediated polymerisation (NMP),[16] atom transfer radical polymerisation (ATRP)[17, 18] and reversible addition-fragmentation chain transfer (RAFT)[19] polymerisation. The key mechanistic step which links these RDRP techniques involves the rapid, dynamic equilibrium between active propagating polymer chains and deactivated or 'dormant' species.[20, 21] This serves to reduce the instantaneous polymer radical concentration and thus suppress the rate of termination (R_t) relative to that of propagation (R_p). This is because $R_t \propto [P_n^{\bullet}]^2$, whereas $R_p \propto [P_n^{\bullet}]$, as shown in Table 1.1. This results in a more controlled polymerisation and produces polymers with relatively narrow MWDs. There are two main ways by which such an equilibrium can be achieved. Firstly, propagating radicals can interact with a capping species, X, and form a deactivation/activation equilibrium as shown in Scheme 1.2, where k_{deact} and k_{act} are the rate constants for deactivation and activation, respectively.

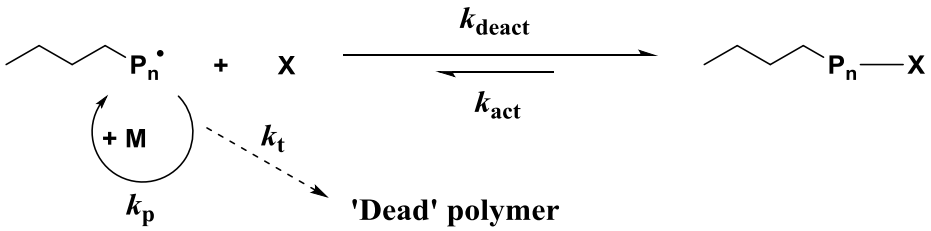

Scheme 1.2. Reversible deactivation/activation of a propagating polymer chain with a capping species, X.[11]

This approach is based on the persistent radical effect (PRE).[21, 22] Typically, the capping species, X, is a stable radical such as a nitroxide (as in NMP)[16] or a halide (as in ATRP).[18] X preferentially deactivates the propagating $P_n^{\bullet}$ radicals ($k_{deact} >> k_{act}$), thus favouring the dormant P_n-X species. The dormant P_n-X is then activated thermally (as in NMP) or catalytically (as in ATRP) to reform the propagating $P_n^{\bullet}$ radicals, which can either propagate (k_p) or terminate (k_t). However, X is a persistent radical and cannot terminate, but instead reversibly caps $P_n^{\bullet}$ (k_{deact}), meaning that the radical-radical ($P_n^{\bullet} + P_n^{\bullet}$) termination is accompanied by the irreversible accumulation of X.[11] Ultimately, this results in a reduction in the concentration of the $P_n^{\bullet}$ radicals and thus the probability of termination during the polymerisation. An alternative mechanistic pathway to achieve a dynamic equilibrium between active propagating radicals and dormant species involves degenerative transfer, as shown in Scheme 1.3, where k_{ex} is the rate constant for exchange.

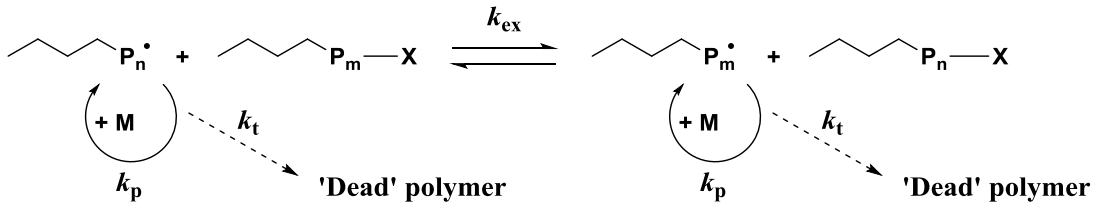

Scheme 1.3. Reversible capping of a propagating polymer chain via degenerative transfer.[11]

RDRP techniques that employ degenerative transfer do not rely on the PRE and are more closely related to the typical kinetics observed for FRP, where the steady-state concentration of $P_n^{\bullet}$ is determined by initiation and termination. Here the concentration of X (in the form of a chain transfer agent, CTA) is higher than that of the radical initiator. In order to achieve good control over the target molecular weight and MWD during the polymerisation, the rate of exchange of the CTA with $P_n^{\bullet}$ must be faster than the rate of propagation ($k_{ex} > k_p$).[11, 14, 23] This degenerative transfer mechanism is utilised in RAFT polymerisation, where X is a RAFT CTA such as a dithioester, trithiocarbonate, dithiocarbamate or xanthate. The specific nature of the RAFT CTA is selected for a given monomer class.[23]

1.3.3.1. Nitroxide-Mediated Polymerisation (NMP)

NMP is an example of a RDRP technique which utilises a PRE mechanism whether initiated using a conventional FRP initiator in the presence of a persistent radical or simply by using an alkoxyamine.[11] This technique is particularly attractive since it produces odourless polymers which do not require post-polymerisation purification.[24] Control is achieved via a dynamic equilibration between propagating radicals and dormant alkoxyamine species such as 2,2,6,6-tetramethylpiperidinyloxy (TEMPO, see Scheme 1.4), which is a sufficiently stable free radical that does not react with either monomer or itself.[16]

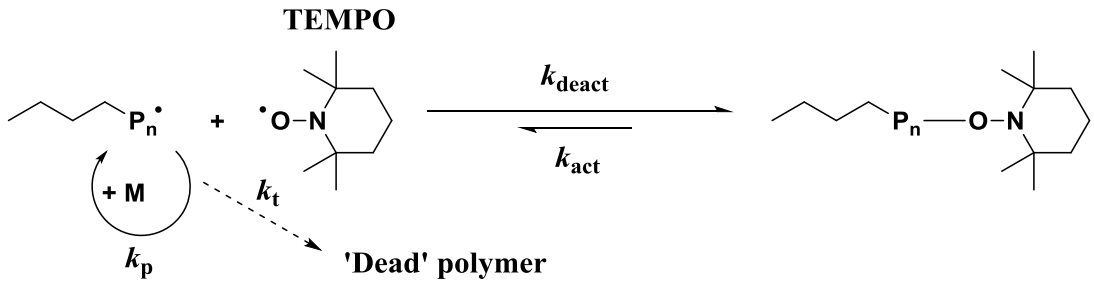

Scheme 1.4. Reversible deactivation/activation equilibrium for TEMPO-mediated NMP.[11]

Although TEMPO was successfully used for the controlled polymerisation of styrene at 120 °C (where $k_{deact} >> k_{act}$),[21] early attempts to perform TEMPO-mediated polymerisations for other monomers were unsuccessful. High temperatures are often required to activate the dormant nitroxide-capped polymer species, since the dynamic equilibrium is very strongly shifted towards the dormant species. This means that polymerisations in solvents with low (< 100 °C) boiling points are problematic. Such problems have been overcome via careful design of alternative nitroxides, where bulky substituents at the α-position can provide a more labile C-O bond and subsequently increase the steady-state concentration of polymer radicals during the polymerisation, so reducing the polymerisation temperature.[25, 26] Additionally, Benoit et al. developed so-called 'universal' alkoxyamines, which enabled the efficient polymerisation of a wide range of functional monomers (e.g. styrene, acrylates, acrylamides and acrylonitrile).[27] Although the introduction of sterically-hindered nitroxides enables NMP to be conducted at lower temperatures, this actually prevents the controlled homopolymerisation of methacrylates. This is because less reactive nitroxide species cannot cap propagating poly(methacrylate) radicals rapidly enough.[11] However, it has

been demonstrated that the bulk NMP copolymerisation of MMA with just 10 mol% styrene comonomer provides control the NMP at temperatures as low as 78 °C.[28, 29]

1.3.3.2. Atom Transfer Radical Polymerisation (ATRP)

ATRP is another example of RDRP developed by Sawamoto and co-workers[30] and Wang and Matyjaszewski[31] in 1995, which utilises the PRE to achieve good control over the target molecular weight and MWD.[11, 18, 32] In ATRP, the dormant species in the deactivation/activation dynamic equilibrium is usually a halide-capped polymer chain (P_n-X, see Scheme 1.5).[32] This dormant species is activated via reaction with a transition metal complex in their lower oxidation state (e.g. Cu^I/L), resulting in the formation of active propagating polymer radicals ($P_n^{\bullet}$) and a transition metal complex of a higher oxidation state (e.g. X-Cu^{II}/L).[33]

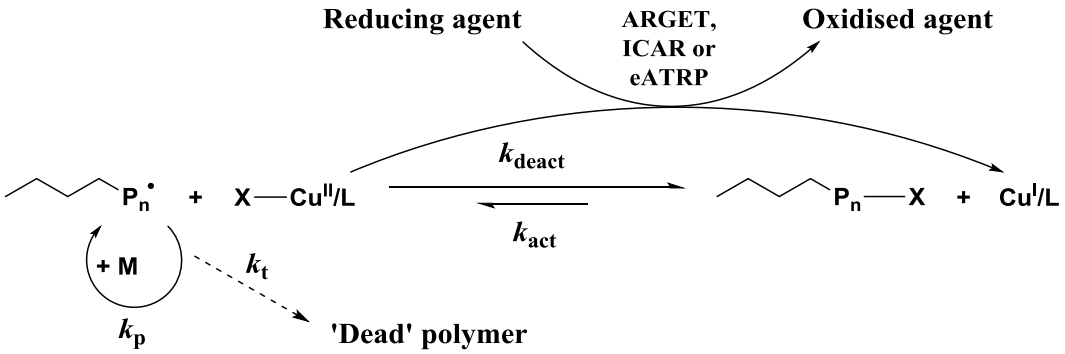

Scheme 1.5. The reversible deactivation/activation equilibrium for Cu-mediated ATRP together with recent advances for Cu(I) regeneration including activator (re)generated by electron transfer (ARGET), initiators for continuous activator regeneration (ICAR) or electrochemically-mediated ATRP (eATRP).[32]

ATRP control requires selection of an appropriate alkyl halide and metal catalyst for a particular monomer class. This may be problematic when attempting to synthesise block copolymers from two or more differing monomers with varying reactivities. Also, the cost of the transition metal catalyst, as well as subsequent removal of spent catalyst is a problem for many potential applications. However, there have been numerous recent advances in this area.[32] The development of new formulations where the metal catalyst is regenerated *in situ* enables lower catalyst concentrations (typically 5-50 ppm) to be used. Generally, this involves the presence of a reducing agent capable of returning the Cu(II) complex to its original Cu(I) state. 'Activator (re)generated by electron transfer' (ARGET)[34, 35] and 'initiators for continuous activator regeneration'

(ICAR)[36] ATRP are examples of this approach. ARGET ATRP involves addition of excess reducing agent which does not form a radical species (e.g. tin(2-ethylhexanoate) or ascorbic acid), whereas ICAR ATRP utilises a conventional free radical initiator (e.g. 2,2'-azobisisobutyronitrile, AIBN). Since the oxidised species produced in ARGET ATRP (e.g. tin(IV) species or dehydroascorbic acid) and ICAR (new propagating polymer chains) may not be as benign as the original reducing agents, electrochemically-mediated ATRP (eATRP) was developed.[37] In eATRP, electrons, rather and chemicals, are used to reduce the Cu(II) complex to the original Cu(I) state and the rate of polymerisation can be controlled by changing the applied potential.[37] Although these advances allow for a significantly lower catalyst concentration, it remains a technical challenge to remove the residual copper in an efficient and economical way.[32]

1.3.3.3. Reversible Addition-Fragmentation chain Transfer (RAFT) polymerisation

In 1998 Chiefari et al.[19] first reported RAFT polymerisation, which is a type of RDRP that utilises the degenerative transfer mechanism of reversibly capping active propagating polymer radicals, as shown in Scheme 1.3. Since this polymerisation technique is employed throughout this Thesis, the detailed RAFT polymerisation mechanism is shown in Figure 1.7. As with conventional FRP, RAFT polymerisation comprises initiation, propagation, transfer and termination steps. The introduction of the RAFT CTA (1) leads to the rapid and reversible capping of the active propagating polymer radical ($P_n^{\bullet}$) to form a dormant radical species (2). The Z group of the RAFT CTA is important, because it must be capable of stabilising this intermediate radical species and thus reducing the instantaneous concentration of $P_n^{\bullet}$ in order to gain control over the polymerisation. The R group of the RAFT CTA must be a good radical leaving group to produce the stable CTA-capped polymer (3). In addition, its radical ($R^{\bullet}$) must be capable of re-initiating polymerisation to form other propagating species ($P_m^{\bullet}$). The 'living' character of RAFT polymerisations is achieved via rapid exchange between the propagating species $P_n^{\bullet}$ and $P_m^{\bullet}$ and their dormant CTA-capped species (4), as shown in the chain equilibrium and propagation step in Figure 1.7. Again, the importance of the Z group is highlighted here, since it must be capable of stabilising the dormant radical species (5).

Initiation and propagation:

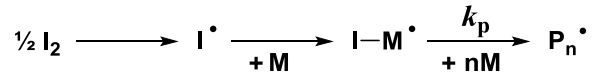

Reversible chain transfer and propagation:

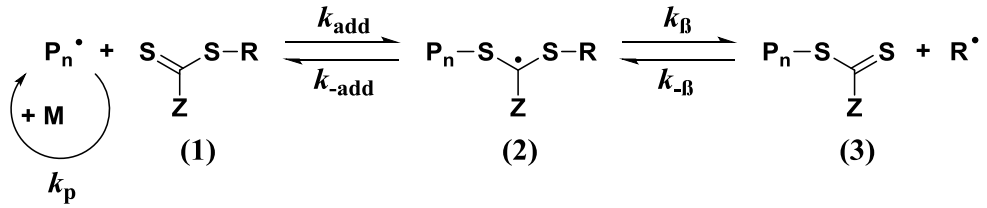

Reinitiation:

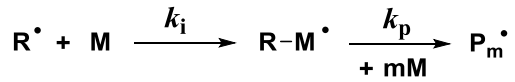

Chain equilibration and propagation:

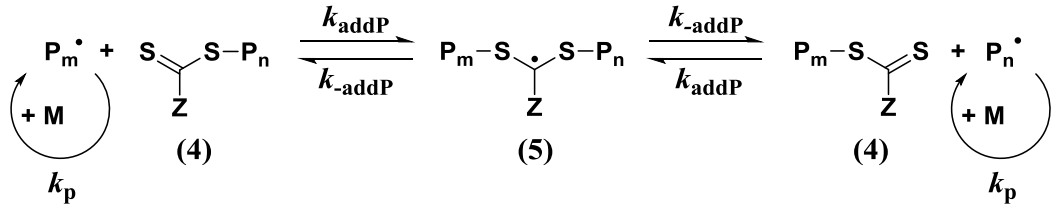

Termination:

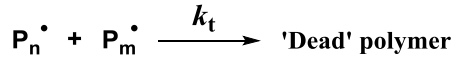

Figure 1.7. The mechanism of RAFT polymerisation.[14, 38, 39]

Efficient RAFT polymerisations should have high k_{add} and k_{β} where $k_{\beta} \geq k_{add}$, thus favouring the dormant species (2) and (3) while generating the R• radicals to re-initiate the polymerisation.[14] This re-initiation must be efficient ($k_i > k_p$) and the ratio of k_{addR} and k_{-addR} should also be considered, as shown in Scheme 1.6 below.

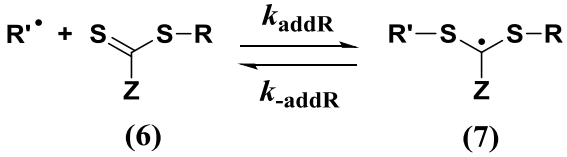

Scheme 1.6. Reversible chain transfer during RAFT polymerisation.[38-40]

It is often assumed that fragmentation is fast and that the lifetime of species (7) is negligible (if $k_{-addR} >> k_{addR}$). However, if fragmentation is slow, potential side reactions involving species (7) cannot be ignored.[39] Coote et al.[41] reported that the equilibrium

constant between active radical species such as $I^{\bullet}$, $I\text{-}M^{\bullet}$ and $P_n^{\bullet}$ and their corresponding dormant species depended on the polymer (or oligomer) chain length and the chemical nature of the groups adjacent to the radical center.

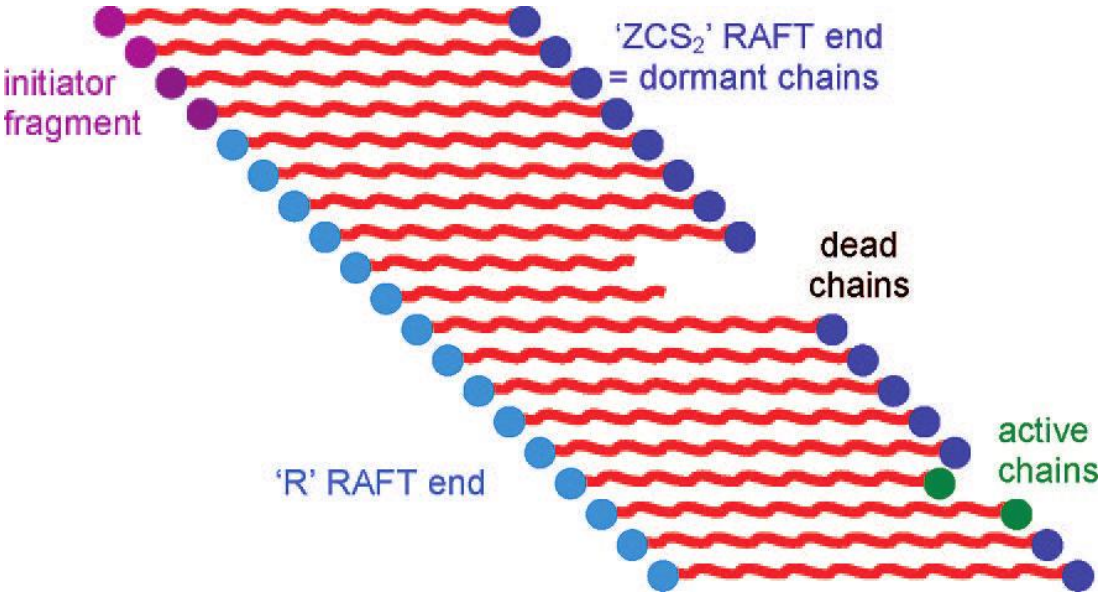

Figure 1.8. Schematic representation of the various types of polymer chain-ends present during the RAFT polymerisation process. The relative proportions of active, dormant and dead chains is not representative of a well-controlled RAFT polymerisation, but merely serves as a useful representation for discussions. In reality, the proportion of dormant chains is much greater than that shown in this schematic. On average, all chains should grow simultaneously provided that the equilibration between dormant and active chains is much faster than the rate of propagation.[14]

In 2008, a review by Moad et al.[14] included a useful schematic representation of the RAFT polymerisation process (see Figure 1.8). Since the equilibrium lies towards dormant polymer species, only a small proportion of active chains propagate at any given time. Additionally, due to the rapid reversible chain transfer between active and dormant species, each of the polymer chains are offered an approximately equal opportunity to propagate and thus polymers with narrow MWDs are achieved.

As previously mentioned, the precise nature of the Z and R groups on the CTA plays a vital role in controlling RAFT polymerisations. Moad et al.[40] reported an extensive set of guidelines for selection of an appropriate RAFT CTA for a particular monomer class (see Figure 1.9).

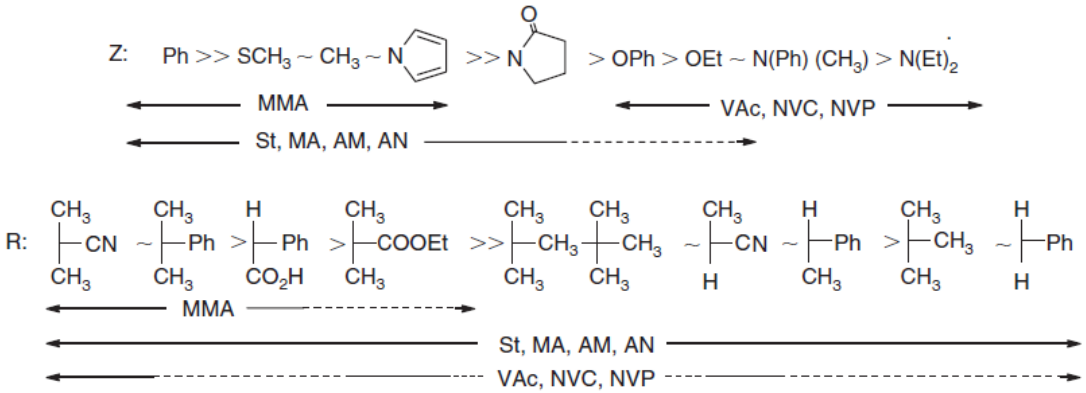

Figure 1.9. Guidelines for the selection of the RAFT CTA for various monomer types. Solid lines indicate that good control can be achieved, whereas dashed lines indicate that only partial control (e.g. broad MWD or substantial retardation) can be achieved. For Z groups, addition rates decrease and fragmentation rates increase from left to right. For R groups, fragmentation rates decrease from left to right.[40]

RAFT polymerisations of so-called 'more activated monomers' (MAMs) [e.g. methyl methacrylate (MMA), styrene (St), methyl acrylate (MA), acrylamide (AM) or acrylonitrile (AN)] are well-controlled by dithioesters (Z = aryl or alkyl) or trithiocarbonates (Z = alkylthio), but less well-controlled by dithiocarbamates and xanthates. Conversely, 'less activated monomers' (LAMs) such as vinyl acetate (VAc), *N*-vinylcarbazole (NVC) or *N*-vinylpyrrolidone (NVP) are well-controlled by dithiocarbamates and xanthates but poorly controlled by dithioesters and trithiocarbonates. However, other reaction conditions such as the choice of solvent, polymerisation temperature, initiator and the CTA/initiator molar ratio must also be carefully selected in order to ensure good control. Nevertheless, RAFT offers an attractive metal-free route to polymers with narrow MWDs and thus opens the door for their use in applications where trace amounts of metal catalyst are problematic. However, it must be noted that the CTA-capped polymers exhibit inherent colour, odour and potential cytotoxicity, which may prevent their use for certain applications.[42] Although it has been suggested that the potential cytotoxicity might not be an issue for some applications,[43] there has been a significant amount of work devoted to the post-polymerisation removal of RAFT chain-ends.[44, 45] Willcock and O'Reilly[45] summarised the main methods of RAFT end group removal, which include thermolysis, aminolysis and radical-induced reduction (see Figure 1.10).

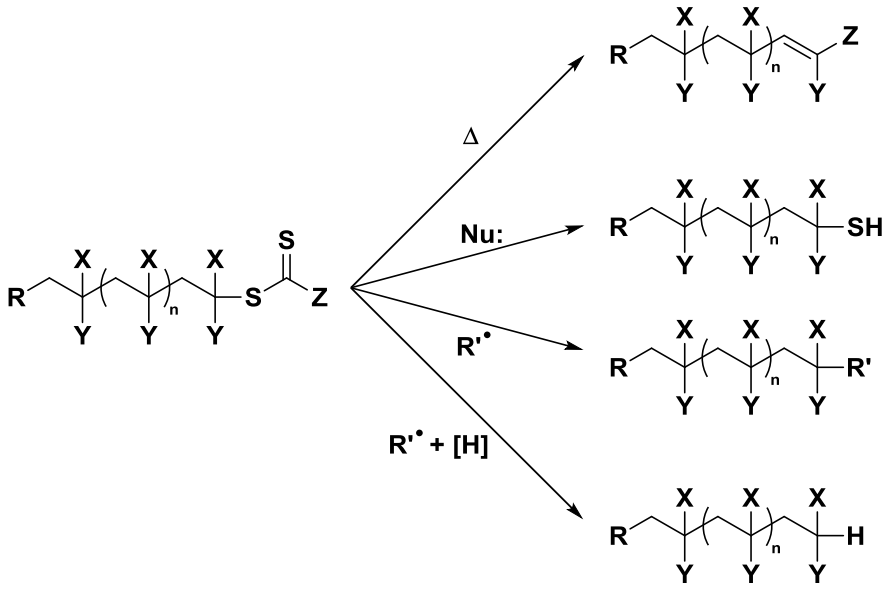

Figure 1.10. Methods for RAFT end group modification/removal. Thermolysis produces a vinyl-capped polymer chain and a suitable nucleophile (e.g. amines or borohydrides) yields a terminal thiol, whereas a free radical initiator (R'•) alone or in the together with a hydrogen atom donor ([H], e.g. tributylsilane) will replace the RAFT end group with R' or H, respectively.[44-46]

A 2009 review by Moad et al.[40] highlighted the growth of RAFT polymerisation in the first ten years after its invention, with over 2,100 publications (including over 100 patents) published in this period. In fact, the total number of publications that mention RAFT polymerisation more than doubled from 2006 to 2009. The industrial relevance of RAFT polymerisation is also becoming increasingly apparent. In particular, Lubrizol Corporation Ltd have successfully commercialised a RAFT-synthesised star copolymer which acts as a viscosity modifier for base oil. Also, the Commonwealth Scientific and Industrial Research Organisation (CSIRO) state that large organisations such as DuPont, Unilever, L'Oréal and Procter & Gamble have filed patents that depend either entirely or partly on the RAFT process.

1.4. Non-Aqueous Dispersion Polymerisation

Although there has been much academic and industrial interest in aqueous emulsion polymerisation,[47] only dispersion polymerisation will be discussed in this Thesis. The general requirement for a dispersion polymerisation is that an initially *soluble* monomer is polymerised to form an *insoluble* polymer.[48, 49] A typical FRP-based dispersion polymerisation formulation consists of monomer(s), solvent, initiator and stabiliser and the mechanism of particle formation is shown in Figure 1.11.[48, 50]

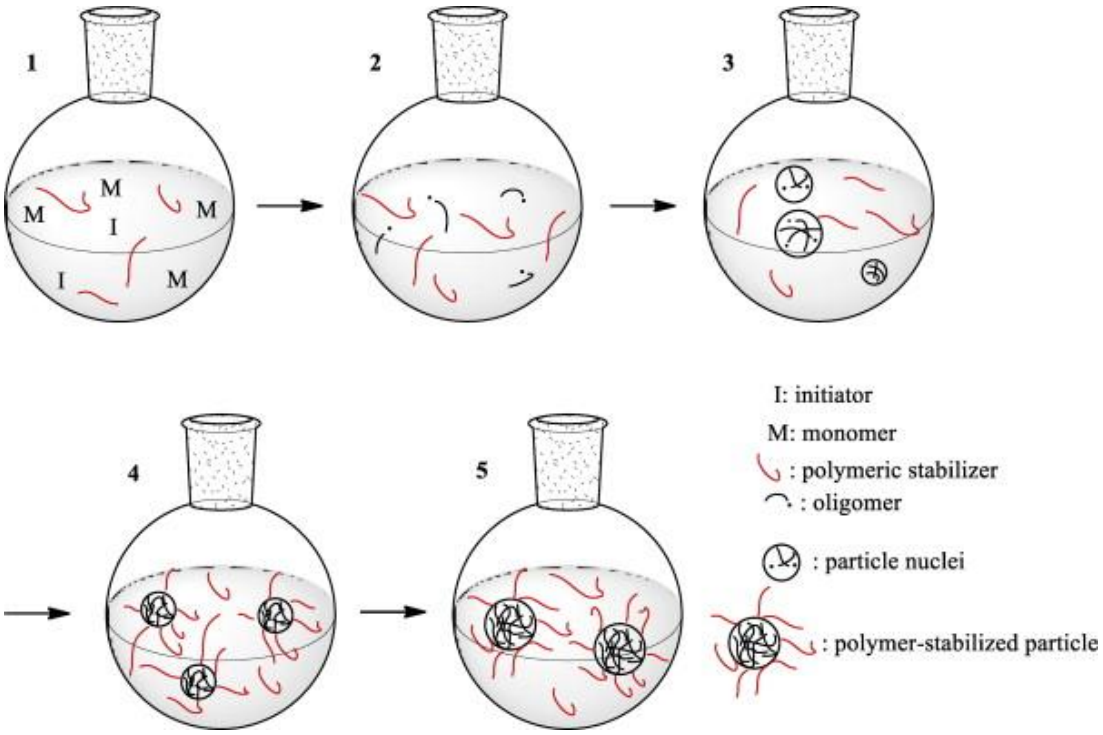

Figure 1.11. Schematic representation of FRP-based dispersion polymerisation displaying (1) initial homogeneous phase, (2) initiation and formation of soluble oligomers, (3) precipitation and coagulation into particles, (4) particle stabilisation by polymer adsorption and (5) particle growth.[50]

Initially, all components are dissolved in the continuous phase at the beginning of the polymerisation. On heating, free radicals are formed that react with the monomer in solution to form linear oligomers/polymers and/or graft copolymers.[48] Precipitation occurs when a certain critical molecular weight is reached, above which the chains are no longer soluble in the continuous phase. The nascent particles aggregate and grow in size, whilst the soluble polymeric stabiliser either physically adsorbs or chemically grafts onto the colloidally unstable particles, thus conferring steric stabilisation.[47] At the point where all precipitating particles have acquired sufficient stabilisation, no new particles are formed and the particles continue to grow until all monomer is consumed.[48] The soluble polymeric stabiliser plays an important role, since precipitation polymerisation would occur in its absence.[48, 49] The particle size distribution obtained by dispersion polymerisation is dictated by the coalescence of growing particles.[51] The mean particle size is primarily dictated by the concentrations of the polymeric stabiliser and monomer respectively, as well as the solvent composition.[48, 50] Higher stabiliser concentrations enable the formation of smaller

particles. Conversely, increasing the monomer concentration results in the formation of larger particles.[48]

Typically, spherical particles of 0.1-15 μm in diameter with very narrow size distributions can be prepared in organic solvents. Osmond and co-workers at Imperial Chemical Industries (ICI)[52] first developed non-aqueous dispersion polymerisation for acrylic and other vinyl monomers in hydrocarbon solvents in the presence of oil-soluble polymeric stabilisers. Since then, a wide range of formulations have been reported, including examples in lower alcohols, water and other organic solvents such as acetonitrile.[48] PMMA and polystyrene latexes are examples of particles produced by non-aqueous dispersion polymerisation, and poly(12-hydroxystearic acid) (PHSA) and polydimethylsiloxane (PDMS) are commonly used as polymeric stabilisers.[50, 53, 54] However, there are many other examples of non-aqueous dispersion polymerisation formulations which utilise different monomers and stabilisers in a wide range of solvents, as reviewed by Richez et al.[50]

1.5. Self-Assembly

Self-assembly is commonly observed in Nature. Perhaps the most important example is the formation of membranes in living cells by the self-assembly of phospholipids, which are amphiphilic molecules consisting of hydrophilic and hydrophobic components. Another example of amphiphile self-assembly in everyday life is soap or detergent, where hydrophobic dirt or soil is removed from the aqueous continuous phase due to micelle formation.

1.5.1. Surfactant self-assembly

Surfactants, or surface-active agents, are small molecule amphiphiles which are capable of reducing the interfacial tension between two liquids or a liquid and a solid by interfacial adsorption. The thermodynamics of surfactant self-assembly in solution is described as the difference in chemical potential between a unimeric species (μ^0_1) and aggregates composed of N molecules (μ^0_N).[55, 56] Aggregates are formed in solution only when the energy required for unimeric species to remain in their free state is larger than the entropic penalty associated with forming the self-assembled structures.

An equilibrium exists between such unimeric and aggregated species, as shown in Figure 1.12.

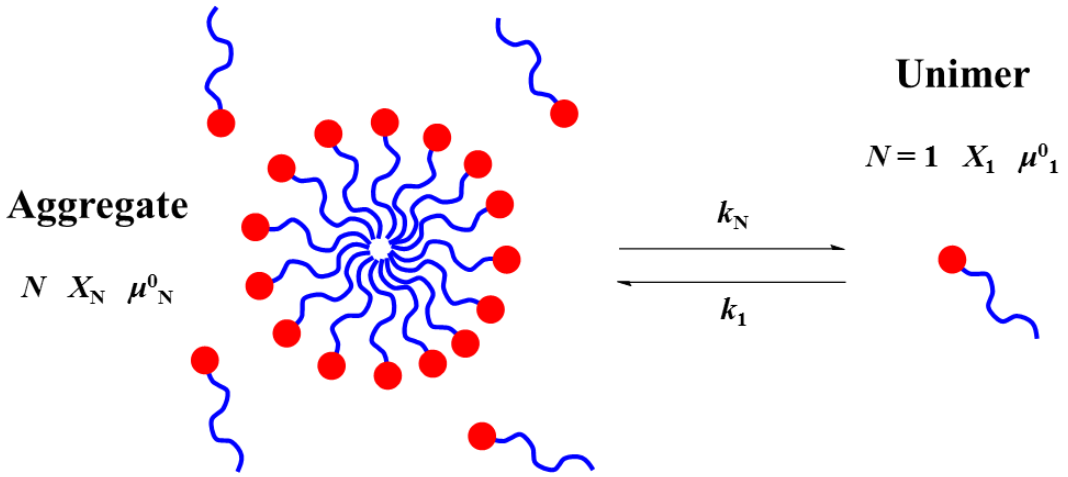

Figure 1.12. Schematic representation of the equilibrium between unimeric surfactant molecules and their aggregated assemblies.[56]

At equilibrium, the following equation can be used to describe the interchange of unimers from solution to an aggregate:

$$K = \frac{k_1}{k_N} = \exp\left[-\frac{N\left(\mu^0{}_N - \mu^0{}_1\right)}{k_B T}\right] \qquad 1.12$$

where K is the equilibrium constant, k_1 is the rate constant for association, k_N is the rate constant for dissociation, k_B is Boltzmann's constant and T is the absolute temperature. This equilibrium can also be considered in terms of X_N, which is the concentration or activity of molecules within an aggregate with aggregation number N:

$$X_N = N\left(X_1 \exp\left[\frac{\mu^0{}_1 - \mu^0{}_N}{k_B T}\right]\right)^N \qquad 1.13$$

Here, X_1 is the concentration or activity of the unimers, which is related to the overall solute concentration, C:

$$C = X_1 + X_2 + X_3 + \cdots = \sum_{N=1}^{\infty} X_N \qquad 1.14$$

Importantly, C and X_N cannot exceed unity. Moreover, the above equations assume ideal mixing and are restricted to dilute conditions where inter-aggregate interactions are negligible. At equilibrium, if all surfactant molecules experience the same interaction with their surroundings, the value of μ^0_N will remain constant in aggregates with differing aggregation numbers and hence Equation 1.13 becomes:

$$X_N = N{X_1}^N \text{ for } \mu^0{}_1 = \mu^0{}_2 = \mu^0{}_3 = \cdots = \mu^0{}_N \qquad 1.15$$

When $X_1 < 1$, $X_N << X_1$ if most of the surfactant molecules remain as unimers (N=1). Considering Equation 1.13, it is clear that, if the value of μ^0_N increases with increasing N, the formation of large aggregates becomes less probable. Thus the condition for the formation of large aggregates is that $\mu^0_N < \mu^0_1$ (i.e. μ^0_N decreases as N increases). Considering the unimer-unimer 'bond' energy between identical amphiphiles arranged in a linear chain ($\alpha k_B T$), the total interaction free energy ($N\ \mu^0_N$) of an aggregate composed of N unimers can be defined as shown below.

$$N\mu^0{}_N = -(N-1)\alpha k_B T \qquad 1.16$$

Considering the overall shape of the aggregates, μ^0_N can be defined as:

$$\mu^0{}_N = \mu^0{}_\infty + \frac{\alpha k_B T}{N^p} \qquad 1.17$$

where μ^0_∞ is the bulk energy per surfactant molecule of an infinite aggregate, α is a positive constant that depends on the strength of the intermolecular interactions and p is a number that depends on the shape or dimensionality of the aggregates.[56] Clearly, as N increases, μ^0_N tends towards μ^0_∞. Combining the above equations gives:

$$X_{\mathrm{N}} = N\left\{X_1 \exp\left[\alpha\left(\frac{1-1}{N^p}\right)\right]\right\}^N \approx N[X_1 e^{\alpha}]^N \qquad 1.18$$

Thus most of the surfactant molecules will be in their unimeric state at low concentrations (i.e. X_1 is small and approximately equal to C). However, since X_{N} cannot exceed unity, X_1 can increase only up to $\exp[-(\mu^0{}_1 - \mu^0{}_{\mathrm{N}})/k_{\mathrm{B}}T]^N$ or $e^{-\alpha}$. The surfactant concentration at which this limit is reached is termed the critical micelle concentration (CMC). In general, this means that:

$$\mathrm{CMC} \approx \exp\left[-\frac{\left(\mu^0{}_1 - \mu^0{}_{\mathrm{N}}\right)}{k_{\mathrm{B}}T}\right] \qquad 1.19$$

Using Equation 1.17, it follows that:

$$\mathrm{CMC} \approx e^{-\alpha} \text{ for all } p \qquad 1.20$$

Equations 1.19 and 1.20 define the concentration at which further addition of surfactant molecules results in the formation of more aggregates (an increase in X_{N}), while the concentration of unimers (X_1) remains relatively constant, as shown in Figure 1.13. One of the advantages of block copolymer vs. surfactant assemblies is that the CMC is much reduced in the former case. In fact, a typical CMC for polystyrene-poly(acrylic acid) diblock copolymer micelles in water is approximately six orders of magnitude lower than that for a well-known anionic surfactant, sodium dodecylsulfate.[57] Also, the large thermodynamic barrier associated with the solvation of free copolymer chains means that block copolymer micelles are often kinetically-frozen, whereas surfactant micelles are invariably in thermodynamic equilibrium with free surfactant.[57]

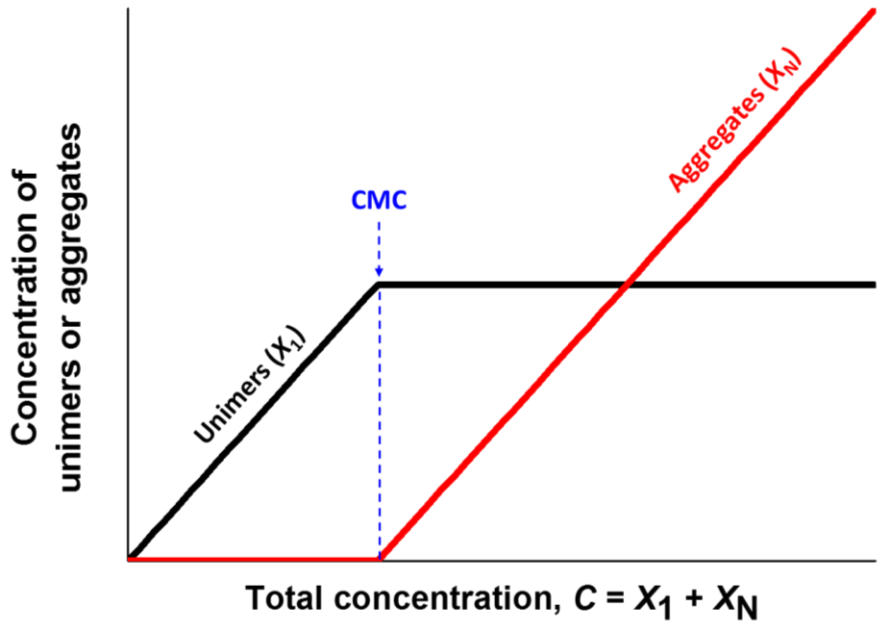

Figure 1.13. Schematic representation of the unimer and aggregate concentrations as a function of the total concentration of surfactant molecules to illustrate the critical micelle concentration (CMC).[56]

Thus far the equations given above do not consider intra- and inter-surfactant interactions. For amphiphiles in water, the major forces for self-assembly arise from the hydrophobic attraction of the amphiphile to the hydrocarbon-water interface and also the electrostatic repulsion between the charged hydrophilic headgroups.[56] This headgroup repulsion dictates the interfacial area per molecule that is exposed to the aqueous phase (a). The interfacial tension that arises from such aggregation can be represented by a positive interfacial free energy per unit area, γ, which is typically between 20 and 50 mJ m^{-2}.[56] Thus the attractive interfacial energy contribution to μ^0_N can be described using the equation:

$$\mu^0{}_N = \gamma a + \frac{K}{a} \qquad 1.21$$

where K is a constant. The minimum energy for inter-aggregate interactions is given by $\delta\mu^0_N/\delta a = 0$, which leads to:

$$\mu^0{}_N(\min) = 2\gamma a_0, \qquad \text{and } a_0 = \sqrt{\frac{K}{\gamma}} \tag{1.22}$$

where a_0 is the optimal interfacial surface area per surfactant molecule, as shown in Figure 1.14.

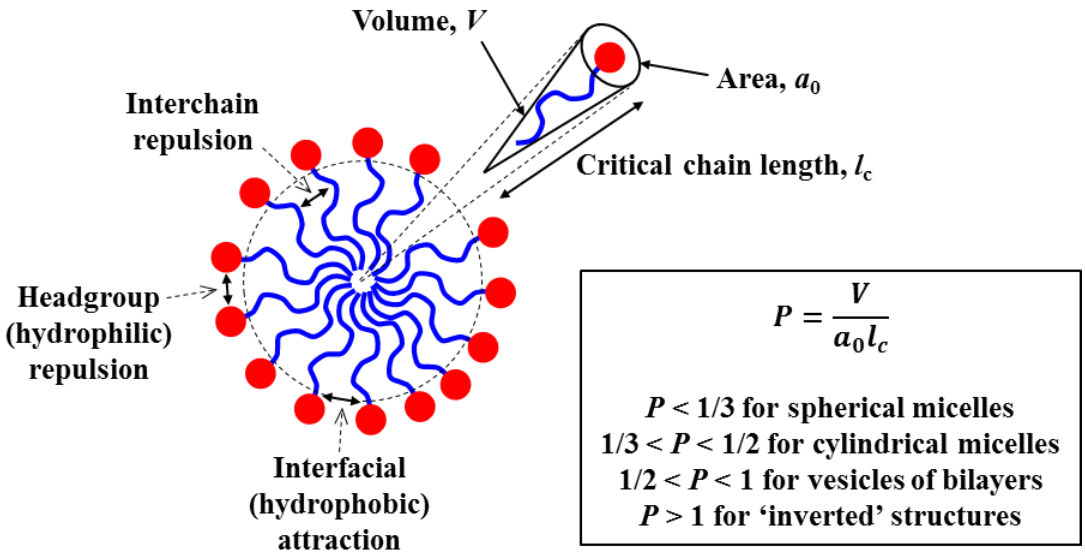

Figure 1.14. Schematic representation of the packing of surfactant molecules within an aggregate. The equation for the packing parameter, *P*, and typical values of *P* predicted for various surfactant morphologies are also given.[56]

The interfacial energy per surfactant molecule can now be described as:

$$\mu^0{}_N = 2\gamma a_0 + \frac{\gamma}{a}(a - a_0)^2 \tag{1.23}$$

This gives rise to the situation where the total interaction area per amphiphile is at a minimum since the attractive and repulsive forces are balanced, as indicated in Figure 1.15.

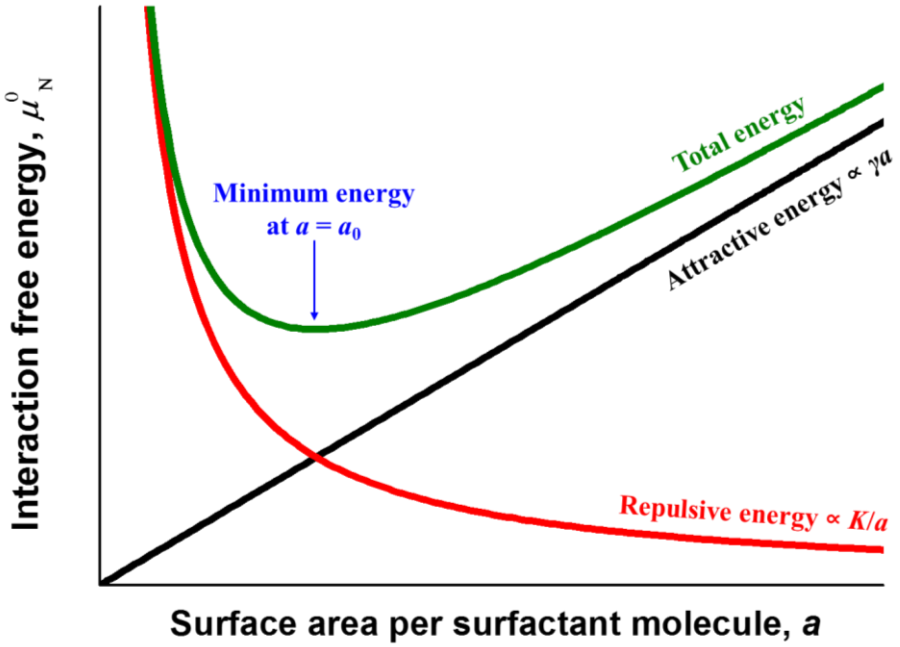

Figure 1.15. Schematic representation of the optimal headgroup area, a_0, where the headgroup repulsion and interfacial hydrophobic attraction forces are balanced within a surfactant aggregate.[56]

Figure 1.14 introduces the dimensionless packing parameter, P, which depends on the hydrophobic volume, V, optimal headgroup area, a_0, and the maximum effective length to which the hydrophobic chains can extend (or the critical chain length), l_c. Israelachvili and co-workers[55, 56] showed that the value of P can be used to predict the morphology adopted by particular amphiphiles, as shown in Figure 1.14.

Relating surfactant self-assembly to the Gibbs equation ($\Delta G_{mix} = \Delta H_{mix} - T\Delta S_{mix}$), micelle formation is characterised by a small positive enthalpy change, and a large positive change in entropy.[58] High ΔS_{mix} values are somewhat surprising, since the formation of ordered aggregates from free surfactant molecules should result in a reduction in entropy. Also, large values of ΔH_{mix} would be expected due to the very low solubility of the hydrocarbon tail in water. Instead of considering only the arrangement of amphiphiles into ordered aggregates, it is important to consider the water molecules. If free amphiphiles exist in solution, the water molecules form clathrate cavities (or cage structures), thus increasing the strength or number of effective hydrogen bonds.[59] This means that introducing surfactant molecules leads to local ordering of the surrounding water molecules and therefore a reduction in the

solvent entropy. This phenomenon is known as the hydrophobic effect and was explored in detail by Tanford.[60] The reverse process occurs on formation of ordered aggregates, since the water molecules revert to the structure of bulk water. This accounts for the apparent large overall positive change in entropy. However, some doubts remain over the validity of such an interpretation at high temperatures where hydrogen bonding is less significant.[58]

1.5.2. Block copolymer self-assembly

As previously discussed, well-defined block copolymers can be prepared via living polymerisation techniques such as LAP, ATRP and RAFT polymerisation (see Figure 1.6). Like small molecule surfactants (see Section 1.5.1), block copolymers can undergo self-assembly in the bulk[61, 62] as well as in solution.[63, 64] Since block copolymer aggregates exhibit higher stability and durability compared to surfactant micelles, they have received considerable interest from both academia and industry for a wide range of applications.[65, 66] In the bulk, microphase separation is observed due to the enthalpic incompatibility of the blocks. Importantly, macroscopic phase separation cannot occur because the blocks are linked by covalent bonds. For AB diblock copolymers, the three parameters that dictate this microphase separation are: (i) the relative volume fractions of the two blocks (f_A and f_B), (ii) the total degree of polymerisation ($N = N_A + N_B$), and (iii) the Flory-Huggins interaction parameter (χ).[66] This χ parameter represents the incompatibility of the A and B blocks and varies with temperature according to the following equation:

$$\chi = \left(\frac{z}{k_B T}\right)\left[\varepsilon_{AB} - \frac{1}{2}(\varepsilon_{AA} + \varepsilon_{BB})\right] \qquad 1.24$$

where z is the coordination number (or number of nearest neighbours per repeat unit), k_B is Boltzmann's constant, T is the absolute temperature (and thus $k_B T$ is the thermal energy), ε_{AB}, ε_{AA} and ε_{BB} are the mean interaction energies per repeat unit for A-B, A-A and B-B, respectively. The Flory-Huggins lattice model[67, 68] can be used to determine the free energy of mixing (ΔG_{mix}) for two incompatible polymers, or a polymer in solution.[69, 70] This model assumes that the lattice is filled with either component A or component B and that the size of each component is the same. Also, random mixing in the lattice is assumed. Thus,

$$\frac{\Delta G_{\mathrm{mix}}}{k_{\mathrm{B}}T} = \left(\frac{\varphi_{\mathrm{A}} ln \varphi_{\mathrm{A}}}{N_{\mathrm{A}}}\right) + \left(\frac{\varphi_{\mathrm{B}} ln \varphi_{\mathrm{B}}}{N_{\mathrm{B}}}\right) + \varphi_{\mathrm{A}}\varphi_{\mathrm{B}}\chi \qquad 1.25$$

where φ_A and φ_B are the volume fractions of components A and B, respectively, and N_A and N_B are the mean number of monomer units per polymer chain (for polymers).[69, 70] In the case of diblock copolymers in the bulk, A and B represent the two chemically distinct blocks, whereas for the case of a homopolymer in a solvent, A represents a repeat unit for the polymer chain and B represents a solvent molecule. Equation 1.25 demonstrates that a negative value of χ is required for spontaneous mixing of components A and B (i.e. $\Delta G_{mix} < 0$), whereas a positive χ value results in de-mixing.[71] It is also clear that χ varies inversely with temperature. Thus higher temperatures are often required for mixing, so an order-disorder transition (ODT) is observed at a specific temperature (T_{ODT}). As N (the total degree of polymerisation) tends to infinity, the number of moles of polymer tends to zero and therefore so does the entropy term. This is because, for larger values of N, an additional reduction in the diffusional and configurational entropy of the polymer chains (also reducing the number of A-B contacts) results in local ordering.[61, 71] Therefore, the degree of microphase separation is determined by the segregation product χN.[66, 71] Self-consistent mean-field (SCMF) theory has been used to predict the phase behaviour of diblock copolymers in the bulk, as shown in Figure 1.16.[70, 72] On increasing the volume fraction of block A (f_A) at a fixed χN above the ODT ($\chi N > 10.5$), order-order transitions (OOTs) are observed: from closely packed spheres (CPS), through spheres (S), cylinders (C) and gyroids (G) to lamellae (L). Further increasing f_A (so that $f_A > f_B$) results in the formation of inverse morphologies. Such phases have been predicted by SCMF theory (Figure 1.16a) and observed experimentally for polyisoprene-polystyrene block copolymers (Figure 1.16b).[66, 70]

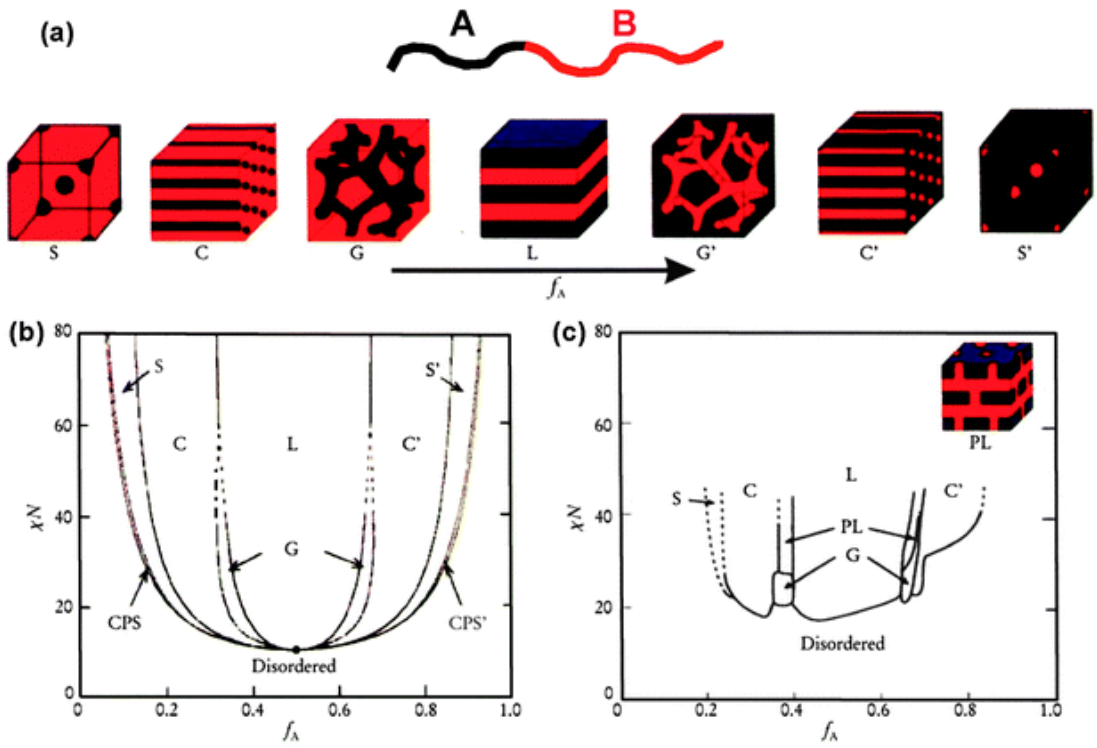

Figure 1.16. (a) AB diblock copolymer morphologies in the bulk: S and S' represent body-centred cubic spheres, C and C' represent hexagonally-packed cylinders, G and G' represent bicontinuous gyroids and L represents lamellae. (b) Phase diagram predicted by self-consistent mean-field theory, depending on the volume fraction (f) of the blocks and the segregation product, χN. CPS and CPS' represent closely packed spheres. (c) Experimentally-determined phase diagram for polyisoprene-polystyrene block copolymers, where f_A represents the volume fraction of polyisoprene. PL represents perforated lamellae.[66, 70]

Multiple regimes for the microphase separation of block copolymers can be considered for $f_A = 0.5$: the weak segregation limit (WSL, where $\chi N < 10$) and the strong segregation limit (SSL, where $\chi N >> 10$), with an intermediate segregation regime (ISR).[61, 66] These segregation regimes relate to the conformation (stretching) of the individual polymer chains as well as the microdomain periods (d), which in turn can be related to the radius of gyration (R_g) of the polymer chains.[61] As defined by Flory,[73] the R_g is defined as a 'measure of the root-mean-square distance of the elements of a chain from its centre of gravity'. In the WSL where the A-B interactions are sufficiently weak, individual polymer chains are unperturbed (or Gaussian) and can adopt a random walk, with an R_g defined as:

$$R_g = \frac{\sqrt{N}\, l}{\sqrt{6}} \qquad 1.26$$

where *l* is the characteristic segment length. Thus in the WSL regime, *d* scales as $\sim N^{1/2}$. However, *d* scales to $\sim N^{2/3}$ in the SSL regime, since the driving force for segregation overcomes the entropically-favoured random coil conformation in order to adopt stretched polymer chains.[61, 71]

Introducing a solvent increases the complexity of block copolymer self-assembly in solution. Considering an AB diblock copolymer in a single solvent that is specific for one block (S), there are now three χ parameters to consider: χ_{AB}, χ_{AS}, χ_{BS}. The complexity is further increased when a mixed solvent system is used, since now six χ-parameters must be considered.[66] However, it is important to realise that AB diblock copolymers self-assemble in a solvent that is a good solvent for just one of the blocks.[74]

1.6. Polymerisation-Induced Self-Assembly of Block Copolymer Nanoparticles via RAFT Non-Aqueous Dispersion Polymerisation

As previously discussed, amphiphilic AB diblock copolymers undergo self-assembly in a selective solvent for one of the two blocks.[74] In principle, the morphology of the resulting diblock copolymer nanoparticles[63, 64, 75, 76] is dictated by the relative block volume fractions, as defined by the so-called packing parameter, *P* (Figure 1.17).[55, 77-79] In practice, the copolymer concentration can also influence the morphology in some cases.[80-83] Similar concentration-dependent behaviour is well-known for small molecule surfactants in water.

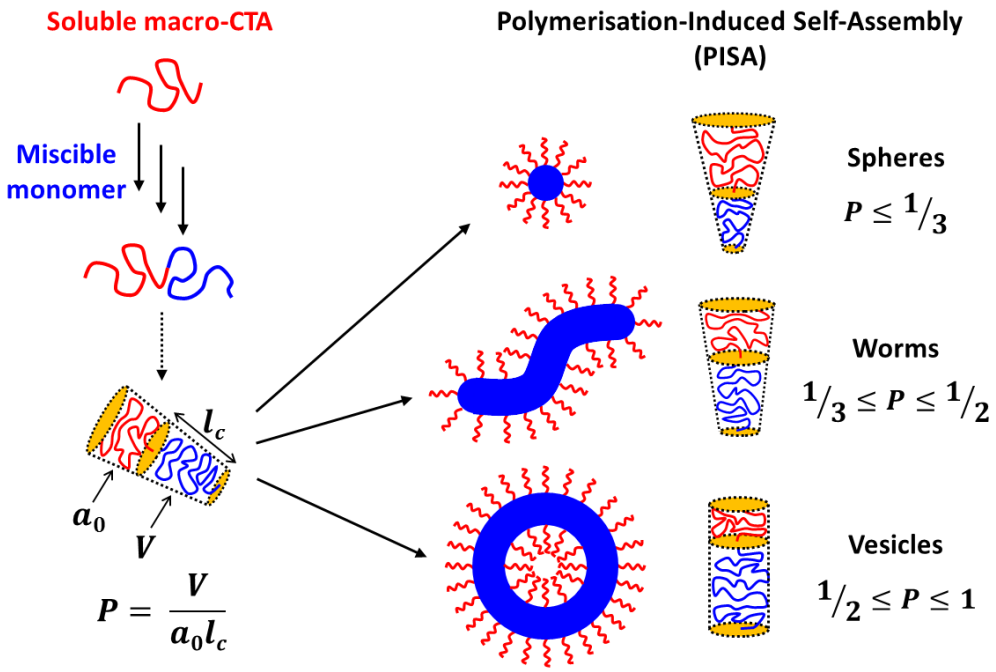

Figure 1.17. (Left) Schematic representation of RAFT dispersion polymerisation, whereby a soluble macromolecular chain transfer agent (macro-CTA, red) is chain-extended by an initially miscible monomer to yield an insoluble polymer block (depicted in blue). (Right) This leads to block copolymer self-assembly, where the packing parameter, *P*, for the resulting individual block copolymer chains in a selective solvent is defined in terms of the volume of the core-forming blue chain, *V*, the optimal head-group area occupied by the stabilising red chain, a_0, and the length of the core-forming blue chain, l_c. The corresponding nanoparticle morphology is normally dictated by the value of *P*.[79]

Recently, many academic groups have examined the use of controlled radical polymerisation techniques, particularly RAFT polymerisation,[19, 38] for the synthesis of amphiphilic diblock copolymer nanoparticles via polymerisation-induced self-assembly (PISA).[78] PISA offers many advantages over traditional self-assembly routes,[78] which often involve post-polymerisation techniques such as solvent[64] or pH-switching[84] and thin film rehydration,[85] and are invariably conducted in dilute (< 1% w/w) solution. Initial research by Hawkett and co-workers focused on RAFT aqueous emulsion polymerisation using water-immiscible monomers such as methyl methacrylate, *n*-butyl acrylate or styrene.[86, 87] Such formulations can be very efficient, but in many cases this approach leads to the formation of kinetically-trapped spheres, rather than the full range of copolymer morphologies.[86-94] Early examples of RAFT dispersion polymerisation syntheses also suffered from this problem.[93, 94] In contrast, there are now many examples of RAFT dispersion polymerisation formulations that yield spheres, worms and vesicles.[78, 88, 95-99] In this approach, a soluble

macromolecular chain transfer agent (macro-CTA) is utilised to polymerise a soluble monomer to form an insoluble polymer block, thus forming amphiphilic diblock copolymers that undergo spontaneous *in situ* self-assembly during chain growth (see Figure 1.17). Considerable research has been devoted to PISA syntheses via RAFT *aqueous* dispersion polymerisation using water-miscible monomers such as 2-hydroxypropyl methacrylate (HPMA), *N*-isopropylacrylamide (NIPAM), *N*,*N*-diethylacrylamide or 2-methyoxyethyl acrylate.[78, 83, 88, 100-105] The construction of phase diagrams enables the reproducible targeting of each copolymer morphology for a stabiliser block of a given mean degree of polymerisation (DP), with the only two synthesis variables being the target DP of the core-forming block and the overall copolymer concentration (or total solids concentration).[78, 83] In particular, there have been many studies focused on the use of PHPMA as the water-insoluble core-forming block, with various water-soluble polymers such as poly(glycerol monomethacrylate) (PGMA), poly(2-(methacryloyloxy)ethyl phosphorylcholine) (PMPC) or poly(ethylene glycol) (PEG) being utilised as the stabiliser block.[78] Such sterically-stabilised nanoparticles have several potential applications, including coatings,[106] drug delivery,[107] sterilisable gels[108] and novel Pickering emulsifiers.[109] More complex morphologies have also been reported for certain RAFT aqueous dispersion polymerisation formulations, including so-called 'lumpy rods', 'framboidal' vesicles, and oligolamellar vesicles.[78]

The literature based on RAFT *aqueous* dispersion polymerisation is now quite extensive.[78, 83, 88, 100, 105] Similarly, there are various examples of RAFT dispersion polymerisation formulations being conducted in either water/(m)ethanol or water/1,4-dioxane mixtures.[110-119] However, we will focus primarily on examples of RAFT dispersion polymerisation *in the absence of water as a co-solvent*, for which there are relatively few literature reports describing high (> 90%) monomer conversions. In most cases, the continuous phase comprises either lower alcohols or various *n*-alkanes, although a few other solvents and solvent mixtures will also be considered. The various RAFT chain transfer agents (CTAs), stabiliser blocks and core-forming blocks that have been deployed in such syntheses are summarised in Figure 1.18.

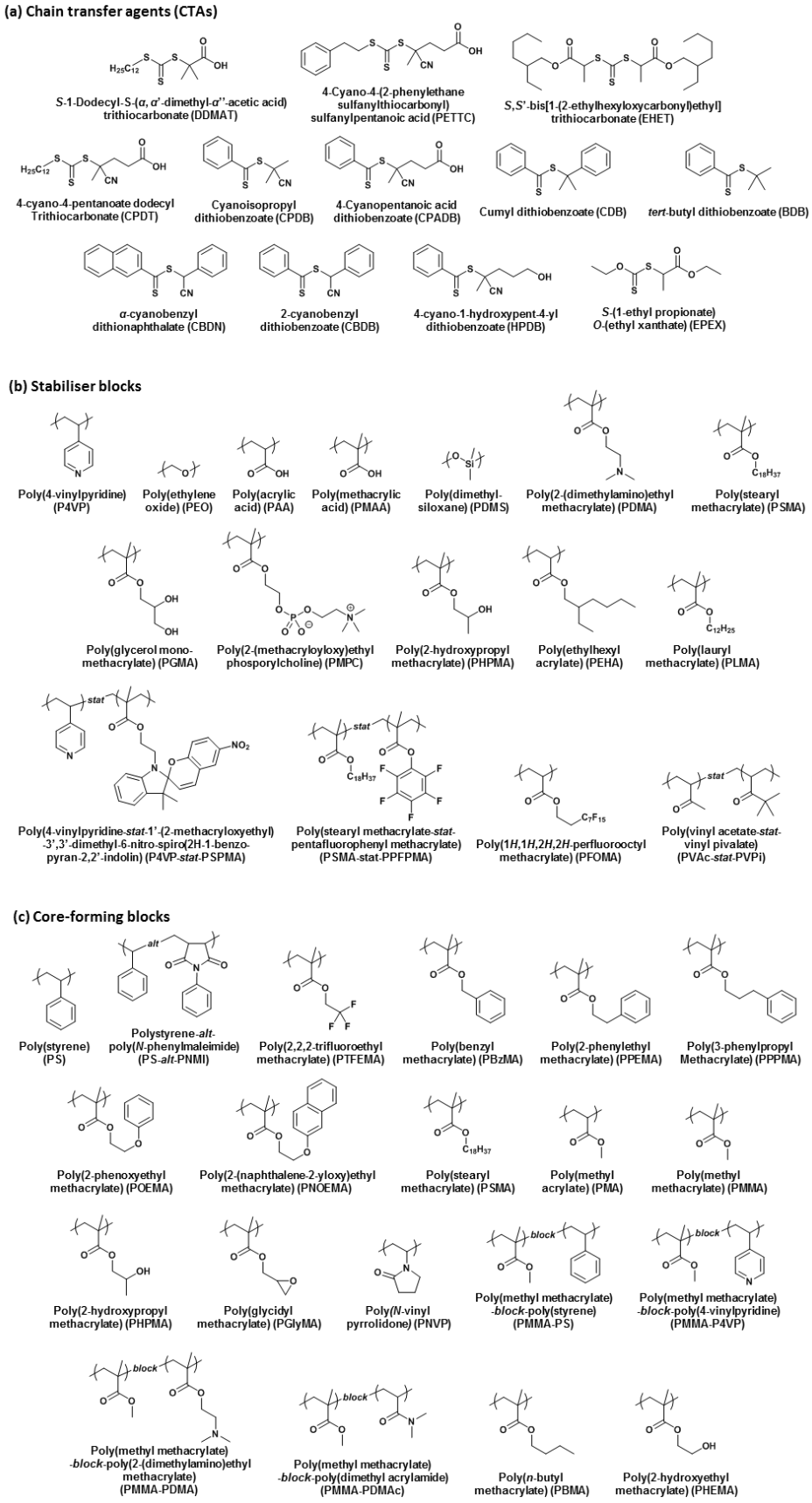

Figure 1.18. (a) Chemical structures of the chain transfer agents (CTAs), (b) stabiliser blocks and (c) core-forming blocks used in various RAFT non-aqueous dispersion formulations reported in the literature.

1.6.1. RAFT alcoholic dispersion polymerisation

1.6.1.1. Dispersion polymerisation of styrene

One of the first RAFT-mediated non-aqueous PISA formulations was the dispersion polymerisation of styrene in lower alcohols. Pan and co-workers[98, 120-125] utilised a trithiocarbonate-based chain transfer agent (DDMAT, see Figure 1.18a) to prepare a range of poly(4-vinylpyridine) (P4VP) macro-CTAs for the subsequent dispersion polymerisation of styrene in methanol. The resulting poly(4-vinylpyridine)-polystyrene (P4VP-PS) nanoparticles formed a wide range of copolymer morphologies (see Figure 1.19 and Figure 1.20).[98, 120-125] Like the analogous RAFT *aqueous* dispersion formulations,[78, 88, 126] purely spherical, worm-like or vesicular morphologies could be targeted by tuning the block composition, which is consistent with the geometric packing argument for surfactant self-assembly introduced by Israelachvili and co-workers,[55] and subsequently extended to block copolymer self-assembly by Antonietti and Förster.[77] This provides a conceptual framework that offers useful qualitative insights when considering mechanisms for morphological transitions, as well as some aspects of phase diagrams. However, as yet this approach cannot be used to gain even a semi-quantitative understanding of the multiple morphological transformations that can occur during an *in situ* PISA synthesis. This is because the core-forming blocks within the block copolymer nano-objects are almost certainly solvated by both monomer and solvent, but the *local* concentrations of these two species are not known. Since this degree of solvation necessarily dictates the *effective* volume fraction of the core-forming block, calculation of the variation in the packing parameter, *P*, during a PISA synthesis is currently an intractable problem. In principle, theoretical advances in this area should enable phase diagrams to be calculated for a given PISA formulation, which would in turn minimise the intensive synthetic effort currently required to identify the phase space for each copolymer morphology. Nevertheless, such empirical experimental studies can be very instructive.

Pan and co-workers have used TEM to investigate *in situ* morphological transformations that occur during the PISA syntheses of P4VP-PS nanoparticles, with spheres and worms being observed as both intermediate and final morphologies.[98, 120, 122, 123] Huang et al.[127] statistically copolymerised a small amount (5 mmol eq.) of the photochromatic spiropyran analogue 1'-(2-methacryloxyethyl)-3',3'-dimethyl-6-

nitro-spiro(2H-1-benzo-pyran-2,2'-indolin) (SPMA, Figure 1.18c) with 4VP to produce a light-responsive stabiliser macro-CTA. This enabled enhanced fluorescence properties of the resulting vesicles upon exposure to UV radiation as a result of photoisomerisation of the SPMA repeat units.

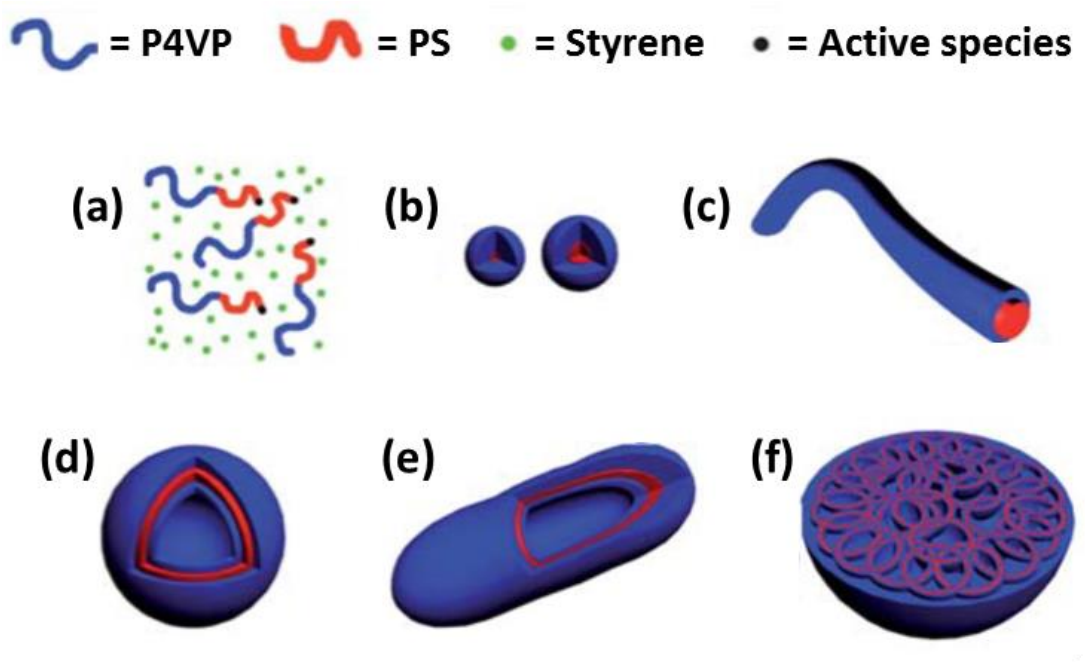

Figure 1.19. Formation of various poly(4-vinylpyridine)-polystyrene (P4VP-PS) diblock copolymer nanoparticles from initially soluble poly(4-vinylpyridine) chains via RAFT dispersion polymerisation of styrene in methanol. Copolymer morphologies that can be obtained using this PISA formulation include (a) soluble chains, (b) spheres, (c) worms, (d) vesicles, (e) nanotubes and (f) large compound vesicles.[122]

In addition to spheres, worms and vesicles, P4VP-PS block copolymer nanoparticles have been used to access more complex structures such as the so-called 'yolk/shell' morphology (Figure 1.20d).[121] In this case, PS homopolymer chains were present during the PISA synthesis of P4VP-PS vesicles. The former component was subsequently stabilised by the P4VP-PS diblock copolymer chains, resulting in the formation of PS spherical nanoparticles within the vesicle lumen and hence the 'yolk/shell' morphology. More recently, Zhang et al.[125] reported the formation of 'multi-shelled' vesicles when targeting highly asymmetric (e.g. $P4VP_{73}$-PS_{9400}) diblock copolymers in methanol (Figure 1.20e). These formulations indicate the complexity of block copolymer morphologies that can be achieved when utilising PISA formulations in methanol. However, it should be emphasised that the RAFT

dispersion polymerisation of styrene invariably suffers from substantially incomplete conversions (e.g. 30-70% after 48 h at 80 °C), despite such syntheses being conducted at relatively high solids. Moreover, the relatively large volume of unreacted monomer solvates the insoluble core-forming PS block and hence most likely influences the nanoparticle morphology. This problem of incomplete monomer conversion has been recently resolved by Zhang and co-workers:[113, 115, 128] addition of 5-20% w/w water as a co-solvent enabled styrene conversions of more than 90% to be obtained within 24 h. This is a pragmatic solution for PISA syntheses involving water-miscible polar solvents, but is unlikely to be useful for water-immiscible non-polar solvents such as *n*-alkanes. Dong et al.[129] extended the initial work by Pan and co-workers by conducting the RAFT dispersion polymerisation of styrene using a P4VP macro-CTA synthesised using a dithiobenzoate-based CTA (cyanoisopropyl dithiobenzoate or CPDB, Figure 1.18a). Dispersion polymerisations were conducted in isopropanol, in the presence and absence of CO_2. On addition of ≤ 8.0 MPa of CO_2, lower packing parameters were obtained for similar P4VP-PS compositions that led to the formation of worms rather than vesicles.

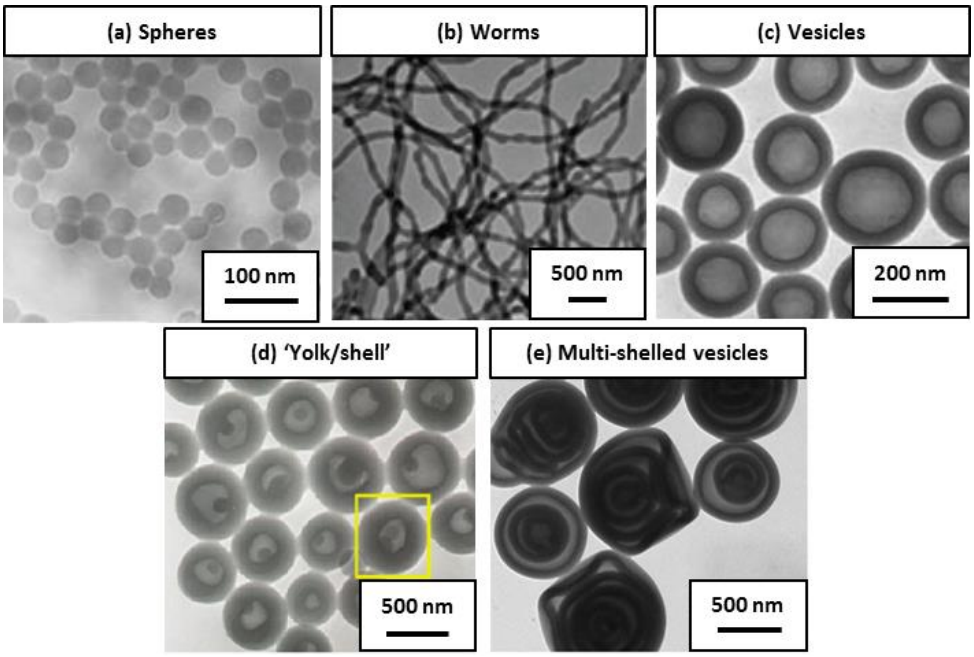

Figure 1.20. Transmission electron micrographs obtained for various diblock copolymer morphologies reported by Pan and co-workers via RAFT dispersion polymerisation of styrene in methanol using various P4VP macro-CTAs: (a) spheres, (b) worms, (c) vesicles, (d) 'yolk/shell' and (e) multi-shelled vesicles.[121, 122, 125]

Pan and co-workers also examined the RAFT dispersion polymerisation of styrene in methanol. A trithiocarbonate-based DDMAT CTA (Figure 1.18a) was used to prepare poly(ethylene oxide)-polystyrene (PEO-PS)[130] and poly(acrylic acid)-polystyrene (PAA-PS)[96] block copolymer nano-objects in methanol, with access to the full range of morphologies (spheres, worms or vesicles) being observed in both cases. Similarly, CPDB was utilised for the synthesis of poly(2-(dimethylamino)ethyl methacrylate)-polystyrene (PDMA-PS) diblock copolymer spheres, worms or vesicles,[97] and even hexagonally-packed hollow hoops[131] in addition to the P4VP-PS formulations previously discussed.[125] Yang et al.[132] reported that high comonomer conversions (> 90%) could be achieved when conducting the RAFT dispersion alternating copolymerisation of styrene with *N*-phenylmaleimide (NMI) using a poly(methacrylic acid) (PMAA) macro-CTA in a solvent mixture. More specifically, PMAA-(PS-*alt*-PNMI) block copolymers formed spheres, worms or lamellae in 50:50 w/w ethanol/1,4-dioxane at ≥ 15% w/w solids.[132] Unusually, the latter morphology was obtained instead of vesicles, which was attributed to the relatively stiff, inflexible nature of the core-forming alternating copolymer chains (T_g > 200 °C).

1.6.2. Dispersion polymerisation of benzyl methacrylate

Although styrene is a relatively cheap monomer, it suffers from a relatively slow rate of polymerisation when utilised in non-aqueous PISA formulations.[98, 120-125] In contrast, Charleux et al. reported that RAFT *aqueous emulsion* polymerisation of styrene led to almost complete conversion within 5 h.[133, 134] There are also various examples of alcohol/water mixtures that enable relatively high styrene conversions to be achieved via RAFT dispersion polymerisation.[110, 112-115, 128, 135] However, for RAFT alcoholic dispersion polymerisation formulations conducted in the *absence* of water as a co-solvent, benzyl methacrylate (BzMA) provides a pragmatic alternative to styrene for the core-forming block. For example, Armes and co-workers[136-140] reported that the RAFT dispersion polymerisation of BzMA conducted in lower alcohols (i.e. methanol, ethanol or isopropanol) usually leads to monomer conversions exceeding 95% within 24 h at 70 °C. The versatility of such a protocol was highlighted by Semsarilar et al.[136] who synthesised PDMA, PMAA, PGMA and PMPC macro-CTAs using 4-cyano-4-(2-phenylethane sulfanylthiocarbonyl)sulfanylpentanoic acid (PETTC, Figure 1.18a), followed by chain extension of each macro-CTA in turn with

BzMA to produce a range of pure spheres, worms or vesicles in ethanol (Figure 1.21a, b and c respectively).

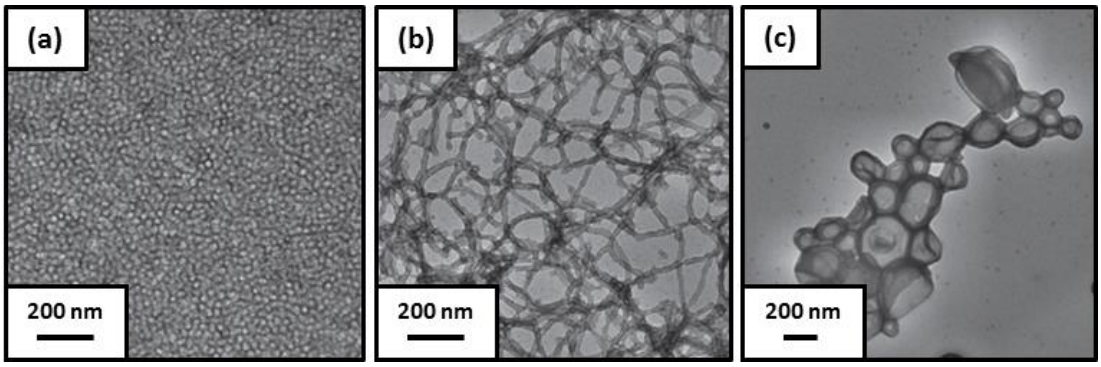

Figure 1.21. Transmission electron micrographs of (a) $PMAA_{67}$-$PBzMA_{50}$ spheres, (b) $PMAA_{67}$-$PBzMA_{100}$ worms and (c) $PMAA_{67}$-$PBzMA_{200}$ vesicles prepared by RAFT dispersion polymerisation of benzyl methacrylate in ethanol at 70 °C. In each case relatively high monomer conversions were obtained (> 95%).[136]

Construction of a suitable phase diagram allowed reproducible targeting of a desired morphology for a given $PMAA_{71}$-$PBzMA_x$ block copolymer composition (Figure 1.22). Generally, only a relatively weak concentration dependence on copolymer morphology was observed. However, only spherical nanoparticles could be obtained at 5% w/w solids regardless of the target DP for the PBzMA core-forming block, which suggests that a kinetically-trapped morphology under these conditions.[78] Presumably, this simply reflects the reduced probability of efficient inter-sphere fusion occurring on the time scale of the BzMA polymerisation for PISA syntheses conducted under more dilute conditions.

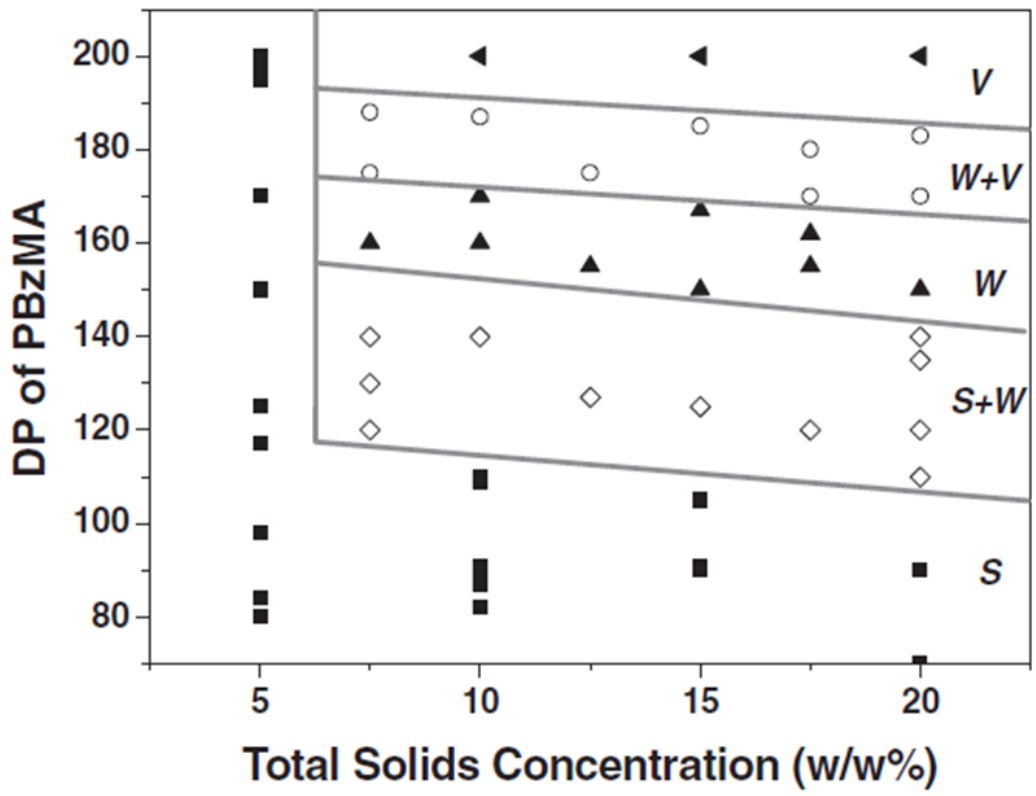

Figure 1.22. Phase diagram constructed for $PMAA_{71}$-$PBzMA_x$ diblock copolymer nanoparticles prepared by RAFT dispersion polymerisation of BzMA in ethanol at 70 °C, where S, W and V represent spheres, worms and vesicles respectively.[136]

The PDMA, PMAA, PGMA and PMPC stabiliser blocks are soluble in both ethanol and water, hence facile transfer of diblock copolymer nano-objects into aqueous solution was conveniently achieved by dialysis of the as-synthesised ethanolic dispersion against water.[136, 137] This transfer allowed nanoparticle characterisation by aqueous electrophoresis, which confirmed the expected cationic character of $PDMA_{31}$-$PBzMA_{37}$ spheres below pH 9 as a result of protonation of the stabiliser chains. Similarly, the anionic character of $PMAA_{67}$-$PBzMA_{50}$ spheres over a wide pH range was verified, whereas $PGMA_{60}$-$PBzMA_{50}$ and $PMPC_{30}$-$PBzMA_{380}$ spheres exhibited almost neutral (slightly anionic) character from pH 3 to pH 10.[136] Thus these alcoholic PISA formulations offer a reasonably efficient route for the preparation of highly charged block copolymer nano-objects. Previously, Semsarilar et al. demonstrated that the direct preparation of highly charged nanoparticles via aqueous PISA formulations is problematic in the absence of added salt. This is because strong lateral electrostatic repulsion between neighbouring polyelectrolytic chains impedes *in situ* self-assembly.[141] In collaboration with Meldrum and co-workers, we have recently shown

that anionic $PMAA_x$-$PBzMA_y$ nano-objects can be efficiently occluded within single crystals of calcite, leading to a series of novel organic-inorganic nanocomposites that exhibit superior mechanical properties to that of calcite alone.[142, 143] Additionally, anionic $PMAA_{71}$-$PBzMA_{200}$ vesicles were successfully coated with cationic 12 nm alumina-coated silica particles (Ludox CL) to form 'armoured' vesicles.[136]

Zehm et al.[138] reported the preparation of poly(2-hydroxypropyl methacrylate)-poly(benzyl methacrylate) (PHPMA-PBzMA) block copolymer spheres, worms and vesicles in either ethanol or isopropanol. This study highlighted the importance of the choice of solvent and the DP of the stabiliser macro-CTA (in addition to the target PBzMA DP and copolymer concentration) in dictating the final morphology of diblock copolymer nanoparticles in alcoholic media. These findings are also consistent with earlier reports of block copolymer nanoparticles prepared via RAFT aqueous dispersion polymerisation.[78, 83] Zehm et al. also provided the first evidence that the worm-to-vesicle transition in non-aqueous PISA formulations proceeds via a transient 'jellyfish' morphology (Figure 1.23). This observation is in good agreement with TEM studies conducted by Blanazs et al., who examined the evolution in copolymer morphology during the synthesis of PGMA-PHPMA vesicles via RAFT aqueous dispersion polymerisation.[103]

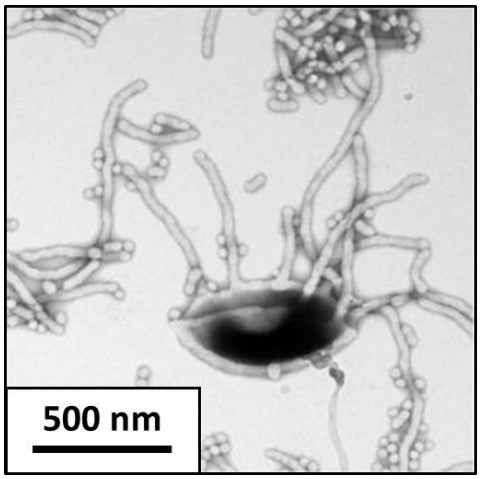

Figure 1.23. Transmission electron micrograph of the 'jellyfish' morphology observed during the formation of $PHPMA_{63}$-$PBzMA_{200}$ diblock copolymer nanoparticles prepared via RAFT dispersion polymerisation of BzMA in ethanol.[138] Similar transient copolymer morphologies have been observed for RAFT aqueous dispersion polymerisation formulations,[103] and also during post-polymerisation processing of block copolymers.[78] This strongly suggests that the 'jellyfish' is a *generic* intermediate for block copolymer self-assembly, rather than a PISA-specific species.

More recently, Gonzato et al.[140] reported the synthesis of low-polydispersity PMAA-PBzMA vesicles via RAFT dispersion polymerisation of BzMA in ethanol. This was achieved by selecting an appropriate binary mixture of a $PMAA_{171}$ and a $PMAA_{62}$ stabiliser macro-CTA, which preferentially occupy the outer and inner leaflets of the vesicle membrane respectively (Scheme 1.7). Control experiments confirmed that, if just the shorter $PMAA_{62}$ stabiliser macro-CTA was utilised for the PISA synthesis, then only relatively large vesicles with broad size distribution could be obtained. Systematic variation of the relative proportions of the two PMAA stabiliser blocks allowed construction of a phase diagram that enabled optimisation of the vesicle size distribution, as judged by TEM, dynamic light scattering (DLS) and small-angle X-ray scattering (SAXS) studies. Given their high efficiency, such rational syntheses of well-defined vesicles are expected to be useful in the context of drug delivery vehicles, for *in vivo* imaging, the design of artificial organelles, for encapsulation and also for potential use as nanoreactors.[144-147]

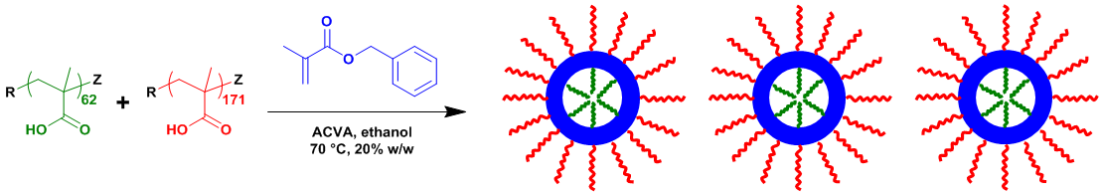

Scheme 1.7. Synthesis of low polydispersity diblock copolymer vesicles in ethanol via RAFT dispersion polymerisation of BzMA using a binary mixture of two PMAA macro-CTAs (with DPs of 62 and 171).[140]

1.6.3. Alternative core-forming blocks for RAFT alcoholic dispersion polymerisation

Following the elegant studies of crystallisation-driven block copolymer self-assembly reported by Manners and Winnik,[148-153] PISA syntheses of diblock copolymer nano-objects with semi-crystalline cores have been recently reported in the literature. For example, Charleux and co-workers conducted the RAFT dispersion polymerisation of a bespoke cholestryl-based (meth)acrylic core-forming monomer in an ethanol/water mixture to produce well-defined diblock copolymer nanorods and nanofibers.[112] Similarly, Armes and co-workers conducted the RAFT dispersion polymerisation of stearyl methacrylate (SMA) in pure ethanol using a PDMA macro-CTA (Figure 1.18c).[154] The latter approach yielded PDMA-PSMA spheres, worms or vesicles with semi-crystalline stearyl side-chains in the PSMA core-forming block.[154] Potential

advantages for such nano-objects could be the preparation of relatively stiff worms of tunable flexibility and perhaps also vesicles with less permeable membranes, thus offering enhanced encapsulation efficiency.

Recently, Lowe and co-workers[99, 155-157] extended the RAFT dispersion polymerisation formulation originally pioneered by Armes et al.[136-140] and Charleux and co-workers.[88, 89, 101, 110, 134] A series of PDMA macro-CTAs were chain-extended via RAFT dispersion polymerisation of either 2-phenylethyl methacrylate (PEMA), 3-phenylpropyl methacrylate (PPMA), 2-(naphthalene-2-yloxy)ethyl methacrylate (NOEMA) or 2-phenoxyethyl methacrylate (POEMA) in ethanol at 70 °C to produce spheres, worms or vesicles.[99, 155, 157] Moreover, a 21% w/w dispersion of $PDMA_{20}$-$PPPMA_{47}$ worms formed a free-standing gel at room temperature, but heating this dispersion to 70 °C for 1 min resulted in the formation of a free-flowing fluid. According to TEM studies, degelation is the result of a reversible worm-to-sphere order-order transition (Figure 1.24). Variable temperature ^{1}H NMR studies revealed that this change in copolymer morphology coincided with greater solvation of the PPPMA core block at elevated temperatures. This alters the relative volume fraction of the two blocks and hence the effective packing parameter for the diblock copolymer chains.[155] Such thermo-reversible degelation has been previously reported for diblock copolymer worms prepared by RAFT *aqueous* dispersion polymerisation, where a worm-to-sphere transition was observed upon *cooling*.[108] This is related to the well-known inverse temperature solubility (LCST-type) behavior exhibited by many non-ionic water-soluble polymers,[158] whereas conventional solvent-soluble polymers typically exhibit UCST-type behaviour in common organic solvents.[159]

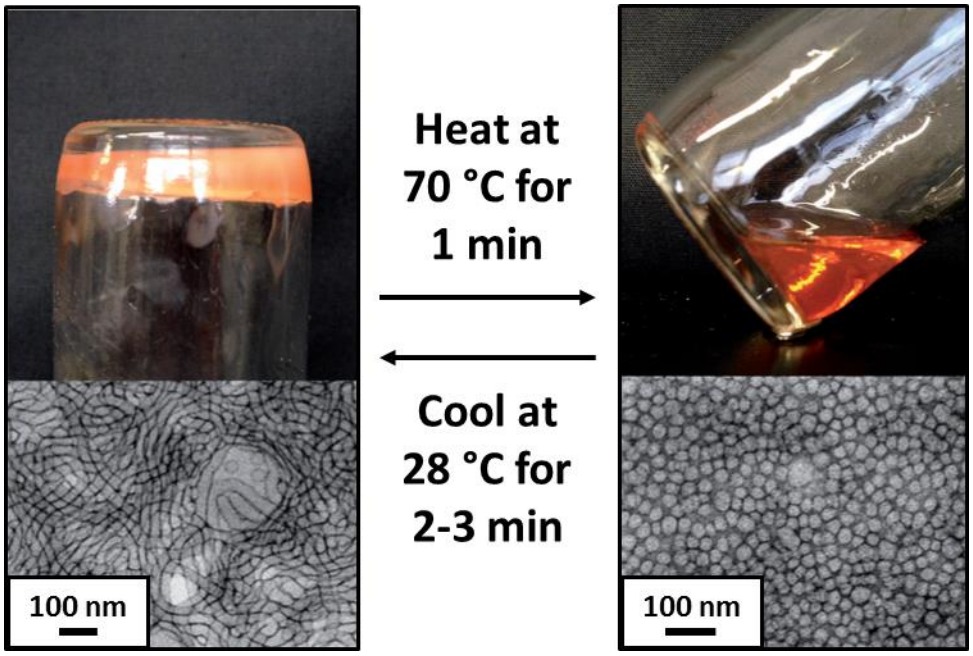

Figure 1.24. Digital photographs of a 21% w/w dispersion of $PDMA_{20}$-$PPPMA_{47}$ diblock copolymer nano-objects in ethanol at room temperature (left) and 70 °C (right), and the corresponding transmission electron micrographs obtained after dilution showing worm-like nanoparticles at room temperature (left) and spherical nanoparticles at 70 °C (right).[155]

1.6.4. RAFT non-polar dispersion polymerisation

Compared to RAFT alcoholic dispersion polymerisation, there are relatively few reports of RAFT dispersion polymerisation being conducted in *non-polar* solvents.[160-167] Charleux and co-workers[160-162] reported an all-acrylic RAFT non-polar dispersion polymerisation formulation that produced poly(2-ethylhexyl acrylate)-poly(methyl acrylate) (PEHA-PMA) diblock copolymer nanoparticles in *iso*-dodecane. However, it is emphasised that only spherical nanoparticles could be accessed in this study. Moreover, using a dithiobenzoate-based CTA led to strong rate retardation and extremely poor RAFT control (M_w/M_n > 6.00) at ≥ 85% conversion for the chain extension of a PEHA macro-CTA using methyl acrylate (MA) compared to a trithiocarbonate-based maco-CTA.[160] Thus it is perhaps debatable whether this constitutes a genuinely successful RAFT formulation. In 2013, Fielding et al.[163] reported the well-controlled RAFT dispersion polymerisation to be conducted in non-polar media. This all-methacrylic formulation utilised cumyl dithiobenzoate (CDB, Figure 1.18a) to prepare poly(lauryl methacrylate)-poly(benzyl methacrylate) (PLMA-PBzMA) diblock copolymer spheres, worms or vesicles in *n*-heptane. A phase diagram containing all three copolymer morphologies was constructed for a series of

$PLMA_{17}$-$PBzMA_x$ (L_{17}-B_x) diblock copolymers. In contrast, using a relatively long $PLMA_{37}$ stabiliser block restricted the morphology to kinetically-trapped spheres (Figure 1.25b). In this case, the mean sphere diameter could be tuned by simply adjusting the target DP of the PBzMA core-forming block, with longer PBzMA blocks resulting in the formation of larger spheres, as previously reported for spherical nanoparticles prepared via RAFT *aqueous* dispersion polymerisation.[102] This suggests some potential for using such spherical methacrylic nanoparticles as lubricity modifiers for automotive engine base oils, as reported by Zheng et al. for all-acrylic nanoparticles prepared via ATRP.[168] One important advantage of the former nanoparticles is that they are likely to be more resistant to *in situ* hydrolysis at elevated temperatures. Moreover, several other disadvantages such as possible copper catalyst contamination, oil discoloration during photo-crosslinking and the undesirable use of protecting chemistry are also avoided by utilising RAFT-mediated PISA syntheses.

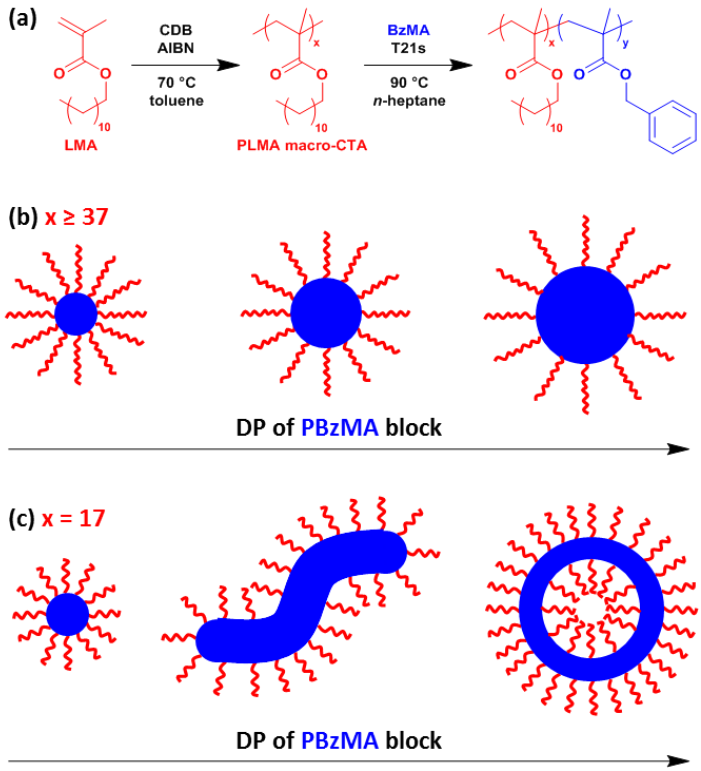

Figure 1.25. Transmission electron micrographs recorded for (a) $PLMA_{17}$-$PBzMA_x$ (L_{17}-B_x) diblock copolymer nanoparticles, where spherical, worm-like and vesicular morphologies are accessible in *n*-heptane, and (b) $PLMA_{37}$-$PBzMA_x$ (L_{37}-B_x) diblock copolymer spheres in the same solvent.[163]

This PLMA-PBzMA formulation was subsequently extended from *n*-heptane to *n*-dodecane.[164] This may seem like a trivial advance, but the high boiling point of the latter solvent facilitates high temperature studies of PLMA-PBzMA nanoparticles and in particular, characterisation of the thermo-responsive behaviour of a $PLMA_{16}$-$PBzMA_{37}$ worm gel via rheology. TEM studies confirm that a worm-to-sphere transition is responsible for the degelation of a 20% w/w $PLMA_{16}$-$PBzMA_{37}$ worm gel that is observed upon heating to 90 °C. Variable temperature DLS, rheology and SAXS studies provided important insights into this morphological transformation, while ^{1}H NMR studies similar to those described by Lowe and co-workers were also undertaken.[155] In particular, it was determined that the worm-to-sphere transition was essentially irreversible when performed at copolymer concentrations below 5% w/w (Figure 1.26). Presumably, this is because the formation of worm-like nanoparticles from the fusion of multiple spheres is highly inefficient for dilute dispersions.

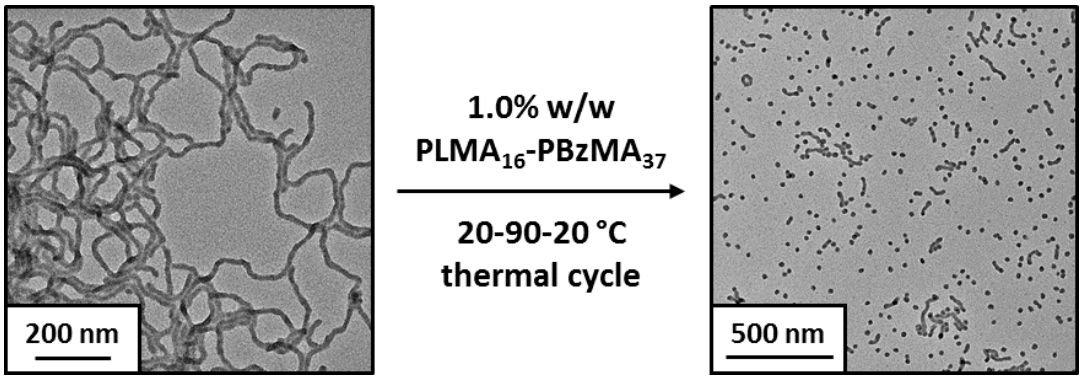

Figure 1.26. Transmission electron micrographs showing the irreversible worm-to-sphere transition of a 1.0% w/w dispersion of $PLMA_{16}$-$PBzMA_{37}$ diblock copolymer nanoparticles in *n*-dodecane.[164]

Moreover, it was not necessary to convert all of the worms into spheres in order to induce degelation of the $PLMA_{16}$-$PBzMA_{37}$ worm gel. Rheological studies indicated that the onset of degelation occurred at approximately 47 °C. In contrast, SAXS studies confirmed that pure spheres (which have a zero gradient at low *q*) were only obtained when the original worms (which have a gradient close to -1 at low *q*) were heated up to 160 °C (Figure 1.27).[164] This suggests that degelation is a consequence of the reduction in the mean worm length, since this leads to fewer inter-worm contacts *per worm*. Two possible mechanisms were considered for the worm-to-sphere transition: (i) sequential budding of spheres from worm ends or (ii) random worm

cleavage to produce gradually shorter worms (see Figure 1.27c). Variable temperature SAXS studies suggested that the former process was more likely to be the dominant mechanism. Finally, it is perhaps worth emphasising that solvation of the core-forming PBzMA block is a necessary but not sufficient condition to account for the worm-to-sphere transition. If *uniform* plasticisation of the core-forming block occurred on heating, this would simply lead to an increase in its effective volume fraction, which would be expected to induce a worm-to-vesicle transition. The worm-to-sphere transition that is actually observed can only be rationalised in terms of a subtle change in packing parameter if *surface* plasticisation of the core-forming block occurs. This is physically reasonable for partial solvent ingress and leads to the BzMA repeat units nearest to the PLMA stabiliser becoming solvated. This increases the effective volume fraction of the *stabiliser* block, which *lowers* the packing parameter and hence accounts for the observed worm-to-sphere transition.

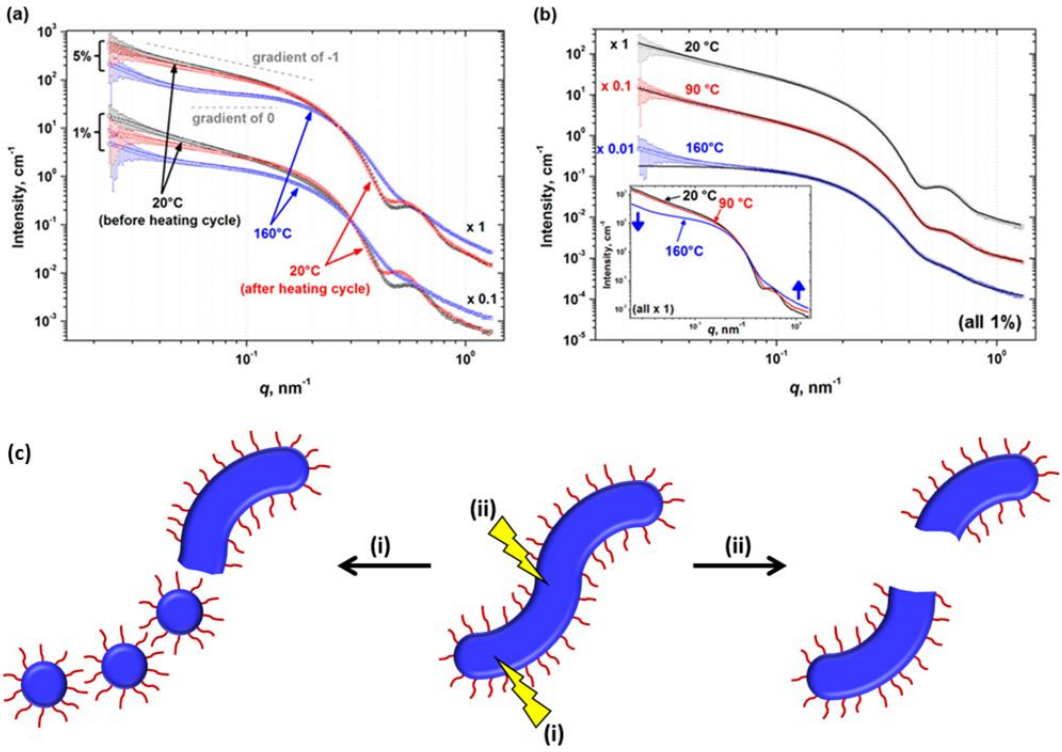

Figure 1.27. (a) Representative SAXS patterns for 5.0 and 1.0% w/w $PLMA_{16}$-$PBzMA_{37}$ diblock copolymer nanoparticles in *n*-dodecane before a 20-160-20 °C thermal cycle (black data), at 160 °C (blue data) and after the thermal cycle (red data). (b) Representative SAXS patterns for the same 1.0% w/w $PLMA_{16}$-$PBzMA_{37}$ diblock copolymer dispersion in *n*-dodecane recorded at 20 °C (black data), 90 °C (red data) and 160 °C (blue data). Data were fitted to a worm-like micelle model, where the scattering pattern at 160 °C indicated the presence of isotropic (spherical) particles. (c) Two possible mechanisms for the thermally-induced worm-to-sphere transition: (i) sequential budding and (ii) random worm cleavage.[164]

In the patent literature, RAFT dispersion polymerisation formulations are described that utilise methyl methacrylate (MMA), 2-hydroxypropyl methacrylate (HPMA) or glycidyl methacrylate (GlyMA) as core-forming monomers for the chain extension of PLMA macro-CTAs.[169] However, it is not yet clear whether such PISA formulations are as well-behaved as those based on BzMA. Lowe and co-workers recently reported using SMA instead of LMA to prepare PSMA stabiliser macro-CTAs (Figure 1.18b) for the synthesis of PSMA-PPPMA diblock copolymer nanoparticles in *n*-tetradecane[165] and *n*-octane.[166] Pure phases of spheres, worms or vesicles were accessible and a thermo-reversible worm-to-sphere transition was characterised by variable temperature TEM, DLS and ^{1}H NMR studies. Like the $PLMA_{16}$-$PBzMA_{37}$ worms in *n*-dodecane,[164] this worm-to-sphere transition is most likely triggered by the surface plasticisation of the PPPMA core block at elevated temperatures. These formulations were later extended by Pei et al. by introducing pentafluorophenyl methacrylate (PFPMA) residues into the PSMA macro-CTA to enable post-polymerisation modification of this stabiliser block via nucleophilic acyl substitution.[167] A further RAFT dispersion polymerisation formulation in non-polar media was recently reported by Lopez-Oliva et al.[170] A near-monodisperse monocarbinol-functionalised polydimethylsiloxane (PDMS) was esterified using PETTC, with the resulting macro-CTA being subsequently used for the RAFT dispersion polymerisation of BzMA in *n*-heptane at 70 °C (Figure 1.28a). In principle, preparing non-vinyl macro-CTAs such as PDMS-PETTC via end-group modification of an existing commercial precursor should provide reproducible access to the same mean stabiliser DP. This is expected to be useful for the construction of phase diagrams, for which remarkably narrow region was observed for the pure worm phase (Figure 1.28c).[170]

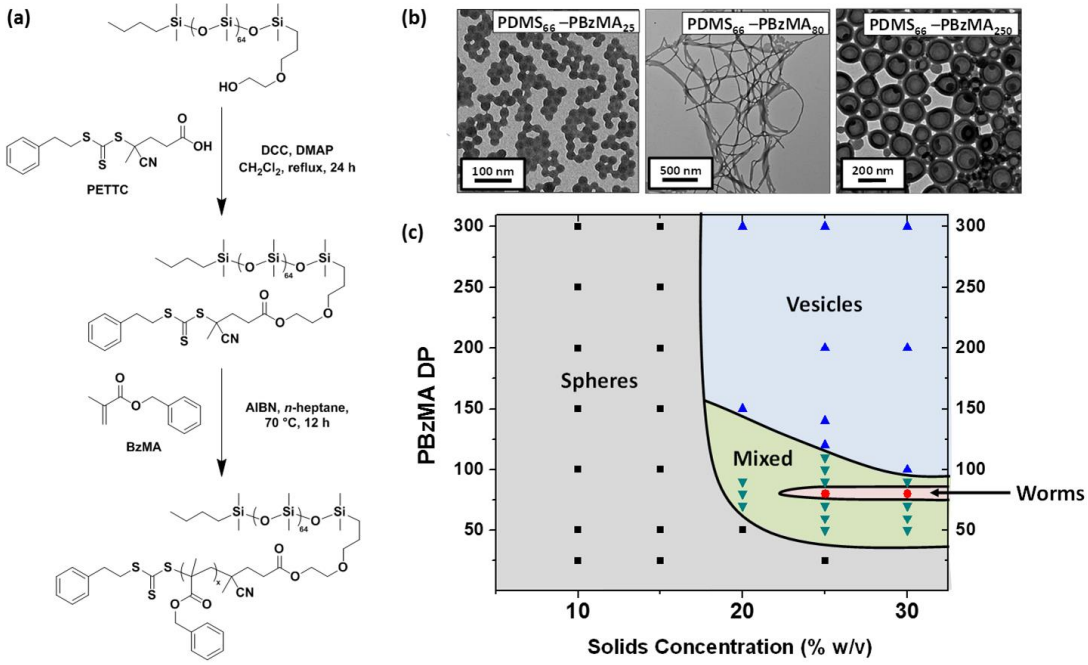

Figure 1.28. (a) Chain-end modification of monocarbinol-functionalised $PDMS_{66}$ and its subsequent chain-extension via RAFT dispersion polymerisation of benzyl methacrylate in *n*-heptane at 70 °C. (b) Representative TEM images of $PDMS_{66}$-$PBzMA_{25}$ spheres, $PDMA_{66}$-$PBzMA_{80}$ worms and $PDMS_{66}$-$PBzMA_{250}$ vesicles in *n*-heptane. (c) Phase diagram constructed for $PDMS_{66}$-$PBzMA_x$ diblock copolymer nanoparticles prepared by RAFT dispersion polymerisation of BzMA in *n*-heptane at 70 °C.[170]

1.6.5. Alternative solvents for RAFT non-aqueous dispersion polymerisation

RAFT non-aqueous dispersion polymerisation is not confined to the conventional organic solvents discussed in earlier sections. Notably, Howdle and co-workers have conducted various syntheses in supercritical carbon dioxide ($scCO_2$). For example, either a $scCO_2$-soluble methacrylate-functionalised PDMS macromonomer[171-173] or a poly(1*H*,1*H*,2*H*,2*H*-perfluorooctyl methacrylate) (PFOMA)[174] macro-CTA was employed to stabilise PMMA particles produced via RAFT dispersion polymerisation. In the former case, a graft copolymer was generated *in situ*, whereas in the latter case a conventional diblock copolymer was obtained. Four CTAs were evaluated for such RAFT dispersion polymerisations: CPDB, *α*-cyanobenzyl dithionaphthalate (CBDN), *α*-cyanobenzyl dithiobenzoate (CBDB) and 4-cyano-1-hydroxypent-4-yl dithiobenzoate (HPDB).[172] Later, various poly(vinyl alkynate)-based steric stabilisers such as the highly $scCO_2$-soluble poly(vinyl acetate-*stat*-vinyl pivalate) (PVAc-*stat*-PVPi)[175, 176] were utilised for the RAFT dispersion polymerisation of *N*-vinyl pyrrolidone (NVP). In principle, this approach eliminates the potential disadvantages of toxicity and high cost associated with PFOMA.[177] In this case a xanthate-based

CTA *S*-(1-ethylpropionate) *O*-ethyl xanthate (EPEX) was employed, but somewhat incomplete (63-90%) NVP conversions were observed.[176] The universal nature of such $scCO_2$ formulations was demonstrated by Jennings et al.,[178, 179] who used PDMS to stabilise PMMA precursor particles, which were then chain-extended with styrene, 4VP, BzMA, DMA and *N*,*N*-dimethylacrylamide (DMAc) via RAFT dispersion polymerisation in $scCO_2$ to produce a series of microphase-separated diblock copolymer particles. TEM and SAXS studies revealed spherical, cylindrical and multi-layered domains within these PDMS-stabilised particles, with the specific target block composition dictating the observed internal morphology (see Figure 1.29).

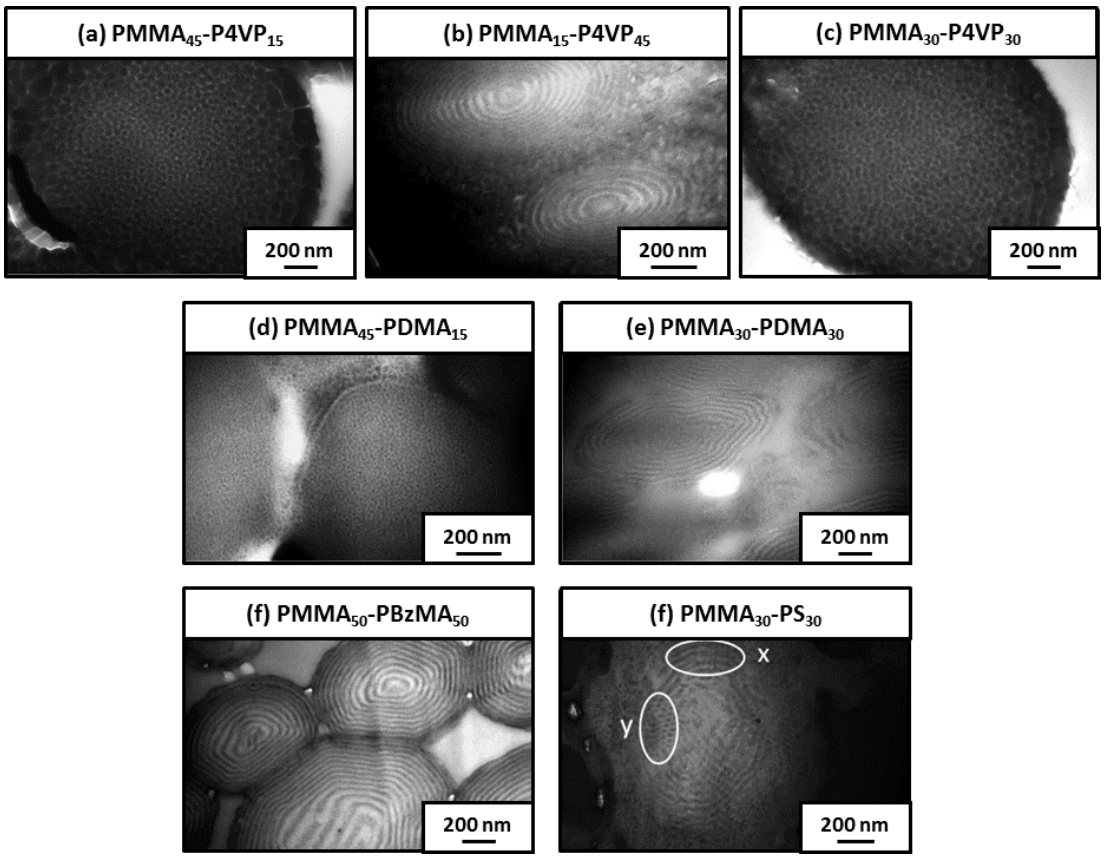

Figure 1.29. Transmission electron micrographs showing the microphase separation within PDMS-stabilised block copolymers of (a) $PMMA_{45}$-$P4VP_{15}$, (b) $PMMA_{15}$-$P4VP_{45}$, (b) $PMMA_{30}$-$P4VP_{30}$, (d) $PMMA_{45}$-$PDMA_{15}$, (e) $PMMA_{30}$-$PDMA_{30}$, (f) $PMMA_{50}$-$PBzMA_{50}$ and (f) $PMMA_{30}$-PS_{30} synthesised via RAFT dispersion polymerisation in supercritical CO_2.[178]

Since no additional solvents are required when conducting RAFT dispersion polymerisations in $scCO_2$, such formulations are deemed environmentally acceptable.[171, 172, 175, 176, 178] Moreover, good control over the molecular weight distribution can be achieved, with M_w/M_n remaining below 1.25 at high ($\geq$ 94%)

monomer conversions.[172, 174] High blocking efficiencies have also been reported for some of these formulations.[179] One other advantage is the relatively easy processing of the final spherical particles, which are isolated as a free-flowing powder. However, such polymerisations require high-pressure autoclave reactors capable of withstanding up to 276 bar for such $scCO_2$ syntheses.[171-179]

1.7. Thesis Outline

The synthesis of well-defined PLMA-PBzMA diblock copolymer spheres, worms or vesicles in industrially-sourced mineral oil and poly(α-olefin) oil is described in Chapter 2. Chapter 3 describes the synthesis of poly(stearyl methacrylate)-poly(benzyl methacrylate) (PSMA-PBzMA) diblock copolymer spheres, worms or vesicles in mineral oil. Specifically, the synthesis of $PSMA_{31}$-$PBzMA_{2000}$ spheres and $PSMA_{13}$-$PBzMA_{150}$ vesicles is studied using *in situ* SAXS, which provides important mechanistic insights into the evolution of the nanoparticle morphology during PISA. The thermo-responsive nature of $PSMA_{13}$-$PBzMA_{96}$ vesicles in mineral oil, which form worms on heating to 150 °C, is discussed in Chapter 4. This thermally-triggered vesicle-to-worm transition offers a potential route to high temperature oil thickening. Chapter 5 describes the physical properties of PSMA-PBzMA worm gels prepared over a range of copolymer concentrations. Maltese cross birefringence patterns confirms worm alignment under applied shear during shear-induced polarised light imaging (SIPLI) studies. A thermally-triggered worm-to-sphere transition leads to immediate loss of this characteristic motif. Various PISA-synthesised block copolymer nanoparticles are evaluated as additives for engine base oils (e.g. lubrication and viscosity modification) and for crude oil (e.g. wax inhibition and asphaltene dispersion) in Chapter 6. Concluding remarks and suggestions for further work are presented in Chapter 7.

1.8. References

1. R. F. T. Stepto, *Pure and Applied Chemistry*, 2009, **81**, 351-353.
2. S. R. Holding and E. Meehan, *Molecular Weight Characterisation of Synthetic Polymers*, Rapra Technology Ltd., Shrewsbury, 1995.
3. P. C. Hiemenz and T. P. Lodge, *Polymer Chemistry, 2nd Ed.*, CRC Press, New York, 2007.
4. B. J. Hunt and S. R. Holding, *Size Exclusion Chromatography*, Chapman and Hall, New York, 1989.

5. S. E. Harding, D. B. Sattelle and V. A. Bloomfield, *Laser Light Scattering in Biochemistry*, The Royal Society of Chemistry, Cambridge, 1992.
6. G. M. Kavanagh and S. B. Ross-Murphy, *Progress in Polymer Science*, 1998, **23**, 533-562.
7. J. W. Goodwin and R. W. Hughes, *Rheology for Chemists: An Introdcution, 2nd Ed.*, The Royal Society of Chemistry, Cambridge, 2008.
8. H. A. Barnes, *A Handbook of Elementary Rheology*, The University of Wales Institute of Non-Newtonian Fluid Mechanics, Aberystwyth, 2000.
9. Y. Y. Won, H. T. Davis and F. S. Bates, *Science*, 1999, **283**, 960-963.
10. G. Odian, *Principles of Polymerization*, McGraw-Hill, New York, 1970.
11. W. A. Braunecker and K. Matyjaszewski, *Progress in Polymer Science*, 2007, **32**, 93-146.
12. M. Szwarc, *Nature*, 1956, **178**, 1168-1169.
13. A. D. Jenkins, R. G. Jones and G. Moad, *Pure and Applied Chemistry*, 2010, **82**, 483-491.
14. G. Moad, E. Rizzardo and S. H. Thang, *Accounts of Chemical Research*, 2008, **41**, 1133-1142.
15. N. Hadjichristidis, H. Iatrou, M. Pitsikalis and J. Mays, *Progress in Polymer Science*, 2006, **31**, 1068-1132.
16. C. J. Hawker, A. W. Bosman and E. Harth, *Chem. Rev.*, 2001, **101**, 3661-3688.
17. J. S. Wang and K. Matyjaszewski, *Macromolecules*, 1995, **28**, 7901-7910.
18. K. Matyjaszewski and J. H. Xia, *Chem. Rev.*, 2001, **101**, 2921-2990.
19. J. Chiefari, Y. K. Chong, F. Ercole, J. Krstina, J. Jeffery, T. P. T. Le, R. T. A. Mayadunne, G. F. Meijs, C. L. Moad, G. Moad, E. Rizzardo and S. H. Thang, *Macromolecules*, 1998, **31**, 5559-5562.
20. D. Greszta, D. Mardare and K. Matyjaszewski, *Macromolecules*, 1994, **27**, 638-644.
21. A. Goto and T. Fukuda, *Progress in Polymer Science*, 2004, **29**, 329-385.
22. H. Fischer, *Chem. Rev.*, 2001, **101**, 3581-3610.
23. G. Moad, E. Rizzardo and S. H. Thang, *Polymer*, 2008, **49**, 1079-1131.
24. C. Detrembleur, C. Jerome, J. De Winter, P. Gerbaux, J.-L. Clement, Y. Guillaneuf and D. Gigmes, *Polymer Chemistry*, 2014, **5**, 335-340.
25. A. Studer, K. Harms, C. Knoop, C. Muller and T. Schulte, *Macromolecules*, 2004, **37**, 27-34.
26. F. Chauvin, P.-E. Dufils, D. Gigmes, Y. Guillaneuf, S. R. A. Marque, P. Tordo and D. Bertin, *Macromolecules*, 2006, **39**, 5238-5250.
27. D. Benoit, V. Chaplinski, R. Braslau and C. J. Hawker, *Journal of the American Chemical Society*, 1999, **121**, 3904-3920.
28. B. Charleux, J. Nicolas and O. Guerret, *Macromolecules*, 2005, **38**, 5485-5492.
29. J. Nicolas, C. Dire, L. Mueller, J. Belleney, B. Charleux, S. R. A. Marque, D. Bertin, S. Magnet and L. Couvreur, *Macromolecules*, 2006, **39**, 8274-8282.
30. M. Kato, M. Kamigaito, M. Sawamoto and T. Higashimura, *Macromolecules*, 1995, **28**, 1721-1723.
31. J. S. Wang and K. Matyjaszewski, *Journal of the American Chemical Society*, 1995, **117**, 5614-5615.
32. K. Matyjaszewski, *Macromolecules*, 2012, **45**, 4015-4039.
33. F. di Lena and K. Matyjaszewski, *Progress in Polymer Science*, 2010, **35**, 959-1021.
34. W. Jakubowski and K. Matyjaszewski, *Macromolecules*, 2005, **38**, 4139-4146.

35. W. Jakubowski, K. Min and K. Matyjaszewski, *Macromolecules*, 2006, **39**, 39-45.
36. T. Pintauer and K. Matyjaszewski, *Chemical Society Reviews*, 2008, **37**, 1087-1097.
37. A. J. D. Magenau, N. C. Strandwitz, A. Gennaro and K. Matyjaszewski, *Science*, 2011, **332**, 81-84.
38. G. Moad, E. Rizzardo and S. H. Thang, *Australian Journal of Chemistry*, 2005, **58**, 379-410.
39. C. Barner-Kowollik, *Handbook of RAFT Polymerization*, Wiley-VCH Verlag GmbH & Co. KGaA, Weinheim, 2008.
40. G. Moad, E. Rizzardo and S. H. Thang, *Australian Journal of Chemistry*, 2009, **62**, 1402-1472.
41. M. L. Coote, E. I. Izgorodina, E. H. Krenske, M. Busch and C. Barner-Kowollik, *Macromolecular Rapid Communications*, 2006, **27**, 1015-1022.
42. C. Barner-Kowollik and S. Perrier, *Journal of Polymer Science Part A-Polymer Chemistry*, 2008, **46**, 5715-5723.
43. C. Boyer, V. Bulmus, T. P. Davis, V. Ladmiral, J. Q. Liu and S. Perrier, *Chem. Rev.*, 2009, **109**, 5402-5436.
44. Y. K. Chong, G. Moad, E. Rizzardo and S. H. Thang, *Macromolecules*, 2007, **40**, 4446-4455.
45. H. Willcock and R. K. O'Reilly, *Polymer Chemistry*, 2010, **1**, 149-157.
46. G. Moad, Y. K. Chong, A. Postma, E. Rizzardo and S. H. Thang, *Polymer*, 2005, **46**, 8458-8468.
47. P. A. Lovell and M. S. El-Aasser, *Emulsion Polymerization and Emulsion Polymers*, John Wiley & Sons, Chichester, 1997.
48. S. Kawaguchi and K. Ito, in *Polymer Particles*, ed. M. Okubo, Springer-Verlag GmbH, Heidelberg, 2005, vol. 175, pp. 299-328.
49. P. B. Zetterlund, S. C. Thickett, S. Perrier, E. Bourgeat-Lami and M. Lansalot, *Chem. Rev.*, 2015, **115**, 9745-9800.
50. A. P. Richez, H. N. Yow, S. Biggs and O. J. Cayre, *Progress in Polymer Science*, 2013, **38**, 897-931.
51. K. P. Lok and C. K. Ober, *Canadian Journal of Chemistry*, 1985, **63**, 209-216.
52. D. W. J. Osmond, 1962, GB Patent 893,429.
53. D. A. Canelas and J. M. DeSimone, *Macromolecules*, 1997, **30**, 5673-5682.
54. G. N. Smith, S. Alexander, P. Brown, D. A. J. Gillespie, I. Grillo, R. K. Heenan, C. James, R. Kemp, S. E. Rogers and J. Eastoe, *Langmuir*, 2014, **30**, 3422-3431.
55. J. N. Israelachvili, D. J. Mitchell and B. W. Ninham, *Journal of the Chemical Society-Faraday Transactions*, 1976, **72**, 1525-1568.
56. J. N. Israelachvili, *Intermolecular and Surface Forces, 3rd Edition*, Academic Press, San Diego, 2011.
57. K. Matyjaszewski, G. Y. and L. Leibler, *Macromolecular Engineering: Precise Synthesis, Materials Properties, Applications*, Wiley-VCH Verlag GmbH & Co. KGaA, Weinheim, 2007.
58. J. Eastoe, in *Colloid Science: Principles, Methods and Applications, 2nd Edition*, ed. T. Cosgrove, John Wiley & Sons Ltd, Chippenham, 2010, pp. 61-89.
59. H. S. Frank and M. W. Evans, *Journal of Chemical Physics*, 1945, **13**, 507-532.
60. C. Tanford, *Science*, 1978, **200**, 1012-1018.

61. F. S. Bates and G. H. Fredrickson, *Annual Review of Physical Chemistry*, 1990, **41**, 525-557.
62. E. L. Thomas, D. M. Anderson, C. S. Henkee and D. Hoffman, *Nature*, 1988, **334**, 598-601.
63. D. E. Discher and A. Eisenberg, *Science*, 2002, **297**, 967-973.
64. L. F. Zhang and A. Eisenberg, *Science*, 1995, **268**, 1728-1731.
65. G. Riess, *Progress in Polymer Science*, 2003, **28**, 1107-1170.
66. Y. Mai and A. Eisenberg, *Chemical Society Reviews*, 2012, **41**, 5969-5985.
67. P. I. Flory, *Journal of Chemical Physics*, 1942, **10**, 51-61.
68. M. L. Huggins, *Journal of the American Chemical Society*, 1942, **64**, 1712-1719.
69. T. Cosgrove, in *Colloid Science: Principles, Methods and Applications, 2nd Edition*, John Wiley & Sons Ltd, Chippenham, 2010, pp. 135-150.
70. F. S. Bates and G. H. Fredrickson, *Physics Today*, 1999, **52**, 32-38.
71. N. Hadjichristidis, S. Pispas and G. Floudas, *Block Copolymers: Synthetic Strategies, Physical Properties, and Applications*, John Wiley & Sons, Inc., Hoboken, 2003.
72. M. W. Matsen and F. S. Bates, *Macromolecules*, 1996, **29**, 1091-1098.
73. P. I. Flory, *Principles of Polymer Chemistry*, Cornell University Press, Ithaca, 1953.
74. S. Krause, *Journal of Physical Chemistry*, 1964, **68**, 1948-1955.
75. S. Jain and F. S. Bates, *Science*, 2003, **300**, 460-464.
76. J. Bang, S. M. Jain, Z. B. Li, T. P. Lodge, J. S. Pedersen, E. Kesselman and Y. Talmon, *Macromolecules*, 2006, **39**, 1199-1208.
77. M. Antonietti and S. Förster, *Advanced Materials*, 2003, **15**, 1323-1333.
78. N. J. Warren and S. P. Armes, *Journal of the American Chemical Society*, 2014, **136**, 10174-10185.
79. A. Blanazs, S. P. Armes and A. J. Ryan, *Macromolecular Rapid Communications*, 2009, **30**, 267-277.
80. Z. Yang, S. Pickard, N. J. Deng, R. J. Barlow, D. Attwood and C. Booth, *Macromolecules*, 1994, **27**, 2371-2379.
81. H. Li, G. E. Yu, C. Price, C. Booth, E. Hecht and H. Hoffmann, *Macromolecules*, 1997, **30**, 1347-1354.
82. C. Booth and D. Attwood, *Macromolecular Rapid Communications*, 2000, **21**, 501-527.
83. S. Sugihara, A. Blanazs, S. P. Armes, A. J. Ryan and A. L. Lewis, *Journal of the American Chemical Society*, 2011, **133**, 15707-15713.
84. V. Bütün, S. P. Armes and N. C. Billingham, *Polymer*, 2001, **42**, 5993-6008.
85. J. R. Howse, R. A. L. Jones, G. Battaglia, R. E. Ducker, G. J. Leggett and A. J. Ryan, *Nature Materials*, 2009, **8**, 507-511.
86. C. J. Ferguson, R. J. Hughes, B. T. T. Pham, B. S. Hawkett, R. G. Gilbert, A. K. Serelis and C. H. Such, *Macromolecules*, 2002, **35**, 9243-9245.
87. C. J. Ferguson, R. J. Hughes, D. Nguyen, B. T. T. Pham, R. G. Gilbert, A. K. Serelis, C. H. Such and B. S. Hawkett, *Macromolecules*, 2005, **38**, 2191-2204.
88. B. Charleux, G. Delaittre, J. Rieger and F. D'Agosto, *Macromolecules*, 2012, **45**, 6753-6765.
89. J. Rieger, F. Stoffelbach, C. Bui, D. Alaimo, C. Jerome and B. Charleux, *Macromolecules*, 2008, **41**, 4065-4068.
90. C. L. Zhang, M. Miao, X. T. Cao and Z. S. An, *Polymer Chemistry*, 2012, **3**, 2656-2664.

91. V. J. Cunningham, A. M. Alswieleh, K. L. Thompson, M. Williams, G. J. Leggett, S. P. Armes and O. M. Musa, *Macromolecules*, 2014, **47**, 5613-5623.
92. Y. Ning, L. A. Fielding, T. S. Andrews, D. J. Growney and S. P. Armes, *Nanoscale*, 2015, **7**, 6691-6702.
93. G. Zheng and C. Pan, *Macromolecules*, 2006, **39**, 95-102.
94. W. Ji, J. Yan, E. Chen, Z. Li and D. Liang, *Macromolecules*, 2008, **41**, 4914-4919.
95. M. Semsarilar, V. Ladmiral, A. Blanazs and S. P. Armes, *Langmuir*, 2012, **28**, 914-922.
96. W.-D. He, X.-L. Sun, W.-M. Wan and C.-Y. Pan, *Macromolecules*, 2011, **44**, 3358-3365.
97. W. Cai, W. Wan, C. Hong, C. Huang and C. Pan, *Soft Matter*, 2010, **6**, 5554-5561.
98. W.-M. Wan, X.-L. Sun and C.-Y. Pan, *Macromolecules*, 2009, **42**, 4950-4952.
99. Y. Pei and A. B. Lowe, *Polymer Chemistry*, 2014, **5**, 2342-2351.
100. Z. An, Q. Shi, W. Tang, C.-K. Tsung, C. J. Hawker and G. D. Stucky, *Journal of the American Chemical Society*, 2007, **129**, 14493-14499.
101. J. Rieger, C. Grazon, B. Charleux, D. Alaimo and C. Jérôme, *Journal of Polymer Science Part A: Polymer Chemistry*, 2009, **47**, 2373-2390.
102. Y. Li and S. P. Armes, *Angewandte Chemie-International Edition*, 2010, **49**, 4042-4046.
103. A. Blanazs, J. Madsen, G. Battaglia, A. J. Ryan and S. P. Armes, *Journal of the American Chemical Society*, 2011, **133**, 16581-16587.
104. C. A. Figg, A. Simula, K. A. Gebre, B. S. Tucker, D. M. Haddleton and B. S. Sumerlin, *Chemical Science*, 2015, **6**, 1230-1236.
105. G. Liu, Q. Qiu, W. Shen and Z. An, *Macromolecules*, 2011, **44**, 5237-5245.
106. H. De Brouwer, M. A. J. Schellekens, B. Klumperman, M. J. Monteiro and A. L. German, *Journal of Polymer Science Part A: Polymer Chemistry*, 2000, **38**, 3596-3603.
107. J. Liu, H. Duong, M. R. Whittaker, T. P. Davis and C. Boyer, *Macromolecular Rapid Communications*, 2012, **33**, 760-766.
108. A. Blanazs, R. Verber, O. O. Mykhaylyk, A. J. Ryan, J. Z. Heath, C. W. I. Douglas and S. P. Armes, *Journal of the American Chemical Society*, 2012, **134**, 9741-9748.
109. K. L. Thompson, C. J. Mable, A. Cockram, N. J. Warren, V. J. Cunningham, E. R. Jones, R. Verber and S. P. Armes, *Soft Matter*, 2014, **10**, 8615-8626.
110. X. W. Zhang, J. Rieger and B. Charleux, *Polymer Chemistry*, 2012, **3**, 1502-1509.
111. X. H. Wang, J. X. Xu, Y. Y. Zhang and W. Q. Zhang, *Journal of Polymer Science Part A: Polymer Chemistry*, 2012, **50**, 2452-2462.
112. X. W. Zhang, S. Boisse, C. Bui, P. A. Albouy, A. Brulet, M. H. Li, J. Rieger and B. Charleux, *Soft Matter*, 2012, **8**, 1130-1141.
113. X. Xiao, S. He, M. Dan, Y. Su, F. Huo and W. Zhang, *Journal of Polymer Science Part A: Polymer Chemistry*, 2013, **51**, 3177-3190.
114. Q. Li, F. Huo, Y. Cui, C. Gao, S. Li and W. Zhang, *Journal of Polymer Science Part A: Polymer Chemistry*, 2014, **52**, 2266-2278.
115. F. Huo, S. T. Li, X. He, S. A. Shah, Q. L. Li and W. Q. Zhang, *Macromolecules*, 2014, **47**, 8262-8269.
116. F. Huo, X. H. Wang, Y. Y. Zhang, X. Zhang, J. X. Xu and W. Q. Zhang, *Macromol. Chem. Phys.*, 2013, **214**, 902-911.

117. F. Huo, S. T. Li, Q. L. Li, Y. Q. Qu and W. Q. Zhang, *Macromolecules*, 2014, **47**, 2340-2349.
118. X. He, Y. Qu, C. Gao and W. Zhang, *Polymer Chemistry*, 2015, **6**, 6386-6393.
119. Z. Song, X. He, C. Gao, H. Khan, P. Shi and W. Zhang, *Polymer Chemistry*, 2015, **6**, 6563-6572.
120. W.-M. Wan, C.-Y. Hong and C.-Y. Pan, *Chemical Communications*, 2009, 5883-5885.
121. W.-M. Wan and C.-Y. Pan, *Macromolecules*, 2010, **43**, 2672-2675.
122. W.-M. Wan and C.-Y. Pan, *Polymer Chemistry*, 2010, **1**, 1475-1484.
123. W.-M. Wan, X.-L. Sun and C.-Y. Pan, *Macromolecular Rapid Communications*, 2010, **31**, 399-404.
124. J.-T. Sun, C.-Y. Hong and C.-Y. Pan, *Polymer Chemistry*, 2013, **4**, 873-881.
125. W. J. Zhang, C. Y. Hong and C. Y. Pan, *Macromolecules*, 2014, **47**, 1664-1671.
126. M. J. Monteiro and M. F. Cunningham, *Macromolecules*, 2012, **45**, 4939-4957.
127. C.-Q. Huang, Y. Wang, C.-Y. Hong and C.-Y. Pan, *Macromolecular Rapid Communications*, 2011, **32**, 1174-1179.
128. Q. L. Li, C. Q. Gao, S. T. Li, F. Huo and W. Q. Zhang, *Polymer Chemistry*, 2014, **5**, 2961-2972.
129. S. Dong, W. Zhao, F. P. Lucien, S. Perrier and P. B. Zetterlund, *Polymer Chemistry*, 2015, **6**, 2249-2254.
130. C.-Q. Huang and C.-Y. Pan, *Polymer*, 2010, **51**, 5115-5121.
131. W.-J. Zhang, C.-Y. Hong and C.-Y. Pan, *Macromolecular Rapid Communications*, 2015, **36**, 1428-1436.
132. P. C. Yang, L. P. D. Ratcliffe and S. P. Armes, *Macromolecules*, 2013, **46**, 8545-8556.
133. W. J. Zhang, F. D'Agosto, O. Boyron, J. Rieger and B. Charleux, *Macromolecules*, 2012, **45**, 4075-4084.
134. X. Zhang, S. Boisse, W. Zhang, P. Beaunier, F. D'Agosto, J. Rieger and B. Charleux, *Macromolecules*, 2011, **44**, 4149-4158.
135. P. Shi, H. Zhou, C. Gao, S. Wang, P. Sun and W. Zhang, *Polymer Chemistry*, 2015, **6**, 4911-4920.
136. M. Semsarilar, E. R. Jones, A. Blanazs and S. P. Armes, *Advanced Materials*, 2012, **24**, 3378-3382.
137. E. R. Jones, M. Semsarilar, A. Blanazs and S. P. Armes, *Macromolecules*, 2012, **45**, 5091-5098.
138. D. Zehm, L. P. D. Ratcliffe and S. P. Armes, *Macromolecules*, 2013, **46**, 128-139.
139. M. Semsarilar, V. Ladmiral, A. Blanazs and S. P. Armes, *Polymer Chemistry*, 2014, **5**, 3466-3475.
140. C. Gonzato, M. Semsarilar, E. R. Jones, F. Li, G. J. P. Krooshof, P. Wyman, O. O. Mykhaylyk, R. Tuinier and S. P. Armes, *Journal of the American Chemical Society*, 2014, **136**, 11100-11106.
141. M. Semsarilar, V. Ladmiral, A. Blanazs and S. P. Armes, *Langmuir*, 2013, **29**, 7416-7424.
142. Y. Y. Kim, A. N. Kulak, Y. T. Li, T. Batten, M. Kuball, S. P. Armes and F. C. Meldrum, *J. Mater. Chem.*, 2009, **19**, 387-398.

143. Y. Y. Kim, K. Ganesan, P. C. Yang, A. N. Kulak, S. Borukhin, S. Pechook, L. Ribeiro, R. Kroger, S. J. Eichhorn, S. P. Armes, B. Pokroy and F. C. Meldrum, *Nature Materials*, 2011, **10**, 890-896.
144. R. P. Brinkhuis, F. Rutjes and J. C. M. van Hest, *Polymer Chemistry*, 2011, **2**, 1449-1462.
145. A. K. Brannan and F. S. Bates, *Macromolecules*, 2004, **37**, 8816-8819.
146. D. E. Discher, V. Ortiz, G. Srinivas, M. L. Klein, Y. Kim, D. Christian, S. Cai, P. Photos and F. Ahmed, *Progress in Polymer Science*, 2007, **32**, 838-857.
147. J. F. Le Meins, O. Sandre and S. Lecommandoux, *European Physical Journal. E, Soft matter*, 2011, **34**, 1-17.
148. J. A. Massey, K. Temple, L. Cao, Y. Rharbi, J. Raez, M. A. Winnik and I. Manners, *Journal of the American Chemical Society*, 2000, **122**, 11577-11584.
149. L. Cao, I. Manners and M. A. Winnik, *Macromolecules*, 2002, **35**, 8258-8260.
150. T. Gaedt, N. S. Ieong, G. Cambridge, M. A. Winnik and I. Manners, *Nature Materials*, 2009, **8**, 144-150.
151. J. B. Gilroy, T. Gadt, G. R. Whittell, L. Chabanne, J. M. Mitchels, R. M. Richardson, M. A. Winnik and I. Manners, *Nature Chemistry*, 2010, **2**, 566-570.
152. S. K. Patra, R. Ahmed, G. R. Whittell, D. J. Lunn, E. L. Dunphy, M. A. Winnik and I. Manners, *Journal of the American Chemical Society*, 2011, **133**, 8842-8845.
153. P. A. Rupar, L. Chabanne, M. A. Winnik and I. Manners, *Science*, 2012, **337**, 559-562.
154. M. Semsarilar, N. J. W. Penfold, E. R. Jones and S. P. Armes, *Polymer Chemistry*, 2015, **6**, 1751-1757.
155. Y. W. Pei, N. C. Dharsana, J. A. Van Hensbergen, R. P. Burford, P. J. Roth and A. B. Lowe, *Soft Matter*, 2014, **10**, 5787-5796.
156. Y. W. Pei, J. M. Noy, P. J. Roth and A. B. Lowe, *Polymer Chemistry*, 2015, **6**, 1928-1931.
157. Y. Pei, N. C. Dharsana and A. B. Lowe, *Australian Journal of Chemistry*, 2015, **68**, 939-945.
158. R. H. Pelton and P. Chibante, *Colloids and Surfaces*, 1986, **20**, 247-256.
159. A. R. Shultz and P. J. Flory, *Journal of the American Chemical Society*, 1952, **74**, 4760-4767.
160. L. Houillot, C. Bui, M. Save, B. Charleux, C. Farcet, C. Moire, J.-A. Raust and I. Rodriguez, *Macromolecules*, 2007, **40**, 6500-6509.
161. L. Houillot, C. Bui, C. Farcet, C. Moire, J.-A. Raust, H. Pasch, M. Save and B. Charleux, *ACS Applied Materials & Interfaces*, 2010, **2**, 434-442.
162. J. A. Raust, L. Houillot, M. Save, B. Charleux, C. Moire, C. Farcet and H. Pasch, *Macromolecules*, 2010, **43**, 8755-8765.
163. L. A. Fielding, M. J. Derry, V. Ladmiral, J. Rosselgong, A. M. Rodrigues, L. P. D. Ratcliffe, S. Sugihara and S. P. Armes, *Chemical Science*, 2013, **4**, 2081-2087.
164. L. A. Fielding, J. A. Lane, M. J. Derry, O. O. Mykhaylyk and S. P. Armes, *Journal of the American Chemical Society*, 2014, **136**, 5790-5798.
165. Y. Pei, L. Thurairajah, O. R. Sugita and A. B. Lowe, *Macromolecules*, 2015, **48**, 236-244.
166. Y. Pei, O. R. Sugita, L. Thurairajah and A. B. Lowe, *RSC Advances*, 2015, **5**, 17636-17646.

167. Y. Pei, J.-M. Noy, P. J. Roth and A. B. Lowe, *Journal of Polymer Science Part A: Polymer Chemistry*, 2015, **53**, 2326-2335.
168. R. Zheng, G. Liu, M. Devlin, K. Hux and T.-C. Jao, *Tribology Transactions*, 2010, **53**, 97-107.
169. S. P. Armes, L. A. Fielding and M. J. Derry, 2013, WO2014049363.
170. A. P. Lopez-Oliva, N. J. Warren, A. Rajkumar, O. O. Mykhaylyk, M. J. Derry, K. E. B. Doncom, M. J. Rymaruk and S. P. Armes, *Macromolecules*, 2015, **48**, 3547-3555.
171. T. Hasell, K. J. Thurecht, R. D. W. Jones, P. D. Brown and S. M. Howdle, *Chemical Communications*, 2007, 3933-3935.
172. A. M. Gregory, K. J. Thurecht and S. M. Howdle, *Macromolecules*, 2008, **41**, 1215-1222.
173. K. J. Thurecht, A. M. Gregory, W. Wang and S. M. Howdle, *Macromolecules*, 2007, **40**, 2965-2967.
174. M. Zong, K. J. Thurecht and S. M. Howdle, *Chemical Communications*, 2008, 5942-5944.
175. H. Lee, E. Terry, M. Zong, N. Arrowsmith, S. Perrier, K. J. Thurecht and S. M. Howdle, *Journal of the American Chemical Society*, 2008, **130**, 12242-12243.
176. N. A. Birkin, N. J. Arrowsmith, E. J. Park, A. P. Richez and S. M. Howdle, *Polymer Chemistry*, 2011, **2**, 1293-1299.
177. N. A. Birkin, O. J. Wildig and S. M. Howdle, *Polymer Chemistry*, 2013, **4**, 3791-3799.
178. J. Jennings, M. Beija, A. P. Richez, S. D. Cooper, P. E. Mignot, K. J. Thurecht, K. S. Jack and S. M. Howdle, *Journal of the American Chemical Society*, 2012, **134**, 4772-4781.
179. J. Jennings, M. Beija, J. T. Kennon, H. Willcock, R. K. O'Reilly, S. Rimmer and S. M. Howdle, *Macromolecules*, 2013, **46**, 6843-6851.

2. Industrially-Relevant Polymerisation-Induced Self-Assembly Formulations in Non-Polar Solvents: RAFT Dispersion Polymerisation of Benzyl Methacrylate

2.1. Introduction

Traditionally, block copolymer self-assembly in solution to form various types of nanoparticles is conducted at high dilution (< 1% w/w) and often involves post-polymerisation processing via solvent[1] or pH switching,[2] or thin film rehydration.[3] Over the last two decades or so, controlled radical techniques such as reversible addition-fragmentation chain transfer (RAFT) polymerisation[4-6] have enabled the convenient synthesis of a wide range of functional diblock copolymers.[7-20] Currently, there is considerable academic interest in performing polymerisation-induced self-assembly (PISA) syntheses, where self-assembly of block copolymers is achieved *in situ*.[21-24] Moreover, PISA provides a convenient route to direct block copolymer self-assembly at relatively high solids contents. The final diblock copolymer nanoparticle morphology typically depends on the relative volume fractions of the two blocks, which is often considered in terms of the so-called packing parameter,[25-27] and also the copolymer concentration.[28] Purely spherical, worm-like or vesicular morphologies have been reported for aqueous,[28-37] alcoholic[38-50] and non-polar[51-56] formulations. The subsequent construction of detailed phase diagrams enables the reproducible targeting of each of these morphologies. Moreover, there appears to be some scope for developing 'one-pot' syntheses,[57-60] which should provide a highly convenient and potentially industrially-relevant protocol for generating organic nanoparticles at high solids contents.

A wide range of potential applications have been explored for RAFT-mediated PISA formulations, including in coatings,[61] drug delivery,[15, 47, 62] contact lenses,[63] sterilisable gels,[64] or as novel Pickering emulsifiers.[65] In principle, block copolymer nanoparticles comprising an oil-soluble stabilising block such as poly(lauryl methacrylate) (PLMA) also have potential applications, including use in drag reduction,[66] as oil absorbency agents,[67, 68] and for viscosity modification in engine oils.[69-71] Of particular relevance to the present work, Zheng et al.[72] recently reported that spherical block copolymer nanoparticles dispersed in non-polar solvents significantly reduced the friction coefficient of lubricant base oils in the boundary lubrication regime. In this case, copper-catalysed atom transfer radical polymerisation (ATRP) was utilised to synthesise all-acrylic block copolymer spheres in 2-butanone, which were subsequently dispersed in base oil after various post-polymerisation

modification and purification steps.[73] Such modification and purification steps may hinder the industrial potential of these particular nanoparticles, and the use of copper during the polymerisation may also cause failure in industry standard engine tests. Considering the recent development of commercial products synthesised using RAFT polymerisation by The Lubrizol Corporation Ltd.,[74] the development of diblock copolymer nanoparticles using RAFT polymerisation is a particularly attractive alternative.

RAFT-mediated PISA in non-polar solvents was first reported by Charleux and co-workers,[51-53] where all-acrylic diblock copolymer spheres were synthesised in *iso*-dodecane. Later, Fielding et al. reported the synthesis of poly(lauryl methacrylate)-poly(benzyl methacrylate) (PLMA-PBzMA) nanoparticles in *n*-heptane[54] and *n*-dodecane.[55] These formulations provided access to pure spherical, worm-like and vesicular morphologies and enabled the construction of predictive phase diagrams, enabling the reproducible synthesis of each morphology.

Herein, an extension to the previously reported PLMA-PBzMA formulations is described. Specifically, PISA syntheses have been conducted in both mineral oil and a poly(*α*-olefin) (PAO) oil (see Scheme 2.1). Predictive phase diagrams have been constructed for both these industrially-sourced oils which indicate subtle differences compared to those constructed for pure *n*-alkane formulations, particularly with respect to the phase space occupied by each copolymer morphology. Moreover, a 'one-pot' synthesis of spherical PLMA-PBzMA nanoparticles was devised, further highlighting the industrial potential of this PISA formulation.

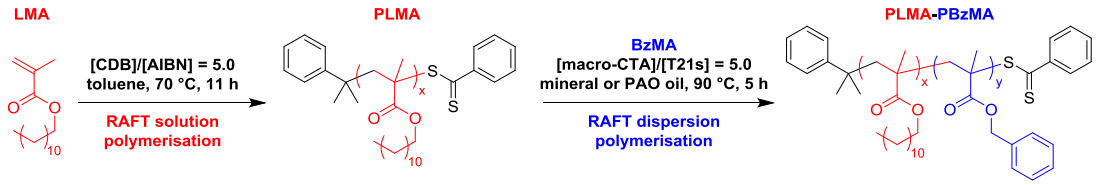

Scheme 2.1. Synthesis of a poly(lauryl methacrylate) (PLMA) macro-CTA via RAFT solution polymerisation in toluene at 70 °C, followed by RAFT dispersion polymerisation of benzyl methacrylate (BzMA) in mineral or poly(*α*-olefin) (PAO) oil at 90 °C.

2.2. Experimental

2.2.1. Materials

Monomers were purchased from Sigma-Aldrich (UK) and passed through basic alumina prior to use to remove inhibitor. *Tert*-butyl peroxy-2-ethylhexanoate (T21s) initiator was purchased from AkzoNobel (The Netherlands). Cumyl dithiobenzoate (CDB), $CDCl_3$ and all other reagents were purchased from Sigma-Aldrich (UK) and were used as received, unless otherwise noted. THF and toluene were purchased from Fisher Scientific (UK), CD_2Cl_2 was purchased from Goss Scientific (UK). Industrial-grade mineral (viscosity at 20 °C = 2.5 mPa s) and poly(α-olefin) (PAO; viscosity at 20 °C = 3.0 mPa s) oils were provided by Lubrizol Corporation Ltd.

2.2.2. Synthesis of poly(lauryl methacrylate) (PLMA) macromolecular chain transfer agent (macro-CTA)

The synthesis of PLMA macro-CTAs has been previously reported.[54] A typical synthesis of a $PLMA_{47}$ macro-CTA was conducted as follows. A 250 mL round-bottomed flask was charged with lauryl methacrylate (LMA; 20.0 g; 78.6 mmol), cumyl dithiobenzoate (CDB; 0.43 g; 1.57 mmol; target degree of polymerisation, DP = 50), 2,2'-azobisisobutyronitrile (AIBN; 51.6 mg, 314 μmol; [CDB]/[AIBN] molar ratio = 5.0) and toluene (30.7 g). The sealed reaction vessel was purged with nitrogen and placed in a pre-heated oil bath at 70 °C for 11 h. The resulting PLMA (LMA conversion = 81 % (see Figure 2.1 and Equations 2.1-2.3); M_n = 11,600 g mol^{-1}, M_w/M_n = 1.24) was purified by twice precipitating into excess methanol.

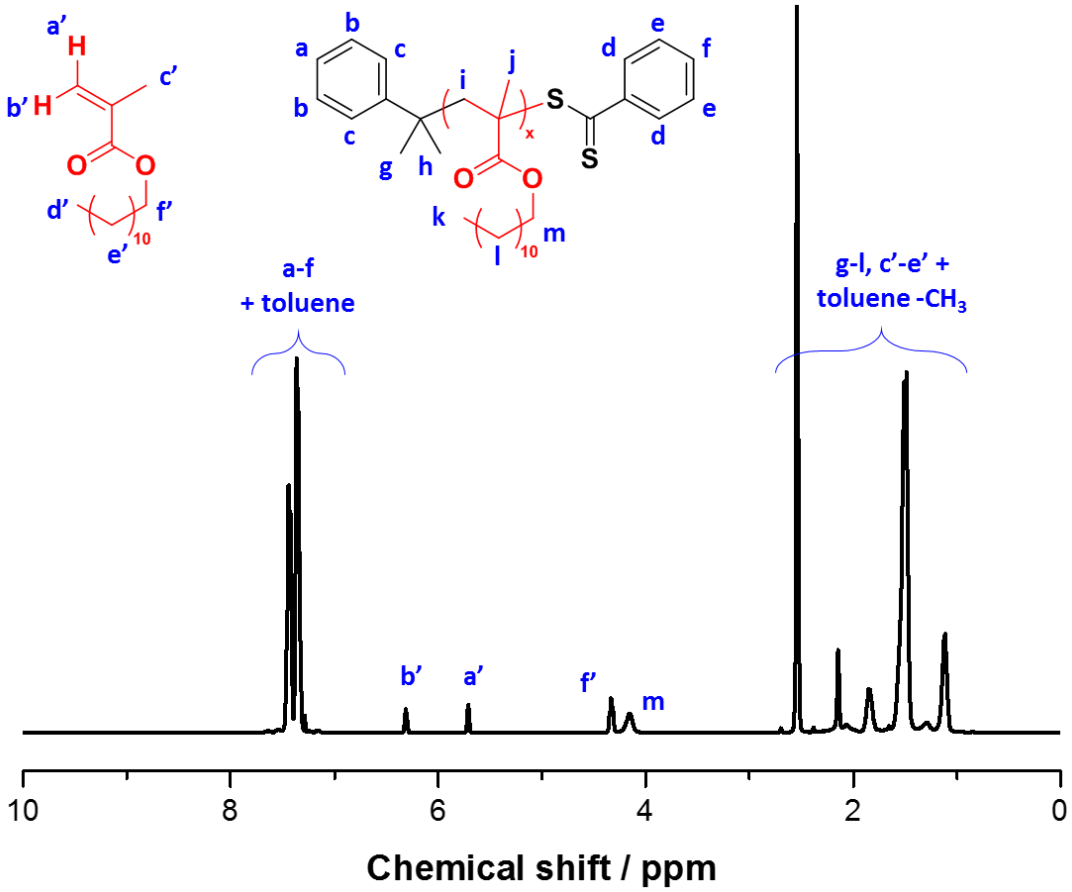

Figure 2.1. Assigned ^{1}H NMR spectrum obtained for the reaction mixture directly after the synthesis of a PLMA macro-CTA (before purification).

$$I_{\mathrm{m}} = [Integral\ (\mathrm{a}' + b')] = 2\mathrm{H} \qquad 2.1$$

$$I_{\mathrm{p}} = [Integral\ (m + f')] - I_{\mathrm{m}} \qquad 2.2$$

$$\%\ Conversion = \left(1 - \frac{I_{\mathrm{m}}}{I_{\mathrm{m}} + I_{\mathrm{p}}}\right) \times 100 \qquad 2.3$$

The mean degree of polymerisation (DP) of this macro-CTA was calculated to be 47 using ^{1}H NMR spectroscopy by comparing the integrated signals corresponding to the CDB aromatic protons at 7.1-8.1 ppm with that assigned to the two oxymethylene protons of PLMA at 3.7-4.2 ppm (see Figure 2.2 and Equations 2.4 and 2.5). Thus the CTA efficiency of the CDB was estimated to be 86% (see Equation 2.6).

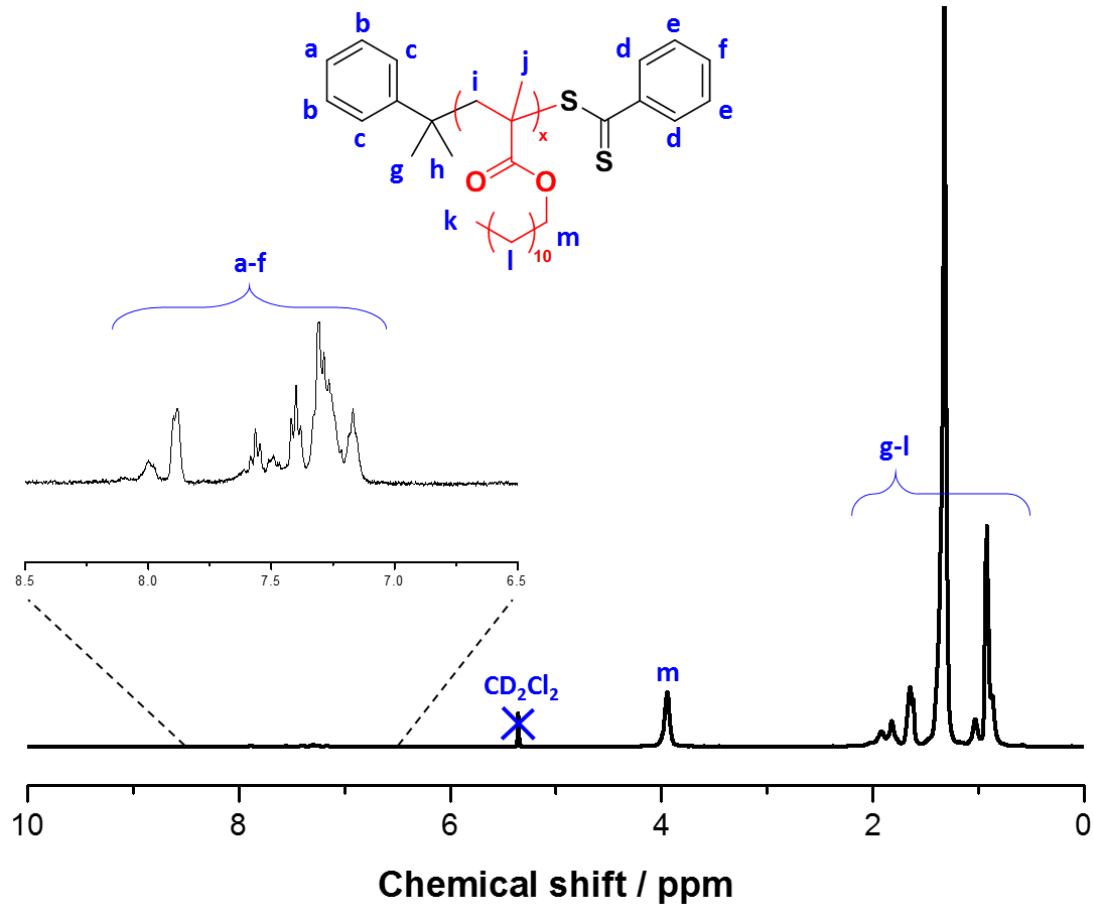

Figure 2.2. Assigned ^{1}H NMR spectrum obtained for a purified PLMA macro-CTA (in CD_2Cl_2).

$$[Integral\ (a-f)] = 10\text{H} \qquad 2.4$$

$$PLMA\ DP = \frac{[Integral\ (m)]}{2} \qquad 2.5$$

$$\%\ CTA\ efficiency = \frac{Target\ DP\ \text{x}\ NMR\ Conversion}{Actual\ PLMA\ DP}\ \text{x}\ 100 \qquad 2.6$$

2.2.3. Synthesis of poly(lauryl methacrylate)-poly(benzyl methacrylate) (PLMA-PBzMA) diblock copolymer nanoparticles

A typical RAFT dispersion polymerisation synthesis of $PLMA_{18}$-$PBzMA_{45}$ diblock copolymer nanoparticles at 25% w/w solids was carried out as follows. Benzyl

methacrylate (BzMA; 0.415 g; 2.36 mmol), T21s initiator (2.26 mg; 10.5 μmol; dissolved at 10.0% v/v in mineral oil) and $PLMA_{18}$ macro-CTA (0.27 g; 52.3 μmol; [$PLMA_{18}$]/[T21s] molar ratio = 5.0; target PBzMA DP = 45) were dissolved in mineral oil (2.06 g). The reaction mixture was sealed in a 10 mL round-bottomed flask and purged with nitrogen gas for 30 min. The deoxygenated solution was then placed in a pre-heated oil bath at 90 °C for 5 h (final BzMA conversion = 99%; M_n = 9,700 g mol^{-1}, M_w/M_n = 1.24).

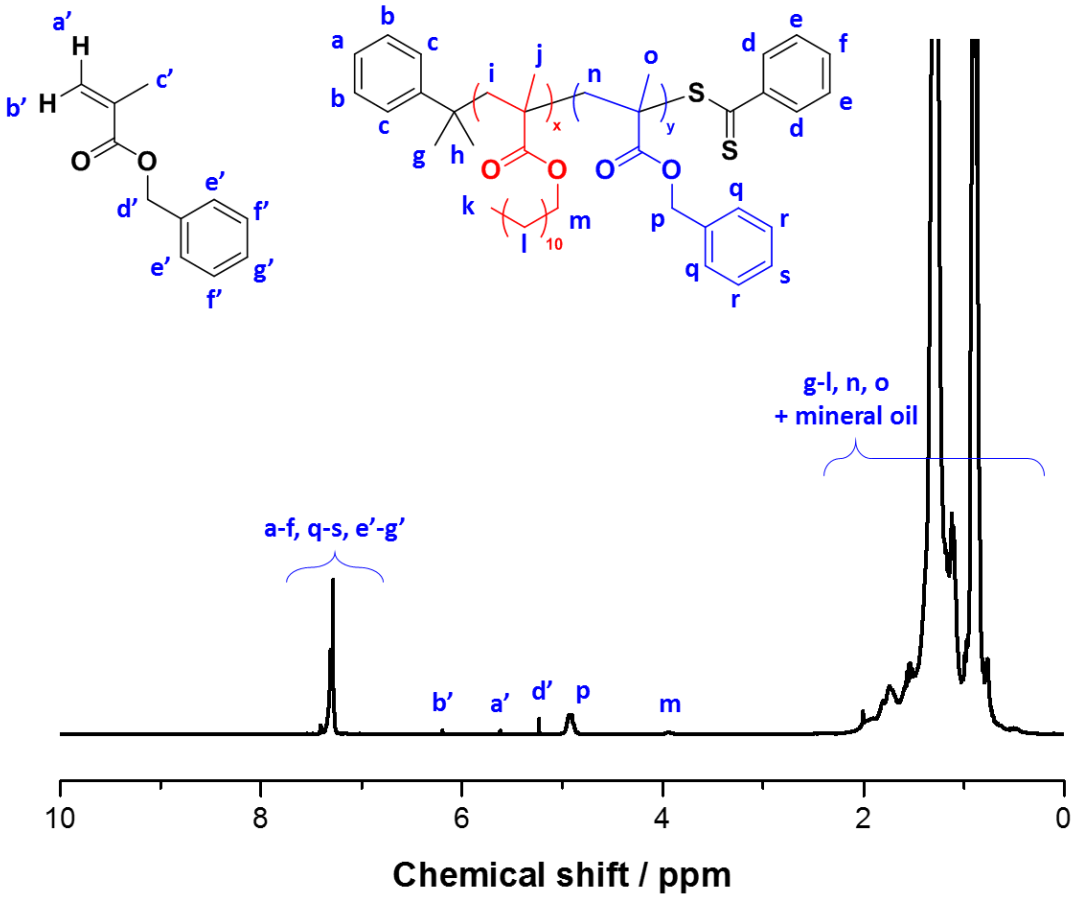

Figure 2.3. Assigned ^{1}H NMR spectrum obtained for the reaction mixture directly after the synthesis of a PLMA-PBzMA diblock copolymer.

Similarly to the solution polymerisation of LMA, BzMA conversions for RAFT dispersion polymerisations are determined via ^{1}H NMR using Equations 2.7 to 2.9 below.

$$I_m = [Integral\ (a' + b')] = 2H \qquad 2.7$$

$$I_{\mathrm{p}} = [Integral\ (p + d')] - I_{\mathrm{m}} \qquad 2.8$$

$$\%\ Conversion = \left(1 - \frac{I_{\mathrm{m}}}{I_{\mathrm{m}} + I_{\mathrm{p}}}\right) \times 100 \qquad 2.9$$

2.2.4. 'One-pot' synthesis of poly(lauryl methacrylate)-poly(benzyl methacrylate) (PLMA-PBzMA) diblock copolymer spheres

A typical 'one-pot' synthesis of $PLMA_{50}$-$PBzMA_{100}$ diblock copolymer spheres was conducted as follows. Lauryl methacrylate (LMA; 0.700 g; 2.75 mmol), cumyl dithiobenzoate (CDB; 15.0 mg; 55.0 μmol; target DP = 50; dissolved at 10% w/w in mineral oil) and T21s initiator (2.14 mg; 9.90 μmol; dissolved at 10% v/v in mineral oil) were dissolved in mineral oil (0.150 g) to obtain a total solids content of 70% w/w. The reaction mixture was sealed in a 25 mL round-bottomed flask and purged with nitrogen gas for 30 min. The deoxygenated solution was then placed in a pre-heated oil bath at 90 °C for 5 h (final LMA conversion = 95%; M_{n} = 12,500 g mol^{-1}; $M_{\mathrm{w}}/M_{\mathrm{n}}$ = 1.18). Benzyl methacrylate (BzMA; 0.970 g; 5.50 mmol; target DP = 100) and T21s initiator (2.14 mg; 9.90 μmol; dissolved at 10 % v/v in mineral oil) were dissolved in mineral oil (3.65 g) and purged with nitrogen gas for 30 min before being added to the original reaction vessel (total solids content now 30% w/w) and stirred for 4 h at 90 °C (final BzMA conversion = 98%; M_{n} = 24,500 g mol^{-1}; $M_{\mathrm{w}}/M_{\mathrm{n}}$ = 1.15).

2.2.5. Gel Permeation Chromatography (GPC)

Molecular weight distributions (MWDs) were assessed by GPC using THF eluent at 30 °C. The THF GPC system was equipped with two 5 μm (30 cm) Mixed C columns and a WellChrom K-2301 refractive index detector operating at 950 ± 30 nm. The mobile phase contained 2.0 % v/v triethylamine and 0.05 % w/v butylhydroxytoluene (BHT) with a toluene flow rate marker and the flow rate was fixed at 1.0 mL min^{-1}. A series of ten near-monodisperse poly(methyl methacrylate) standards (M_{p} values ranging from 645 to 2,480,000 g mol^{-1}) were used for calibration.

2.2.6. ^{1}H Nuclear Magnetic Resonance (NMR) spectroscopy

^{1}H NMR spectra were recorded in either CD_2Cl_2 or $CDCl_3$ using a Bruker AV1-400 or AV1-250 MHz spectrometer. Typically 64 scans were averaged per spectrum.

2.2.7. Dynamic light scattering (DLS)

DLS studies were performed at 25 °C using a Zetasizer Nano-ZS instrument (Malvern Instruments, UK) at a fixed back scattering angle of 173°. Copolymer dispersions were diluted to 0.10% w/w using *n*-dodecane prior to light scattering studies. Temperature-dependent DLS studies were performed on 0.10% w/w dispersions in *n*-dodecane and heated from 20 °C to 90 °C at 5 °C intervals, allowing 5 min for thermal equilibration between measurements. In both sets of experiments, the intensity-average diameter and polydispersity of the diblock copolymer particles were calculated by cumulants analysis of the experimental correlation function using Dispersion Technology Software version 6.20. Data were averaged over thirteen runs each of thirty seconds duration.

2.2.8. Transmission Electron Microscopy (TEM)

TEM studies were conducted using a Philips CM 100 instrument operating at 100 kV and equipped with a Gatan 1 k CCD camera. Diluted block copolymer solutions (0.10% w/w) were placed on carbon-coated copper grids and exposed to ruthenium(VIII) oxide vapour for 7 min at 20 °C prior to analysis.[75] This heavy metal compound acted as a positive stain for the core-forming PBzMA block to improve contrast. The ruthenium(VIII) oxide was prepared as follows: ruthenium(IV) oxide (0.30 g) was added to water (50 g) to form a black slurry; subsequent addition of sodium periodate (2.0 g) with stirring produced a yellow solution of ruthenium(VIII) oxide within 1 min.

2.2.9. Oscillatory rheology measurements

A TA Instruments AR-G2 rheometer equipped with a variable temperature Peltier plate and a 40 mm 2° aluminium cone was used for all experiments. The storage (*G*') and loss (*G*") moduli were measured as a function of temperature at a fixed strain of 1.0% and an angular frequency of 10 rad s^{-1} so as to assess the gel stiffness and critical gelation temperature (CGT). During temperature sweeps, the temperature was varied

at 5 °C intervals, with an equilibration time of five minutes being allowed prior to each measurement. In all cases the gap between the cone and plate was 58 μm.

2.3. Results and Discussion

2.3.1. Synthesis of PLMA macro-CTAs

Low-polydispersity PLMA macro-CTAs with mean DPs of 16, 18, or 47 (see Table 2.1) were synthesised via RAFT solution polymerisation in toluene at 70 °C using cumyl dithiobenzoate (CDB) as a CTA. In all macro-CTA syntheses, the polymerisation was quenched at 71-81% conversion in order to avoid monomer-starved conditions and therefore ensure retention of the RAFT end-groups.[76, 77] This is usually considered to be desirable for high blocking efficiencies and hence well-defined PLMA-PBzMA diblock copolymers. All PLMA macro-CTAs had a polydispersity (M_w/M_n) of less than 1.25, suggesting well controlled RAFT polymerisations.

Table 2.1. Summary of monomer conversions, mean degrees of polymerisation and GPC molecular weights for three PLMA macro-CTAs prepared by RAFT solution polymerisation of LMA in toluene at 70 °C using AIBN and CDB. Conditions: total solids concentration = 40% w/w, [CDB]/[AIBN] molar ratio = 5.0.

Target DP	Conv.[a]	Actual DP[a]	M_n[b] / g mol^{-1}	M_w[b] / g mol^{-1}	M_w/M_n[b]
$PLMA_{10}$	79%	16	4,900	5,800	1.19
$PLMA_{10}$	71%	18	4,800	5,800	1.20
$PLMA_{50}$	81%	47	11,600	14,400	1.24

[a]Determined by ^{1}H NMR spectroscopy. [b]Determined by THF GPC against poly(methyl methacrylate) standards.

A representative kinetic study of the RAFT solution polymerisation of LMA to prepare a $PLMA_{18}$ macro-CTA indicated a near-linear evolution of molecular weight with conversion (see Figure 2.4b). After an initial induction period of ~100 min, this reaction obeyed first-order kinetics (see Figure 2.4a) and was quenched after 11 h (71% conversion).

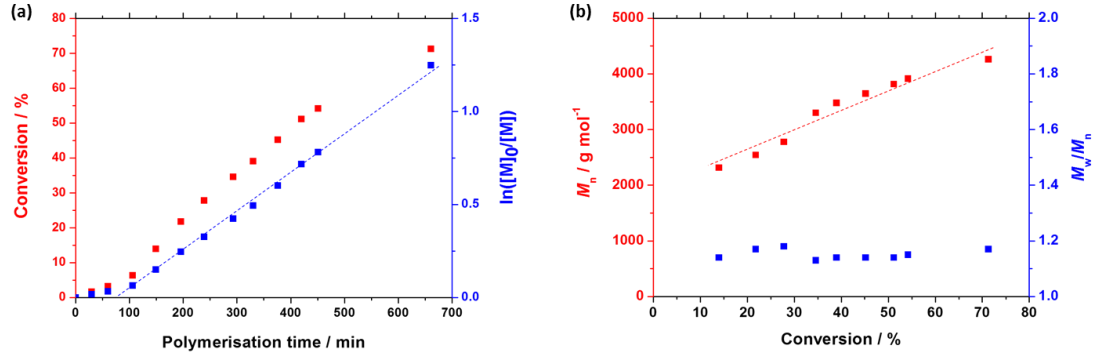

Figure 2.4. (a) LMA conversion vs. polymerisation time and (b) M_n and M_w/M_n vs. conversion for the RAFT solution polymerisation of LMA in toluene at 70 °C using AIBN and CDB, for a target DP of 10. Conditions: total solids concentration = 40% w/w, [CDB]/[AIBN] molar ratio = 5.0. Conversions were determined using ^{1}H NMR spectroscopy.

2.3.2. PLMA-PBzMA block copolymer syntheses and phase diagrams

One important trend in the commercial engine oil sector is a general shift from mineral oil towards wholly synthetic oils such as poly(α-olefins). Preliminary experiments confirmed that both these industrially-sourced oils were good solvents for PLMA and bad solvents for PBzMA. Hence phase diagrams for PLMA-PBzMA block copolymer nanoparticles prepared in these two oils were constructed in order to assess the effect of the nature of the solvent on the positions of the phase boundaries. Firstly, a low-polydispersity PLMA macro-CTA with a sufficiently low mean DP to enable the synthesis of higher-order morphologies (e.g. $PLMA_{18}$)[54, 55] was selected. Varying amounts of BzMA monomer were polymerised using the same PLMA macro-CTA via RAFT dispersion polymerisation in mineral oil to produce a series of well-defined PLMA-PBzMA diblock copolymer nanoparticles at various copolymer concentrations. More than 95% BzMA monomer conversion was achieved in all dispersion polymerisations within 5 h at 90 °C, as judged by ^{1}H NMR spectroscopy. Pure spherical, worm-like, or vesicular morphologies were confirmed by TEM studies (see Figure 2.5a, b and c, respectively) and a predictive phase diagram was constructed for $PLMA_{18}$-$PBzMA_x$ diblock copolymers in mineral oil (Figure 2.5).

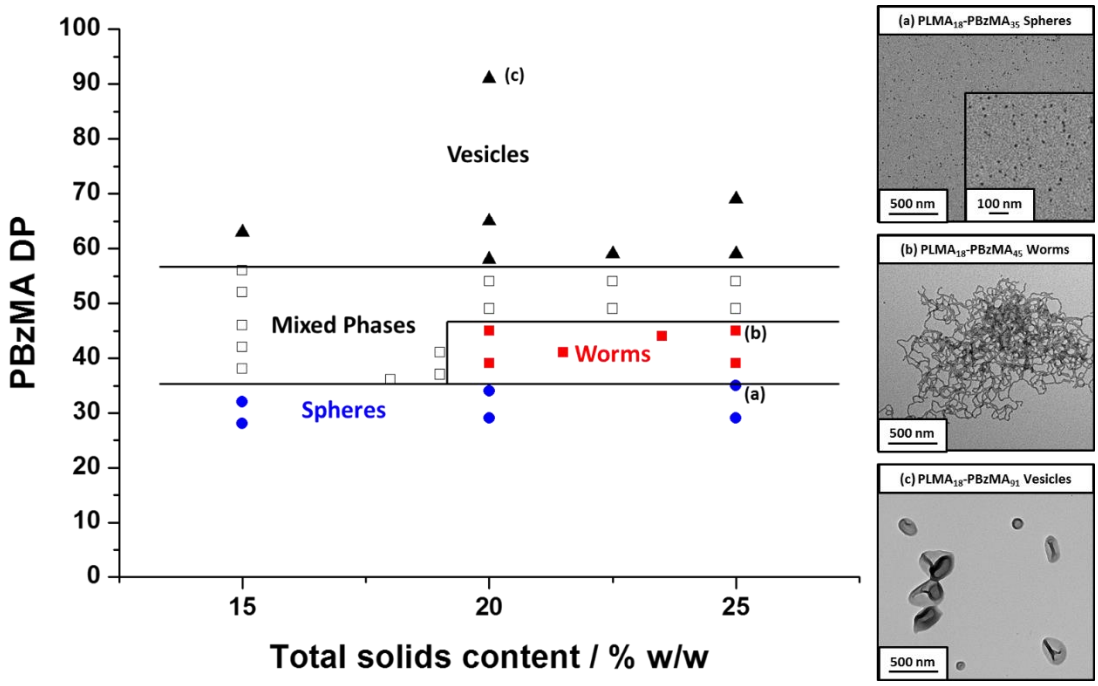

Figure 2.5. Phase diagram constructed for $PLMA_{18}$-$PBzMA_x$ diblock copolymer nanoparticles prepared by RAFT dispersion polymerisation of BzMA in mineral oil using T21s at 90 °C ([PLMA]/[T21s] molar ratio = 5.0). The post mortem diblock copolymer morphologies were assigned from TEM images obtained from 0.10% w/w copolymer dispersions at 20 °C. TEM images (a), (b) and (c) represent examples of purely vesicular, worm-like or spherical morphologies, respectively.

Previously reported phase diagrams for PLMA-PBzMA diblock copolymer formulations in *n*-heptane[54] and *n*-dodecane[55] exhibited purely spherical and vesicular phases at copolymer concentrations ranging from 12.5 to 25% w/w, whereas solely worm-like micelles could only be obtained at copolymer concentrations at or above 18% w/w. Although the phase diagram for PLMA-PBzMA nanoparticles in mineral oil (Figure 2.5) is similar to that reported for *n*-heptane, the precise block copolymer compositions required to access each individual morphology are subtly different. This shift in phase boundaries is best highlighted when comparing the pure worm phase in each oil. In *n*-heptane, the worm phase for $PLMA_{17}$-$PBzMA_x$ diblock copolymers corresponds to $x \approx 50$-70, whereas worms are obtained at $x \approx 37$-47 for a $PLMA_{18}$-$PBzMA_x$ formulation in mineral oil (see Figure 2.5), which is close to that observed for *n*-dodecane (for $PLMA_{17}$-$PBzMA_x$, where x = 36-44).[55]

Using an industrially-sourced PAO as the continuous phase for the synthesis of PLMA-PBzMA diblock copolymer nano-objects enables the role of the solvent in such PISA syntheses to be examined. Accordingly, a $PLMA_{16}$ macro-CTA was chain-

extended with varying amounts of BzMA at various solids contents in order to construct a phase diagram (Figure 2.6).

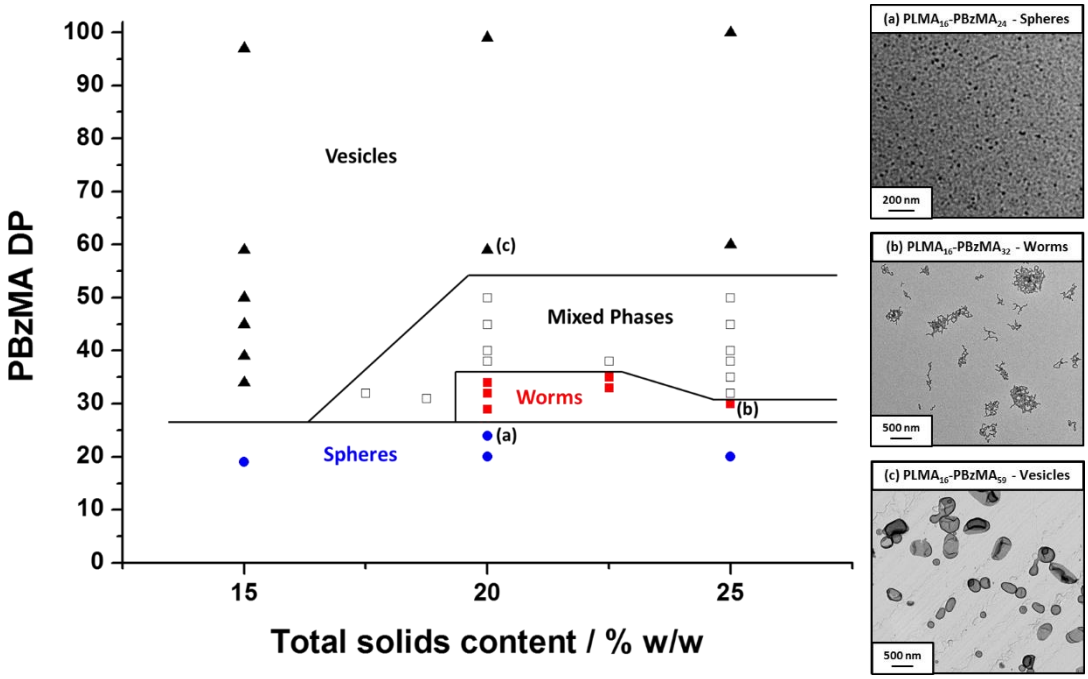

Figure 2.6. Phase diagram constructed for $PLMA_{16}$-$PBzMA_x$ diblock copolymer nanoparticles prepared by RAFT dispersion polymerisation of BzMA in poly(α-olefin) oil using T21s at 90 °C ([PLMA]/[T21s] molar ratio = 5.0). The post mortem diblock copolymer morphologies were assigned from TEM images obtained from 0.10% w/w copolymer dispersions at 20 °C. TEM images (a), (b) and (c) represent examples of pure vesicular, worm-like or spherical morphologies, respectively.

Although this phase diagram exhibits obvious similarities to that obtained for $PLMA_{18}$-$PBzMA_x$ in mineral oil (Figure 2.5), some subtle differences are observed. In particular, for $PLMA_{16}$-$PBzMA_x$ syntheses conducted at ≥ 20% w/w solids, the worm phase in PAO is observed for x ≈ 28-35. In contrast, the worm phase obtained for $PLMA_{18}$-$PBzMA_x$ when using mineral oil occurs for x ≈ 37-47. Even allowing for the small differences between the mean DPs of the PLMA stabiliser blocks, it is clear that a somewhat longer PBzMA block is required to access the worm phase in mineral oil. This suggests that PAO is a slightly poorer solvent for the growing PBzMA chains than the mineral oil. In order to further illustrate this point, $PLMA_{18}$-$PBzMA_{45}$ nano-objects were prepared at 20% w/w solids in both PAO and mineral oil (see Figure 2.7).

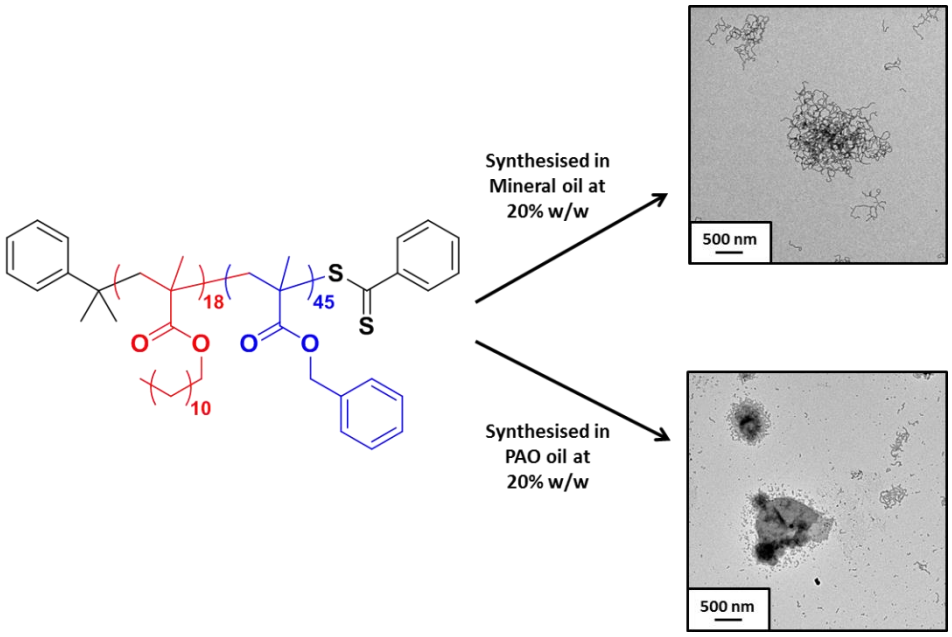

Figure 2.7. Synthesis of $PLMA_{18}$-$PBzMA_{45}$ diblock copolymer nanoparticles in either mineral or PAO oil at 20% w/w solids. In the former case a pure worm phase is obtained, whereas in the latter case a mixed phase of spheres, worms and vesicles is obtained as judged by TEM.

Inspecting Figure 2.5, $PLMA_{18}$-$PBzMA_{45}$ diblock copolymers at 20% w/w occupy a pure worm morphology in mineral oil. However, *precisely the same diblock copolymer composition* forms a mixed phase of spheres, worms and vesicles in PAO at the same concentration (Figure 2.7). Thus, it can be deduced that the phase space occupied by the pure worm morphology in the mineral and PAO oils is different.

2.3.3. Evaluation of the effect of the solvent on PLMA-PBzMA worm gels

In view of these subtle solvent effects, the physical properties of free-standing worm gels prepared in *n*-dodecane,[55] mineral oil and PAO oil were compared using rheology (see Figure 2.8 and Table 2.1). A series of temperature jumps were conducted at a constant strain of 1.0% and angular frequency of 10 rad s^{-1}. These parameters were previously reported to represent the linear viscoelastic region, where the storage (*G*') and loss (*G*") moduli were found to be frequency-independent at a fixed strain of 1.0%.[55] Thus the same parameters were used to monitor the temperature-dependent physical properties of the PLMA-PBzMA worm gels in mineral and PAO oils.

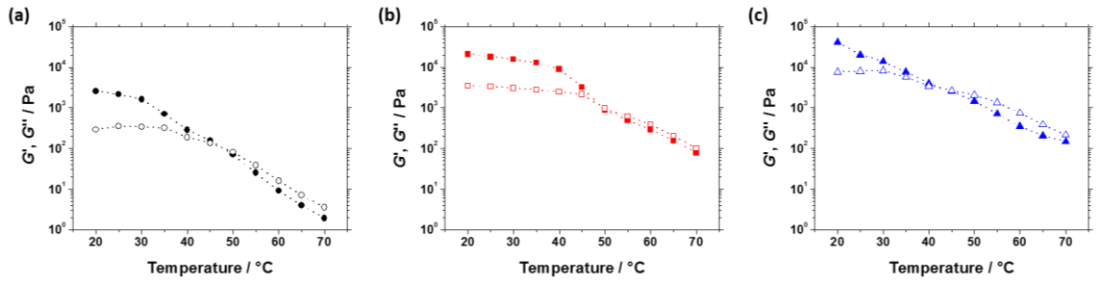

Figure 2.8. Storage moduli (*G*', filled symbols) and loss moduli (*G*", open symbols) vs. temperature for (a) 20% w/w $PLMA_{18}$-$PBzMA_{37}$ worms in *n*-dodecane,[55] (b) 20% w/w $PLMA_{18}$-$PBzMA_{45}$ worms in mineral oil and (c) $PLMA_{16}$-$PBzMA_{32}$ worms in poly(*α*-olefin) oil. Data were recorded at 1.0% strain using an angular frequency of 10 rad s^{-1} with an equilibration time of 5 min at 5 °C intervals from 20 °C to 80 °C.

The initial *G*' values recorded at 20 °C for PLMA-PBzMA worm gels in mineral and PAO oils were approximately an order of magnitude greater than for the gel in *n*-dodecane. This could be due to the worms being either significantly longer and/or that there are stronger inter-worm interactions in these gels. The *G'* for the 20% w/w $PLMA_{16}$-$PBzMA_{32}$ worm gel in PAO oil is approximately twice the value of that for the $PLMA_{18}$-$PBzMA_{45}$ worm gel in mineral oil, which may also be due to the presence of longer worms in PAO oil compared to mineral oil.

Table 2.2. Summary of physical properties of 20% w/w PLMA-PBzMA worm gels in various non-polar solvents. Initial storage modulus (*G*', Pa) at 20 °C, critical gelation temperature (CGT, °C) and critical gelation concentration (CGC, % w/w). Measurements were obtained at a fixed strain of 1.0 % and an angular frequency of 10 rad s^{-1} and the temperature was varied at 5 °C intervals from 20 °C to 80 °C, with a 5 min equilibration time at each temperature.

Solvent	Block Composition	Initial *G*' at 20 °C / Pa	CGT / °C	CGC[a] / % w/w
n-Dodecane[55]	$PLMA_{18}$-$PBzMA_{37}$	2,300	47	~11
Mineral oil	$PLMA_{18}$-$PBzMA_{45}$	21,000	49	9
PAO oil	$PLMA_{16}$-$PBzMA_{32}$	41,000	44	9

[a]CGC determined upon systematically diluting dispersions until the worm gel formed a viscous, free-flowing fluid as determined by tube inversion.

The critical gelation temperature (CGT) of these worm gels is defined as the temperature at which the dispersion no longer forms a gel (i.e. when *G*" > *G*').[78] Previous studies[55] indicated that a worm-to-sphere transition was responsible for the degelation of such worm gels at elevated temperatures due to the decreased amount of efficient inter-particle contacts required for gel formation in these dispersed systems.

In order to determine whether this morphological transformation is responsible for the temperature-dependent degelation observed for PLMA-PBzMA worm gels in mineral oil, variable-temperature TEM and DLS studies were carried out (see Figure 2.9). A 0.10% w/w dispersion of $PLMA_{18}$-$PBzMA_{40}$ worms was heated from 20 °C to 90 °C and DLS data were collected at 5 °C intervals. At 20 °C, the sphere-equivalent DLS diameter was reported to be 163 nm (PDI = 0.39), indicating the presence of worm-like nanoparticles. This observation was subsequently confirmed by TEM analysis (see Figure 2.9a).

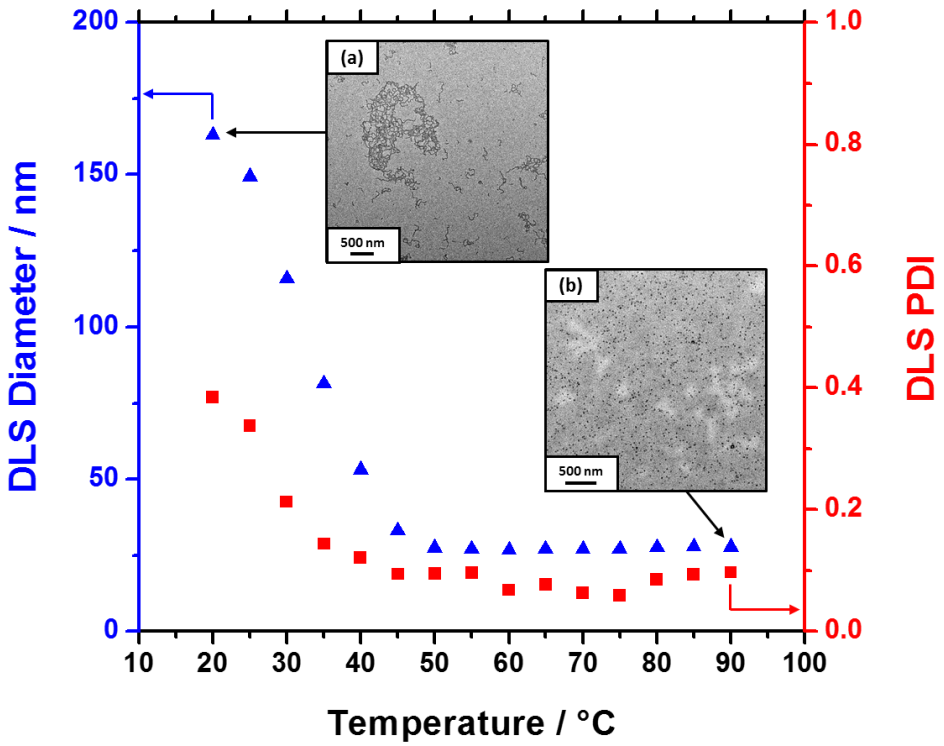

Figure 2.9. Variable-temperature dynamic light scattering (DLS) studies showing the variation of intensity-average diameter (blue triangles) and polydispersity (red squares) for a 0.10% w/w dispersion of $PLMA_{18}$-$PBzMA_{40}$ nanoparticles on heating from 20 °C to 90 °C, with data recorded at 5 °C intervals with 5 min equilibration. Representative transmission electron microscopy (TEM) images obtained for 0.10% w/w dispersions indicate (a) worm-like nanoparticles at 20 °C, and (b) spherical nanoparticles at 90 °C.

The intensity-average diameter decreases dramatically upon increasing the temperature to 50 °C and remains relatively constant upon further heating to 90 °C (DLS diameter = 28 nm, PDI = 0.10). Such small nanoparticles with a relatively narrow size distribution are characteristic of spherical particles, which was also confirmed by TEM studies (see Figure 2.9b). Therefore, the observed degelation of

PLMA-PBzMA worm gels in mineral oil is due to the same worm-to-sphere order-order transition. It must be noted that at such dilute conditions (0.10% w/w), the hot dispersion of spheres cannot re-form worms upon cooling due to the inefficient sphere-sphere fusion that must occur. Thus, the same spherical nanoparticles are persistent after the temperature ramp described in Figure 2.9. This irreversible worm-to-sphere transition is also observed when diluting the hot, concentrated (20% w/w) dispersion with mineral oil at the same temperature. This technique was utilised to obtain representative TEM images of the kinetically 'trapped' spheres which are present at 90 °C.

For PLMA-PBzMA worm gels prepared in the three oils, the CGT ranged from 44 to 49 °C. Interestingly, the $PLMA_{16}$-$PBzMA_{32}$ worm gel produced in PAO oil, which provided the highest *G*', possessed the lowest CGT. The DP of the PBzMA core-forming block may influence this parameter, since higher CGTs are observed for longer core-forming PBzMA blocks for the three worm gels characterised in this study. It is known that the thermally-triggered worm-to-sphere transition occurs due to the surface plasticisation of the core-forming block, which alters the relative volume fractions of the solvophilic and solvophobic blocks.[55] Therefore, it is logical that a smaller PBzMA block would require a lesser extent of surface plasticisation to induce a significant change in the molecular curvature and therefore the preferred morphology occupied by the diblock copolymer nanoparticles. The dispersion is a free-flowing fluid below the critical gelation concentration (CGC) due to inefficient inter-worm contacts which are now unable to form a network sufficient to form a free-standing gel. The value for the CGC is slightly lower for the industrially-sourced oils than for *n*-dodecane. However, all of the non-polar worm gels investigated in the present work exhibit much higher CGCs than previously reported *aqueous* worm gels.[78] This might perhaps reflect the lack of inter-worm hydrogen bonding in the non-aqueous formulations.

2.3.4. Synthesis of PLMA-PBzMA diblock copolymer spheres at high total solids contents

In many RAFT dispersion polymerisation formulations, it has been reported that only spherical nanoparticles are obtained when chain-extending a sufficiently long macro-

CTA.[42, 54, 55] This is presumably because the initial process in which so-called higher order morphologies (e.g. worms) are formed is multiple sphere-sphere fusion events. Using a longer stabiliser block confers more effective steric stabilisation, which inevitably leads to a higher proportion of elastic inter-particle collisions, thus preventing the formation of higher order morphologies. A $PLMA_{47}$ macro-CTA is sufficiently long to ensure an exclusively spherical morphology when preparing $PLMA_{47}$-$PBzMA_{x}$ block copolymer nanoparticles by RAFT dispersion polymerisation in mineral oil, regardless of the targeted PBzMA DP. Thus, well-defined spherical nanoparticles are obtained for both $PLMA_{47}$-$PBzMA_{99}$ and $PLMA_{47}$-$PBzMA_{495}$ diblock copolymers when synthesised at 20% w/w solids. Conversely, this copolymer concentration allows access to pure worm-like and vesicular morphologies when using shorter PLMA macro-CTAs (PLMA DP ≤ 18).[54, 55] As expected, $PLMA_{47}$-$PBzMA_{495}$ (intensity-average diameter = 149 nm, PDI = 0.01) diblock copolymer spheres are significantly larger than $PLMA_{47}$-$PBzMA_{99}$ (intensity-average diameter = 54 nm, PDI = 0.01). TEM studies also confirm this difference in sphere size (see Figure 2.10).

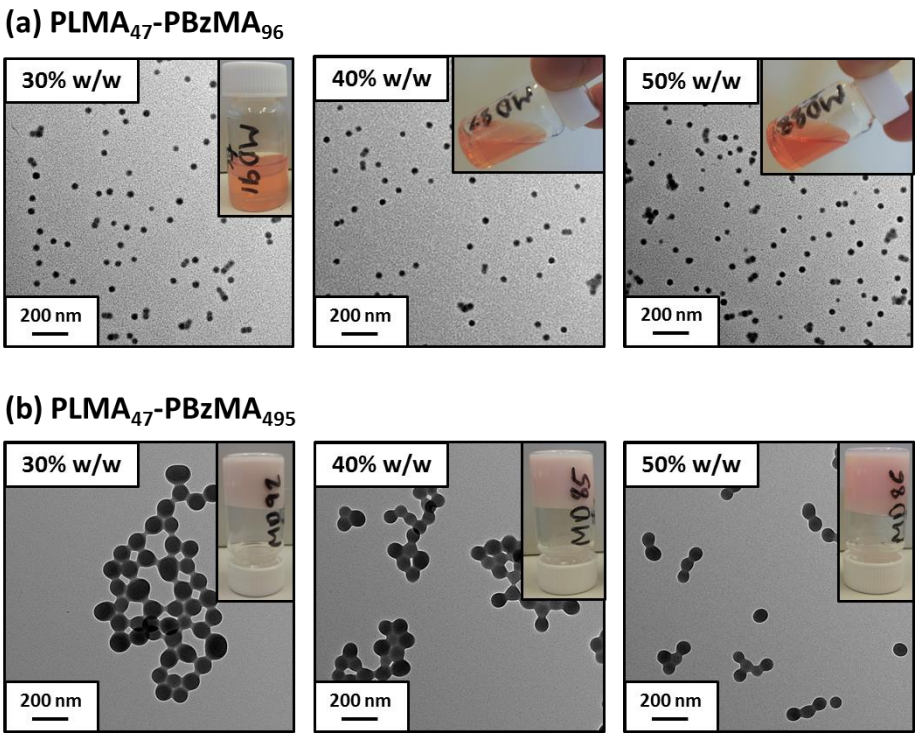

Figure 2.10. Transmission electron micrographs of 0.10% w/w dispersions of (a) $PLMA_{47}$-$PBzMA_{99}$ and (b) $PLMA_{47}$-$PBzMA_{495}$ diblock copolymer spheres prepared via RAFT dispersion polymerisation in mineral oil at 90 °C conducted at 30, 40 or 50% w/w solids. Inset digital photos depict the physical appearance of each concentrated dispersion.

Given the asymmetry for $PLMA_{47}$-$PBzMA_{495}$ diblock copolymers, the spherical nanoparticles most likely represent a kinetically-trapped morphology, since such relative volume fractions of the solvophilic and solvophobic blocks would generally provide a vesicular morphology.[35, 79] Interestingly, such spherical nanoparticles can be synthesised at copolymer concentrations up to 50% w/w, with the smaller $PLMA_{47}$-$PBzMA_{99}$ spheres producing a viscous free-flowing dispersion (see Figure 2.10a, inset digital images). In contrast, the larger $PLMA_{47}$-$PBzMA_{495}$ spheres lead to stirring problems at concentrations as low as 30% w/w solids, with a gel-like paste being obtained (see Figure 2.10b, inset digital images). Nevertheless, the synthesis of relatively small spherical nanoparticles at high solids bodes well for the industrial relevance of such PISA formulations.

2.3.5. 'One-pot' synthesis of PLMA-PBzMA spheres at high total solids contents

To further examine the robust nature (and hence potential industrial relevance) of this particular PISA formulation, a series of 'one-pot' polymerisations were conducted in mineral oil. Firstly, a kinetic study of the RAFT solution polymerisation of LMA in mineral oil was conducted (Figure 2.11).

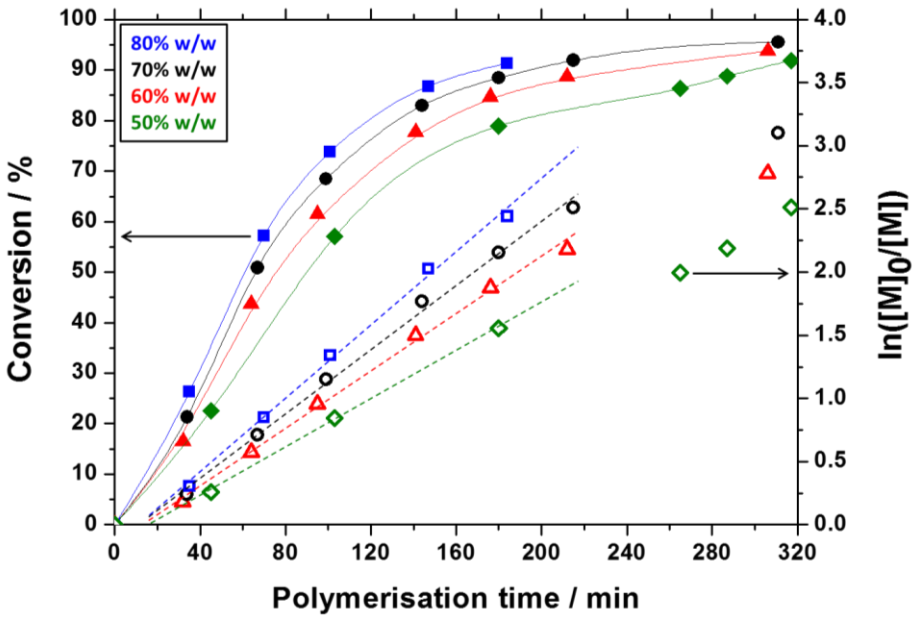

Figure 2.11. Kinetic data obtained for the RAFT solution polymerisation of a $PLMA_{50}$ macro-CTA in mineral oil at 90 °C conducted at 50 (green diamonds), 60 (red triangles), 70 (black circles) and 80% w/w (blue squares) total solids using CDB as a RAFT chain transfer agent and T21s initiator ([CDB]/[T21s] molar ratio = 5.0). Filled symbols represent conversion data and open symbols represent $\ln([M]_0/[M])$. All conversions were assessed by ^{1}H NMR spectroscopy.

Efficient stirring was maintained for the solution polymerisations of LMA conducted at up to 70% w/w solids when targeting a $PLMA_{50}$ macro-CTA with a linear semi-logarithmic plot indicating first-order kinetics up to 90% LMA conversion. At 80% w/w solids, the solution viscosity became too high for efficient stirring above 90% LMA conversion, but similar first-order polymerisation kinetics were observed up to this point. As expected, polymerisations conducted at higher LMA concentrations exhibited faster rates of polymerisation, with conversions reaching 90% within 180 min at 80% w/w, 220 min at 70% w/w, 300 min at 60% w/w, and more than 320 min at 50% w/w. Since the homopolymerisation of LMA conducted at 70% w/w reached > 95% conversion within 320 min and remained sufficiently fluid for efficient stirring, these conditions were selected for the first stage of a 'one-pot' synthesis of targeted $PLMA_{50}$-$PBzMA_{100}$ diblock copolymer nanoparticles. It was previously observed that similar $PLMA_{47}$-$PBzMA_{99}$ block copolymer spheres prepared via a traditional two-step synthesis exhibited relatively high viscosities above 30% w/w solids, see Figure 2.10. Thus, the subsequent RAFT dispersion polymerisation of BzMA was conducted at 30% w/w solids in order to enable the reaction mixture to be efficiently stirred throughout the polymerisation. Kinetic data were obtained for both the RAFT solution polymerisation of LMA at 70% w/w solids and the RAFT dispersion polymerisation of BzMA at 30% w/w solids in mineral oil (Figure 2.12).

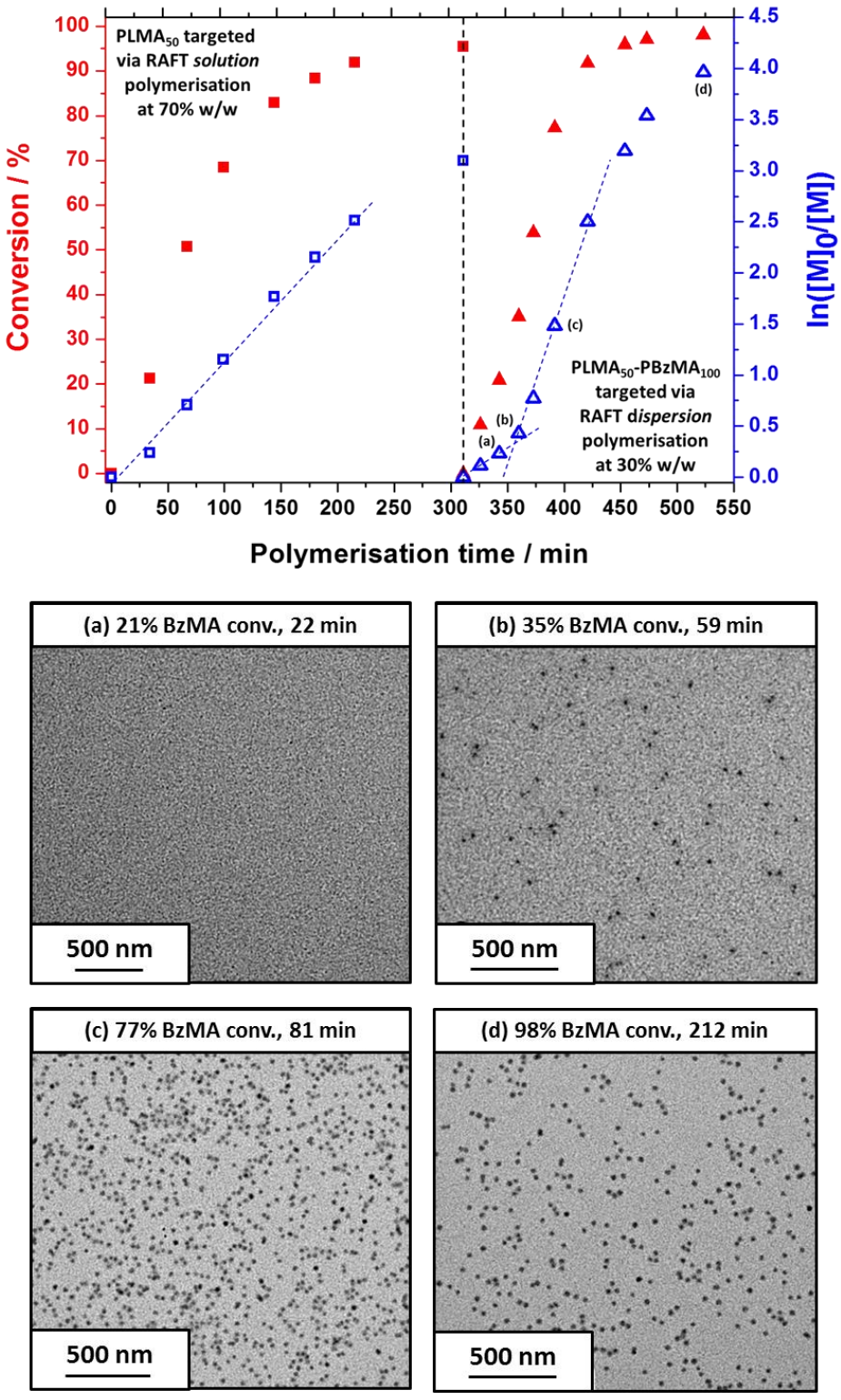

Figure 2.12. Conversion and ln([M]$_0$/[M]) vs. polymerisation time for the 'one-pot' synthesis of targeted PLMA$_{50}$-PBzMA$_{100}$ diblock copolymer spheres in mineral oil. The RAFT solution polymerisation of LMA at 70% w/w solids (squares) was followed by the RAFT dispersion polymerisation of BzMA at 30% w/w solids (triangles). Filled symbols represent conversion data and open symbols represent ln([M]$_0$/[M]) data. All conversions were assessed by ^{1}H NMR spectroscopy. TEM images (a), (b), (c) and (d) represent various points in the kinetic data for the dispersion polymerisation step and indicate the onset of micellisation at (b). Throughout both polymerisation steps, the temperature was constant at 90 °C and the [CDB]/[T21s] and [PLMA macro-CTA]/[T21s] molar ratio was 5.0.

A degassed solution of BzMA in mineral oil containing additional T21s initiator was added to the reaction mixture once the LMA conversion had reached 95%. For the first 40 min, a relatively slow rate of BzMA polymerisation was observed until a critical DP of the growing PBzMA chains was reached, at which point micellar nucleation occurred (see in Figure 2.12b). This PBzMA DP is estimated to be 30 by considering the intersect of the two linear polymerisation time vs. $\ln([M]_0/[M])$ regions. This observation is in line with that seen for the phase diagram for $PLMA_{18}$-$PBzMA_x$ diblock copolymer nanoparticles in mineral oil (see Figure 2.5), where the critical PBzMA DP for self-assembly was judged to be ~28. After this initial period, the polymerisation proceeds much faster, presumably because the unreacted BzMA migrates into the PBzMA micelle cores, thus producing a higher local monomer concentration as previously described by Blanazs et al.[33] Nonetheless, first-order kinetics were observed for BzMA conversions up to 90% (see Figure 2.12). A relatively monodisperse spherical morphology was obtained from the final diblock copolymer dispersion with an intensity-average diameter of 39 nm and PDI of 0.03, as judged by DLS (see Figure 2.13).

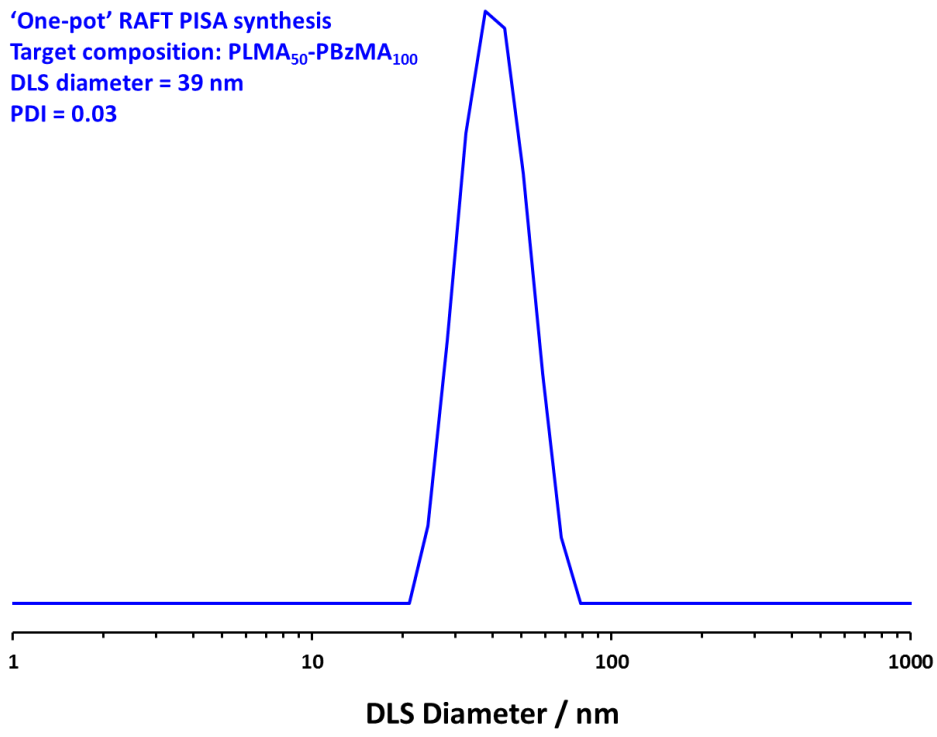

Figure 2.13. Intensity-average particle diameter distribution obtained by DLS for a 0.10% w/w dispersion of $PLMA_{50}$-$PBzMA_{100}$ diblock copolymer spheres targeted via a 'one-pot' protocol at 30% w/w solids.

Molecular weight distributions (MWDs) for each of the aliquots taken during the 'one-pot' PISA synthesis shown in Figure 2.12 were assessed via GPC (Figure 2.14). A linear evolution in M_n with monomer conversion was observed for both the solution and dispersion polymerisations (Figure 2.14a), and relatively narrow MWDs (M_w/M_n < 1.20) were maintained throughout (Figure 2.14b). Thus excellent RAFT control was achieved for this 'one-pot' synthesis.

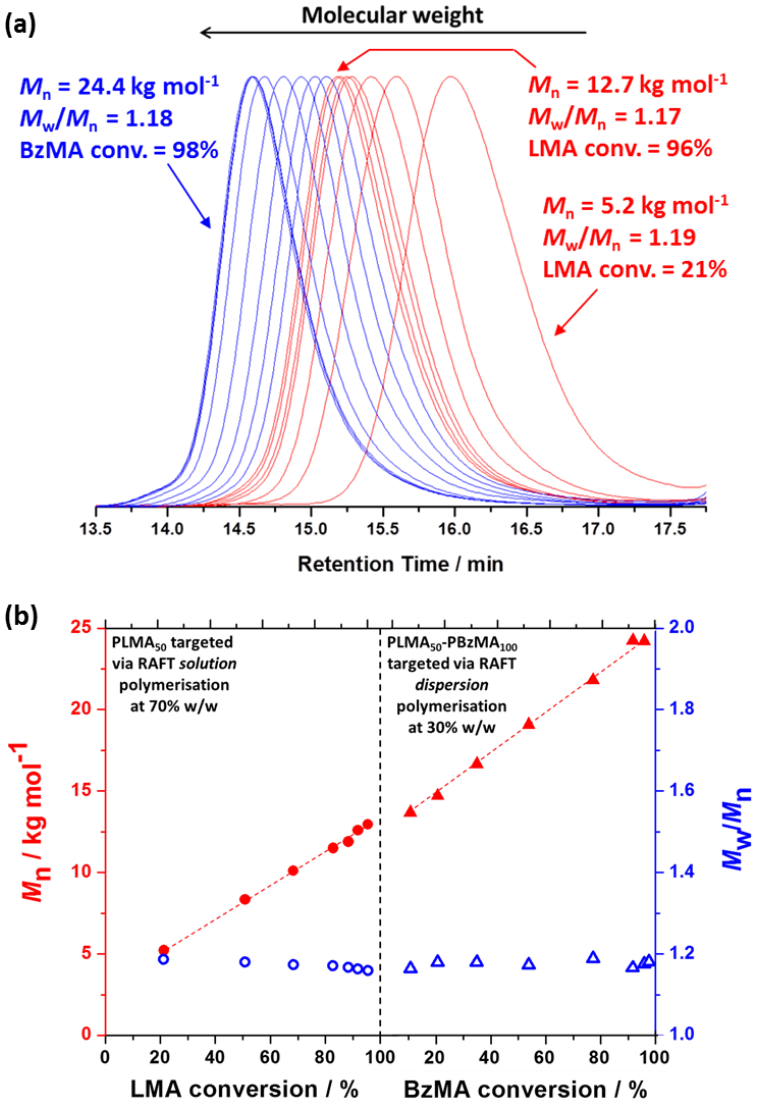

Figure 2.14. (a) THF gel permeation chromatograms obtained for the 'one-pot' synthesis of targeted PLMA$_{50}$-PBzMA$_{100}$ diblock copolymer spheres via solution and dispersion RAFT polymerisation steps in mineral oil. Red GPC traces indicate MWDs obtained during the solution polymerisation of LMA and blue GPC traces represent those obtained during the dispersion polymerisation of BzMA. (b) M_n (red data) and M_w/M_n (blue data) vs. monomer conversion for the RAFT solution polymerisation of LMA at 70% w/w solids (circles) and the RAFT dispersion polymerisation of BzMA at 30% w/w solids in mineral oil (triangles). Filled symbols represent M_n and open symbols represent M_w/M_n. Throughout both polymerisation steps, the temperature was constant at 90 °C and the [CDB]/[T21s] and [PLMA macro-CTA]/[T21s] molar ratio was 5.0.

2.4. Conclusions

In summary, well-defined PLMA-PBzMA block copolymer spheres, worms or vesicles can be reproducibly prepared via polymerisation-induced self-assembly in industrially-sourced mineral and poly(*α*-olefin) (PAO) oils at 90 °C, provided that the mean degree of polymerisation of the PLMA stabiliser block is sufficiently low (e.g., DP 18 or 16). The phase diagram constructed for $PLMA_{18}$-$PBzMA_x$ diblock copolymers in mineral oil is very similar to that previously reported for *n*-dodecane.[55] However, subtle variation in the precise location of phase boundaries is observed for $PLMA_{16}$-$PBzMA_x$ diblock copolymers in PAO oil. PLMA-PBzMA worm gels produced in *n*-dodecane, mineral oil and PAO oil displayed similar rheological properties, although the worm gels in the mineral and PAO oils exhibited storage moduli (*G*') an order of magnitude higher than the gel prepared in *n*-dodecane. In all cases, the critical gelation temperature (CGT) was found to be between 44 °C and 49 °C, with the stiffest worm gel (in PAO oil) having the lowest CGT, and the critical gelation concentrations (CGCs) were found to be between 9 and 11% w/w. Purely spherical nanoparticles are obtained when using a PLMA stabiliser with a relatively high DP (e.g. 47). When targeting $PLMA_{50}$-$PBzMA_{100}$, PISA syntheses can be conducted at up to 50% w/w solids with efficient stirring being maintained throughout the polymerisation. A convenient 'one-pot' synthetic protocol has also been achieved. A PLMA macro-CTA was first synthesised at 70% w/w solids in mineral oil via RAFT solution polymerisation, before subsequent chain extension with BzMA via RAFT dispersion polymerisation at 30% w/w solids. The final PLMA-PBzMA spherical nanoparticles displayed a relatively narrow size distribution, as judged by TEM and DLS studies. TEM and DLS were also utilised to monitor the evolution of the spherical nanoparticles during the RAFT dispersion polymerisation step, with a clear onset of micellisation being observed. Moreover, GPC studies confirmed that relatively high blocking efficiencies and narrow molecular weight distributions ($M_w/M_n < 1.20$) were achieved throughout the 'one-pot' process.

2.5. References

1. L. F. Zhang and A. Eisenberg, *Science*, 1995, **268**, 1728-1731.
2. V. Bütün, S. P. Armes and N. C. Billingham, *Polymer*, 2001, **42**, 5993-6008.
3. J. R. Howse, R. A. L. Jones, G. Battaglia, R. E. Ducker, G. J. Leggett and A. J. Ryan, *Nature Materials*, 2009, **8**, 507-511.

4. J. Chiefari, Y. K. Chong, F. Ercole, J. Krstina, J. Jeffery, T. P. T. Le, R. T. A. Mayadunne, G. F. Meijs, C. L. Moad, G. Moad, E. Rizzardo and S. H. Thang, *Macromolecules*, 1998, **31**, 5559-5562.
5. G. Moad, E. Rizzardo and S. H. Thang, *Australian Journal of Chemistry*, 2005, **58**, 379-410.
6. G. Moad, E. Rizzardo and S. H. Thang, *Accounts of Chemical Research*, 2008, **41**, 1133-1142.
7. Y. Mitsukami, M. S. Donovan, A. B. Lowe and C. L. McCormick, *Macromolecules*, 2001, **34**, 2248-2256.
8. A. B. Lowe, B. S. Sumerlin, M. S. Donovan and C. L. McCormick, *Journal of the American Chemical Society*, 2002, **124**, 11562-11563.
9. C. Barner-Kowollik, T. P. Davis, J. P. A. Heuts, M. H. Stenzel, P. Vana and M. Whittaker, *Journal of Polymer Science Part A-Polymer Chemistry*, 2003, **41**, 365-375.
10. S. Perrier and P. Takolpuckdee, *Journal of Polymer Science Part A-Polymer Chemistry*, 2005, **43**, 5347-5393.
11. M. Mertoglu, S. Garnier, A. Laschewsky, K. Skrabania and J. Storsberg, *Polymer*, 2005, **46**, 7726-7740.
12. D. Quémener, T. P. Davis, C. Barner-Kowollik and M. H. Stenzel, *Chemical Communications*, 2006, 5051-5053.
13. A. B. Lowe and C. L. McCormick, *Progress in Polymer Science*, 2007, **32**, 283-351.
14. C. Barner-Kowollik and S. Perrier, *Journal of Polymer Science Part A-Polymer Chemistry*, 2008, **46**, 5715-5723.
15. C. Boyer, V. Bulmus, T. P. Davis, V. Ladmiral, J. Q. Liu and S. Perrier, *Chem. Rev.*, 2009, **109**, 5402-5436.
16. A. E. Smith, X. Xu and C. L. McCormick, *Progress in Polymer Science*, 2010, **35**, 45-93.
17. R. K. O'Reilly, *Polym. Int.*, 2010, **59**, 568-573.
18. C. Boyer, M. H. Stenzel and T. P. Davis, *Journal of Polymer Science Part A-Polymer Chemistry*, 2011, **49**, 551-595.
19. A. Lu, T. P. Smart, T. H. Epps, D. A. Longbottom and R. K. O'Reilly, *Macromolecules*, 2011, **44**, 7233-7241.
20. Y. Kang, A. Pitto-Barry, H. Willcock, W. D. Quan, N. Kirby, A. M. Sanchez and R. K. O'Reilly, *Polymer Chemistry*, 2015, **6**, 106-117.
21. B. Charleux, G. Delaittre, J. Rieger and F. D'Agosto, *Macromolecules*, 2012, **45**, 6753-6765.
22. M. J. Monteiro and M. F. Cunningham, *Macromolecules*, 2012, **45**, 4939-4957.
23. J.-T. Sun, C.-Y. Hong and C.-Y. Pan, *Polymer Chemistry*, 2013, **4**, 873-881.
24. N. J. Warren and S. P. Armes, *Journal of the American Chemical Society*, 2014, **136**, 10174-10185.
25. J. N. Israelachvili, D. J. Mitchell and B. W. Ninham, *Journal of the Chemical Society-Faraday Transactions*, 1976, **72**, 1525-1568.
26. M. Antonietti and S. Förster, *Advanced Materials*, 2003, **15**, 1323-1333.
27. A. Blanazs, S. P. Armes and A. J. Ryan, *Macromolecular Rapid Communications*, 2009, **30**, 267-277.
28. S. Sugihara, A. Blanazs, S. P. Armes, A. J. Ryan and A. L. Lewis, *Journal of the American Chemical Society*, 2011, **133**, 15707-15713.

29. Z. An, Q. Shi, W. Tang, C.-K. Tsung, C. J. Hawker and G. D. Stucky, *Journal of the American Chemical Society*, 2007, **129**, 14493-14499.
30. J. Rieger, C. Grazon, B. Charleux, D. Alaimo and C. Jérôme, *Journal of Polymer Science Part A: Polymer Chemistry*, 2009, **47**, 2373-2390.
31. S. Boisse, J. Rieger, K. Belal, A. Di-Cicco, P. Beaunier, M.-H. Li and B. Charleux, *Chemical Communications*, 2010, **46**, 1950-1952.
32. Y. Li and S. P. Armes, *Angewandte Chemie-International Edition*, 2010, **49**, 4042-4046.
33. A. Blanazs, J. Madsen, G. Battaglia, A. J. Ryan and S. P. Armes, *Journal of the American Chemical Society*, 2011, **133**, 16581-16587.
34. G. Liu, Q. Qiu, W. Shen and Z. An, *Macromolecules*, 2011, **44**, 5237-5245.
35. A. Blanazs, A. J. Ryan and S. P. Armes, *Macromolecules*, 2012, **45**, 5099-5107.
36. N. J. Warren, O. O. Mykhaylyk, D. Mahmood, A. J. Ryan and S. P. Armes, *Journal of the American Chemical Society*, 2014, **136**, 1023-1033.
37. C. A. Figg, A. Simula, K. A. Gebre, B. S. Tucker, D. M. Haddleton and B. S. Sumerlin, *Chemical Science*, 2015, **6**, 1230-1236.
38. W.-M. Wan and C.-Y. Pan, *Polymer Chemistry*, 2010, **1**, 1475-1484.
39. W.-M. Wan, X.-L. Sun and C.-Y. Pan, *Macromolecular Rapid Communications*, 2010, **31**, 399-404.
40. C.-Q. Huang and C.-Y. Pan, *Polymer*, 2010, **51**, 5115-5121.
41. W. Cai, W. Wan, C. Hong, C. Huang and C. Pan, *Soft Matter*, 2010, **6**, 5554-5561.
42. E. R. Jones, M. Semsarilar, A. Blanazs and S. P. Armes, *Macromolecules*, 2012, **45**, 5091-5098.
43. M. Semsarilar, E. R. Jones, A. Blanazs and S. P. Armes, *Advanced Materials*, 2012, **24**, 3378-3382.
44. M. Semsarilar, V. Ladmiral, A. Blanazs and S. P. Armes, *Polymer Chemistry*, 2014, **5**, 3466-3475.
45. C. Gonzato, M. Semsarilar, E. R. Jones, F. Li, G. J. P. Krooshof, P. Wyman, O. O. Mykhaylyk, R. Tuinier and S. P. Armes, *Journal of the American Chemical Society*, 2014, **136**, 11100-11106.
46. Y. Pei and A. B. Lowe, *Polymer Chemistry*, 2014, **5**, 2342-2351.
47. B. Karagoz, L. Esser, H. T. Duong, J. S. Basuki, C. Boyer and T. P. Davis, *Polymer Chemistry*, 2014, **5**, 350-355.
48. B. Karagoz, C. Boyer and T. P. Davis, *Macromolecular Rapid Communications*, 2014, **35**, 417-421.
49. W. Zhao, G. Gody, S. M. Dong, P. B. Zetterlund and S. Perrier, *Polymer Chemistry*, 2014, **5**, 6990-7003.
50. S. Dong, W. Zhao, F. P. Lucien, S. Perrier and P. B. Zetterlund, *Polymer Chemistry*, 2015, **6**, 2249-2254.
51. L. Houillot, C. Bui, M. Save, B. Charleux, C. Farcet, C. Moire, J.-A. Raust and I. Rodriguez, *Macromolecules*, 2007, **40**, 6500-6509.
52. L. Houillot, C. Bui, C. Farcet, C. Moire, J.-A. Raust, H. Pasch, M. Save and B. Charleux, *ACS Applied Materials & Interfaces*, 2010, **2**, 434-442.
53. J. A. Raust, L. Houillot, M. Save, B. Charleux, C. Moire, C. Farcet and H. Pasch, *Macromolecules*, 2010, **43**, 8755-8765.
54. L. A. Fielding, M. J. Derry, V. Ladmiral, J. Rosselgong, A. M. Rodrigues, L. P. D. Ratcliffe, S. Sugihara and S. P. Armes, *Chemical Science*, 2013, **4**, 2081-2087.

55. L. A. Fielding, J. A. Lane, M. J. Derry, O. O. Mykhaylyk and S. P. Armes, *Journal of the American Chemical Society*, 2014, **136**, 5790-5798.
56. Y. Pei, L. Thurairajah, O. R. Sugita and A. B. Lowe, *Macromolecules*, 2015, **48**, 236-244.
57. I. Chaduc, W. J. Zhang, J. Rieger, M. Lansalot, F. D'Agosto and B. Charleux, *Macromolecular Rapid Communications*, 2011, **32**, 1270-1276.
58. L. P. D. Ratcliffe, A. J. Ryan and S. P. Armes, *Macromolecules*, 2013, **46**, 769-777.
59. W. Zhang, F. D'Agosto, P.-Y. Dugas, J. Rieger and B. Charleux, *Polymer*, 2013, **54**, 2011-2019.
60. L. Guo, Y. Jiang, T. Qiu, Y. Meng and X. Li, *Polymer*, 2014, **55**, 4601-4610.
61. H. De Brouwer, M. A. J. Schellekens, B. Klumperman, M. J. Monteiro and A. L. German, *Journal of Polymer Science Part A: Polymer Chemistry*, 2000, **38**, 3596-3603.
62. J. Liu, H. Duong, M. R. Whittaker, T. P. Davis and C. Boyer, *Macromolecular Rapid Communications*, 2012, **33**, 760-766.
63. C. W. Scales, E. R. George, C. D. Anderson, R. D. Gleim and B. M. Healy, 2013, WO2013085814-A2013085812.
64. A. Blanazs, R. Verber, O. O. Mykhaylyk, A. J. Ryan, J. Z. Heath, C. W. I. Douglas and S. P. Armes, *Journal of the American Chemical Society*, 2012, **134**, 9741-9748.
65. K. L. Thompson, C. J. Mable, A. Cockram, N. J. Warren, V. J. Cunningham, E. R. Jones, R. Verber and S. P. Armes, *Soft Matter*, 2014, **10**, 8615-8626.
66. Y. X. Ma, X. L. Zheng, F. M. Shi, Y. Li and S. J. Sun, *Journal of Applied Polymer Science*, 2003, **88**, 1622-1626.
67. J. Jang and B. S. Kim, *Journal of Applied Polymer Science*, 2000, **77**, 903-913.
68. Y. Feng and C. F. Xiao, *Journal of Applied Polymer Science*, 2006, **101**, 1248-1251.
69. Z. Janovic, K. Saric and K. Sertic-Bionda, *Chemical and Biochemical Engineering Quarterly*, 1998, **12**, 19-24.
70. A. Jukic, E. Vidovic and Z. Janovic, *Chemistry and Technology of Fuels and Oils*, 2007, **43**, 386-394.
71. R. L. Stambaugh and B. G. Kinker, *Viscosity Index Improvers and Thickeners*, Springer-Verlag Berlin, Berlin, 2010.
72. R. Zheng, G. Liu, M. Devlin, K. Hux and T.-C. Jao, *Tribology Transactions*, 2010, **53**, 97-107.
73. R. Zheng, G. Liu and T.-C. Jao, *Polymer*, 2007, **48**, 7049-7057.
74. J. T. Lai and R. Shea, *Journal of Polymer Science Part A: Polymer Chemistry*, 2006, **44**, 4298-4316.
75. J. S. Trent, *Macromolecules*, 1984, **17**, 2930-2931.
76. P. Cacioli, D. G. Hawthorne, R. L. Laslett, E. Rizzardo and D. H. Solomon, *Journal of Macromolecular Science-Chemistry*, 1986, **23**, 839-852.
77. M. Rodlert, E. Harth, I. Rees and C. J. Hawker, *Journal of Polymer Science Part A-Polymer Chemistry*, 2000, **38**, 4749-4763.
78. R. Verber, A. Blanazs and S. P. Armes, *Soft Matter*, 2012, **8**, 9915-9922.
79. N. J. Warren, O. O. Mykhaylyk, A. J. Ryan, M. Williams, T. Doussineau, P. Dugourd, R. Antoine, G. Portale and S. P. Armes, *Journal of the American Chemical Society*, 2015, **137**, 1929-1937.

3. *In Situ* Small-Angle X-Ray Scattering Studies of Sterically-Stabilised Diblock Copolymer Nanoparticles Formed During Polymerisation-Induced Self-Assembly in Non-Polar Media

3.1. Introduction

Small-angle X-ray scattering (SAXS) is a powerful *in situ* technique for determining the average size and shape of millions of particles within a colloidal dispersion.[1, 2] This highlights the advantage of SAXS over other techniques such as transmission electron microscopy (TEM), where particles are imaged in their 'dry' state and typically only hundreds of particles are counted to give a number-average size, or dynamic light scattering (DLS), where only spherical particles can be accurately analysed and intensity-averaged sizes are highly biased towards larger particles. The incident X-rays interact with electrons within a sample and emit coherent secondary waves which are capable of interfering with each other.[1] Thus, one requirement for SAXS is that the constituents of the particles must have a different electron density compared to that of the continuous phase, which is described by the difference in scattering length density (ξ) between the particles and the solvent.[1]

$$\xi = \frac{b_e \rho_m N_A}{M_w} \sum_i n_i z_i \qquad 3.1$$

Here b_e is the scattering length of an electron, ρ_m is the density of the molecule, N_A is Avogadro's constant, M_w is the weight-average molecular weight of the molecule (constituents of the particle or solvent), n_i is the number of atoms within the molecule with atomic number z_i.

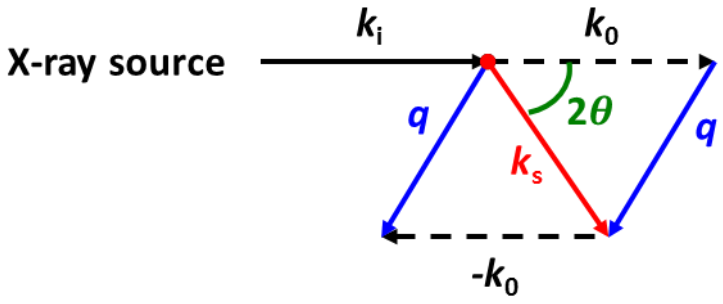

Figure 3.1. Schematic diagram of the interaction of an electron with incident X-rays. The vector k_i represents the incoming X-rays, k_0 represents the non-scattered X-rays, k_s represents the scattered X-rays, q represents the scattering vector and θ is one-half of the scattering angle.

Figure 3.1 shows a schematic diagram for scattering from a one point scatterer, an electron. The momentum transfer or scattering vector (q) is a measure of the magnitude and direction of the scattering.

$$q = \frac{4\pi}{\lambda} sin\theta \qquad 3.2$$

Here λ is the wavelength of the incident X-rays and θ is one-half of the scattering angle. Bragg's law relates q and length d such that $d = 2\pi/q$. Thus there is an inverse relationship between particle size and scattering angle (2θ), so larger q-vectors describe scattering from smaller objects.[1] The scattering intensity at a given q, $I(q)$, is given by:

$$I(q) = NV^2\Delta\xi^2 P(q)S(q) \qquad 3.3$$

where N is the number density, V is the volume of particles, $\Delta\xi$ is the contrast in scattering length density between the particles and the continuous phase, $P(q)$ is the form factor and $S(q)$ is the structure factor. $P(q)$ describes the shape of the particles, whereas $S(q)$ represents the spatial arrangement of the scattering objects. For dilute dispersions, $S(q) = 1$, thus eliminating the contribution of $S(q)$ and simplifying SAXS analysis.[1, 2] The X-ray scattering of a sample is detected at varying sample-to-detector distances (depending on the limitations of the instrument or the length scale of interest), with a 2D scattering pattern being generated. This 2D pattern is converted to a 1D scattering pattern by radial integration to provide an $I(q)$ vs. q plot. There are two important regions to consider: the Guinier region (at low q) and the Porod region (at high q). The Guinier approximation can be applied at very low q (i.e. when $qR_g << 1$, where R_g is the radius of gyration) where any $P(q)$ can be approximated as a Gaussian curve due to the overall size (or R_g) of the scattering object:

$$P(q) \approx a_0 exp\left(-\frac{{R_g}^2 q^2}{3}\right) \qquad 3.4$$

Here a_0 is the extrapolated intensity at zero angle. A Guinier plot of ln[$I(q)$] vs. q^2 gives a straight line with a slope equal to $-R_g^2/3$ and an intercept equal to ln[a_0].[2] At low q, the slope of the $I(q)$ vs. q plot indicates the particle morphology. In this region, $I(q) \sim q^0$ for spherical particles, $I(q) \sim q^{-1}$ for rods (or to a first approximation worm-like nanoparticles) and $I(q) \sim q^{-2}$ for disks (or vesicles/lamellae).[1, 2] The Porod approximation can be used at high q, which provides information on the surface or interface of the scattering object. For smooth surfaces, $I(q) \sim q^{-4}$ in this region, whereas $I(q) \sim q^{-2}$ for polymer-stabilised particles (such as diblock copolymer nanoparticles) due to the Gaussian chains at the interface. 1D scattering patterns also exhibit characteristic features (i.e. local minima) due to specific dimensions of the particle. Typical SAXS patterns for diblock copolymer spheres (red data), worms (green data) and vesicles (blue data) are shown in Figure 3.2.

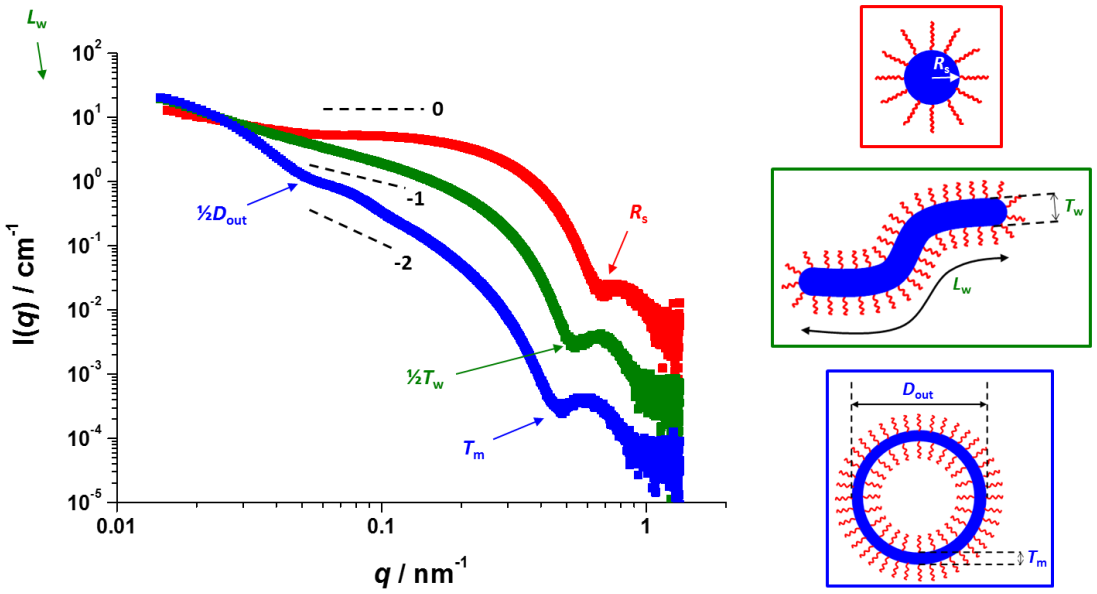

Figure 3.2. Typical SAXS patterns obtained for diblock copolymer spheres (red data), worms (green data) and vesicles (blue data). Features of the relevant scattering patterns that provide information on the radius of the sphere (R_s), mean worm thickness (T_w), outer vesicle diameter (D_{out}) and vesicle membrane thickness (T_m) are shown. The feature indicating the worm length (L_w) appears at a lower q range than that shown here. Slopes of 0, -1 and -2 are shown for reference. Also shown are schematic representations of a sphere, worm and vesicle, together with their dimensions as represented by features in the corresponding SAXS pattern.

SAXS techniques have been employed to characterise nanoparticle morphologies obtained by various RAFT-mediated PISA formulations.[3-15] Of particular relevance to

this Chapter is the work described by Warren et al.,[10] where *post mortem* SAXS analysis was utilised to examine the growth of poly(glycerol monomethacrylate)-poly(2-hydroxypropyl methacrylate) (PGMA-PHPMA) diblock copolymer vesicles dispersed in water. It was found that $PGMA_{55}$-$PHPMA_x$ vesicles with increasing x values were of very similar overall size, but had thicker membranes. This mechanism of vesicle growth was shown to be the only means by which the growing vesicles can reduce their interfacial area, which is favourable since it minimises their free energy. Interestingly, increasing the PHPMA DP ultimately induces 'vesicle death', whereby the original well-defined vesicle morphology is eventually lost (see Figure 3.3).

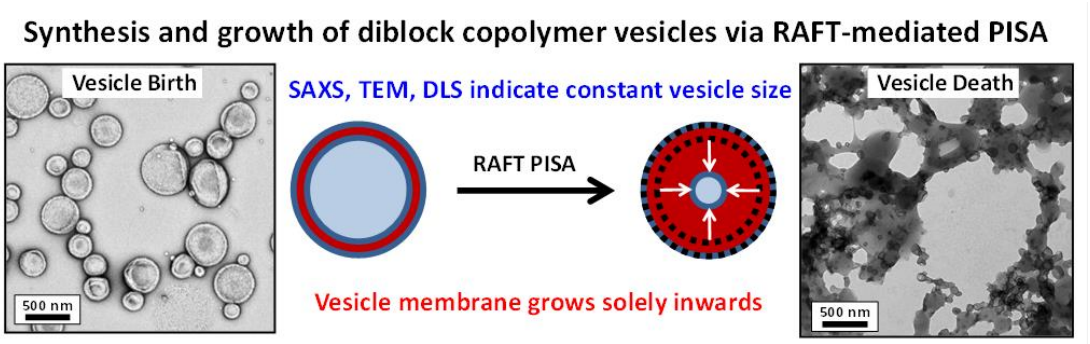

Figure 3.3. 'Birth' and 'death' of poly(glycerol monomethacrylate)-poly(2-hydroxypropyl methacrylate) (PGMA-PHPMA) diblock copolymer vesicles in water.[10]

Also of some relevance to this Chapter are the *in situ* morphology transformations observed during the RAFT-mediated PISA synthesis of PGMA-PHPMA vesicles described by Blanazs and co-workers.[16] Although SAXS was not employed in this work, detailed TEM studies indicated that worms form vesicles via various intermediate morphologies when targeting $PGMA_{47}$-$PHPMA_{200}$ vesicles, including octopi and jellyfish structures (see Figure 3.4). Initial small spheres formed short worms, which continued to grow in length. A significant degree of worm branching became evident as the polymerisation proceeded, and these branched worms then began to cluster and underwent partial coalescence to form nascent bilayers with protruding worms (termed 'octopi'). These octopi then began to wrap up and form 'jellyfish'. These jellyfish structures appeared to be the final intermediate stage in the morphology evolution, since well-defined vesicles were observed soon after, presumably due to the fusion of the pendent worms protruding from the jellyfish.[16]

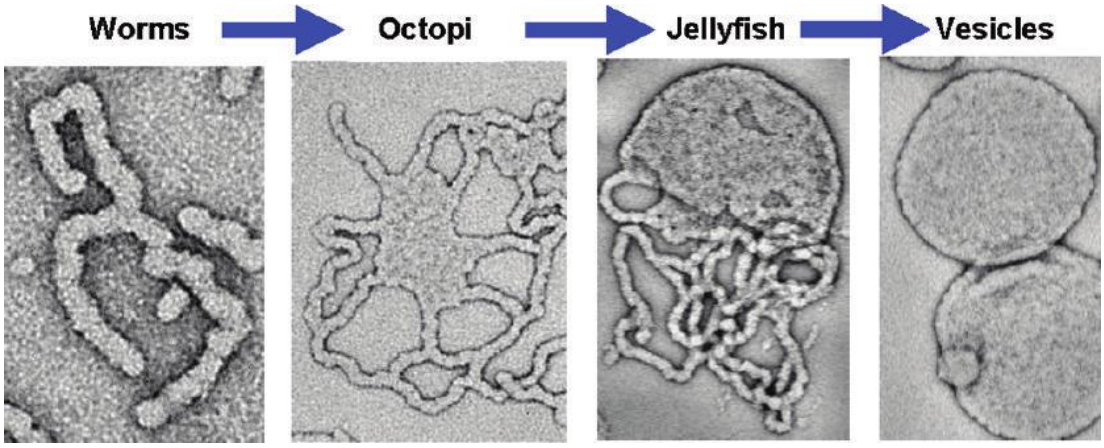

Figure 3.4. Transmission electron micrographs displaying the morphology transformation from (branched) worms to vesicles via intermediate octopi and jellyfish structures during the PISA synthesis of $PGMA_{47}$-$PHPMA_{200}$ vesicles in water.[16]

There have been various examples of *in situ* SAXS monitoring of particle formation and evolution.[17-19] One literature example is of particular relevance to the current work. Howdle and co-workers[20-28] developed several RAFT dispersion polymerisation formulations in supercritical CO_2, as discussed in Chapter 1 (see Section 1.6.5). In collaboration with beamline scientists on BM26 at the European Synchrotron Research Facility (ESRF), a high-pressure cell was developed which enabled monitoring of such RAFT dispersion polymerisations via *in situ* SAXS.[18] The evolution in particle morphology with concomitant internal microphase separation was monitored during the synthesis of polydimethylsiloxane (PDMS)-stabilised poly(methyl methacrylate)-poly(benzyl methacrylate) (PMMA-PBzMA) diblock copolymer microparticles (see Figure 3.5).

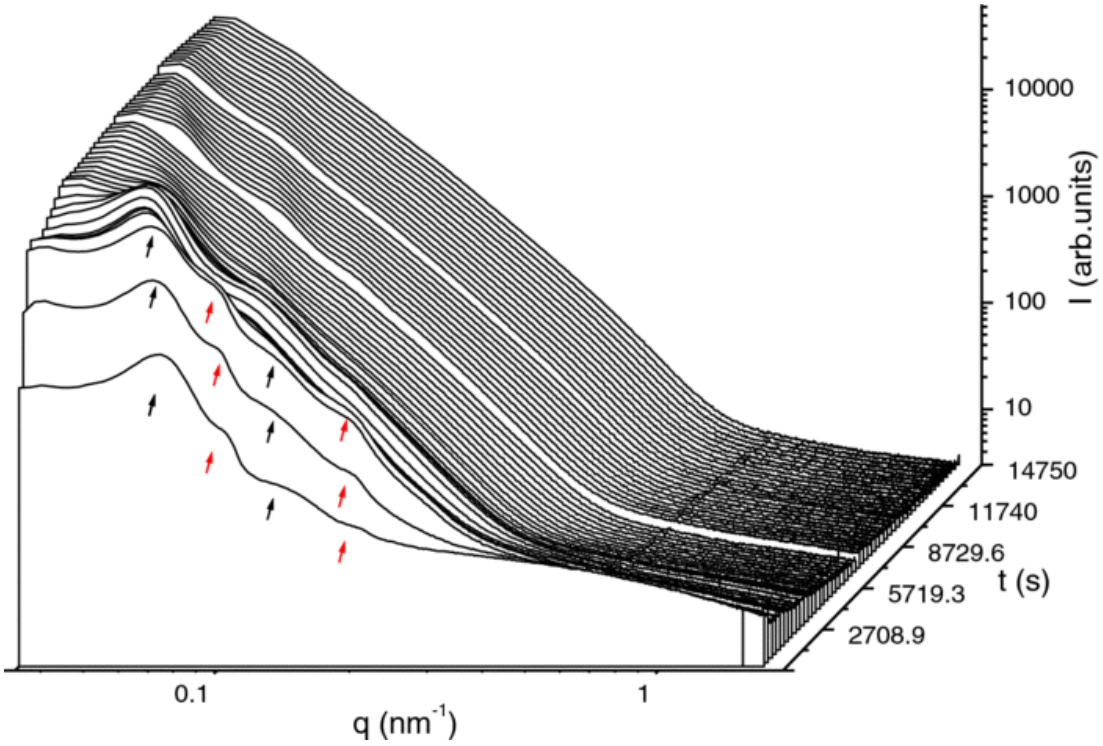

Figure 3.5. Time-resolved SAXS patterns obtained during the RAFT dispersion polymerisation of PDMS-stabilised PMMA-PBzMA block copolymer nanoparticles in supercritical CO_2 at 200 bar and 65 °C, with SAXS patterns being collected every 60 s.[18]

In this Chapter, the PISA synthesis of poly(stearyl methacrylate)-poly(benzyl methacrylate) (PSMA-PBzMA) diblock copolymer nanoparticles in mineral oil is reported (see Scheme 3.1). A predictive phase diagram has been constructed for $PSMA_{13}$-$PBzMA_x$ diblock copolymers and two series of spherical nanoparticles have been synthesised for $PSMA_{18}$-$PBzMA_x$ and $PSMA_{31}$-$PBzMA_x$ diblock copolymers. TEM, DLS and SAXS are used to characterise such nanoparticles after their PISA synthesis. In particular, a synchrotron source is utilised to conduct SAXS studies of the *in situ* evolution of the copolymer morphology during PISA. This approach provides remarkably detailed insights regarding the sphere-to-worm and worm-to vesicle transitions that occur during this non-aqueous PISA formulation and also sheds light on the mechanism of *in situ* vesicle growth.

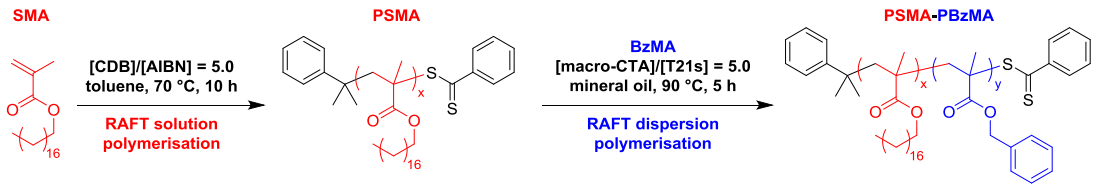

Scheme 3.1. Synthesis of a poly(stearyl methacrylate) (PSMA) macro-CTA via RAFT solution polymerisation of SMA in toluene at 70 °C, followed by RAFT dispersion polymerisation of benzyl methacrylate (BzMA) in mineral oil at 90 °C.

3.2. Experimental

3.2.1. Materials

Monomers were purchased from Sigma-Aldrich (UK) and passed through a basic alumina column prior to use to remove inhibitor. Tert-butyl peroxy-2-ethylhexanoate (T21s) initiator was purchased from AkzoNobel (The Netherlands). Cumyl dithiobenzoate (CDB), $CDCl_3$, and all other reagents were purchased from Sigma-Aldrich (UK) and were used as received, unless otherwise noted. THF and toluene were purchased from Fisher Scientific (UK), CD_2Cl_2 was purchased from Goss Scientific (UK) and industrial-grade mineral oil was provided by Lubrizol Corporation Ltd.

3.2.2. Synthesis of poly(stearyl methacrylate) (PSMA) macromolecular-chain transfer agent (macro-CTA)

A typical synthesis of $PSMA_{31}$ macro-CTA was conducted as follows. A 250 mL round-bottomed flask was charged with stearyl methacrylate (SMA; 37.3 g; 110 mmol), cumyl dithiobenzoate (CDB; 1.00 g; 3.67 mmol; target degree of polymerisation (DP) = 30), 2,2'-azobisisobutyronitrile (AIBN; 121 mg, 0.74 mmol; CDB/AIBN molar ratio = 5.0) and toluene (57.5 g). The sealed reaction vessel was purged with nitrogen and placed in a pre-heated oil bath at 70 °C for 10 h. The resulting PSMA (SMA conversion = 72 %; M_n = 9,200 g mol^{-1}, M_w = 11,100 g mol^{-1}, M_w/M_n = 1.21) was purified by precipitation into excess ethanol. The mean DP of this macro-CTA was calculated to be 31 using ^{1}H NMR spectroscopy by comparing the integrated signals corresponding to the CDB aromatic protons at 7.0-7.5 ppm with that assigned to the two oxymethylene protons of PSMA at 3.4-4.2 ppm. Thus the CTA efficiency was calculated to be 70%.

3.2.3. Synthesis of poly(stearyl methacrylate)-poly(benzyl methacrylate) (PSMA-PBzMA) diblock copolymer nanoparticles

A typical RAFT dispersion polymerisation synthesis of $PSMA_{31}$-$PBzMA_{196}$ diblock copolymer nanoparticles at 20% w/w solids was conducted as follows. Benzyl methacrylate (BzMA; 0.393 g; 2.23 mmol), T21s initiator (4.82 mg; 2.23 μmol; dissolved at 10.0 % v/v in mineral oil) and $PSMA_{31}$ macro-CTA (0.12 g; 11.1 μmol; macro-CTA/initiator molar ratio = 5.0; target PBzMA DP = 200) were dissolved in mineral oil (2.05 g). The reaction mixture was sealed in a 10 mL round-bottomed flask and purged with nitrogen gas for 30 min. The deoxygenated solution was then placed in a pre-heated oil bath at 90 °C for 5 h (final BzMA conversion = 98 %; M_n = 30,100 g mol^{-1}, M_w/M_n = 1.19).

3.2.4. Gel permeation chromatography (GPC)

Molecular weight distributions (MWDs) were assessed by GPC using THF eluent at 30 °C. The THF GPC system was equipped with two 5 μm (30 cm) Mixed C columns and a WellChrom K-2301 refractive index detector operating at 950 ± 30 nm. The mobile phase contained 2.0% v/v triethylamine and 0.05% w/v butylhydroxytoluene (BHT) with a toluene flow rate marker and the flow rate was fixed at 1.0 mL min^{-1}. A series of ten near-monodisperse poly(methyl methacrylate) standards (M_p values ranging from 645 to 2,480,000 g mol^{-1}) were used for calibration.

3.2.5. ^{1}H Nuclear Magnetic Resonance (NMR) spectroscopy

^{1}H NMR spectra were recorded in either CD_2Cl_2 or $CDCl_3$ using a Bruker AV1-400 or AV1-250 MHz spectrometer. Typically 64 scans were averaged per spectrum.

3.2.6. Dynamic light scattering (DLS)

DLS studies were performed at 25 °C using a Zetasizer NanoZS instrument (Malvern Instruments, UK) at a fixed scattering angle of 173°. Copolymer dispersions were diluted to 0.10% w/w using *n*-dodecane prior to light scattering studies. The intensity-average diameter and polydispersity of the diblock copolymer nanoparticles were

calculated by cumulants analysis of the experimental correlation function using Dispersion Technology Software version 6.20. Data were averaged over thirteen runs each of thirty seconds duration.

3.2.7. Transmission electron microscopy (TEM)

TEM studies were conducted using a Philips CM 100 instrument operating at 100 kV and equipped with a Gatan 1 k CCD camera. Diluted diblock copolymer solutions (0.10% w/w) were placed on carbon-coated copper grids and exposed to ruthenium(VIII) oxide vapour for 7 min at 20 °C prior to analysis.[29] This heavy metal compound acted as a positive stain for the core-forming PBzMA block to improve contrast. The ruthenium(VIII) oxide was prepared as follows: ruthenium(IV) oxide (0.30 g) was added to water (50 g) to form a black slurry; subsequent addition of sodium periodate (2.0 g) with stirring produced a yellow solution of ruthenium(VIII) oxide within 1 min.

3.2.8. Small-angle X-ray scattering (SAXS)

SAXS patterns were collected at a synchrotron source (Diamond Light Source, station I22, Didcot, UK) using monochromatic X-ray radiation (wavelength, λ = 0.124 nm, with q ranging from 0.015 to 1.3 nm^{-1}, where $q = 4\pi \sin \theta/\lambda$ is the length of the scattering vector and θ is one-half of the scattering angle) and a 2D Pilatus 2M pixel detector (Dectris, Switzerland). Glass capillaries of 2.0 mm diameter were used as a sample holder. For *in situ* SAXS studies, all reagents were first purged with nitrogen gas for 30 min, as described earlier, before a portion of the deoxygenated solution was transferred into a glass capillary. The capillary was then sealed in order to prevent exposure to oxygen before being placed into the brass holding stage, which was pre-heated to 90 °C using a water circulating bath. SAXS patterns were collected every 2 min for 3 h, or until no further evolution in the pattern was observed. SAXS data were reduced (integration and normalisation) using Dawn software supplied by Diamond Light Source.[30]

Selected static SAXS patterns were obtained for 1.0% w/w copolymer dispersions using a Bruker AXS Nanostar instrument modified with microfocus X-ray tube (GeniX3D, Xenocs) and motorised scatterless slits for the beam collimation (sample to detector distance 1.46 m, Cu Kα radiation and 2D HiSTAR multiwire gas detector). SAXS patterns were recorded over a q range of 0.08 nm^{-1} < q < 1.6 nm^{-1}. Glass capillaries of 2.0 mm diameter were used as a sample holder, and an exposure time of 1.0 h was utilised for each sample. SAXS data were reduced using Nika macros for Igor Pro by J. Ilavsky. All SAXS data collected at different locations were analysed (background subtraction, data modelling and fitting) using Irena SAS macros for Igor Pro.[31]

3.2.9. Renormalisation of kinetic data for the RAFT dispersion polymerisation of BzMA

Polymerisation kinetic data were obtained for normal 10 mL laboratory-scale PISA syntheses (targeting $PSMA_{31}$-$PBzMA_{2000}$ spheres and $PSMA_{13}$-$PBzMA_{150}$ vesicles, respectively) by withdrawing multiple aliquots of the reaction solution prior to ^1H NMR analysis (see Figure 3.12a and Figure 3.17a; blue data sets in each case). In each case these data were fitted to a sigmoid function using Igor Pro software using the equation shown below:

$$y = a + \frac{b}{\left(1 + \exp\left(\frac{c - x}{d}\right)\right)} \qquad 3.5$$

Here, y is the BzMA conversion (%), x is the relative polymerisation time and a, b, c and d are arbitrary fitting parameters. This function was then utilised to calculate the polymerisation kinetics for the two PISA syntheses conducted in a 2.0 mm glass capillary for the *in situ* SAXS experiments described above (see Figure 3.12a and Figure 3.17a; red data sets in each case).

3.2.10. Determination of BzMA volume fraction in $PSMA_{31}$-$PBzMA_x$ spherical nanoparticle cores

$PSMA_{31}$-$PBzMA_x$ spheres prepared at 20% w/w solids in mineral oil with x values of 396, 582, 784 or 1470 were diluted to 10% w/w in the same solvent. Then the relevant amounts of BzMA (4-170 μL) were added to 2.0 mL aliquots of the above dispersion in order to replicate various time points during the RAFT dispersion polymerisation of $PSMA_{31}$-$PBzMA_{2000}$ spheres that correspond to BzMA conversions of 19.8%, 29.1%, 39.2% or 73.5%, respectively. Each BzMA-doped dispersion was then heated to 90 °C for 1 h before being sedimented using a Heraeus Biofuge Pico centrifuge at 13,000 rpm (16,060 g) until the spheres were fully sedimented.

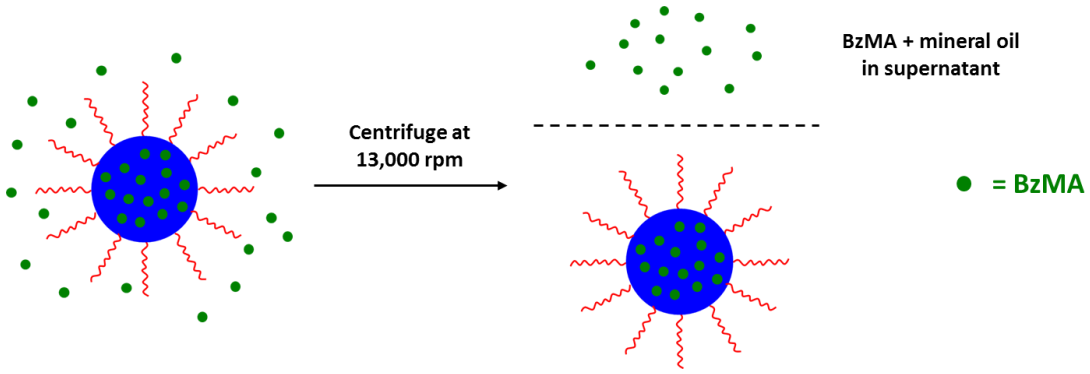

Figure 3.6. Schematic representation of the centrifugation studies to determine the volume fraction of BzMA within the core domain (φ_{BzMA}) of spherical nanoparticles.

The resulting clear supernatant, which contains any BzMA monomer not located within the nanoparticle cores, was removed and analysed via ^{1}H NMR spectroscopy in CD_2Cl_2 using triethoxymethylsilane (TEMS) as an internal standard (present at the same concentration as the BzMA monomer prior to centrifugation). The integrated oxymethylene signal due to the TEMS (~ 3.8 ppm) was set to six protons and the NMR signals corresponding to the aromatic protons ([Ar]) of the BzMA monomer were then integrated. The mole fraction of BzMA monomer present within the nanoparticle cores is therefore equal to 1-([Ar]/5). The BzMA volume fraction within the core domain (φ_{BzMA}) was subsequently calculated by considering the relative volumes of the monomer (as calculated using ^{1}H NMR spectroscopy; see Figure 3.7 below for the calibration plot) and the PBzMA core-forming chains within the nanoparticle cores.

Given that 100% BzMA conversion corresponds to $\varphi_{BzMA} = 0$, these data can be used to calculate φ_{BzMA} at any time point during the PISA synthesis of $PSMA_{31}$-$PBzMA_{2000}$ spheres. A plot of BzMA conversion (x) vs. φ_{BzMA} (y) gave a satisfactory fit ($R^2 > 0.95$) to a logarithmic function of the form $y = -0.234*\ln(x) + 1.0656$.

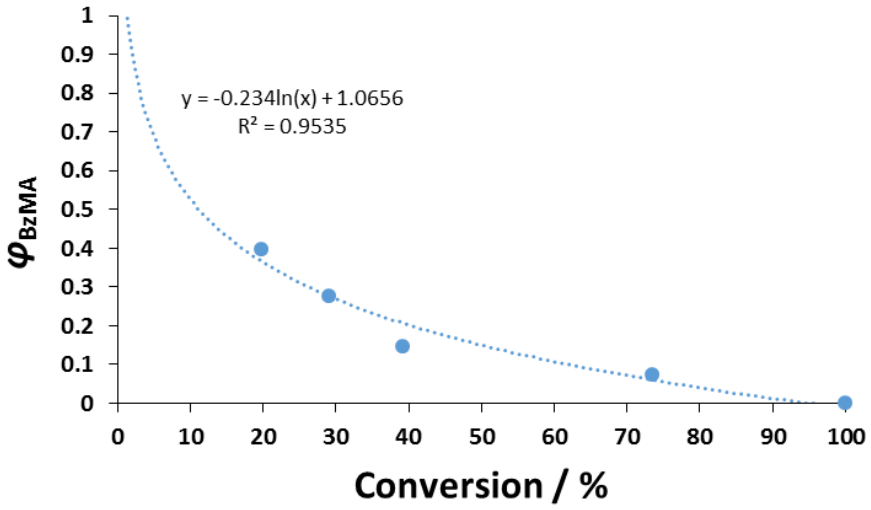

Figure 3.7. Conversion vs. volume fraction of BzMA monomer within growing spherical cores (φ_{BzMA}) calculated for the PISA synthesis of $PSMA_{31}$-$PBzMA_{2000}$ spheres at 10% w/w.

3.2.11. Determination of the standard deviation in the molecular weight distribution (MWD)

The standard deviation in the MWD is required in order to determine the maximum error that should be attributed to the number of copolymer chains per self-assembled sphere or vesicle (N_s or N_v, respectively). This is because the dominant error in this calculation comes from the uncertainty in the mean volume occupied by one PBzMA core-forming block (V_{PBzMA}), which is in turn determined by the MWD. Therefore the unimodal MWD determined by THF GPC analysis was fitted to a Gaussian model to determine its standard deviation using the equation below:

$$y = a \exp\left(-\frac{(x-b)^2}{2\sigma^2}\right) \qquad 3.6$$

Here, y is the retention time (min), x is the detector response, a and b are constants and σ is the standard deviation. This σ value corresponded to either 9.5% or 3.4% of the peak retention time for $PSMA_{13}$-$PBzMA_{2000}$ and $PSMA_{13}$-$PBzMA_{150}$ diblock copolymers respectively. This parameter was subsequently used as the maximum percentage error for the relevant N_s and N_v calculations, respectively.

3.3. Results and Discussion

3.3.1. Synthesis of PSMA macro-CTAs

RAFT solution polymerisation of stearyl methacrylate (SMA) was conducted in toluene at 70 °C using cumyl dithiobenzoate (CDB) as a CTA. Three PSMA macro-CTAs were characterised using ^{1}H NMR spectroscopy and the mean degree of polymerisation (DP) was calculated to be 13, 18 or 31 (see Table 3.1).

Table 3.1. Summary of monomer conversions, mean degrees of polymerisation and GPC molecular weights for three PSMA macro-CTAs prepared by RAFT solution polymerisation of LMA in toluene at 70 °C using AIBN and CDB. Conditions: total solids concentration = 40% w/w, [CDB]/[AIBN] molar ratio = 5.0.

Target DP	Conv.[a]	Actual DP[a]	M_n[b] / g mol^{-1}	M_w[b] / g mol^{-1}	M_w/M_n[b]
$PSMA_{30}$	72%	31	9,200	11,100	1.21
$PSMA_{10}$	75%	18	5,500	6,900	1.24
$PSMA_5$	76%	13	4,900	5,700	1.17

[a]Determined by ^{1}H NMR spectroscopy. [b]Determined by THF GPC against poly(methyl methacrylate) standards.

Each homopolymerisation was quenched at 72%-76% conversion in order to avoid monomer-starved conditions, thus ensuring the retention of RAFT end-groups.[32, 33] This is usually required for high blocking efficiencies and hence well-defined PSMA-PBzMA diblock copolymers. Each PSMA macro-CTA had a polydispersity (M_w/M_n) of ≤ 1.24, which is consistent with previous studies reporting well-controlled RAFT syntheses under these conditions.[34] A typical kinetic study of the synthesis of a $PSMA_{31}$ macro-CTA via RAFT solution polymerisation was conducted (Figure 3.8). After an initial induction period, first-order kinetics were observed prior to quenching

at 72% conversion after 10 h. GPC analysis indicated a linear evolution of molecular weight with conversion (Figure 3.8b).

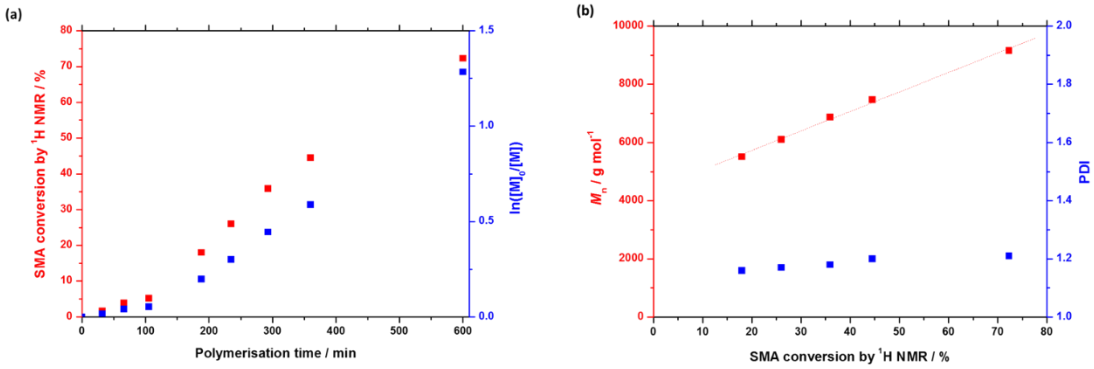

Figure 3.8. (a) SMA conversion vs. polymerisation time and (b) M_n and M_w/M_n vs. conversion for the RAFT solution polymerisation of SMA in toluene using AIBN and CDB, for a target DP of 30. Conditions: total solids concentration = 40% w/w, [CDB]/[AIBN] molar ratio = 5.0. Conversions were determined by ^{1}H NMR spectroscopy.

3.3.2. PSMA$_{31}$-PBzMA$_x$ and PSMA$_{18}$-PBzMA$_x$ diblock copolymer spheres

BzMA monomer was polymerised using two of the low polydispersity PSMA macro-CTAs (DP = 18, or 31) in turn via RAFT dispersion polymerisation (see Table 3.2). In all cases, ≥ 97% BzMA conversion was achieved within 5 h at 90 °C, as judged by ^{1}H NMR spectroscopy. Only spherical morphologies were obtained when using a longer PSMA stabiliser block (DP = 31 or 18). This indicates that the upper limit PSMA DP for access to higher order morphologies (i.e. worms or vesicles) is relatively low for this PISA formulation in mineral oil. Longer PSMA stabiliser blocks confer enhanced steric stabilisation, which prevents the efficient 1D fusion of multiple spheres and therefore the formation of anisotropic worms. Similar observations were reported for PLMA-PBzMA diblock copolymers prepared via RAFT dispersion polymerisation of BzMA in *n*-heptane,[34] *n*-dodecane[5] and mineral oil (see Chapter 2). In these earlier studies, the upper limit PLMA stabiliser DP which allowed access to higher order morphologies was 16-18. Given the relative molecular volumes of the LMA (C_{12} side-chain) and SMA (C_{18} side-chain) repeat units, it is reasonable that using PSMA$_{18}$ only allows access to spheres. Clearly, PSMA$_{13}$ has a comparable

molecular volume to that of $PLMA_{18}$, which is why using the former macro-CTA allows access to worms and vesicles, as well as spheres.

Table 3.2. Summary of targeted copolymer composition, BzMA conversion, GPC molecular weights, DLS diameter (*D*) and PDI for two series of $PSMA_{31}$-$PBzMA_x$ and $PSMA_{18}$-$PBzMA_x$ diblock copolymer spheres prepared by RAFT dispersion polymerisation of BzMA in mineral oil at 90 °C and 20% w/w, using T21s initiator ([macro-CTA]/[T21s] molar ratio = 5.0).

Target Composition	**Conv.**[a]	M_n[b] **/ g mol^{-1}**	M_w/M_n[b]	D[c] **/ nm**	**PDI**[c]
$PSMA_{31}$-$PBzMA_{50}$	99	14,300	1.20	25	0.04
$PSMA_{31}$-$PBzMA_{100}$	98	18,300	1.23	34	0.02
$PSMA_{31}$-$PBzMA_{200}$	98	30,100	1.19	44	0.01
$PSMA_{31}$-$PBzMA_{300}$	99	38,000	1.25	54	0.01
$PSMA_{31}$-$PBzMA_{400}$	99	51,400	1.22	62	0.01
$PSMA_{31}$-$PBzMA_{500}$	99	55,700	1.30	67	0.07
$PSMA_{31}$-$PBzMA_{600}$	97	66,800	1.36	82	0.16
$PSMA_{31}$-$PBzMA_{800}$	98	86,300	1.40	101	0.18
$PSMA_{31}$-$PBzMA_{1000}$	99	113,400	1.42	114	0.17
$PSMA_{31}$-$PBzMA_{1500}$	98	132,200	1.56	125	0.07
$PSMA_{31}$-$PBzMA_{2000}$	98	140,200	1.91	154	0.01
$PSMA_{18}$-$PBzMA_{50}$	99	9,000	1.26	23	0.02
$PSMA_{18}$-$PBzMA_{75}$	99	11,600	1.25	39	0.08
$PSMA_{18}$-$PBzMA_{100}$	98	15,800	1.25	41	0.01
$PSMA_{18}$-$PBzMA_{150}$	98	18,600	1.24	48	0.02
$PSMA_{18}$-$PBzMA_{200}$	98	23,300	1.24	58	0.03
$PSMA_{18}$-$PBzMA_{400}$	98	42,700	1.26	93	0.02
$PSMA_{18}$-$PBzMA_{500}$	98	48,800	1.34	114	0.04
$PSMA_{18}$-$PBzMA_{800}$	98	69,200	1.41	135	0.01

[a]Determined by ^{1}H NMR spectroscopy. [b]Determined by THF GPC against poly(methyl methacrylate) standards. [c]Determined by DLS of a 0.10% w/w dispersion of spheres in *n*-dodecane at 20 °C.

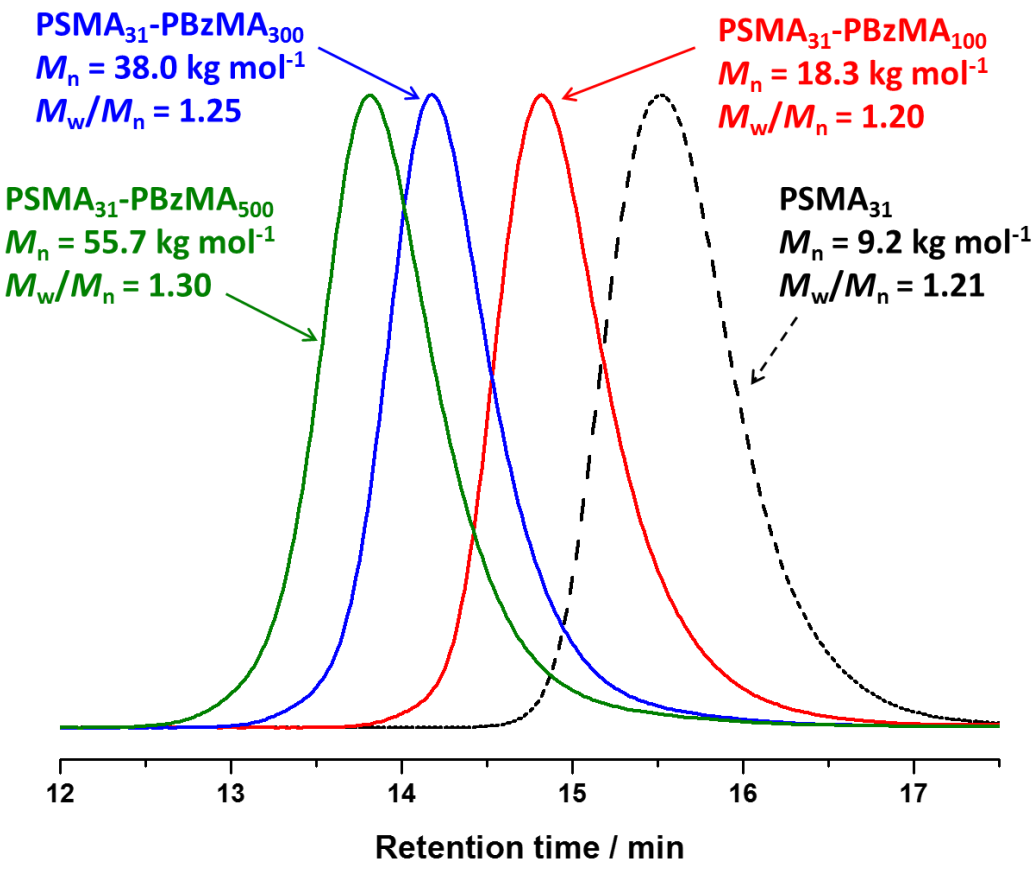

Figure 3.9. THF gel permeation chromatograms (vs. poly(methyl methacrylate) standards) obtained for three $PSMA_{31}$-$PBzMA_x$ diblock copolymers prepared via RAFT dispersion polymerisation of BzMA in mineral oil at 90 °C and 20% w/w solids. The precursor $PSMA_{31}$ macro-CTA (prepared in toluene at 70 °C and 40% w/w solids; black dashed curve) is also shown for reference.

Compared to related RAFT dispersion polymerisation syntheses conducted in non-polar media,[5, 34-37] the present PSMA-PBzMA formulation enables relatively narrow MWDs to be obtained even when targeting PBzMA DPs as high as 500, which corresponds to an experimentally determined M_n of ~56 kg mol^{-1} (Figure 3.9). GPC analysis of $PSMA_{31}$-$PBzMA_x$ ($x \leq 500$) diblock copolymers in THF eluent indicates M_w/M_n values ranging between 1.20 and 1.30, which suggests good RAFT control. Also, the unimodal nature of these curves and the clear shift from the original $PSMA_{31}$ macro-CTA indicates relatively high blocking efficiencies. In contrast, relatively broad MWDs ($M_w/M_n > 1.50$) were reported by Fielding et al.[34] when targeting x values above 300 for $PLMA_{37}$-$PBzMA_x$ diblock copolymers via closely-related PISA syntheses conducted in *n*-heptane. However, it is not yet understood why merely using

a PSMA macro-CTA instead of a PLMA macro-CTA leads to significantly better pseudo-living character during the dispersion polymerisation of BzMA.

A series of spherical nanoparticles with tunable diameters was conveniently prepared in mineral oil at 20% w/w solids simply by varying the target DP of the core-forming PBzMA block when using a PSMA macro-CTA with a sufficiently high DP. For example, $PSMA_{18}$-$PBzMA_x$ spheres ranging from 23 to 135 nm diameter (as judged by DLS) were obtained when targeting x values of 50 to 800. Similarly, well-defined $PSMA_{31}$-$PBzMA_x$ spheres of 25 to 154 nm diameter were produced for x = 50 to 2000. The mean sphere diameter (D) is related to the mean DP of the core-forming block (x) by a scaling exponent (α) as indicated by the equation $D \sim k.x^{\alpha}$, where k is a constant.[38, 39] Figure 3.10 shows double-logarithmic plots of D, as judged by DLS, against x for each series of $PSMA_{18}$-$PBzMA_x$ and $PSMA_{31}$-$PBzMA_x$ spheres. A clear relationship is observed in each case, which enables the corresponding α value to be determined. This parameter provides important information regarding the behaviour of the PBzMA core-forming chains. For the $PSMA_{31}$-$PBzMA_x$ series we find that α = 0.50, which corresponds to fully collapsed PBzMA chains.[38-40] According to the literature, such low α values suggest weak segregation (and minimal solvation).[38-40] On the other hand, we find that α = 0.61 for the $PSMA_{18}$-$PBzMA_x$ series, indicating that the PBzMA chains are more stretched and may have a finite degree of solvation. This means that, for a given $PBzMA_x$ block (where x > 50), larger spheres are always obtained when using the shorter $PSMA_{18}$ stabiliser block.

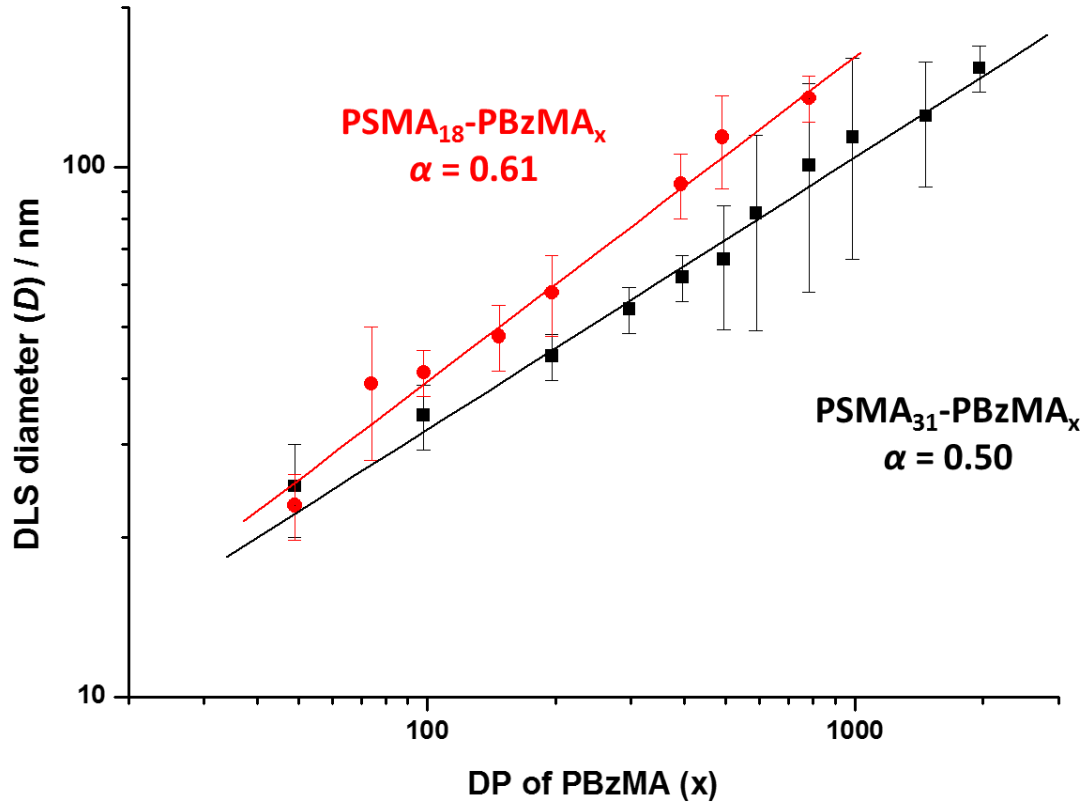

Figure 3.10. Intensity-average sphere diameter (D_S) vs. target DP of the PBzMA block (x) for series of $PSMA_{18}$-$PBzMA_x$ (red circles) and $PSMA_{31}$-$PBzMA_x$ (black squares) diblock copolymer spheres prepared via RAFT dispersion polymerisation of BzMA in mineral oil at 90 °C and 20% w/w solids. The error bars represent the standard deviation of the diameter and α is the scaling factor.

3.3.3. In situ SAXS studies of the PISA synthesis of $PSMA_{31}$-$PBzMA_{2000}$ spheres

A synchrotron X-ray source was used to acquire SAXS patterns *in situ* during the PISA synthesis of $PSMA_{31}$-$PBzMA_{2000}$ diblock copolymer spheres at 90 °C in mineral oil at 10% w/w solids. The sample cell was a 2 mm glass capillary and scattering patterns were recorded every 2 min for 120 min (see Figure 3.11). The onset of micellisation occurs when the growing PBzMA chains become sufficiently long to induce nucleation.[41] This occurred within around 2 min of the polymerisation, as indicated by the presence of a local minimum at q~0.23 nm^{-1}. The characteristic length scale corresponding to this feature is the mean core radius of the spherical nanoparticles (R_s), which was observed to be 15 nm. Since the PISA synthesis was conducted at 10% w/w solids, it was necessary to incorporate an appropriate structure factor[42] into

a well-known spherical micelle model[43-45] in order to obtain satisfactory fits to the SAXS patterns.

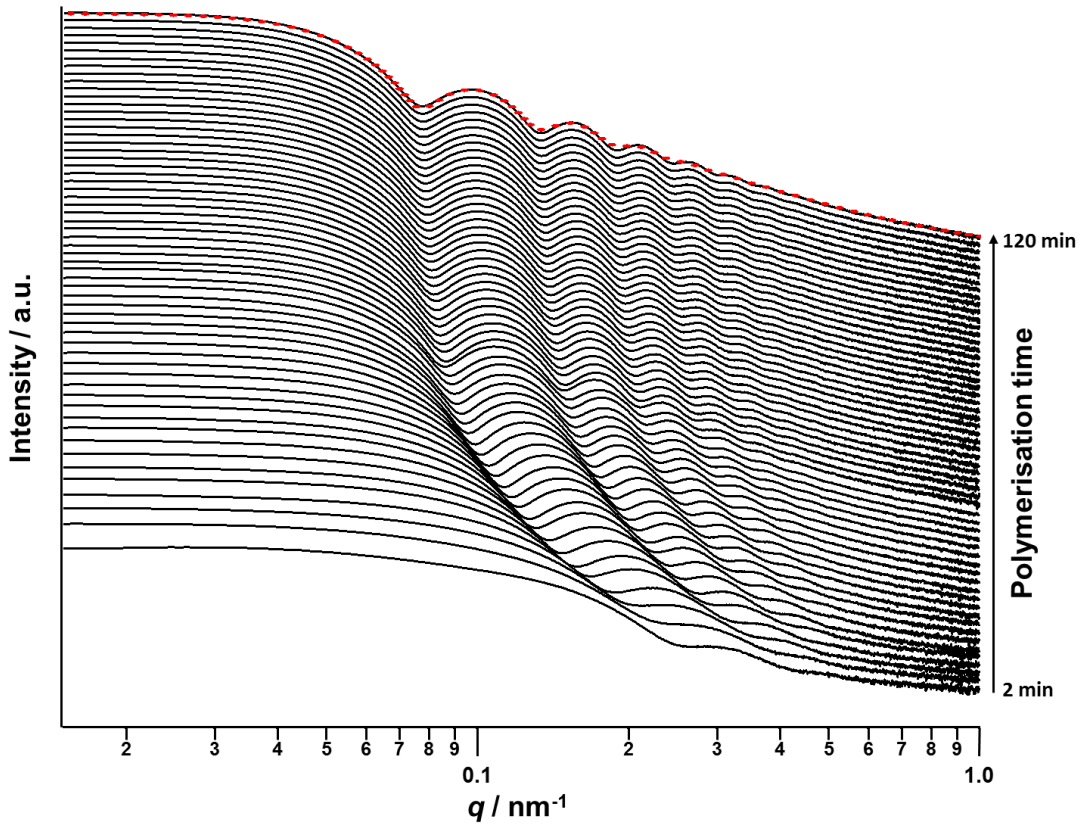

Figure 3.11. SAXS patterns obtained *in situ* during the PISA synthesis of $PSMA_{31}$-$PBzMA_{2000}$ diblock copolymer spheres at 90 °C in mineral oil at 10% w/w solids. Red dashes indicate the data fit to the final SAXS pattern recorded after 120 min using a spherical micelle model.[43-46]

Monitoring this minimum as it shifts to lower q (larger radii) as the BzMA polymerisation proceeded provides useful information regarding the kinetics of nanoparticle growth. However, in order to fit the SAXS data shown in Figure 3.11 to a spherical micelle model,[43-46] the *instantaneous BzMA conversion* is required, since this in turn determines the mean DP and hence the molecular volume occupied by a single growing core-forming PBzMA block [$V_s = (DP_{PBzMA}.M_{n,BzMA})/(N_A.\rho)$], where $M_{n,BzMA}$ corresponds to the molecular weight of the one BzMA unit within the PBzMA block and ρ is the density of PBzMA. No further change in the SAXS patterns shown in Figure 3.11 was taken to signify the end of the polymerisation. Unfortunately, the

BzMA polymerisation was complete within 120 min during the *in situ* SAXS studies, whereas around 500 min was required for the same formulation in a typical laboratory-scale synthesis (~20 mL reaction volume) conducted using an oil bath and stirrer hot plate. A possible reason for this significant increase in polymerisation rate could be additional radical species generated by the intense X-ray photon flux provided by the synchrotron source.[47, 48] The ~125 μL reaction volume of the capillary used for the SAXS studies precludes sampling of the polymerising reaction mixture. Instead, intermediate BzMA conversions were calculated by renormalising the kinetic data set obtained for the laboratory-scale synthesis. More specifically, a sigmoid function (see Section 3.2.9) was used to calculate intermediate BzMA conversions (see Figure 3.12a) since this best described the conversion vs. time curve.[49] The resulting BzMA conversions were subsequently used to calculate the instantaneous PBzMA DP during the PISA synthesis (see Figure 3.12b, red data). It must be noted that due to the nature of the renormalisation using the sigmoid function, the predicted kinetic data for the *in situ* SAXS measurements are a smooth representation of the somewhat scattered experimental data obtained under standard laboratory conditions.

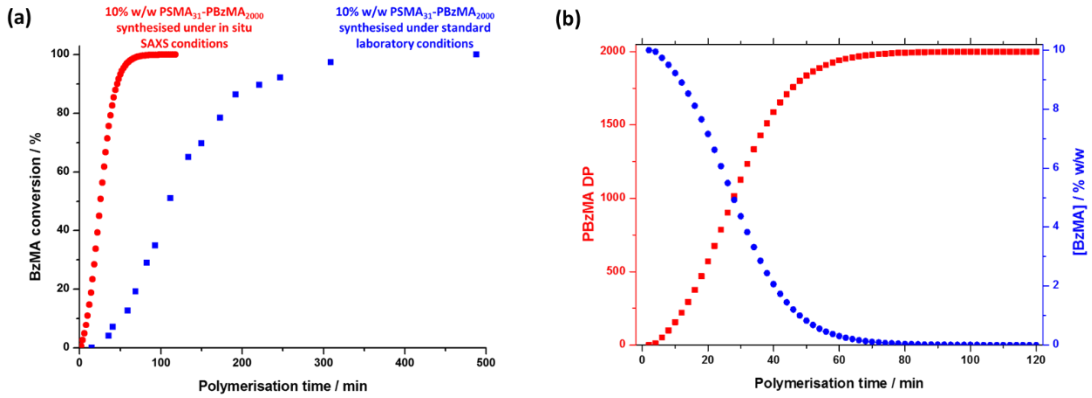

Figure 3.12. (a) Conversion vs. time curve (blue squares) for the RAFT dispersion polymerisation of BzMA in mineral oil at 90 °C when targeting $PSMA_{31}$-$PBzMA_{2000}$ block copolymer spheres at 10% w/w solids using T21s initiator under normal laboratory conditions and the renormalised conversion vs. time curve (red circles) calculated for the same PISA synthesis during *in situ* SAXS studies. (b) Change in the PBzMA DP (red circles) and the concentration of BzMA monomer ([BzMA], blue squares) during the *in situ* SAXS studies when targeting $PSMA_{31}$-$PBzMA_{2000}$ spheres.

As expected, the spherical core diameter of the growing nanoparticles (D_s) increases monotonically with polymerisation time (see Figure 3.13a and Table 3.3). At the end of the BzMA polymerisation, at least six minima are visible in the final scattering

pattern (120 min, Figure 3.11), indicating a relatively narrow size distribution for the resulting $PSMA_{31}$-$PBzMA_{2000}$ spheres. Data fitting for various SAXS patterns during the RAFT dispersion polymerisation of $PSMA_{31}$-$PBzMA_{2000}$ spheres indicated essentially no solvent associated with the core-forming PBzMA block, which is consistent with the $PSMA_{31}$ data set shown in Figure 3.10. Moreover, ^{1}H NMR studies of the latter laboratory-scale syntheses confirmed that the volume fraction of solvent within the core domain (φ_{sol}) is essentially zero. Thus, when fitting SAXS patterns recorded during the polymerisation, the mean number of copolymer chains per sphere (N_s) was calculated based solely on the volume fraction of BzMA monomer within the core domain (φ_{BzMA}), R_s and V_s as shown below.

$$N_s = (1 - \varphi_{BzMA}) \times \frac{\frac{4}{3}\pi {R_s}^3}{V_s} \qquad 3.7$$

Values for φ_{BzMA} were estimated via centrifugation of selected dispersions of $PSMA_{31}$-$PBzMA_x$ spheres (obtained at full BzMA conversion via laboratory-scale syntheses). Varying amounts of BzMA monomer were added in order to replicate specific intermediate BzMA conversions during the synthesis of $PSMA_{31}$-$PBzMA_{2000}$ spheres in the *in situ* SAXS studies. Firstly, the BzMA-swollen $PSMA_{31}$-$PBzMA_x$ spheres were heated at 90 °C for 1 h and then centrifuged at 13,000 rpm for 1 to 10 h at 20 °C to ensure complete sedimentation of the spheres. Since centrifugation was not possible at 90 °C, it is assumed that the amount of BzMA monomer within the PBzMA cores is the same at 20 °C and 90 °C. Each supernatant was then analysed for its BzMA content against an internal standard (triethoxymethylsilane, TEMS) via ^{1}H NMR spectroscopy (see Section 3.2.10 for details). The experimentally-determined values of φ_{BzMA} at particular BzMA conversions were then fitted to a logarithmic decay function ($R^2 > 0.95$, see Figure 3.7), which was subsequently utilised to calculate φ_{BzMA} values for all entries in Table 3.3 via interpolation. Equation 3.7 was then used to calculate the corresponding N_s values. According to the SAXS fittings, the uncertainty in R_s is small (see Table 3.3), hence the error in N_s is dominated by that associated with V_s, which is in turn dictated by the MWD of the growing core-forming PBzMA block. Given that the $PSMA_{31}$ stabiliser block is relatively short, this MWD is approximately the same as that of the diblock copolymer. However, since the *in situ*

SAXS experiments were conducted on such a small scale, it was not feasible to determine the copolymer MWD at intermediate times during the polymerisation. Therefore, the maximum error in V_s at any given time during the polymerisation was estimated from the final MWD obtained for the laboratory-scale synthesis of the equivalent $PSMA_{31}$-$PBzMA_{2000}$ spheres. The unimodal MWD determined by THF GPC was fitted to a Gaussian model to determine its standard deviation (see Section 3.2.11 for details), which was found to be approximately 9.5%.

N_s gradually increased with polymerisation time, as indicated in Figure 3.13b (black data). This is not unexpected in view of recent observations made by both Jones et al.[14] and Zhang and co-workers[50] for non-aqueous PISA formulations. Nevertheless, it provides the first direct experimental evidence that the mean number of copolymer chains per nanoparticle increases during PISA syntheses. Likely mechanisms are either efficient fusion between monomer-swollen spheres and/or continuous aggregation of molecularly-dissolved copolymer chains.[14] The latter seems more likely to occur during the early stages of the polymerisation (just after nucleation), rather than in the latter stages. The average number of copolymer chains per unit surface area (S_{agg}) during the polymerisation was calculated using Equation 3.8 below:

$$S_{\mathrm{agg}} = \frac{N_{\mathrm{s}}}{4\pi {R_{\mathrm{s}}}^2} \qquad 3.8$$

Interestingly, S_{agg} values (Figure 3.13b, red data) decrease from 0.075 nm^{-2} to a limiting value of about 0.04 nm^{-2} after around 40 min, suggesting an optimum surface packing density of copolymer chains within the sterically-stabilised $PSMA_{31}$-$PBzMA_{2000}$ spherical nanoparticles.[14]

The average distance between neighbouring chains at the core-shell interface (d_{int}) was calculated using Equation 3.9 below:[39]

$$d_{\mathrm{int}} = \sqrt{\frac{4\pi {R_{\mathrm{s}}}^2}{N_{\mathrm{s}}}} = \sqrt{\frac{1}{S_{\mathrm{agg}}}} \qquad 3.9$$

For small spheres (i.e., D_s = 35.4 nm), d_{int} was calculated to be 3.67 nm after 8 min (or 5.0% BzMA conversion, which corresponds to $PSMA_{31}$-$PBzMA_{99}$). This is comparable to that reported by Förster et al.[39] for similar-sized polystyrene-poly(4-vinyl pyridine) block copolymer micelles, for which d_{int} was found to be 3.20 nm. Subsequently, d_{int} increased up to 5.04 nm at full conversion (i.e. $PSMA_{31}$-$PBzMA_{2000}$; D_s = 116.9 nm), indicating that copolymer chains with longer core-forming PBzMA blocks occupy a larger surface area at the core-shell interface.

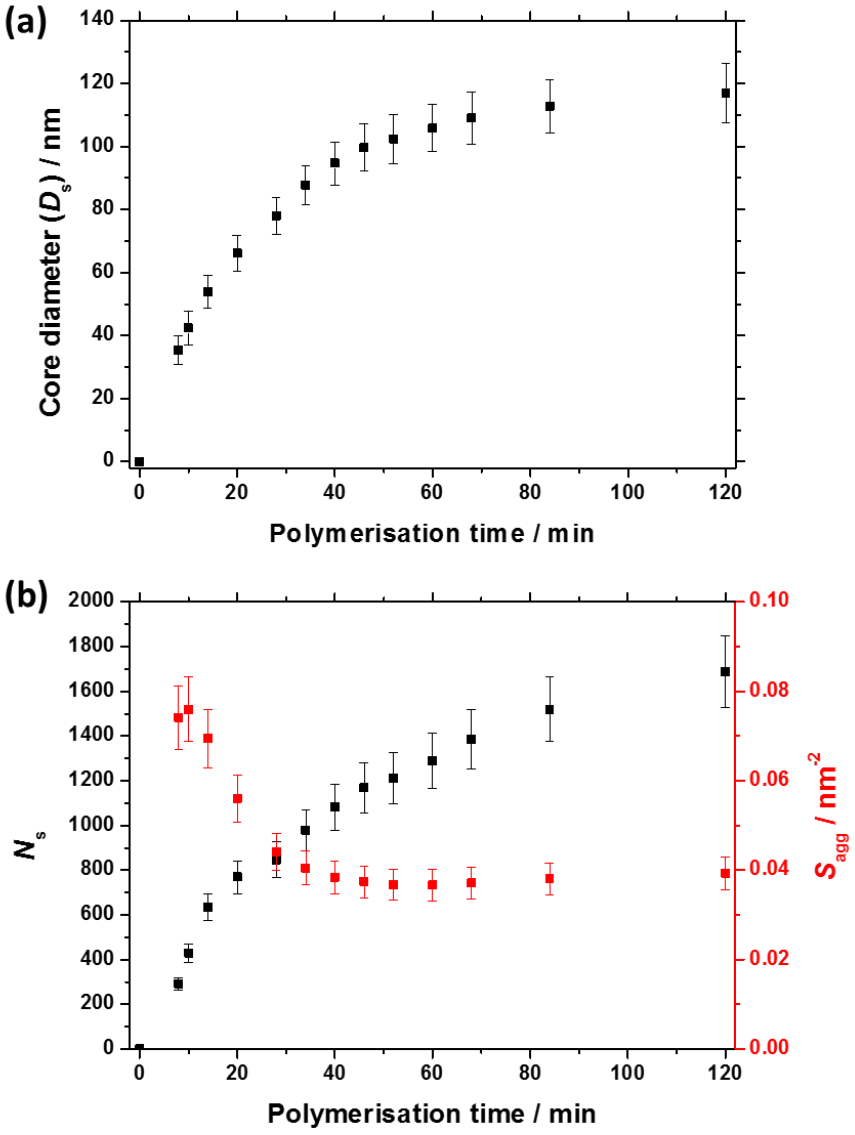

Figure 3.13. (a) Evolution of the mean core diameter (D_s) and (b) mean aggregation number per sphere (N_s, black data) and number of aggregated chains per unit surface area (S_{agg}, red data) during the PISA synthesis of $PSMA_{31}$-$PBzMA_{2000}$ diblock copolymer spheres, as judged by *in situ* SAXS studies.

Table 3.3. Evoution of BzMA conversion, mean degree of polymerisation (DP) of the core-forming PBzMA block, the molecular volume occupied by a single PBzMA chain (V_s), the nanoparticle core diameter ($D_s = 2R_s$), volume fraction of BzMA monomer within the core domain (φ_{BzMA}), mean aggregation number per sphere (N_s), number of copolymer chains per unit surface area (S_{agg}) and mean distance between neighbouring chains at the core-shell interface (d_{int}) during the PISA synthesis of $PSMA_{31}$-$PBzMA_{2000}$ diblock copolymer spheres. The standard deviation in D_s ($\sigma_{Ds} = 2\sigma_{Rs}$) and the associated error in V_s, N_s, S_{agg} and d_{int} are indicated.

Time / min	% BzMA	PBzMA DP	V_s / nm^3	D_s / nm	φ_{BzMA}	N_s	S_{agg} / nm^{-2}	d_{int} / nm
8	5.0	99	25 ± 2	35 ± 5	0.691	292 ± 28	0.074 ± 0.007	3.7 ± 0.4
10	7.8	155	39 ± 4	42 ± 5	0.586	429 ± 41	0.076 ± 0.007	3.6 ± 0.3
14	14.7	294	73 ± 7	54 ± 5	0.437	633 ± 60	0.069 ± 0.007	3.8 ± 0.4
20	28.4	569	141 ± 13	66 ± 6	0.282	769 ± 73	0.056 ± 0.005	4.2 ± 0.4
28	50.8	1015	252 ± 24	78 ± 6	0.147	845 ± 80	0.044 ± 0.004	4.8 ± 0.5
34	66.8	1335	331 ± 32	88 ± 6	0.083	978 ± 93	0.040 ± 0.004	5.0 ± 0.5
40	79.3	1587	394 ± 37	95 ± 7	0.042	1082 ± 103	0.038 ± 0.004	5.1 ± 0.5
46	87.9	1758	436 ± 41	100 ± 8	0.018	1168 ± 111	0.037 ± 0.004	5.2 ± 0.5
52	93.2	1864	463 ± 44	102 ± 8	0.004	1210 ± 115	0.037 ± 0.003	5.2 ± 0.5
60	97.0	1939	481 ± 46	106 ± 8	0.000	1289 ± 122	0.037 ± 0.003	5.2 ± 0.5
68	98.7	1973	490 ± 47	109 ± 8	0.000	1385 ± 132	0.037 ± 0.004	5.2 ± 0.5
84	99.8	1995	495 ± 47	113 ± 8	0.000	1519 ± 144	0.038 ± 0.004	5.1 ± 0.5
120	100	2000	496 ± 47	117 ± 9	0.000	1688 ± 160	0.039 ± 0.004	5.0 ± 0.5

3.3.4. $PSMA_{13}$-$PBzMA_x$ block copolymer syntheses and corresponding phase diagram

Utilising a shorter $PSMA_{13}$ macro-CTA to target PBzMA core-forming block DPs of 20 to 150 at various copolymer concentrations enabled access to spherical, worm-like or vesicular morphologies *at relatively low copolymer concentrations* (≥ 5% w/w solids). In contrast, well-defined vesicular morphologies were only obtained at copolymer concentrations of at least 12.5% w/w solids for the PISA synthesis of PLMA-PBzMA diblock copolymer nanoparticles, whereas somewhat higher copolymer concentrations (≥ 17.5% w/w solids) were required to access a pure worm phase.[5, 34] A detailed phase diagram was constructed for the present $PSMA_{13}$-$PBzMA_x$ formulation, with diblock copolymer morphologies assigned via *post mortem* TEM studies, see Figure 3.14.

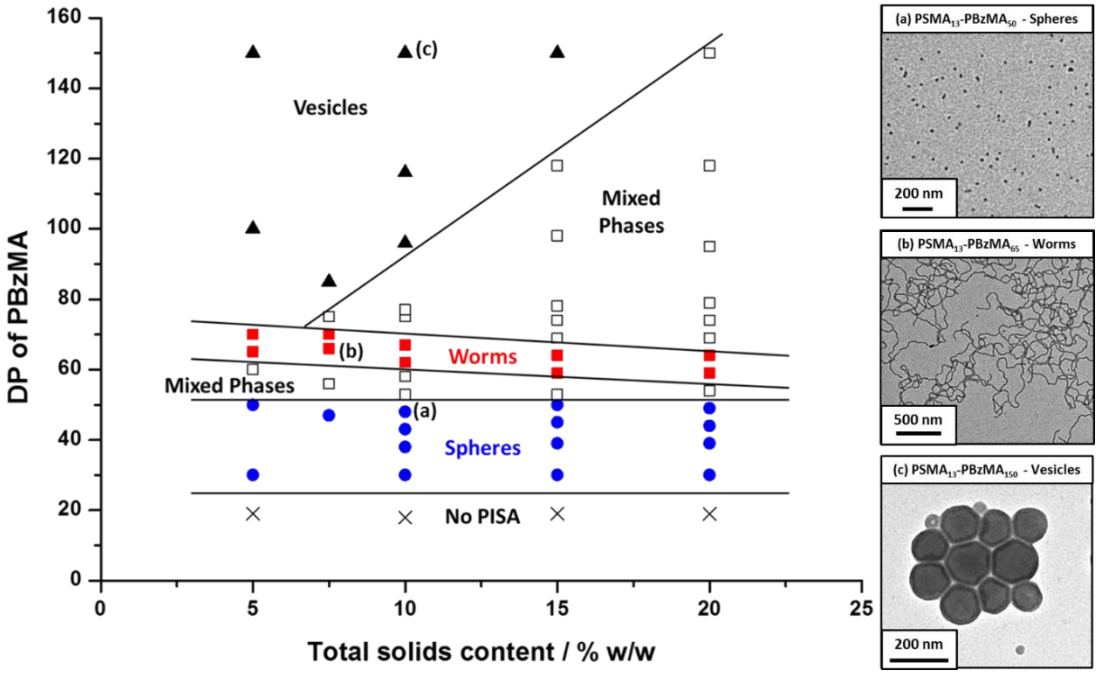

Figure 3.14. Phase diagram constructed for $PSMA_{13}$-$PBzMA_x$ diblock copolymer nanoparticles prepared by RAFT dispersion polymerisation of BzMA in mineral oil using a $PSMA_{13}$ macro-CTA and T21s initiator at 90 °C ([$PSMA_{13}$]/[T21s] molar ratio = 5.0). The *post mortem* diblock copolymer morphologies obtained at full conversion were assigned on the basis of TEM studies. TEM images (a), (b) and (c) correspond to typical examples of the three pure copolymer morphologies (spheres, worms and vesicles) respectively.

Such phase diagrams are essential to ensure reproducible targeting of the desired copolymer morphology. Spheres were obtained at all copolymer concentrations

investigated (5-20% w/w) when targeting PBzMA block DPs of 30 to 50. As reported for related PISA formulations,[5, 11, 34, 41, 51-53] the worm phase space is relatively narrow and is bounded by mixed phase regions. As expected, pure vesicles were obtained by targeting asymmetric $PSMA_{13}$-$PBzMA_x$ diblock copolymers (i.e. x > 80). However, for PBzMA DPs of up to 150 this phase appears to be confined to copolymer concentrations of 5-15% w/w solids, with mixed phases being obtained at 20% w/w solids. It is perhaps worth emphasising that the ability to prepare vesicles at copolymer concentrations as low as 5% w/w solids is an important advantage for *in situ* SAXS studies. This is because lower copolymer concentrations minimise structural effects arising from inter-particle interactions.

Post mortem SAXS patterns recorded for 1.0% w/w dispersions of eight $PSMA_{13}$-$PBzMA_x$ diblock copolymer nano-objects (originally prepared at 10% w/w solids; see phase diagram in Figure 3.14) are depicted in Figure 3.15. Each of the three examples of spherical nanoparticles exhibit an approximate zero gradient at low q, as expected.[1, 2] Some deviations from zero gradient observed at low q values could be associated with an aggregation of the spherical micelles. The local minimum observed for each scattering curve at $q \approx 0.5$-0.7 nm^{-1} gradually shifted to lower q on increasing the mean PBzMA DP from 40 to 50, indicating a progressive increase in the sphere dimensions. This is consistent with previously reported PISA syntheses conducted using a fixed stabiliser block DP, where increasing the DP of the core-forming block led to larger spherical nanoparticles.[34, 54] According to theory, rigid rods should exhibit a limiting gradient of -1 at low q.[1, 2] However, TEM studies (see Figure 3.14b) suggest that these particular worms exhibit appreciable flexibility. Nevertheless, the SAXS patterns recorded for $PSMA_{13}$-$PBzMA_{65}$ and $PSMA_{13}$-$PBzMA_{70}$ worms in Figure 3.15 do indeed exhibit gradients of approximately -1 at low q. For these two copolymer dispersions, the local minimum observed at $q \approx 0.5$-0.6 nm^{-1} is associated with the mean worm width or thickness (T_w). Vesicular morphologies were also confirmed for $PSMA_{13}$-$PBzMA_{100\text{-}150}$, since SAXS patterns indicated a slope of approximately -2 at low q for these three dispersions. For such hollow spheres, there are two characteristic local minima. Firstly, the minimum observed at $q \approx 0.4$-0.6 nm^{-1} is associated with the vesicle membrane thickness (T_m), which increases monotonically as higher PBzMA

DPs are targeted. Secondly, the local minimum observed at $q \approx 0.04$-0.05 nm^{-1} is characteristic of the overall vesicle dimensions. Interestingly, this parameter remains relatively constant (109 ± 5 nm) for the series of three PSMA$_{13}$-PBzMA$_{100\text{-}150}$ vesicles prepared at 10% w/w solids shown in Figure 3.14.

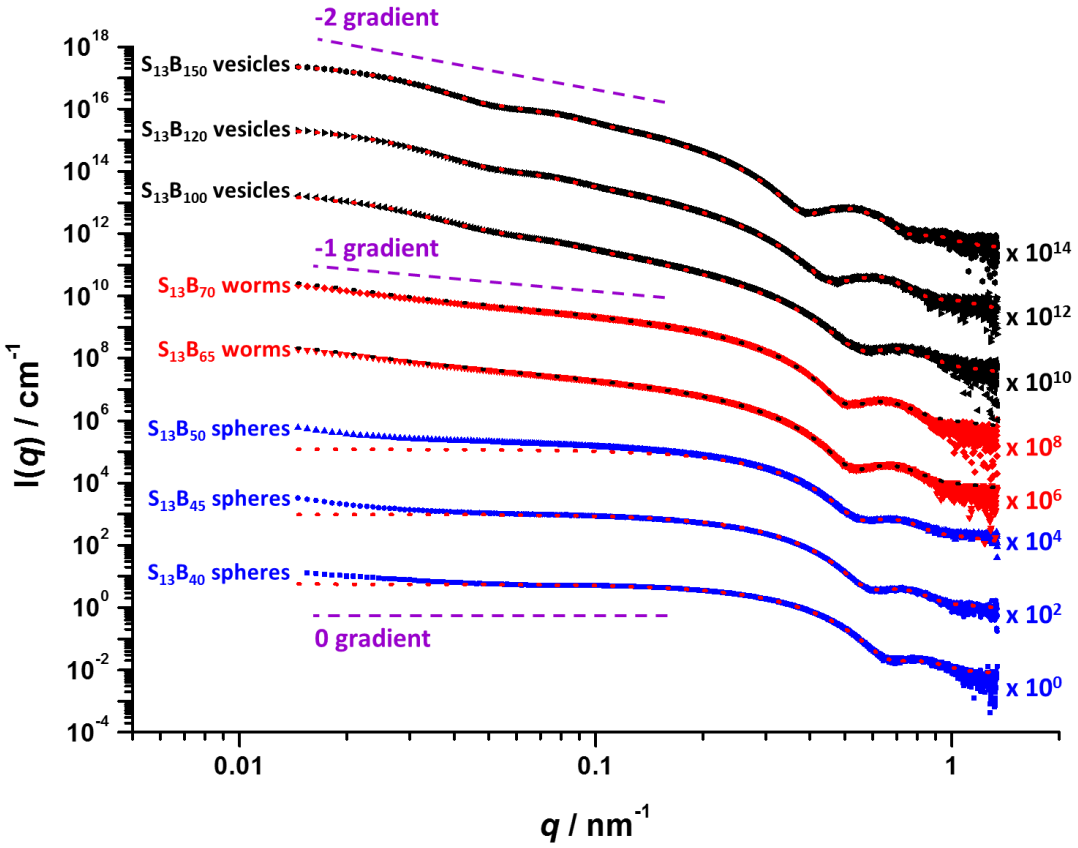

Figure 3.15. SAXS patterns and data fits (dashed lines) for 1.0% w/w dispersions of PSMA$_{13}$-PBzMA$_x$ (denoted as S$_{13}$-B$_x$ for brevity) diblock copolymer nanoparticles synthesised via RAFT dispersion polymerisation of BzMA at 10% w/w solids in mineral oil. Purple dashed lines indicate zero, -1 and -2 gradients for guidance.

3.3.5. In situ SAXS studies of the PISA synthesis of PSMA$_{13}$-PBzMA$_{150}$ vesicles

A series of *in situ* SAXS patterns were also recorded when targeting PSMA$_{13}$-PBzMA$_{150}$ vesicles at 10% w/w solids in mineral oil. This core-forming block DP was chosen to guarantee access to vesicle phase space (see Figure 3.14) while maximising the time scales for the existence of the intermediate sphere and worm phases. Inspecting Figure 3.16, this strategy was clearly successful since the full range of copolymer morphologies is observed, from initially soluble copolymer chains through

to the final vesicular morphology via intermediate spherical and worm-like nanoparticles.[16]

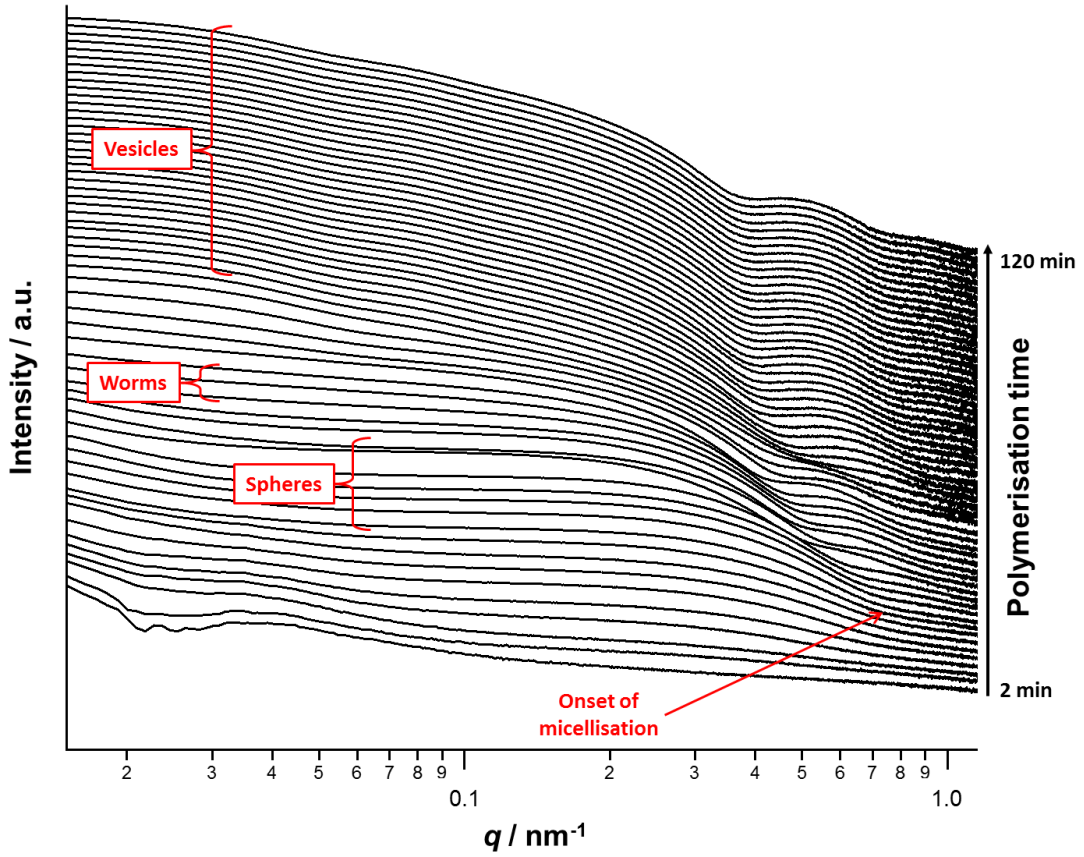

Figure 3.16. *In situ* SAXS patterns recorded for the PISA synthesis of $PSMA_{13}$-$PBzMA_{150}$ diblock copolymer vesicles prepared at 90 °C in mineral oil at 10% w/w solids. The onset of micellar nucleation is indicated by the red arrow.

Again, the polymerisation kinetics required renormalisation prior to detailed data analyses (see Figure 3.17). In this case, a significantly longer polymerisation time (and hence a somewhat higher BzMA conversion) is required for the onset of micellisation. Inspecting Figure 3.14, it is clear that the critical DP for the core-forming PBzMA block required to induce nucleation is around 30. This is because $PSMA_{13}$-$PBzMA_{20}$ diblock copolymers do not self-assemble in mineral oil at 90 °C, whereas $PSMA_{13}$-$PBzMA_{30}$ diblock copolymer spheres are observed under these conditions. Thus approximately 20% BzMA conversion is required to trigger *in situ* self-assembly for this particular $PSMA_{13}$-$PBzMA_{150}$ PISA formulation. In contrast, when targeting $PSMA_{31}$-$PBzMA_{2000}$ diblock copolymer spheres (see Figure 3.11), a BzMA

conversion of only ~1.5% is required to achieve the same critical PBzMA DP for micellar nucleation.

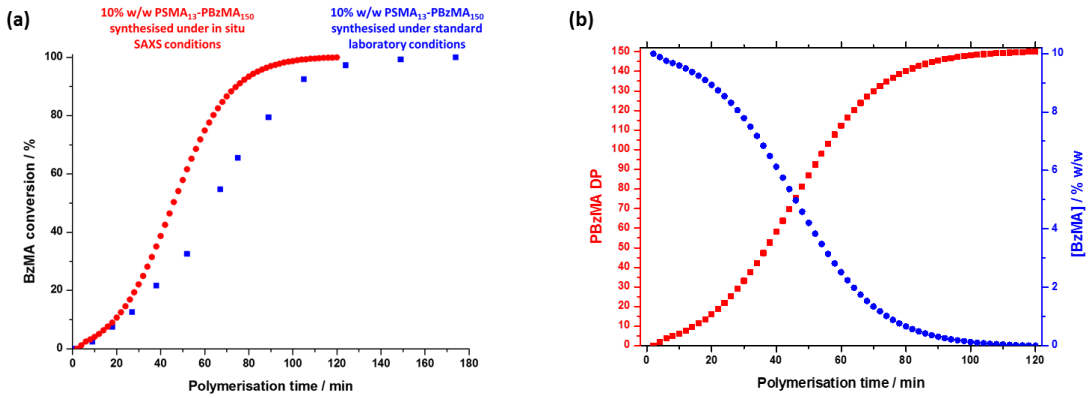

Figure 3.17. (a) Conversion vs. time curve for the RAFT dispersion polymerisation of BzMA in mineral oil at 90 °C when targeting $PSMA_{13}$-$PBzMA_{150}$ block copolymer vesicles at 10% w/w solids using T21s initiator under normal laboratory conditions (blue squares) and the renormalised conversion vs. time curve (red circles) calculated for the same PISA synthesis during *in situ* SAXS studies. (b) Change in the PBzMA DP (red circles) and the concentration of BzMA monomer ([BzMA], blue squares) during the *in situ* SAXS studies when targeting $PSMA_{13}$-$PBzMA_{150}$ vesicles.

Spherical nanoparticles are formed just after the onset of micellisation, as confirmed by the approximately zero gradient at low *q*.[1, 2] However, just 10 min after nucleation this low *q* gradient tends towards -1, indicating that the nascent spherical nanoparticles undergo multiple 1D fusion events leading to the formation of highly anisotropic worms. This second morphology is relatively short-lived (~6 min), which is consistent with the narrow worm phase space observed in the phase diagram (see Figure 3.14). A mixed phase of worms and vesicles is apparent from 46 to 56 min. This corresponds to a PBzMA DP of 76 to 104 and is consistent with the mixed phase region observed in Figure 3.14. Finally, well-defined vesicles are present as a pure phase in the latter stages of the polymerisation (~58-120 min), as indicated by the slope of -2 at low *q*.

For this particular *in situ* SAXS study (see Figure 3.16), the experimental protocol used to renormalise the polymerisation kinetics can be validated by comparing the PBzMA DP ranges within which pure spheres, worms and vesicles are observed to those indicated within the phase diagram shown in Figure 3.14 (see Table 3.4). The generally good agreement between the upper and lower DPs at which each pure

morphology provides strong evidence that the analytical approach employed to renormalise the kinetic data is indeed valid. It is also worth emphasising that the relatively well-defined phase boundaries shown in Figure 3.14 enable a particularly robust comparison.

Table 3.4. Comparison of the lower and upper limit PBzMA DPs for the three pure copolymer morphologies (spheres, worms and vesicles) determined by (i) inspecting the phase diagram constructed for $PSMA_{13}$-$PBzMA_x$ diblock copolymer nanoparticles (Figure 3.14) and (ii) *in situ* SAXS analysis of the synthesis of $PSMA_{13}$-$PBzMA_{150}$ vesicles (Figure 3.16).

Pure copolymer morphology		**PBzMA DP indicated by phase diagram**	**PBzMA DP indicated by *in situ* SAXS studies**
Spheres	Lower limit boundary	25 ± 5	29 ± 3
	Upper limit boundary	51 ± 1	48 ± 4
Worms	Lower limit boundary	60 ± 1	59 ± 5
	Upper limit boundary	70 ± 1	70 ± 6
Vesicles	Lower limit boundary	93 ± 2	108 ± 4

SAXS patterns assigned to pure vesicles exhibit two local minima: one is a rather subtle feature at $q \approx 0.04$-0.07 nm^{-1} representing the overall vesicle dimensions and the other is a more pronounced feature at $q \approx 0.3$-0.7 nm^{-1} that is associated with the vesicle membrane thickness (T_m).[10] Figure 3.18a shows selected SAXS patterns taken from Figure 3.16 over a much narrower q range in order to better illustrate the evolution in T_m at $q \approx 0.3$-0.7 nm^{-1}. A pure vesicle phase is observed after 58 min, with subsequent data fits indicating that T_m increases monotonically from 10 nm to 14 nm for PBzMA DPs ranging from 108 to 150 (see Figure 3.18b and Table 3.5). There is also an apparent increase in the outer core radius (R_{out}) with increasing PBzMA DP (see Table 3.5), but this rather modest increase appears to be within the relatively large error associated with these data.

Precise knowledge of the dimensions of the growing vesicles is important, because in principle this enables the vesicle growth mechanism to be deduced. For example, Warren et al.[10] reported that the overall diameter of PGMA-PHPMA vesicles prepared via aqueous RAFT dispersion polymerisation remained constant while T_m increased

when targeting higher PHPMA DPs. This indicates that the constrained vesicles grow inwards, with the thickening membrane leading to a reduction in the vesicle lumen volume (see Figure 3.3).

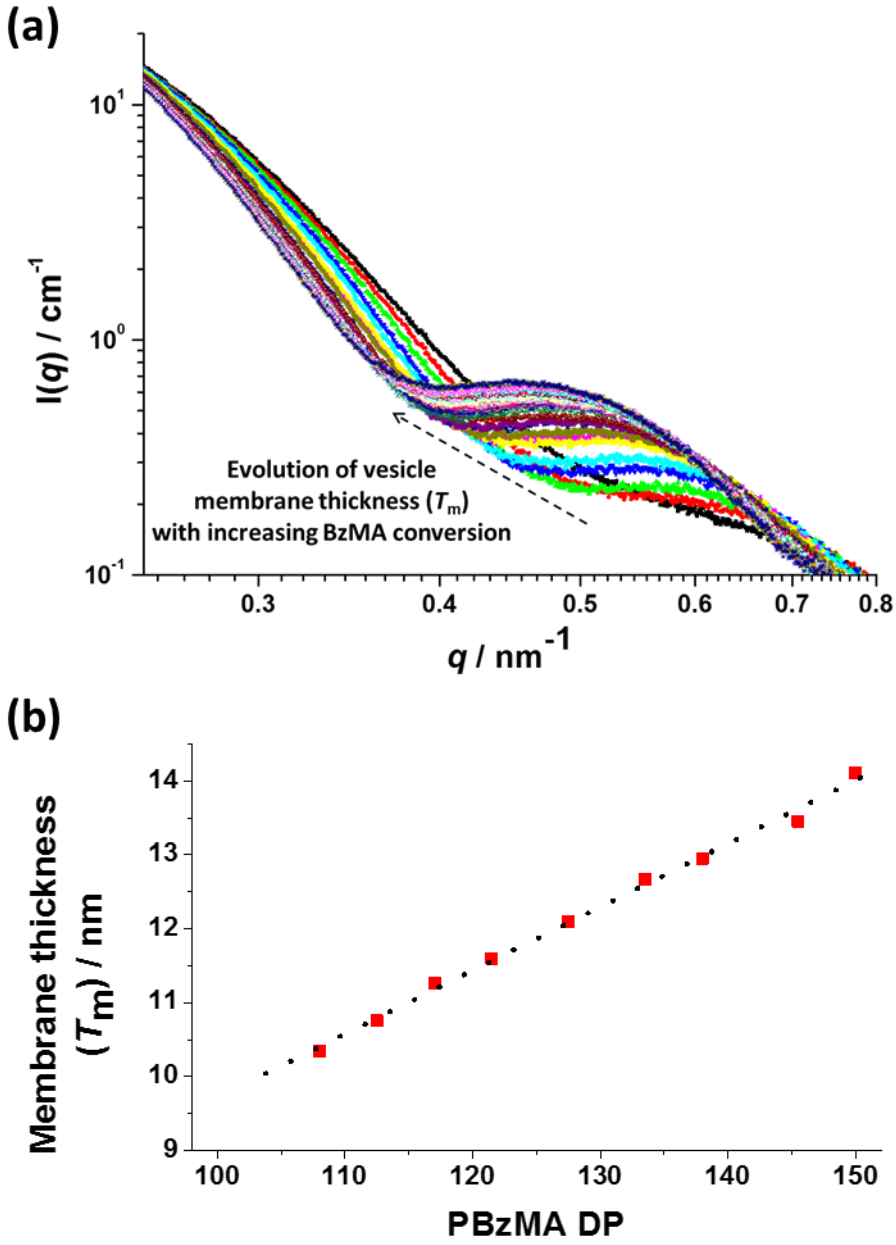

Figure 3.18. (a) *In situ* SAXS patterns showing the evolution of the vesicular membrane thickness (T_m) and the proposed mechanism for the *in situ* evolution of the vesicular morphology. (b) The relationship between T_m and PBzMA DP for the PISA synthesis of $PSMA_{13}$-$PBzMA_{150}$ vesicles at 90 °C in mineral oil at 10% w/w solids.

Table 3.5. Evolution of the BzMA conversion, mean degree of polymerization (DP) for the core-forming PBzMA block, molecular volume of a single PBzMA core-forming block (V_m), outer core radius (R_{out}), membrane thickness (T_m) and inner core radius ($R_{in} = R_{out} - T_m$) during the PISA synthesis of $PSMA_{13}$-$PBzMA_{150}$ diblock copolymer vesicles. The standard deviation ($\pm \sigma$) of each value is shown where relevant.

Time / min	% BzMA	PBzMA DP	V_m / nm^3	R_{out} / nm	T_m / nm	R_{in} / nm
58	72.3	108	27 ± 1.0	53 ± 18	10 ± 1.6	43 ± 18
60	75.4	113	28 ± 1.0	56 ± 19	11 ± 1.6	45 ± 19
62	78.2	117	29 ± 1.0	56 ± 19	11 ± 1.6	45 ± 19
64	80.7	122	30 ± 1.0	56 ± 19	12 ± 1.6	44 ± 19
68	85.2	128	32 ± 1.1	57 ± 20	12 ± 1.8	45 ± 20
72	88.9	134	33 ± 1.1	57 ± 20	13 ± 1.8	44 ± 20
76	91.8	138	34 ± 1.2	57 ± 19	13 ± 1.9	44 ± 19
88	97.1	146	36 ± 1.2	57 ± 20	14 ± 2.0	44 ± 20
120	100	150	37 ± 1.3	59 ± 20	14 ± 2.2	45 ± 21

3.3.6. Intermediate morphologies during the in situ worm-to-vesicle morphology transformation

Informed by these *in situ* studies, multiple aliquots were taken from the same polymerisation (targeting $PSMA_{13}$-$PBzMA_{150}$) conducted under standard laboratory conditions, with particular attention being paid to the DP range identified between the pure worm and vesicle phases. TEM analyses confirmed that vesicles are formed from worms via octopi (see Figure 3.19b) and jellyfish (see Figure 3.19c and d) intermediates. Such transient structures were also reported by Blanazs and co-workers[16] for an aqueous PISA formulation when targeting vesicles as the final copolymer morphology (see Figure 3.4). This provides the first evidence of octopi and jellyfish intermediates for a non-polar PISA formulation and suggests that the worm-to-vesicle morphology transition via such structures is likely to be universal for all vesicles prepared via PISA syntheses.

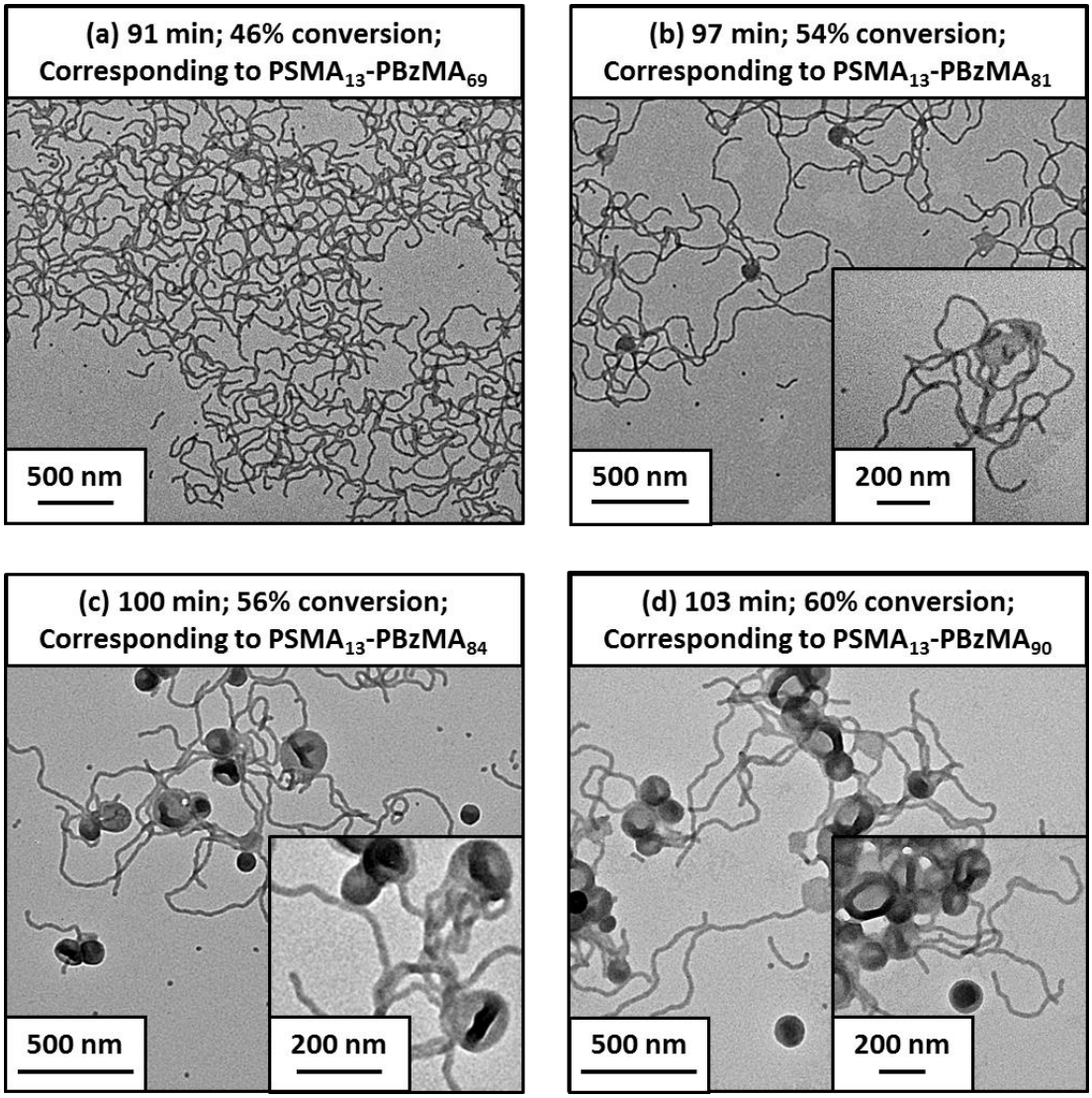

Figure 3.19. Transmission electron micrographs obtained for 0.1% w/w dispersions of $PSMA_{13}$-$PBzMA_x$ nanoparticles obtained at various time points during the PISA synthesis of $PSMA_{13}$-$PBzMA_{150}$ vesicles under standard laboratory conditions at 10% w/w in mineral oil. (a) A pure worm morphology is observed after 91 min, (b) worms and octopi structures are observed after 97 min and worms, vesicles, octopi and jellyfish structures are observed after (c) 100 min and (d) 103 min.

3.3.7. Verification of the universal 'inward growth' mechanism for vesicles synthesised by PISA

In order to elucidate the growth mechanism for the $PSMA_{13}$-$PBzMA_x$ vesicles described in this work, much higher PBzMA DPs must be targeted. Consequently, $PSMA_{13}$-$PBzMA_x$ vesicles with PBzMA DPs up to 2000 (prepared at 10% w/w solids on a 5.0 mL scale) were subjected to *post mortem* analysis using DLS, TEM and SAXS. DLS studies indicated that the overall vesicle diameter remained essentially

constant (140-145 nm) for PBzMA DPs of between 100 and 400 (see Figure 3.20a, blue data). The overall vesicle diameter systematically increased for PBzMA DPs between 500 and 2000, while the size distributions significantly broadened for PBzMA DPs above 400. These data suggest that the vesicles become unstable for PBzMA DPs greater than 400, as previously described by Warren et al. for PGMA-PHPMA vesicles.[10] TEM studies (see Figure 3.20b) support these DLS data: vesicles with narrow size distributions and approximately constant diameters were observed for PBzMA DPs up to 400. This indicates that the *apparent* increase in overall vesicle dimensions observed in the *in situ* SAXS studies (see Table 3.5) is actually an artefact. Moreover, T_m increases with PBzMA DP over this range, which suggests a similar 'inward growth' mechanism. Furthermore, large, ill-defined species are observed for PBzMA DPs above 500 (see vertical dashed line in Figure 3.20a). This is consistent with observations made by Warren et al.,[10] who reported loss of the vesicular morphology for PHPMA DPs above 1000. In view of these observations, further *post mortem* SAXS studies were undertaken to monitor the evolution of the $PSMA_{13}$-$PBzMA_x$ morphology (see Figure 3.20c). It should be noted that these additional SAXS measurements were performed using an in-house NanoStar instrument, rather than a synchrotron X-ray source. Thus the accessible q range was only sufficient to allow the evolution in T_m to be monitored – no information regarding the overall vesicle dimensions could be obtained. T_m increased monotonically from 9 nm to 30 nm on increasing the target PBzMA DP from 100 to 400. The data were fitted to the power law $T_m = k.x^{\alpha}$ where k is a constant and x is the PBzMA DP. The α exponent was calculated to be 0.86, which is consistent with that reported by Warren et al.[10] via *post mortem* SAXS analysis of PGMA-PHPMA vesicles ($\alpha = 0.79$). For PBzMA DPs above 400, the T_m feature at $q \approx 0.2$-0.6 nm^{-1} becomes increasingly indistinct. This indicates the gradual loss of the vesicular morphology, which is consistent with the corresponding TEM studies. Since the DLS data indicate the same overall vesicle dimensions for PBzMA DPs of 100-400, this indicates that the 'inward growth' mechanism is valid for both aqueous and non-polar media. This is important, because it implies a *generic* vesicle growth mechanism for all PISA formulations. This is perfectly reasonable, because Warren et al. showed that this hitherto unrecognised mechanism is the *only* means by which the vesicles can lower their total surface area, and hence reduce their overall free energy.[10]

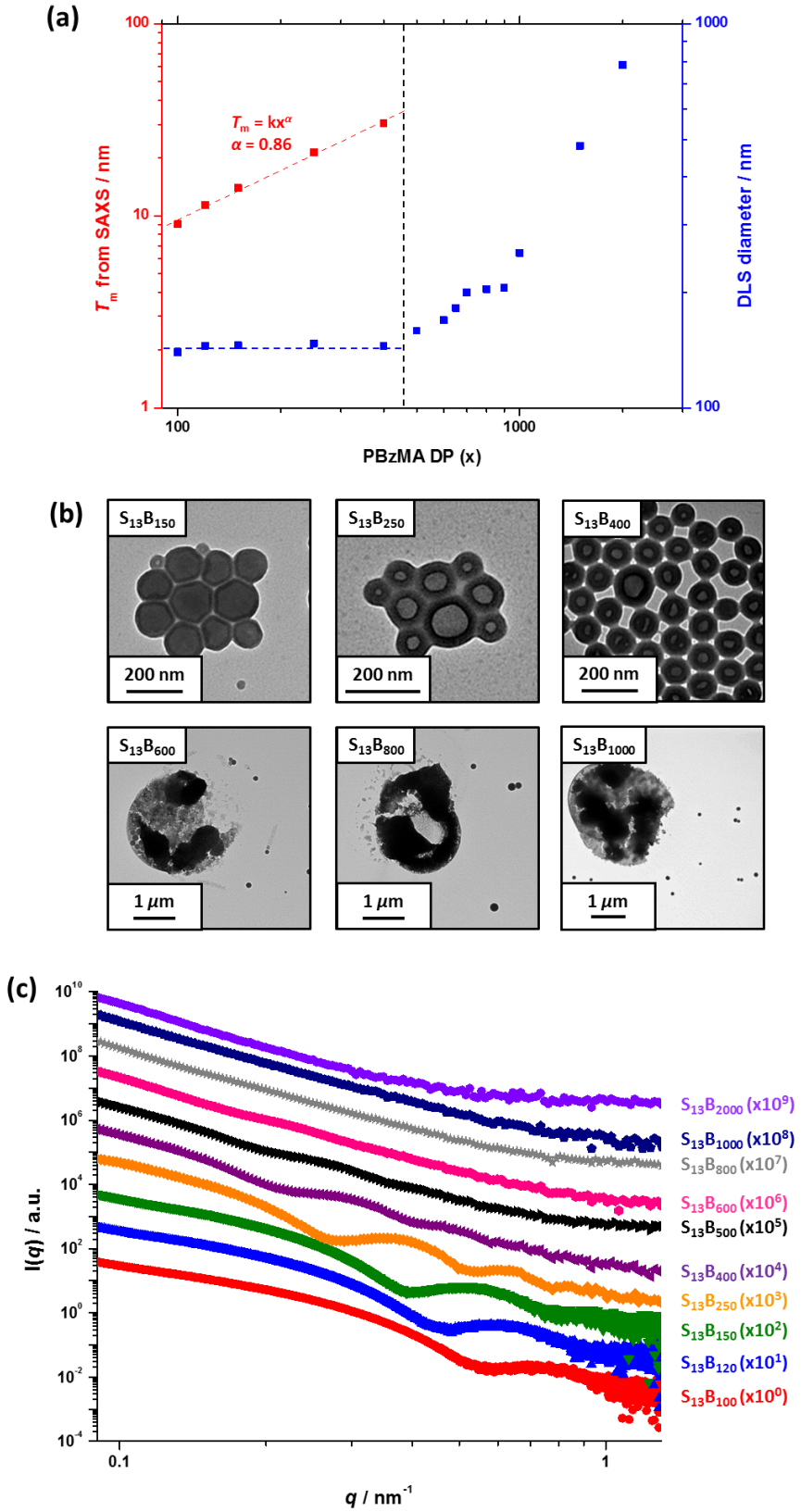

Figure 3.20. (a) T_m as judged by *post mortem* SAXS (red data) and DLS diameter (blue data), (b) transmission electron micrographs obtained for 0.1% w/w dispersions, and (c) SAXS patterns obtained for 1.0% w/w dispersions for selected $PSMA_{13}$-$PBzMA_x$ (denoted $S_{13}B_x$) nanoparticles synthesised at 10% w/w solids.

3.3.8. Arrangement of copolymer chains within PSMA$_{13}$-PBzMA$_{150}$ vesicles

In the case of vesicles, different equations are required for the calculation of the number of copolymer chains per vesicle (N_v), S_{agg} and d_{int}, as indicated below (see Equations 3.10, *3.11* and 3.12). By definition, the volume fraction of BzMA *monomer* within the core domain (φ_{BzMA}) at full conversion must be zero. Moreover, the SAXS data fits suggest that the volume fraction of *solvent* within the PBzMA chains forming the vesicle membrane (x_{sol}) is close to zero. In this case, N_v for the final PSMA$_{13}$-PBzMA$_{150}$ vesicles can be calculated using Equation 3.10 below:

$$N_v = \frac{\frac{4}{3}\pi\left({R_{out}}^3 - {R_{in}}^3\right)}{V_m} \qquad 3.10$$

As for the earlier *in situ* SAXS studies conducted when targeting PSMA$_{31}$-PBzMA$_{2000}$ spheres, the leading error in the calculation of N_v is the MWD of the core-forming PBzMA block, which dictates the error in V_m. From the GPC data obtained for PSMA$_{13}$-PBzMA$_{150}$ vesicles prepared on a laboratory scale, the standard deviation in V_m was estimated to be 3.4% using the same method used for the spheres (see Section 3.2.11). S_{agg} and d_{int} are subsequently calculated using Equations *3.11* and 3.12, respectively:

$$S_{agg} = \frac{N_v}{4\pi\left({R_{out}}^2 + {R_{in}}^2\right)} \qquad 3.11$$

$$d_{int} = \sqrt{\frac{4\pi\left({R_{out}}^2 + {R_{in}}^2\right)}{N_v}} = \sqrt{\frac{1}{S_{agg}}} \qquad 3.12$$

The N_v value calculated for PSMA$_{13}$-PBzMA$_{150}$ vesicles at full conversion was 12,709 ± 432, with the corresponding S_{agg} determined to be 0.187 ± 0.006 nm^{-2} and d_{int} was 2.31 ± 0.08 nm. These data are somewhat different to those calculated for related aqueous[10] and alcoholic[7] PISA formulations, where d_{int} was (retrospectively) calculated to be 3.1-3.4 nm. However, the volume fraction of solvent within the vesicle membrane (x_{sol}) was found to be more than 0.35 in these earlier literature examples compared to zero in the present work. This suggests that the copolymer chains are

more densely packed in the current non-polar PISA formulation. Notably, the value of d_{int} calculated for these $PSMA_{13}$-$PBzMA_{150}$ vesicles is comparable to that determined for densely-packed polybutadiene-poly(L-lysine) block copolymer chains within vesicle membranes formed in saline solution (d_{int} = 2.4 nm at pH 10.3).[55] The S_{agg} and d_{int} values calculated for $PSMA_{13}$-$PBzMA_{150}$ vesicles can also be compared to those for $PSMA_{31}$-$PBzMA_{2000}$ spheres (S_{agg} = 0.039 ± 0.004 nm^{-2}, d_{int} = 5.04 ± 0.48 nm). It is evident that the copolymer chains are packed more densely within the $PSMA_{13}$-$PBzMA_{150}$ vesicles compared to the $PSMA_{31}$-$PBzMA_{2000}$ spheres. This is likely to be the result of the differing interfacial curvatures associated with each copolymer morphology, but the significant difference in target DP for the core-forming PBzMA blocks may also be a factor.

3.4. Conclusions

In summary, a range of sterically-stabilised PSMA-PBzMA diblock copolymer nanoparticles have been prepared via RAFT dispersion polymerisation in mineral oil. Improved control over the copolymer MWD is achieved compared to previously reported PISA syntheses conducted in non-polar media, with relatively narrow MWDs ($M_w/M_n \leq 1.30$) being achieved even when targeting PBzMA DPs of up to 500. As expected, only spherical nanoparticles were obtained when using relatively long $PSMA_{18}$ or $PSMA_{31}$ macro-CTAs. In both cases, a clear correlation was observed between the mean sphere diameter (as judged by DLS) and the core-forming PBzMA DP. $PSMA_{31}$–$PBzMA_x$ spheres indicated a scaling exponent of 0.50, suggesting essentially non-solvated PBzMA chains within the core-forming PBzMA block, whereas a scaling exponent of 0.61 was obtained for $PSMA_{18}$–$PBzMA_x$ spheres, suggesting a finite degree of solvation for the PBzMA chains in this case. In contrast, using a relatively short $PSMA_{13}$ macro-CTA allows the synthesis of spherical, worm-like or vesicular morphologies. Construction of a detailed phase diagram for $PSMA_{13}$-$PBzMA_x$ diblock copolymers confirmed that pure spheres, worms or vesicles could be obtained at relatively low solids concentrations. This is important, because in principle it facilitates *in situ* SAXS studies of the formation of $PSMA_{31}$-$PBzMA_{2000}$ spheres and $PSMA_{13}$-$PBzMA_{150}$ nano-objects at 10% w/w solids. However, the rate of BzMA polymerisation during such scattering experiments is significantly faster than that

observed under normal laboratory conditions. Thus the latter kinetic data sets require renormalisation to enable detailed analysis of the *in situ* SAXS data. When targeting $PSMA_{31}$-$PBzMA_{2000}$ spheres, a systematic increase in core diameter (D_s) and mean aggregation number per sphere (N_s) are clearly discernible during the BzMA polymerisation, with the final scattering pattern indicating the formation of near-monodisperse $PSMA_{31}$-$PBzMA_{2000}$ spheres. Interestingly, the number of copolymer chains per unit surface area (S_{agg}) decreased rapidly during the initial stages of the polymerisation until a limiting value of ~0.038 nm^{-2} is attained. This indicated that the mean distance between copolymer chains at the core-shell interface (d_{int}) at full conversion was approximately 5.0 nm. When targeting $PSMA_{13}$-$PBzMA_{150}$ vesicles, characteristic scattering patterns for the dissolved copolymer chains, intermediate spheres and worms, and the final vesicle morphology were obtained. Importantly, revisiting the phase diagram constructed for this formulation enabled validation of the renormalisation protocol adopted for the kinetic data. More specifically, the mean PBzMA DPs corresponding to the various phase boundaries were in relatively good agreement with those DPs assigned to the corresponding pure phases indicated by analysis of the *in situ* SAXS patterns. Within the mixed phase space, it was shown that vesicles are formed from worms via octopi and jellyfish intermediates as first reported for an aqueous PISA formulation. Combined DLS, TEM and SAXS studies indicate that the overall vesicle dimensions remain relatively constant as the vesicle membrane gradually thickens with increasing PBzMA DP. These observations indicate an 'inward growth' mechanism, as recently reported for an aqueous PISA formulation. This suggests a *generic* vesicle growth mechanism is most likely applicable for all PISA syntheses.

3.5. References

1. O. Glatter and O. Kratky, *Small-angle X-ray Scattering*, Academic Press: London, 1982.
2. H. Schnablegger and Y. Singh, *The SAXS Guide: Getting Acquainted with the Principles, 2nd Edition*, Anton Paar GmbH, Graz, 2011.
3. A. Blanazs, R. Verber, O. O. Mykhaylyk, A. J. Ryan, J. Z. Heath, C. W. I. Douglas and S. P. Armes, *Journal of the American Chemical Society*, 2012, **134**, 9741-9748.
4. V. J. Cunningham, L. P. D. Ratcliffe, A. Blanazs, N. J. Warren, A. J. Smith, O. O. Mykhaylyk and S. P. Armes, *Polymer Chemistry*, 2014, **5**, 6307-6317.

5. L. A. Fielding, J. A. Lane, M. J. Derry, O. O. Mykhaylyk and S. P. Armes, *Journal of the American Chemical Society*, 2014, **136**, 5790-5798.
6. M. K. Kocik, O. O. Mykhaylyk and S. P. Armes, *Soft Matter*, 2014, **10**, 3984-3992.
7. C. Gonzato, M. Semsarilar, E. R. Jones, F. Li, G. J. P. Krooshof, P. Wyman, O. O. Mykhaylyk, R. Tuinier and S. P. Armes, *Journal of the American Chemical Society*, 2014, **136**, 11100-11106.
8. N. J. Warren, O. O. Mykhaylyk, D. Mahmood, A. J. Ryan and S. P. Armes, *Journal of the American Chemical Society*, 2014, **136**, 1023-1033.
9. C. J. Mable, N. J. Warren, K. L. Thompson, O. O. Mykhaylyk and S. P. Armes, *Chemical Science*, 2015, **6**, 6179-6188.
10. N. J. Warren, O. O. Mykhaylyk, A. J. Ryan, M. Williams, T. Doussineau, P. Dugourd, R. Antoine, G. Portale and S. P. Armes, *Journal of the American Chemical Society*, 2015, **137**, 1929-1937.
11. A. P. Lopez-Oliva, N. J. Warren, A. Rajkumar, O. O. Mykhaylyk, M. J. Derry, K. E. B. Doncom, M. J. Rymaruk and S. P. Armes, *Macromolecules*, 2015, **48**, 3547-3555.
12. Y. Kang, A. Pitto-Barry, H. Willcock, W. D. Quan, N. Kirby, A. M. Sanchez and R. K. O'Reilly, *Polymer Chemistry*, 2015, **6**, 106-117.
13. X. W. Zhang, S. Boisse, C. Bui, P. A. Albouy, A. Brulet, M. H. Li, J. Rieger and B. Charleux, *Soft Matter*, 2012, **8**, 1130-1141.
14. E. R. Jones, O. O. Mykhaylyk, M. Semsarilar, M. Boerakker, P. Wyman and S. P. Armes, *Macromolecules*, 2016, **49**, 172-181.
15. C. J. Mable, R. R. Gibson, S. Prevost, B. E. McKenzie, O. O. Mykhaylyk and S. P. Armes, *Journal of the American Chemical Society*, 2015, **137**, 16098-16108.
16. A. Blanazs, J. Madsen, G. Battaglia, A. J. Ryan and S. P. Armes, *Journal of the American Chemical Society*, 2011, **133**, 16581-16587.
17. D. J. Tobler and L. G. Benning, *Geochimica Et Cosmochimica Acta*, 2013, **114**, 156-168.
18. D. Hermida-Merino, G. Portale, P. Fields, R. Wilson, S. P. Bassett, J. Jennings, M. Dellar, C. Gommes, S. M. Howdle, B. C. M. Vrolijk and W. Bras, *Review of Scientific Instruments*, 2014, **85**, 093905.
19. R. H. Utama, M. Dulle, S. Foerster, M. H. Stenzel and P. B. Zetterlund, *Macromol. Rapid Commun.*, 2015, DOI: 10.1002/marc.201500096, Ahead of Print.
20. T. Hasell, K. J. Thurecht, R. D. W. Jones, P. D. Brown and S. M. Howdle, *Chemical Communications*, 2007, 3933-3935.
21. K. J. Thurecht, A. M. Gregory, W. Wang and S. M. Howdle, *Macromolecules*, 2007, **40**, 2965-2967.
22. M. Zong, K. J. Thurecht and S. M. Howdle, *Chemical Communications*, 2008, 5942-5944.
23. A. M. Gregory, K. J. Thurecht and S. M. Howdle, *Macromolecules*, 2008, **41**, 1215-1222.
24. H. Lee, E. Terry, M. Zong, N. Arrowsmith, S. Perrier, K. J. Thurecht and S. M. Howdle, *Journal of the American Chemical Society*, 2008, **130**, 12242-12243.
25. N. A. Birkin, N. J. Arrowsmith, E. J. Park, A. P. Richez and S. M. Howdle, *Polymer Chemistry*, 2011, **2**, 1293-1299.

26. J. Jennings, M. Beija, A. P. Richez, S. D. Cooper, P. E. Mignot, K. J. Thurecht, K. S. Jack and S. M. Howdle, *Journal of the American Chemical Society*, 2012, **134**, 4772-4781.
27. N. A. Birkin, O. J. Wildig and S. M. Howdle, *Polymer Chemistry*, 2013, **4**, 3791-3799.
28. J. Jennings, M. Beija, J. T. Kennon, H. Willcock, R. K. O'Reilly, S. Rimmer and S. M. Howdle, *Macromolecules*, 2013, **46**, 6843-6851.
29. J. S. Trent, *Macromolecules*, 1984, **17**, 2930-2931.
30. M. Basham, J. Filik, M. T. Wharmby, P. C. Y. Chang, B. El Kassaby, M. Gerring, J. Aishima, K. Levik, B. C. A. Pulford, I. Sikharulidze, D. Sneddon, M. Webber, S. S. Dhesi, F. Maccherozzi, O. Svensson, S. Brockhauser, G. Naray and A. W. Ashton, *Journal of Synchrotron Radiation*, 2015, **22**, 853-858.
31. J. Ilavsky and P. R. Jemian, *Journal of Applied Crystallography*, 2009, **42**, 347-353.
32. P. Cacioli, D. G. Hawthorne, R. L. Laslett, E. Rizzardo and D. H. Solomon, *Journal of Macromolecular Science-Chemistry*, 1986, **23**, 839-852.
33. M. Rodlert, E. Harth, I. Rees and C. J. Hawker, *Journal of Polymer Science Part A-Polymer Chemistry*, 2000, **38**, 4749-4763.
34. L. A. Fielding, M. J. Derry, V. Ladmiral, J. Rosselgong, A. M. Rodrigues, L. P. D. Ratcliffe, S. Sugihara and S. P. Armes, *Chemical Science*, 2013, **4**, 2081-2087.
35. L. Houillot, C. Bui, C. Farcet, C. Moire, J.-A. Raust, H. Pasch, M. Save and B. Charleux, *ACS Applied Materials & Interfaces*, 2010, **2**, 434-442.
36. L. Houillot, C. Bui, M. Save, B. Charleux, C. Farcet, C. Moire, J.-A. Raust and I. Rodriguez, *Macromolecules*, 2007, **40**, 6500-6509.
37. J. A. Raust, L. Houillot, M. Save, B. Charleux, C. Moire, C. Farcet and H. Pasch, *Macromolecules*, 2010, **43**, 8755-8765.
38. F. S. Bates and G. H. Fredrickson, *Annual Review of Physical Chemistry*, 1990, **41**, 525-557.
39. S. Forster, M. Zisenis, E. Wenz and M. Antonietti, *Journal of Chemical Physics*, 1996, **104**, 9956-9970.
40. G. Battaglia and A. J. Ryan, *Journal of the American Chemical Society*, 2005, **127**, 8757-8764.
41. N. J. Warren and S. P. Armes, *Journal of the American Chemical Society*, 2014, **136**, 10174-10185.
42. J. S. Pedersen, *Journal of Chemical Physics*, 2001, **114**, 2839-2846.
43. J. S. Pedersen and M. C. Gerstenberg, *Macromolecules*, 1996, **29**, 1363-1365.
44. J. S. Pedersen and P. Schurtenberger, *Macromolecules*, 1996, **29**, 7602-7612.
45. J. S. Pedersen, *Journal of Applied Crystallography*, 2000, **33**, 637-640.
46. S. Förster and C. Burger, *Macromolecules*, 1998, **31**, 879-891.
47. S. J. Tseng, C.-C. Chien, Z.-X. Liao, H.-H. Chen, Y.-D. Kang, C.-L. Wang, Y. Hwu and G. Margaritondo, *Soft Matter*, 2012, **8**, 1420-1427.
48. M. H. Qiao, F. Q. Yan, W. S. Sim, J. F. Deng and G. Q. Xu, *Surface Science*, 2000, **460**, 67-73.
49. M. A. Winnik, R. Lukas, W. F. Chen, P. Furlong and M. D. Croucher, *Makromolekulare Chemie-Macromolecular Symposia*, 1987, **10**, 483-501.
50. Y. Su, X. Xiao, S. Li, M. Dan, X. Wang and W. Zhang, *Polymer Chemistry*, 2014, **5**, 578-587.

51. S. Sugihara, A. Blanazs, S. P. Armes, A. J. Ryan and A. L. Lewis, *Journal of the American Chemical Society*, 2011, **133**, 15707-15713.
52. E. R. Jones, M. Semsarilar, A. Blanazs and S. P. Armes, *Macromolecules*, 2012, **45**, 5091-5098.
53. M. Semsarilar, E. R. Jones, A. Blanazs and S. P. Armes, *Advanced Materials*, 2012, **24**, 3378-3382.
54. Y. Li and S. P. Armes, *Angewandte Chemie-International Edition*, 2010, **49**, 4042-4046.
55. R. Sigel, M. Łosik and H. Schlaad, *Langmuir*, 2007, **23**, 7196-7199.

4. A Vesicle-to-Worm Transition for Block Copolymer Vesicles Prepared by RAFT Dispersion Polymerisation Enables High-Temperature Thickening of Automotive Engine Oils

4.1. Introduction

Small molecule amphiphiles such as surfactants are well-known to self-assemble into spherical micelles,[1] worm-like micelles,[2, 3] lamellae or vesicles.[4, 5] In 1976, Israelachvili and co-workers introduced the concept of a geometric packing parameter for surfactants,[6] thus allowing the morphology to be predicted based on the relative volume fractions of the hydrophilic and hydrophobic components. In 1995, Eisenberg and co-workers[7] reported the first examples of block copolymer vesicles using highly asymmetric polystyrene-poly(acrylic acid) (PS-PAA) block copolymers. Here, self-assembly was achieved via the addition of water, a non-solvent for PS, to a dilute copolymer solution in DMF. Bates and co-workers reported the formation of well-defined block copolymer worms in aqueous solution using poly(ethylene oxide)-polybutadiene diblock copolymers.[8] Antonietti and Förster subsequently extended the packing parameter concept to include block copolymer spheres, cylinders and vesicles.[9]

More recently, polymerisation-induced self-assembly (PISA) has provided a versatile and convenient route for the synthesis of block copolymer spheres, worms or vesicles at relatively high copolymer concentrations in aqueous,[10-12] alcoholic[13-15] and non-polar[16-18] media. TEM studies have shed new light on the nature of the worm-to-vesicle transition that can occur during PISA syntheses, which proceeds via 'octopi' and 'jellyfish' intermediates.[19, 20] These studies were conducted on aqueous[19] and alcoholic[20] PISA formulations, and the work discussed in Chapter 3 highlights that such intermediates are also observed in a non-polar PISA formulation. This therefore suggests that the mechanism for the transformation from worms to vesicles may be universal. Specific PISA formulations have also enabled the rational synthesis of low-polydispersity vesicles, where a binary mixture of relatively long and relatively short stabilising poly(methacrylic acid) (PMAA) macro-CTAs was used during the alcoholic RAFT dispersion polymerisation of benzyl methacrylate (BzMA).[21] Under these conditions, the shorter stabilising chains preferentially occupy the inner membrane surface and hence vesicles with narrow size distributions were produced. Additionally, Warren et al.[22] studied the mechanism of vesicle growth upon targeting poly(glycerol monomethacrylate)-poly(2-hydroxypropyl methacrylate) (PGMA-

PHPMA) vesicles with varying core-forming PHPMA DPs. SAXS studies indicated that the overall vesicle diameter remained relatively constant with increasing PHPMA DPs, whereas there was a monotonic increase in vesicle membrane thickness (T_m) over the same DP range. This 'inward growth' mechanism was hypothesised and experimentally shown for the $PSMA_{13}$-$PBzMA_x$ diblock copolymer vesicles discussed in Chapter 3. Thus it seems that this mechanism is observed for all PISA formulations.

For PGMA-PHPMA worms formed during aqueous PISA, a post-polymerisation worm-to-sphere transition is observed for PGMA-PHPMA diblock copolymer nanoparticles upon *cooling*, since the core-forming PHPMA block becomes more hydrated at lower temperatures.[23] This phenomenon has previously been observed for alternative diblock copolymers with PHPMA cores.[24] In contrast, worm-to-sphere transitions are observed on *heating* certain alcoholic and non-polar PISA formulations.[18, 25, 26] In both cases, the ingress of solvent into the cores causes surface plasticisation, which increases the effective volume fraction of the stabiliser block relative to the core-forming block and hence triggers the morphological transition. At copolymer concentrations above the critical gelation concentration (CGC), such worm-to-sphere transitions lead to degelation, because the multiple inter-particle contacts formed by the anisotropic worms cannot be maintained by the isotropic spherical nanoparticles.[18, 23, 25, 26]

In the present study, a thermally-triggered vesicle-to-worm transition for poly(stearyl methacrylate)-poly(benzyl methacrylate) (PSMA-PBzMA) diblock copolymer nanoparticles in mineral oil is identified. SAXS, rheology and ^{1}H NMR studies indicate that this morphological transition occurs at elevated temperatures, similar to that previously described for the temperature-dependent worm-to-sphere transition for poly(lauryl methacrylate)-poly(benzyl methacrylate) (PLMA-PBzMA) diblock copolymer nanoparticles.[26] Since worms are known to form free-standing gels at sufficiently high concentrations (i.e. above the CGC),[23, 26] this vesicle-to-worm transition in mineral oil offers a unique high-temperature oil-thickening mechanism. Such behaviour is widely perceived as a 'holy grail' for the automotive engine oil

sector, since it should widen the operating temperature range of oils, offering improved lubrication and fuel economy.[27]

4.2. Experimental

4.2.1. Materials

Monomers were purchased from Sigma-Aldrich (UK) and passed through basic alumina prior to use to remove inhibitor. *Tert*-butyl peroxy-2-ethylhexanoate (T21s) initiator was purchased from AkzoNobel (The Netherlands). Cumyl dithiobenzoate (CDB), $CDCl_3$ and all other reagents were purchased from Sigma-Aldrich (UK) and were used as received, unless otherwise noted. THF and toluene were purchased from Fisher Scientific (UK), CD_2Cl_2 and d_{26}-dodecane were purchased from Goss Scientific (UK) and industrial mineral oil was provided by Lubrizol Corporation Ltd.

4.2.2. Synthesis of poly(stearyl methacrylate) (PSMA) macromolecular chain transfer agent (macro-CTA)

The $PSMA_{13}$ macro-CTA used in the present work was synthesised as follows: A 250 mL round-bottomed flask was charged with stearyl methacrylate (SMA; 30.6 g; 90.4 mmol), cumyl dithiobenzoate (CDB; 4.93 g, 18.1 mmol), 2,2'-azobisisobutyronitrile (AIBN; 594 mg, 3.62 mmol; [CDB]/[AIBN] molar ratio = 5.0) and toluene (54.2 g). The sealed reaction vessel was purged with nitrogen and placed in a pre-heated oil bath at 70 °C for 10 h. The resulting PSMA (SMA conversion = 76%; M_n = 4,900 g mol^{-1}, M_w = 5,700 g mol^{-1}, M_w/M_n = 1.17) was purified by twice precipitating into excess ethanol. The mean degree of polymerisation (DP) of this macro-CTA was calculated to be 13 using ^{1}H NMR spectroscopy by comparing the integrated signals corresponding to the CDB aromatic protons at 7.0-7.5 ppm with that assigned to the two oxymethylene protons of PSMA at 3.4-4.2 ppm.

4.2.3. Synthesis of poly(stearyl methacrylate)-poly(benzyl methacrylate) (PSMA-PBzMA) diblock copolymer vesicles

A typical RAFT non-polar dispersion polymerisation synthesis of $PSMA_{13}$-$PBzMA_{96}$ diblock copolymer vesicles at 10% w/w solids was carried out as follows: A 50 mL round-bottomed flask was charged with benzyl methacrylate (BzMA; 1.89 g; 10.7

mmol), T21s initiator (4.62 mg; 21.4 μmol; dissolved at 10.0% v/v in mineral oil), $PSMA_{13}$ macro-CTA (0.5 g; 107 μmol; [$PSMA_{13}$]/[T21s] molar ratio = 5.0) and mineral oil (21.5 g). The reaction mixture purged with nitrogen gas for 30 min and the deoxygenated solution was then placed in a pre-heated oil bath at 90 °C for 5 h (final BzMA conversion = 97 %; M_n = 16,600 g mol^{-1}, M_w/M_n = 1.16).

4.2.4. Gel permeation chromatography (GPC)

Molecular weight distributions (MWDs) were assessed by GPC using THF eluent at 30 °C. The THF GPC system was equipped with two 5 μm (30 cm) Mixed C columns and a WellChrom K-2301 refractive index detector operating at 950 ± 30 nm. The mobile phase contained 2.0% v/v triethylamine and 0.05% w/v butylhydroxytoluene (BHT) with a toluene flow rate marker and the flow rate was fixed at 1.0 mL min^{-1}. A series of ten near-monodisperse poly(methyl methacrylate) standards (M_p values ranging from 645 to 2,480,000 g mol^{-1}) were used for calibration.

4.2.5. ^{1}H Nuclear Magnetic Resonance (NMR) spectroscopy

^{1}H NMR spectra were recorded in either CD_2Cl_2 or $CDCl_3$ using a Bruker AV1-400 or AV1-250 MHz spectrometer. Typically 64 scans were averaged per spectrum. For variable temperature ^{1}H NMR studies, the 10% w/w dispersion of $PSMA_{13}$-$PBzMA_{96}$ vesicles in mineral oil was centrifuged for at 13,000 rpm (16,060 g) for 1 h. The sedimented vesicles were then redispersed and the centrifugation step was repeated until 3 cycles were completed. Finally, the sedimented vesicles were redispersed using d_{26}-dodecane to produce a 5.0% w/w dispersion. ^{1}H NMR spectra were recorded at various temperatures ranging from 25 to 150 °C (64 scans per spectrum) using a Bruker Avance III 400 (NanoBay) spectrometer fitted with a ^{1}H-X broadband observe probe. These variable temperature ^{1}H NMR studies were conducted by Dr. Geoff Akien (Lancaster University), for which he is thanked.

4.2.6. Dynamic light scattering (DLS)

DLS studies were performed at 25 °C using a Zetasizer Nano-ZS instrument (Malvern Instruments, UK) at a fixed scattering angle of 173°. Copolymer dispersions were diluted to 0.10% w/w solids in *n*-dodecane prior to light scattering studies. The

intensity-average diameter and polydispersity of the diblock copolymer particles were calculated by cumulants analysis of the experimental correlation function using Dispersion Technology Software version 6.20. Data were averaged over three sets of thirteen runs each of thirty seconds duration.

4.2.7. Transmission electron microscopy (TEM)

TEM studies were conducted using a Philips CM 100 instrument operating at 100 kV and equipped with a Gatan 1 k CCD camera. Diluted block copolymer solutions (0.10% w/w) were placed on carbon-coated copper grids and exposed to ruthenium(VIII) oxide vapour for 7 min at 20 °C prior to analysis.[28] This heavy metal compound acted as a positive stain for the core-forming PBzMA block to improve contrast. The ruthenium(VIII) oxide was prepared as follows: ruthenium(IV) oxide (0.30 g) was added to water (50 g) to form a black slurry; subsequent addition of sodium periodate (2.0 g) with stirring produced a yellow solution of ruthenium(VIII) oxide within 1 min.

4.2.8. Oscillatory rheology measurements

An Anton Paar MCR502 rheometer equipped with a variable temperature Peltier plate and hood and a 50 mm 2° aluminium cone was used for all experiments. The storage (G') and loss (G'') moduli were measured as a function of temperature at a fixed strain of 1.0% and an angular frequency of 10 rad s^{-1}. During temperature ramps, the temperature was varied at 2 °C min^{-1}, with data recorded every 2.5 min, corresponding to 5 °C intervals. During time sweeps, the temperature was set at 20 °C and data were recorded every 10 min using 1.0% strain and an angular frequency of 10 rad s^{-1}. For all measurements, the distance between the cone and plate was 207 μm.

4.2.9. Small-angle X-ray scattering (SAXS)

SAXS patterns were collected at a synchrotron source (ESRF, station ID02, Grenoble, France) using monochromatic X-ray radiation (wavelength λ = 0.0995 nm, with q ranging from 0.004 to 2.5 nm^{-1}, where $q = 4\pi \sin \theta/\lambda$ is the length of the scattering vector and θ is one-half of the scattering angle) and a FReLoN Kodak CCD detector. Glass capillaries of 2 mm diameter were used as a sample holder and the sample

temperature was controlled using a heating/cooling capillary holding stage (Linkam Scientific Instruments Ltd., Tadworth, UK), with 2 min equilibration before data collection. X-ray scattering data were reduced using standard routines from the beamline and were further analysed using Irena SAS macros for Igor Pro.[29] Measurements were conducted on a 5.0% w/w dispersion of $PSMA_{13}$-$PBzMA_{96}$ particles in mineral oil.

4.3. Results and Discussion

4.3.1. Synthesis of $PSMA_{13}$-$PBzMA_{96}$ diblock copolymer vesicles

A low-polydispersity poly(stearyl methacrylate) (PSMA; mean degree of polymerisation, DP = 13) macro-CTA was chain-extended using BzMA monomer via RAFT dispersion polymerisation in mineral oil to generate well-defined $PSMA_{13}$-$PBzMA_{96}$ diblock copolymer vesicles at 10% w/w solids (see Scheme 4.1).

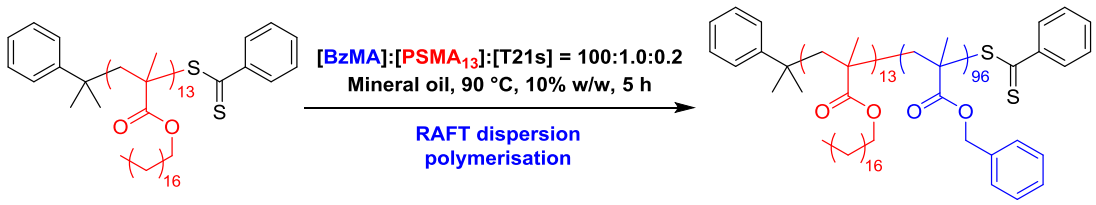

Scheme 4.1. Synthesis of poly(stearyl methacrylate)$_{13}$-poly(benzyl methacrylate)$_{96}$ ($PSMA_{13}$-$PBzMA_{96}$) vesicles via RAFT dispersion polymerisation in mineral oil at 90 °C and 10% w/w solids.

For this PISA formulation, 96% BzMA conversion was achieved within 5 h at 90 °C, as judged by ^{1}H NMR spectroscopy. THF GPC analysis confirmed that the resulting $PSMA_{13}$-$PBzMA_{96}$ diblock copolymer chains exhibited a relatively narrow unimodal molecular weight distribution (MWD, M_w/M_n = 1.17). Moreover, the clear shift in the MWD curve relative to that of the $PSMA_{13}$ macro-CTA indicated a high blocking efficiency (see Figure 4.1).

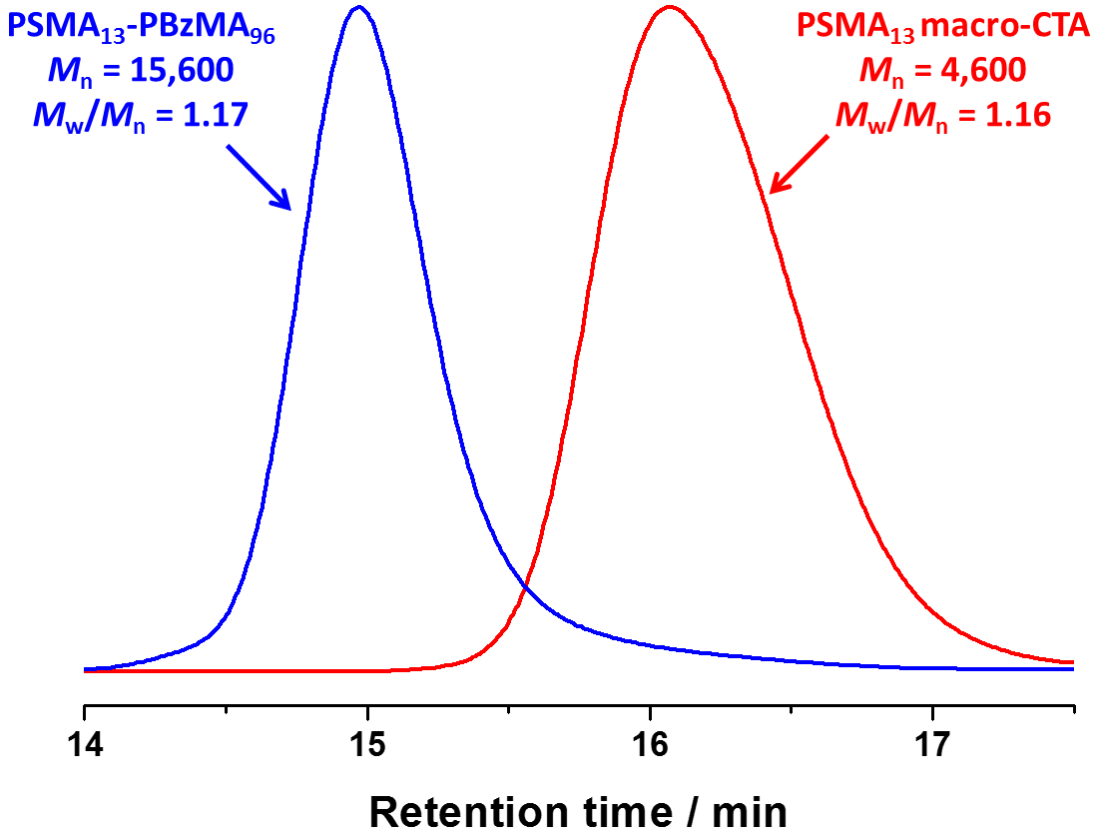

Figure 4.1. Gel permeation chromatograms (vs. poly(methyl methacrylate) standards) obtained for the vesicle-forming $PSMA_{13}$-$PBzMA_{96}$ diblock copolymers synthesised via RAFT dispersion polymerisation in mineral oil at 90 °C and 10% w/w solids (blue data). The $PSMA_{13}$ macro-CTA (prepared in toluene at 70 °C at 40% w/w solids) is also shown as a reference (red data).

4.3.2. Thermo-responsive $PSMA_{13}$-$PBzMA_{96}$ vesicles

Fielding et al. reported that PLMA-PBzMA worms prepared in *n*-dodecane undergo a worm-to-sphere transition upon heating as a result of surface plasticisation of the PBzMA core-forming block.[26] Similarly, the $PSMA_{13}$-$PBzMA_{96}$ vesicles described in this study exhibit a vesicle-to-worm morphological transition upon heating to 150 °C, as confirmed by TEM studies (see Figure 4.2). Firstly, a well-defined vesicular morphology at 20 °C was confirmed (see Figure 4.2a). DLS studies for these $PSMA_{13}$-$PBzMA_{96}$ vesicles indicated an intensity-average diameter of 140 nm. In order to observe the true nanoparticle morphology at 150 °C by TEM, a 10% w/w dispersion of $PSMA_{13}$-$PBzMA_{96}$ vesicles was equilibrated at 150 °C for 10 min and diluted with *n*-dodecane *at the same temperature* to produce a 0.10% w/w dispersion. This ensured

that the worms are retained as a kinetically-trapped morphology on cooling to 20 °C (see Figure 4.2b).

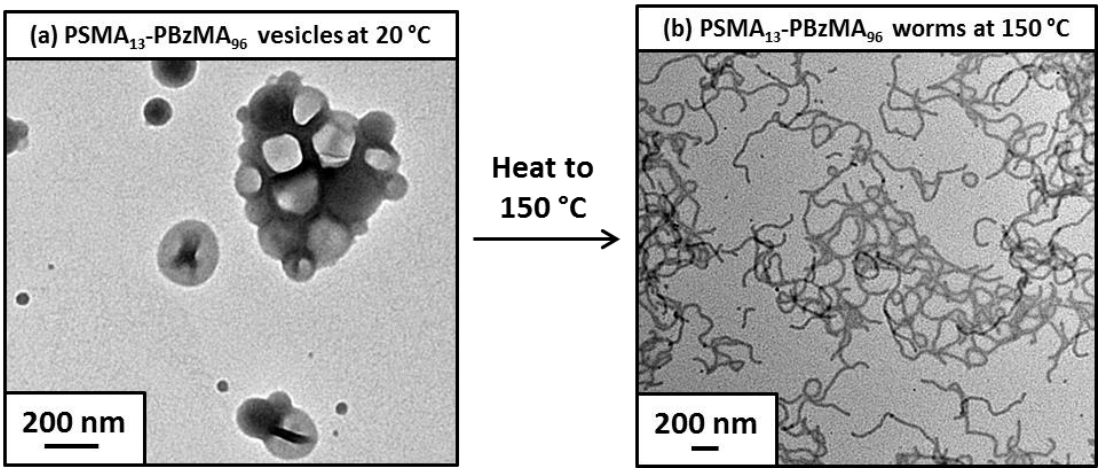

Figure 4.2. Transmission electron micrographs of 0.1% w/w dispersions of (a) $PSMA_{13}$-$PBzMA_{96}$ vesicles at 20 °C and (b) the highly anisotropic worms formed by the same concentrated vesicle dispersion after heating up to 150 °C.

The vesicle-to-worm transition was then studied by variable-temperature SAXS (Figure 4.3). Representative SAXS patterns for 5.0% w/w $PSMA_{13}$-$PBzMA_{96}$ nanoparticles in mineral oil at 20 °C (red data), 90 °C (blue data) and 130 °C (green data) are very similar, with an approximate -2 gradient at low q and two distinct local minima in the scattering pattern. The local minimum at q~0.05 nm^{-1} represents the overall vesicle dimensions, whereas that at q~0.5 nm^{-1} represents the vesicle membrane thickness (T_m). This indicated that the vesicular morphology is retained throughout this temperature range. Notably, the local minimum at high q~0.5 nm^{-1} gradually shifts to higher q, suggesting that that T_m *decreases* over this temperature range. These observations support the surface plasticisation mechanism, whereby PBzMA residues nearest the block junction become solvated on heating, which reduces the effective volume fraction of the PBzMA core-forming block relative to the PSMA stabilising block (hence reducing T_m). Upon heating to 135 °C (orange data), a shallower gradient is observed at low q and the local minimum at high q is shifted to lower q. This indicates the onset of the vesicle-to-worm transition. SAXS patterns continued to evolve on heating further, with a pure worm phase being observed at 145 °C (pink data) and 150 °C (black data). This assignment of pure

worms was based on a gradient of approximately -1 at low *q*, as well as the loss of the feature representing the overall vesicle diameter at q~0.05 nm^{-1}.

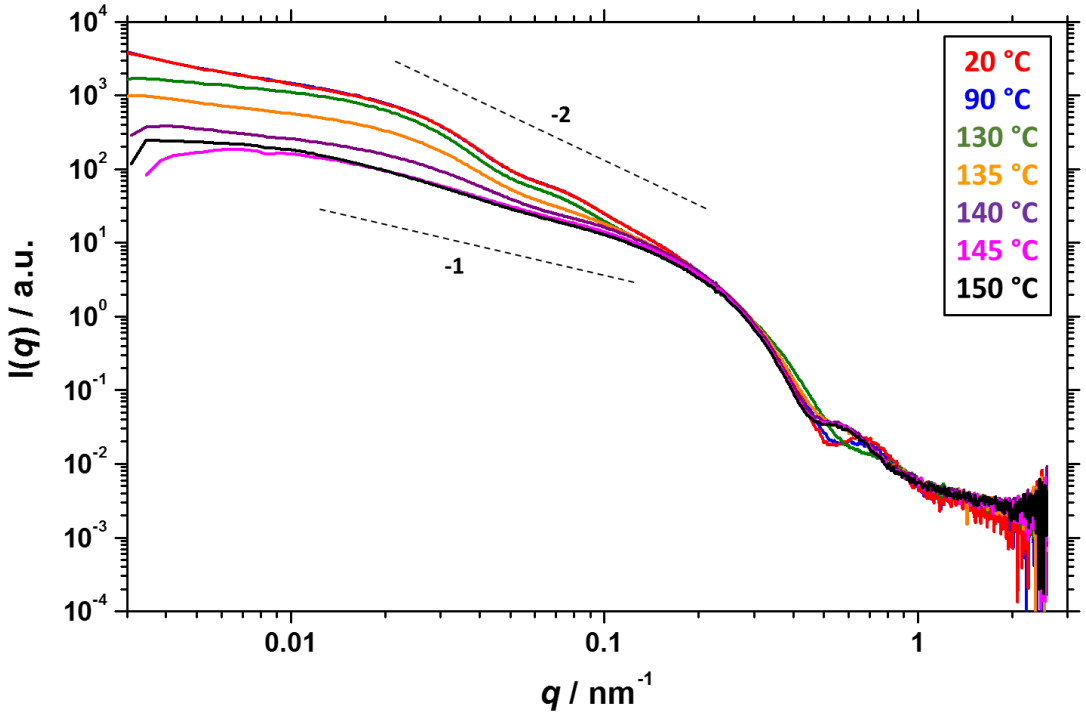

Figure 4.3. Small-angle X-ray scattering (SAXS) patterns recorded for a 5.0% w/w dispersion of $PSMA_{13}$-$PBzMA_{96}$ nanoparticles in mineral oil at various temperatures (2 min equilibration time). Gradients of -2 and -1 are also shown as a guide.

In order to confirm that the observed vesicle-to-worm transition is caused by the surface plasticisation of the core-forming PBzMA block, as reported by Fielding et al.[26] for PLMA-PBzMA nanoparticles, a variable-temperature ^1H NMR study was conducted. Firstly, the initial $PSMA_{13}$-$PBzMA_{96}$ vesicles were carefully transferred from mineral oil into d_{26}-dodecane via three centrifugation-redispersion cycles (see Experimental section). Importantly, TEM studies confirmed that the $PSMA_{13}$-$PBzMA_{96}$ vesicles survived this centrifugation-redispersion process (see Figure 4.4).

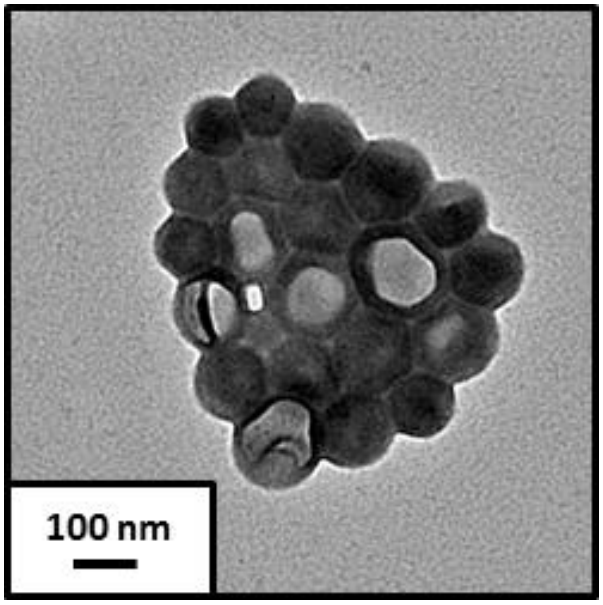

Figure 4.4. Transmission electron micrograph of $PSMA_{13}$-$PBzMA_{96}$ vesicles in *n*-dodecane after three centrifugation-redispersion cycles (centrifugation at 13,000 rpm for 60 min).

^{1}H NMR studies of a 5.0% w/w dispersion of $PSMA_{13}$-$PBzMA_{96}$ nano-objects in d_{26}-dodecane were conducted from 25 °C to 150 °C (see Figure 4.5). This aliphatic solvent was chosen because it is very similar to the mean chemical composition of the mineral oil. The benzylic proton signal at ~4.9 ppm became progressively more intense relative to the oxymethylene proton signal of the PSMA block at ~4.0 ppm, which indicates greater solvation of the PBzMA block at increasing temperatures. However, these variable-temperature ^{1}H NMR studies merely serve to confirm that the solvation of the core-forming PBzMA block increases with increasing temperature. Thus two potential mechanisms for solvation must be considered: (i) uniform solvation of the core-forming PBzMA block and (ii) surface plasticisation of the BzMA repeat units closest to the PSMA-PBzMA block junction. In order to deduce the nature of the PBzMA solvation, it is important to consider the critical packing parameter (*P*):

$$P = \frac{V}{a_0 l_c} \qquad 4.1$$

where V is the volume occupied by the core-forming block, a_o is the optimal head-group area occupied by the stabilising chains and l_c is the length of the core-forming block.

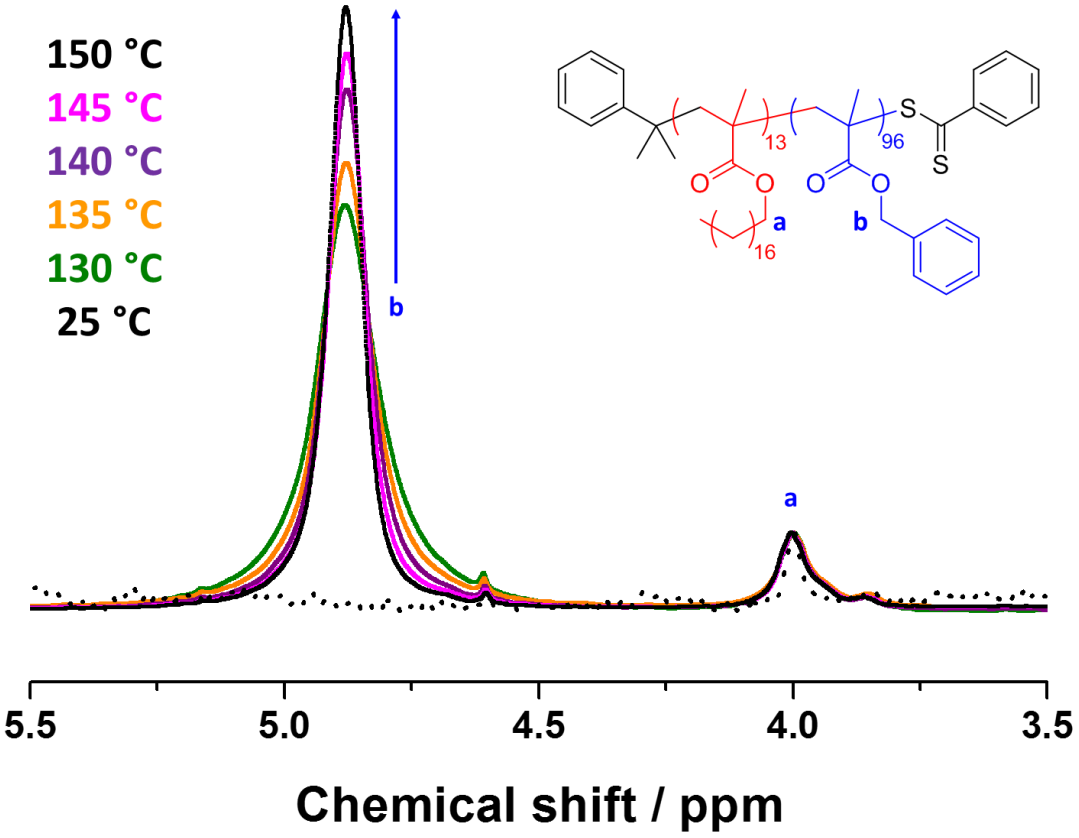

Figure 4.5. Variable-temperature ^{1}H NMR spectra recorded for 5.0% w/w $PSMA_{13}$-$PBzMA_{96}$ nanoparticles in d_{26}-dodecane. No obvious PBzMA solvation is evident at 25 °C (dotted data), whereas an increasing degree of solvation is seen upon heating from 130 °C (green data) to 150 °C (black solid data).

Since vesicles are formed when $½ \leq P \leq 1$ and worms are favoured when $⅓ \leq P \leq ½$,[6, 9] the observed vesicle-to-worm transition must correspond to a decrease in the value of P. For this reduction in P to occur, it is apparent that V (i.e. the volume of the core-forming block) must decrease. If uniform solvation of the core-forming PBzMA block were to occur at elevated temperatures, the volume of the PBzMA core-forming block would increase. Conversely, if surface plasticisation occurs and the BzMA residues closest to the PSMA-PBzMA block junction become solvated, V would decrease as shown in Figure 4.6. It can therefore be deduced that surface plasticisation caused by

the ingress of hot solvent is responsible for the observed vesicle-to-worm transition confirmed by TEM and SAXS studies.

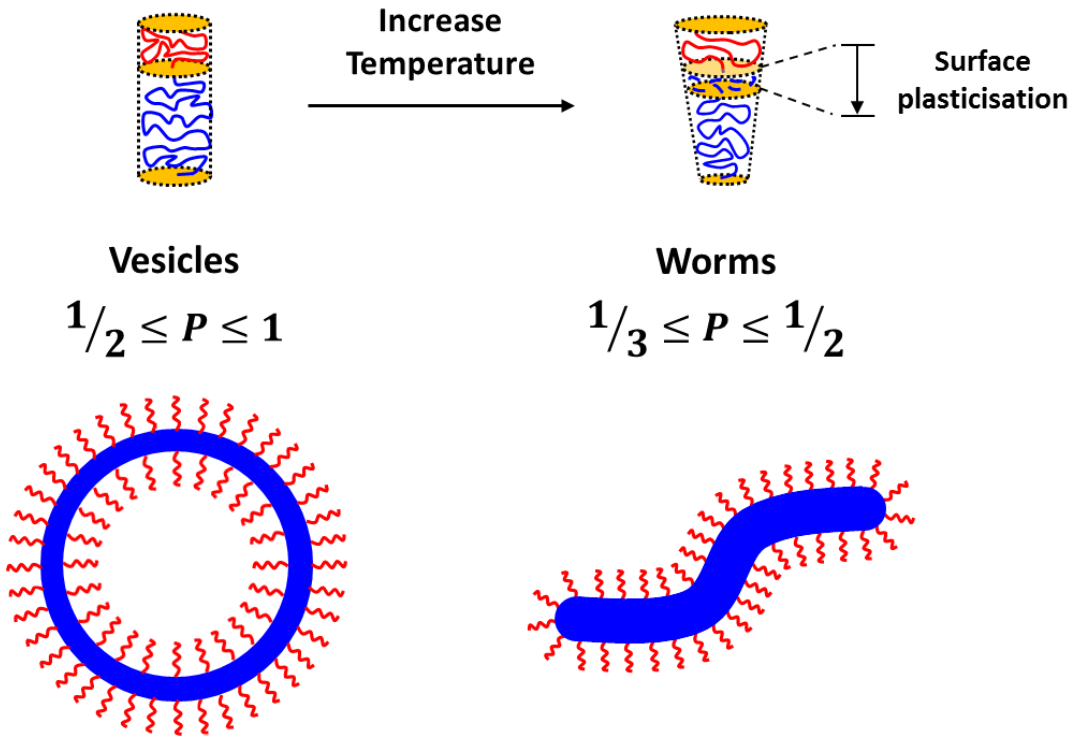

Figure 4.6. Surface plasticisation of the core-forming PBzMA block (depicted in blue) upon heating the vesicle dispersion above 135 °C results in the observed vesicle-to-worm transition for $PSMA_{13}$-$PBzMA_{96}$ nanoparticles in mineral oil.

4.3.3. Geometric considerations of the vesicle-to-worm transition

Upon fitting the SAXS patterns for $PSMA_{13}$-$PBzMA_{96}$ vesicles at 20 °C (red data, Figure 4.7) and $PSMA_{13}$-$PBzMA_{96}$ worms at 150 °C (black data, Figure 4.7), important information regarding the dimensions of each nanoparticle morphology can be determined. The local minimum at q~0.5 nm^{-1} for $PSMA_{13}$-$PBzMA_{96}$ worms at 150 °C represents a mean worm thickness (T_w) of 14.5 nm, which is larger than the T_m (8.8 nm) of the $PSMA_{13}$-$PBzMA_{96}$ vesicles observed at 20 °C.

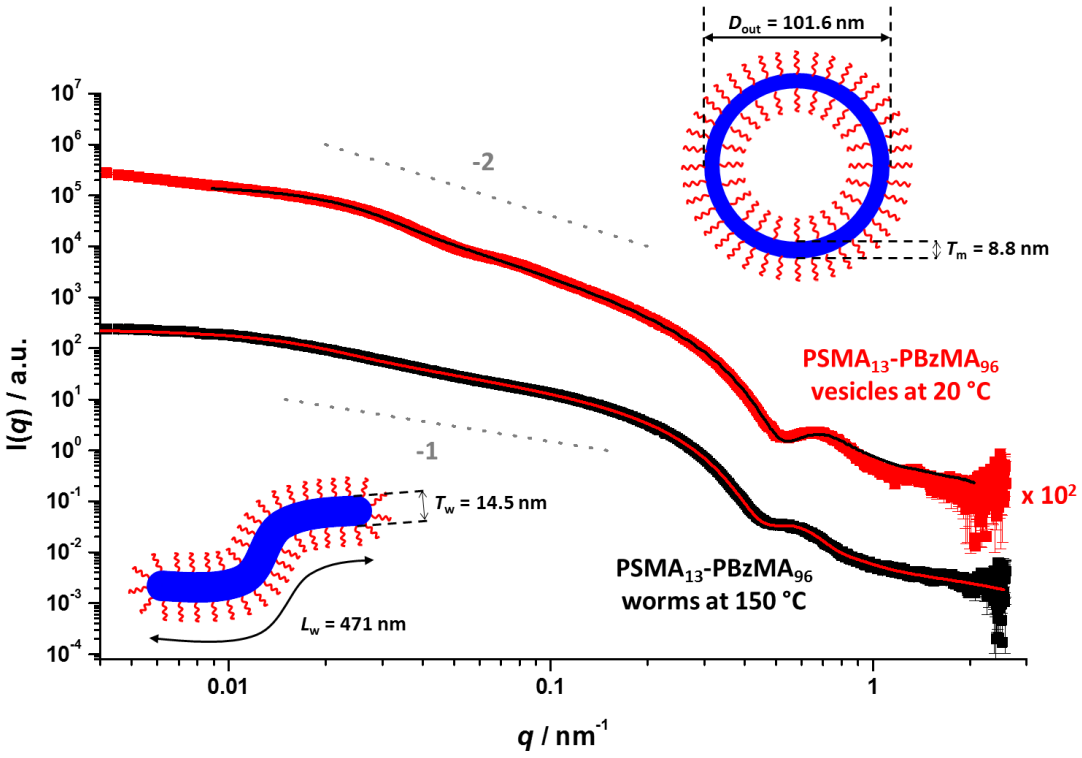

Figure 4.7. Representative SAXS patterns and fittings for a 5.0% w/w dispersion of $PSMA_{13}$-$PBzMA_{96}$ vesicles in mineral oil at 20 °C (top, red data) and $PSMA_{13}$-$PBzMA_{96}$ worms at 150 °C (bottom, black data). Cartoons illustrate the outer core diameter of the vesicle (D_{out}), vesicle membrane thickness (T_m), worm length (L_w) and worm thickness (T_w). Gradients of -2 and -1 are also shown as a guide.

Similar differences were also observed by Rank et al.[30] for poly(2-vinyl pyridine)$_{66}$-poly(ethylene oxide)$_{46}$ ($P2VP_{66}$-PEO_{46}) block copolymer vesicles, which undergo and vesicle-to-worm transition on *cooling* from 25 °C to 4 °C. The $P2VP_{66}$-PEO_{46} vesicles at 25 °C exhibited a T_m of 12 nm compared to a T_w of 16 nm for worms formed from the same diblock copolymers at 4 °C. This observation was attributed to the interdigitation of core-forming chains within the near-planar membrane. Since the copolymer chains are arranged with a higher degree of interfacial curvature within worm-like nanoparticles, they are less likely to interdigitate and the value of T_w will be larger than that of T_m (see Figure 4.8). Interdigitation has also been observed by Battaglia and Ryan[31] for poly(ethylene oxide)-poly(1,2-butylene oxide) (PEO-PBO) diblock copolymer and PEO-PBO-PEO and PBO-PEO-PBO triblock copolymer vesicles. In this work, SAXS and TEM studies were used to show that copolymer chains within the membrane do in fact interdigitate. These observations were supported by self-consistent mean field theory (SCFT) calculations described by

Matsen and Bates.[32] Here, it was demonstrated that a significant fraction of copolymer chains are able to penetrate beyond the mid-plane of the membrane (as shown in Figure 4.8a), much more than predicted by the traditional strong segregation theory.

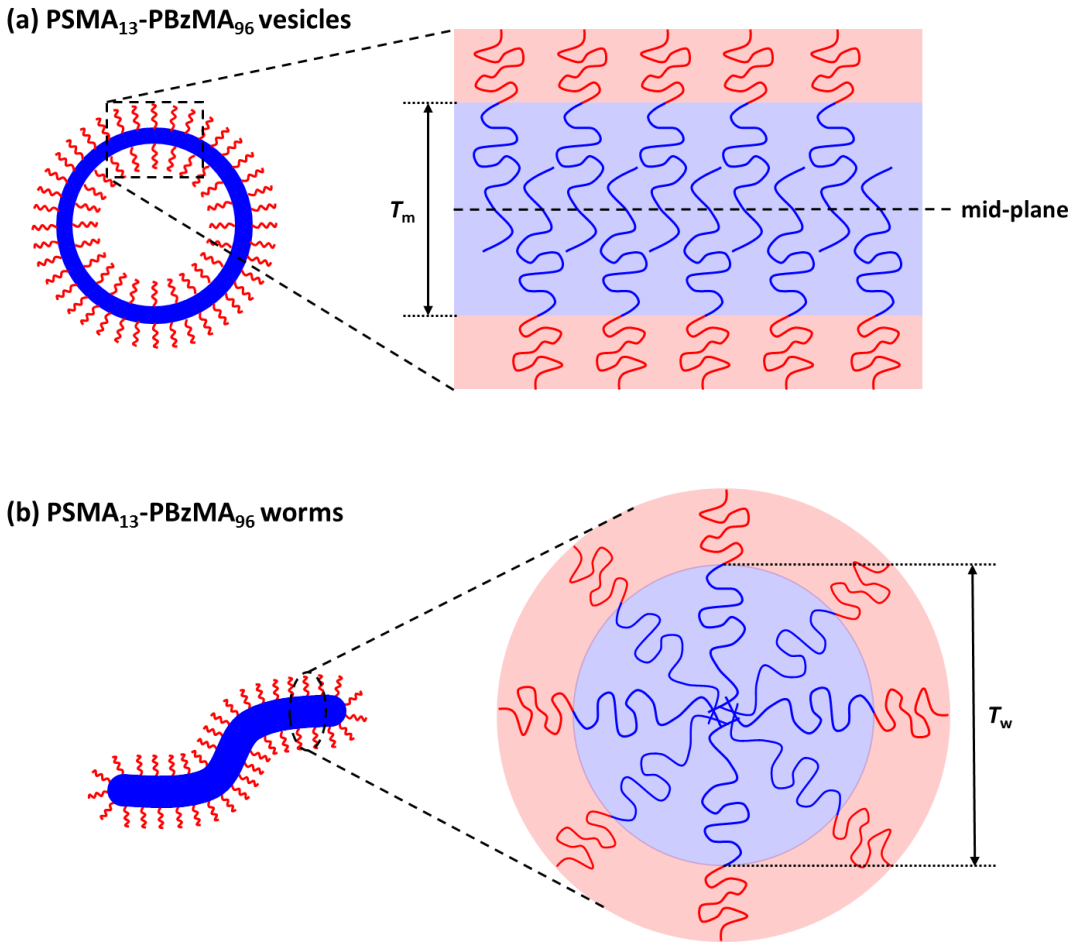

Figure 4.8. Cross-sectional representation of the probable arrangement of copolymer chains within $PSMA_{13}$-$PBzMA_{96}$ diblock copolymer (a) vesicles and (b) worms. Interdigitation is suggested within the vesicle membrane with copolymer chains penetrating beyond the mid-plane, whereas such interdigitation is less likely within the worm core. Thus, for $PSMA_{13}$-$PBzMA_{96}$ nanoparticles, the worm core thickness (T_w) is larger than the vesicle membrane thickness (T_m).

In addition to these insights into the relative thicknesses of the vesicle membrane and worm core, the average number of worms formed from one vesicle during the thermally-triggered vesicle-to-worm transition can be calculated. Firstly, the volume occupied by the vesicle membrane (V_{vm}) was calculated using the outer (D_{out}) and inner (D_{in}) core diameters of the vesicle and the membrane thickness (T_m) as follows.

$$D_{\mathrm{in}} = D_{\mathrm{out}} - 2T_{\mathrm{m}} \quad (4.2)$$

$$D_{\mathrm{in}} = 101.6\ \mathrm{nm} - (2 \times 8.8\ \mathrm{nm}) = 84.0\ \mathrm{nm} \quad (4.3)$$

$$V_{\mathrm{vm}} = V_{\mathrm{out}} - V_{\mathrm{in}} = \frac{4}{3}\pi\left[\left(\frac{D_{\mathrm{out}}}{2}\right)^3 - \left(\frac{D_{\mathrm{in}}}{2}\right)^3\right] \quad (4.4)$$

$$V_{\mathrm{vm}} = \frac{4}{3}\pi\left[\left(\frac{101.6\ \mathrm{nm}}{2}\right)^3 - \left(\frac{84.0\ \mathrm{nm}}{2}\right)^3\right] = 2.39 \times 10^5\ \mathrm{nm}^3 \quad (4.5)$$

Then, the volume of the worm core (V_{wc}) was calculated using the worm contour length (L_{w}) and the worm thickness (T_{w}) as follows:

$$V_{\mathrm{wc}} = \left[\pi\left(\frac{T_{\mathrm{w}}}{2}\right)^2 L_{\mathrm{w}}\right] + \left[\frac{4}{3}\pi\left(\frac{T_{\mathrm{w}}}{2}\right)^3\right] \quad (4.6)$$

$$V_{\mathrm{wc}} = \left[\pi\left(\frac{14.5\ \mathrm{nm}}{2}\right)^2 \times 471\ \mathrm{nm}\right] + \left[\frac{4}{3}\pi\left(\frac{14.5\ \mathrm{nm}}{2}\right)^3\right] = 7.94 \times 10^4\ \mathrm{nm}^3 \quad (4.7)$$

Upon calculating the average volume occupied by the core domain for both $PSMA_{13}$-$PBzMA_{96}$ vesicles at 20 °C and $PSMA_{13}$-$PBzMA_{96}$ worms at 150 °C, the average number of worms formed from one vesicle was calculated using the ratio of V_{vm} and V_{wc} as shown below.

$$\frac{V_{\mathrm{vm}}}{V_{\mathrm{wc}}} = \frac{2.39 \times 10^5\ \mathrm{nm}^3}{7.94 \times 10^4\ \mathrm{nm}^3} = 3.01 \quad (4.8)$$

Therefore, the average number of worms formed from one vesicle during the thermally-triggered vesicle-to-worm transition for $PSMA_{13}$-$PBzMA_{96}$ nanoparticles

dispersed in mineral oil is approximately three. This value was verified by considering the mean number of copolymer chains per nanoparticle, or the aggregation number. For $PSMA_{13}$-$PBzMA_{96}$ vesicles at 20 °C, the mean number of copolymer chains per vesicle (N_v) was calculated using V_{vm} and the volume occupied by one core-forming PBzMA block within the membrane ($V_m = (DP_{PBzMA}.M_{n,BzMA})/(N_A.\rho)$, where DP_{PBzMA} is the mean degree of polymerisation of the PBzMA block, $M_{n,BzMA}$ corresponds to the molecular weight of one BzMA unit within the PBzMA block, N_A is Avagadro's number and ρ is the density of PBzMA) as follows:

$$N_v = \frac{V_{vm}}{V_m} = \frac{2.39 \times 10^5 \text{nm}^3}{24.426 \text{ nm}^3} = 9{,}784 \qquad \textit{4.9}$$

Similarly, for $PSMA_{13}$-$PBzMA_{96}$ worms at 150 °C, the mean number of copolymer chains per worm-like nanoparticle (N_w) was calculated using V_{wc} and the volume occupied by one core-forming PBzMA block within the worm core (V_s) as follows:

$$N_w = \frac{V_{wc}}{V_s} = \frac{7.94 \times 10^4 \text{nm}^3}{24.426 \text{ nm}^3} = 3{,}130 \qquad \textit{4.10}$$

The average number of worms formed from one vesicle can therefore be determined by considering the mean number of copolymer chains per nanoparticle in each case.

$$\frac{N_v}{N_w} = \frac{9{,}784}{3{,}130} = 3.13 \qquad \textit{4.11}$$

Considering N_v and N_w for each morphology comprised of the same diblock copolymers, the average number of worms formed from vesicles is confirmed to be approximately three, thus supporting the value determined by geometry. These findings could offer important mechanistic insights into morphological transitions involving diblock copolymer nanoparticles.

4.3.4. High-temperature thickening of oils

It is well known that (i) dispersions of diblock copolymer worms form free-standing gels at sufficiently high copolymer concentrations,[8] and (ii) a thermally-triggered worm-to-sphere transition results in rapid in situ degelation.[18, 23, 25, 26] A 10% w/w dispersion of $PSMA_{13}$-$PBzMA_{96}$ vesicles in mineral oil was studied to assess the effect of the vesicle-to-worm transition on its rheological behaviour (see Figure 4.9).

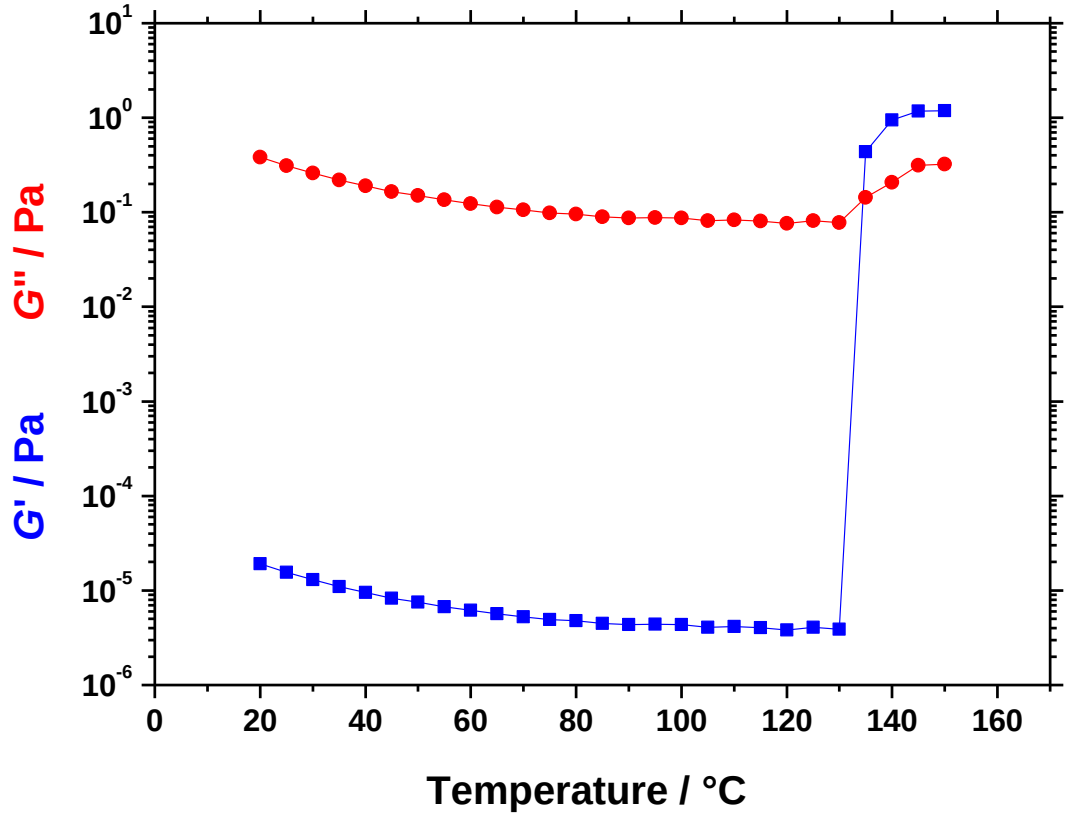

Figure 4.9. Dependence of the storage modulus (*G*', blue data) and loss modulus (*G*'', red data) of a 10% w/w dispersion of $PSMA_{13}$-$PBzMA_{96}$ nanoparticles in mineral oil upon heating from 20 °C to 150 °C. Data were recorded at 1.0% strain using an angular frequency of 10 rad s^{-1}, with a heating rate of 2 °C min^{-1}.

Initially, the dispersion of vesicles exhibits typical rheology of a free-flowing fluid, with the loss modulus (*G*'') much greater than the storage modulus (*G*'). On heating from 20 °C to 130 °C, the *G*' and *G*'' are both systematically reduced, with the value of *G*' always remaining much smaller than that for *G*''. Over this temperature range, the dynamic viscosity ($\eta' = G''/\omega$, where ω is the angular frequency) varies with

temperature as expected for Newtonian fluids, which can be approximated using the Andrade equation shown below.[33, 34]

$$log_{10}\eta' = A + \frac{B}{T} \qquad 4.12$$

Here, *T* is the temperature in K and *A* and *B* are constants. However, on further heating from 130 °C to 135 °C, *G*' increases by over five orders of magnitude from 3.89 μPa to 0.438 Pa. This dramatic increase in *G*' at 135 °C coincides with the critical gelation temperature (CGT), defined as the temperature above which the dispersion behaves as a viscoelastic gel (since *G*' now exceeds *G*''). These observations are supported by the SAXS data shown in Figure 4.3, where $PSMA_{13}$-$PBzMA_{96}$ vesicles are observed at temperatures between 20 °C and 130 °C, with the onset of the vesicle-to-worm transition identified to be at ~135 °C. The first appearance of anisotropic worm-like particles as judged by SAXS is in close agreement with the CGT determined by rheology, which strongly suggests that multiple inter-worm contacts are responsible for the observed gelation. The change in *G*'' over the same temperature range corresponds to an increase in η' from 7.77 mPa s at 130 °C to 14.4 mPa s at 135 °C and eventually 32.3 mPa s at 150 °C, an approximate four-fold increase. As far as we are aware, there are very few, if any, literature examples of significantly higher viscosities being achieved at elevated temperatures for soft matter formulations. One example is the reversible worm-to-sphere transition for PGMA-PHPMA worms in aqueous media, where spheres re-form worms upon heating from 4 °C to 25 °C.[23] Also, Pluronic F-127, a poly(ethylene oxide)-poly(propylene oxide)-poly(ethylene oxide) (PEO-PPO-PEO) ABA triblock copolymer, has also been shown to increase the viscosity of water via the formation of pseudo cross-links at elevated temperatures.[35] However, these transitions in aqueous media occur at relatively low temperatures (4 °C to 30 °C). Similar to the present work, it has been shown that ionic surfactant vesicles can form elongated micelles at increased temperatures, which also corresponds to an increase in viscosity.[36, 37] However, the viscosity was shown to go through a maximum at ~50-60 °C. The present work thus offers significant potential

for high-temperature thickening in non-aqueous media; an ongoing technical challenge in the automotive industry.

4.3.5. Reversibility of the vesicle-to-worm transition

One drawback for the vesicle-to-worm transition described in this Chapter is the fact that it is not fully reversible. On cooling to 20 °C after the thermal ramp shown in Figure 4.9, a mixed phase of vesicles and worms is observed by TEM studies (see Figure 4.10).

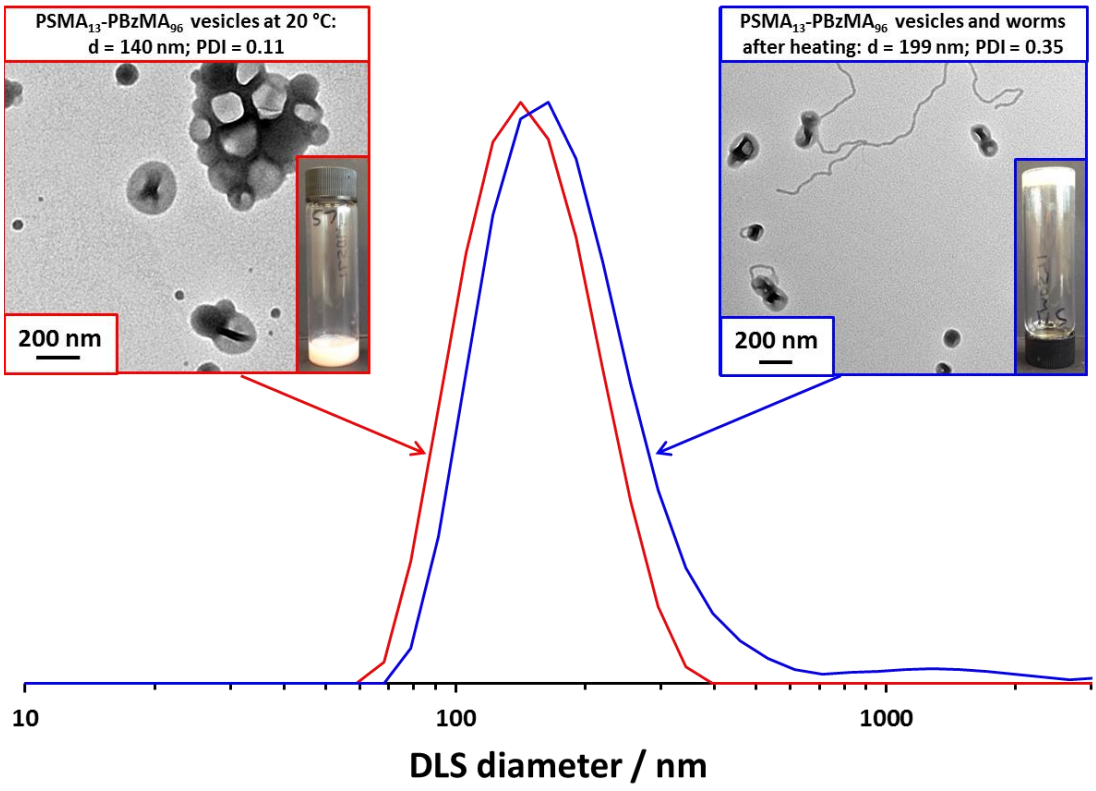

Figure 4.10. Transmission electron micrographs and particle size distributions obtained by dynamic light scattering (DLS) for a 0.10% w/w dispersion of $PSMA_{13}$-$PBzMA_{96}$ nanoparticles at 20 °C before (red data) and after (blue data) at 20-150-20 °C thermal cycle. Inset digital images show the 10% w/w dispersions of the nanoparticles at 20 °C before (red data) and after (blue data) a 20-150-20 °C thermal cycle.

This partially reversible transition also corresponded to a broadening in the particle size distribution and a shift to larger average size, presumably due to the presence of long anisotropic worms as observed by TEM studies (blue data, Figure 4.10). The physical appearance of the 10% w/w dispersions also indicated the presence of worms

after the thermal cycle, since a turbid, free-standing gel is formed compared to the free-flowing dispersion observed before the 20-150-20 °C thermal cycle (see inset digital image in Figure 4.10).

Rheological studies of the 10% w/w dispersion directly after the 20-150-20 °C thermal cycle indicated that the dispersion remained a gel (G' > G'') for 90 min (see Figure 4.11).

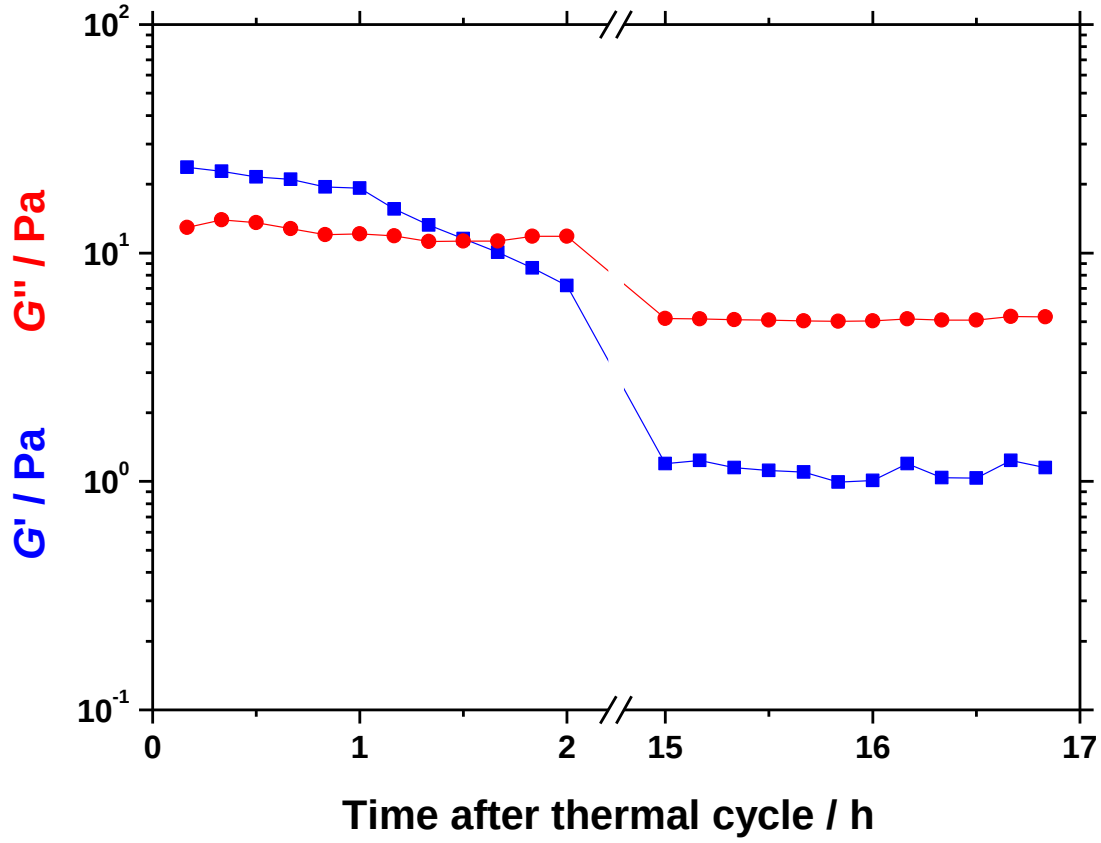

Figure 4.11. Dependence of the storage modulus (G', blue data) and loss modulus (G'', red data) of a 10% w/w dispersion of $PSMA_{13}$-$PBzMA_{96}$ nanoparticles in mineral oil at 20 °C immediately after a 20-150-20 °C thermal cycle. Data were recorded every 10 min at 1.0% strain using an angular frequency of 10 rad s^{-1}.

After this initial time period, the dispersion remained a viscous liquid for the duration of the study. Although the dispersion returned to this state, the values of G' and G'' were much higher (G' = 1.10 Pa, G'' = 5.25 Pa) than those for the original dispersion of $PSMA_{13}$-$PBzMA_{96}$ vesicles at 20 °C (G' = 19.2 μPa, G'' = 0.384 Pa). This

corresponds to an increase in η' from 38.4 mPa s to 525 mPa s, which is evidently due to the remaining $PSMA_{13}$-$PBzMA_{96}$ worms. The formation of this high-viscosity dispersion after the thermal cycle would render this particular formulation as an unviable option for high temperature viscosity modification.

4.4. Conclusions

In summary, $PSMA_{13}$-$PBzMA_{96}$ vesicles prepared directly in mineral oil via PISA undergo a vesicle-to-worm transition on heating from 20 °C to 150 °C. This order-order morphological transition was characterised using TEM, SAXS, variable temperature ^{1}H NMR spectroscopy, DLS and rheology. It is attributed to surface plasticisation of the PBzMA core-forming block, with the onset of worm formation identified to be ~135 °C by SAXS and rheology. The morphological transition is complete at 145-150 °C as confirmed by the similarity in the SAXS patterns obtained on a 5.0% w/w dispersion of $PSMA_{13}$-$PBzMA_{96}$ nanoparticles in mineral oil, where a -1 gradient at low *q* confirmed the presence of worms. This vesicle-to-worm transition offers a potential route to high-temperature thickening of engine oils, which is one of the 'holy grails' of the automotive industry. Upon heating from 20 °C to 150 °C, a sharp increase in the viscosity of a 10% w/w dispersion of $PSMA_{13}$-$PBzMA_{96}$ nanoparticles in mineral oil was observed. Interestingly, this increase in viscosity occurred at ~130-135 °C, which aligns with the onset of the vesicle-to-worm transition observed by SAXS studies. Unfortunately, this morphological transition is only partially reversible; a mixed phase of vesicles and worms was observed by TEM studies after the 20-150-20 °C thermal cycle. This directly affects the rheological properties of the 10% w/w dispersion, with a viscous fluid obtained compared to the initial low-viscosity free flowing dispersion of vesicles. Due to this partial irreversibility, the current formulation does not offer a viable route to high temperature thickening of automotive engine oils. However, there is obvious potential for such a vesicle-to-worm transition to provide significant viscosity modification over a useful temperature range for the automotive industry. Therefore, more research is warranted in order to determine whether a closely related formulation would offer full reversibility for the morphological transition and thus provide a more reliable method of reversible thickening.

4.5. References

1. H. Wennerström and B. Lindman, *Physics Reports*, 1979, **52**, 1-86.
2. J. N. Israelachvili, *Intermolecular and Surface Forces, 3rd Edition*, Academic Press, San Diego, 2011.
3. K. Trickett and J. Eastoe, *Advances in Colloid and Interface Science*, 2008, **144**, 66-74.
4. A. D. Bangham and R. W. Horne, *Journal of Molecular Biology*, 1964, **8**, 660-&.
5. A. D. Bangham, *Progress in biophysics and molecular biology*, 1968, **18**, 29-95.
6. J. N. Israelachvili, D. J. Mitchell and B. W. Ninham, *Journal of the Chemical Society-Faraday Transactions*, 1976, **72**, 1525-1568.
7. L. F. Zhang and A. Eisenberg, *Science*, 1995, **268**, 1728-1731.
8. Y. Y. Won, H. T. Davis and F. S. Bates, *Science*, 1999, **283**, 960-963.
9. M. Antonietti and S. Förster, *Advanced Materials*, 2003, **15**, 1323-1333.
10. B. Charleux, G. Delaittre, J. Rieger and F. D'Agosto, *Macromolecules*, 2012, **45**, 6753-6765.
11. M. J. Monteiro and M. F. Cunningham, *Macromolecules*, 2012, **45**, 4939-4957.
12. N. J. Warren and S. P. Armes, *Journal of the American Chemical Society*, 2014, **136**, 10174-10185.
13. M. Semsarilar, E. R. Jones, A. Blanazs and S. P. Armes, *Advanced Materials*, 2012, **24**, 3378-3382.
14. Y. Pei and A. B. Lowe, *Polymer Chemistry*, 2014, **5**, 2342-2351.
15. J.-T. Sun, C.-Y. Hong and C.-Y. Pan, *Polymer Chemistry*, 2013, **4**, 873-881.
16. L. Houillot, C. Bui, M. Save, B. Charleux, C. Farcet, C. Moire, J.-A. Raust and I. Rodriguez, *Macromolecules*, 2007, **40**, 6500-6509.
17. L. A. Fielding, M. J. Derry, V. Ladmiral, J. Rosselgong, A. M. Rodrigues, L. P. D. Ratcliffe, S. Sugihara and S. P. Armes, *Chemical Science*, 2013, **4**, 2081-2087.
18. Y. Pei, L. Thurairajah, O. R. Sugita and A. B. Lowe, *Macromolecules*, 2015, **48**, 236-244.
19. A. Blanazs, J. Madsen, G. Battaglia, A. J. Ryan and S. P. Armes, *Journal of the American Chemical Society*, 2011, **133**, 16581-16587.
20. D. Zehm, L. P. D. Ratcliffe and S. P. Armes, *Macromolecules*, 2013, **46**, 128-139.
21. C. Gonzato, M. Semsarilar, E. R. Jones, F. Li, G. J. P. Krooshof, P. Wyman, O. O. Mykhaylyk, R. Tuinier and S. P. Armes, *Journal of the American Chemical Society*, 2014, **136**, 11100-11106.
22. N. J. Warren, O. O. Mykhaylyk, A. J. Ryan, M. Williams, T. Doussineau, P. Dugourd, R. Antoine, G. Portale and S. P. Armes, *Journal of the American Chemical Society*, 2015, **137**, 1929-1937.
23. A. Blanazs, R. Verber, O. O. Mykhaylyk, A. J. Ryan, J. Z. Heath, C. W. I. Douglas and S. P. Armes, *Journal of the American Chemical Society*, 2012, **134**, 9741-9748.
24. J. Madsen, S. P. Armes, K. Bertal, S. MacNeil and A. L. Lewis, *Biomacromolecules*, 2009, **10**, 1875-1887.

25. Y. W. Pei, N. C. Dharsana, J. A. Van Hensbergen, R. P. Burford, P. J. Roth and A. B. Lowe, *Soft Matter*, 2014, **10**, 5787-5796.
26. L. A. Fielding, J. A. Lane, M. J. Derry, O. O. Mykhaylyk and S. P. Armes, *Journal of the American Chemical Society*, 2014, **136**, 5790-5798.
27. R. W. Bruce, *Handbook of Lubrication and Tribology, Volume II: Theory and Design*, CRC Press, 2012.
28. J. S. Trent, *Macromolecules*, 1984, **17**, 2930-2931.
29. J. Ilavsky and P. R. Jemian, *Journal of Applied Crystallography*, 2009, **42**, 347-353.
30. A. Rank, S. Hauschild, S. Förster and R. Schubert, *Langmuir*, 2009, **25**, 1337-1344.
31. G. Battaglia and A. J. Ryan, *Journal of the American Chemical Society*, 2005, **127**, 8757-8764.
32. M. W. Matsen and F. S. Bates, *Macromolecules*, 1995, **28**, 8884-8886.
33. E. Andrade, *Nature*, 1930, **125**, 309-310.
34. H. A. Barnes, *A Handbook of Elementary Rheology*, The University of Wales Institute of Non-Newtonian Fluid Mechanics, Aberystwyth, 2000.
35. V. Lenaerts, C. Triqueneaux, M. Quarton, F. Riegfalson and P. Couvreur, *International Journal of Pharmaceutics*, 1987, **39**, 121-127.
36. P. A. Hassan, B. S. Valaulikar, C. Manohar, F. Kern, L. Bourdieu and S. J. Candau, *Langmuir*, 1996, **12**, 4350-4357.
37. T. S. Davies, A. M. Ketner and S. R. Raghavan, *Journal of the American Chemical Society*, 2006, **128**, 6669-6675.

5. Rheology Studies and Shear-Induced Alignment of Diblock Copolymer Worm Gels

5.1. Introduction

The synthesis of diblock copolymer worm gels has been reported for RAFT-mediated PISA formulations conducted in water,[1-6] lower alcohols[7, 8] and *n*-alkanes[9-13]. Chapter 3 described the synthesis of $PSMA_{13}$-$PBzMA_x$ diblock copolymer spheres, worms or vesicles in mineral oil and the construction of a phase diagram for this PISA formulation indicated a very narrow worm phase. Nevertheless, a pure worm morphology could be accessed at copolymer concentrations ranging from 5.0 to 20% w/w when targeting $PSMA_{13}$-$PBzMA_{65}$ diblock copolymer nanoparticles. Closely related PLMA-PBzMA worms synthesised in *n*-dodecane,[10] mineral oil or a poly(*α*-olefin) (see Chapter 2) exhibit a thermo-reversible worm-to-sphere transition on heating. This is caused by the surface plasticisation of the core-forming PBzMA block by ingress of hot solvent, which alters the relative volume fractions of the solvophobic and solvophilic blocks and thus changes the preferred diblock copolymer morphology.[10] In addition to the interesting rheological properties of diblock copolymer worms dispersed in non-polar solvents, it is well-known that anisotropic particles can be aligned when such structured gels are subjected to an applied shear.[14] In particular, shear-induced alignment of worm-like micelles has been reported for both surfactant[14-18] and block copolymer[18, 19] formulations. This shear alignment is most commonly monitored using a combination of rheology (using a Couette shear cell) with techniques such as small-angle neutron scattering (SANS)[14-17] or small-angle X-ray scattering (SAXS).[18, 19] In both cases, evidence for alignment is provided by the 2D scattering pattern. Non-aligned objects produce symmetric 2D scattering patterns due to their random orientation.[20] This is also true for isotropic spherical objects under shear, since such species cannot be aligned.[20] Conversely, shear-aligned anisotropic objects such as fibres or worm-like nanoparticles display asymmetric 2D scattering patterns (see Figure 5.1).[15, 18, 20] The long axis of the scattering pattern indicates the direction perpendicular to the alignment ($q_{\perp}$), whereas the shorter axis is parallel to the direction of alignment ($q_{\parallel}$).[18] The degree of alignment can be quantified using the anisotropy factor (Δ) of the 2D scattering pattern. Δ is defined as the ratio of the long axis (a) to the short axis (b), i.e. $\Delta = a/b$.[18] Thus, $\Delta = 1$ for a symmetric 2D scattering pattern and represents random orientation of the sample. Δ exceeds unity for anisotropic 2D scattering patterns, with larger values of Δ indicating a greater degree of alignment. However, this apparent degree of alignment may be artificially

reduced when polydisperse worms are studied, because a broader ellipsoidal 2D scattering pattern would be observed.[18]

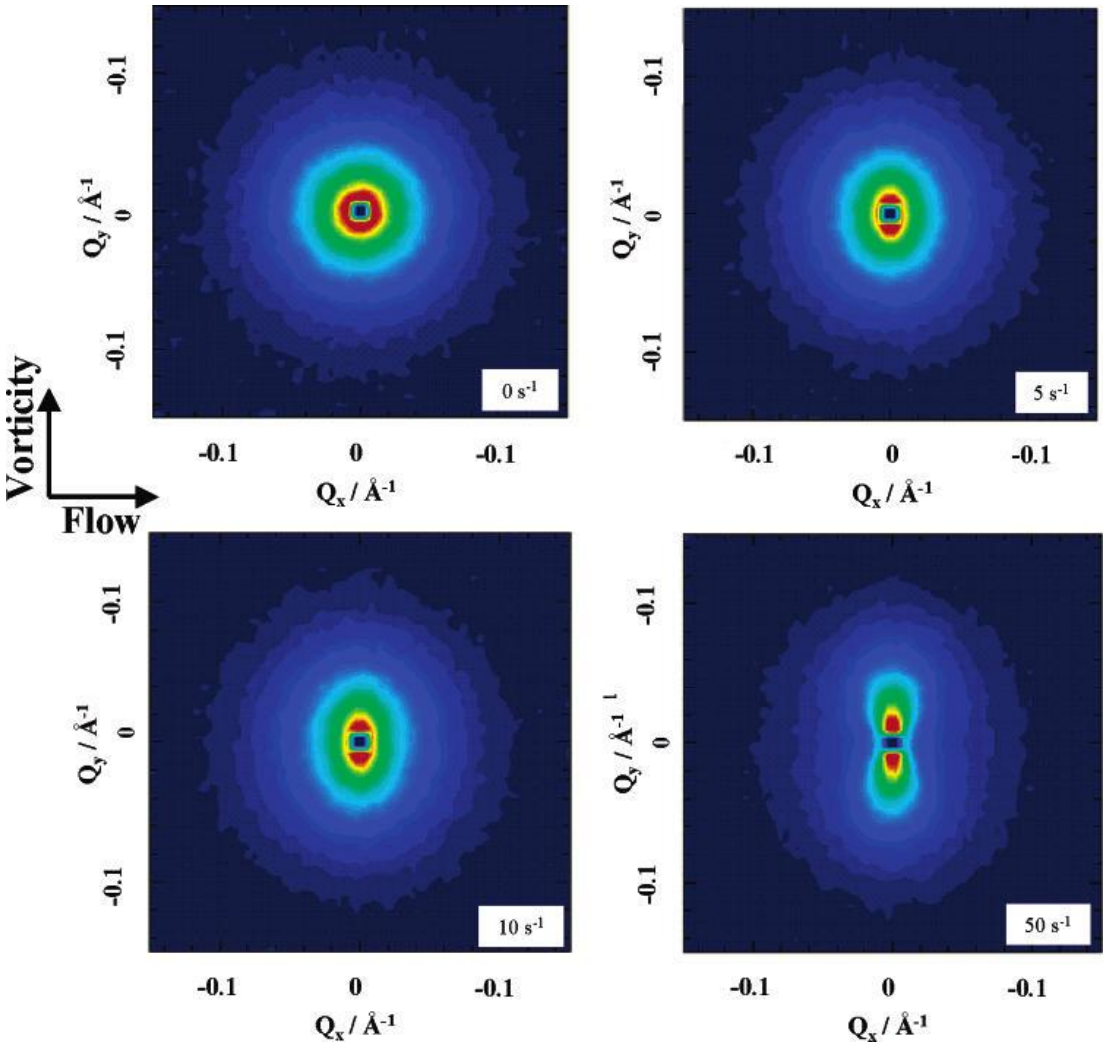

Figure 5.1. 2D scattering patterns obtained for a 4.5% w/w dispersion of erucyl bis(hydroxyethyl) methylammonium chloride worm-like surfactant micelles in the presence of 6.0% w/w KCl at shear rates of 0, 5, 10 and 50 s^{-1}. Symmetrical scattering is observed in the absence of shear, but higher shear rates result in a greater degree of anisotropy in the 2D scattering pattern.[15]

Above a certain critical shear rate, worm dispersions display shear-thinning behaviour due to alignment of these anisotropic particles in the direction of the flow.[21, 22] This relationship between viscosity and shear alignment can be assessed using the shear-induced polarised light imaging (SIPLI) technique.[23-26] SIPLI utilises a modified parallel plate geometry, where the lower plate is made of transparent fused quartz and the upper plate is a polished steel mirror. Linearly-polarised white light is directed

through the fused quartz plate and sample towards the polished steel plate (see Figure 5.2a). The reflected light is analysed at 90° to the plane of polarisation and detected using a CCD camera. The presence of a Maltese cross pattern indicates birefringence as a result of particle alignment (see Figure 5.2b). Birefringence arises due to the difference in refractive index ($\Delta n'$) in two principal axes of optical indicatrix of the nano-object (n_1 and n_2), $\Delta n' = n_1 - n_2$.[27] Thus birefringence does not occur if no specific orientation is observed. For SIPLI measurements, there must also be net orientation within the sample and the wave vector of the incident light must be normal to the sample surface (see Figure 5.2b). Plane-polarised light interacts differently with shear-aligned objects of differing orientations. This is because the aligned species rotates the plane of light polarisation if the optical axes of the material are not in the same plane as the incident polarised light. Since the reflected light is analysed at 90° to the plane of polarisation, light will only be detected where the optical axes of the aligned species are not in the same plane as the incident polarised light, giving rise to the characteristic Maltese cross pattern (see Figure 5.2b).

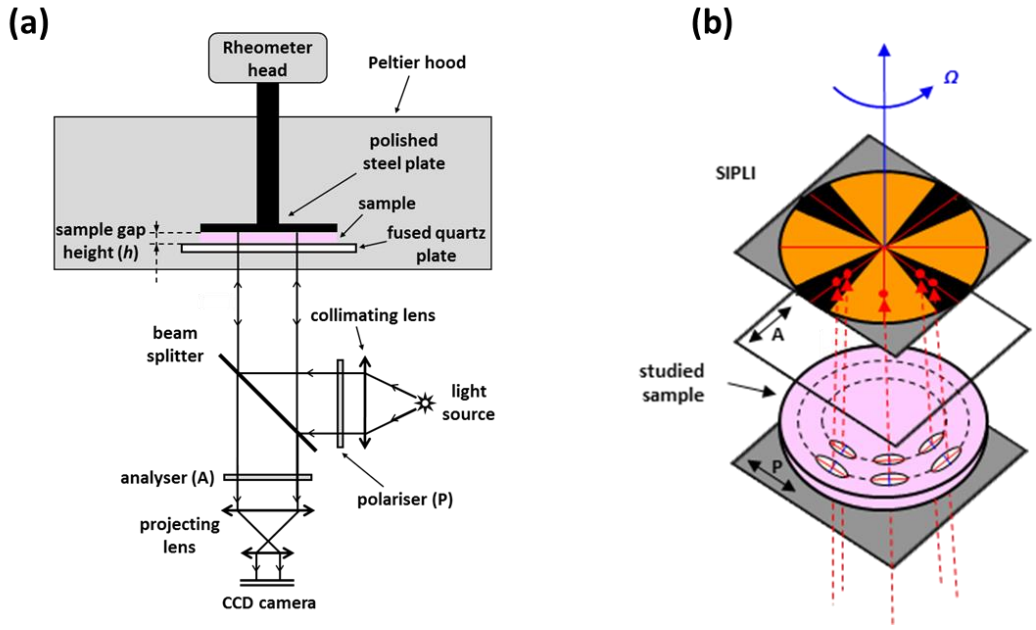

Figure 5.2. Schematic diagram for (a) the modified parallel plate geometry including the arrangement of the light source, polariser, analyser and CCD camera in relation to the rheometer, and (b) the formation of shear-induced polarised light imaging (SIPLI), simplified to show a linear arrangement. Double-sided arrows show the perpendicular planes of polarisation for the polariser (P) and the analyser (A). Lines within the white ellipsoids represent the optical axes of the sheared object, with the long axis corresponding to n_1 (red lines) being parallel to the direction of shear-alignment (dashed circles). The angular speed (Ω) indicates the direction of rotation for the polished steel plate.[23]

Since a parallel plate geometry is used for the SIPLI measurements, a gradient of shear rates is obtained across the plate (see Figure 5.3). This enables the simultaneous investigation of the effect of a range of shear rates on alignment. For example, if there is a critical shear rate below which no alignment occurs, a dark circular area should be observed at the centre of the image, which can be used to determine this critical shear rate. Conversely, if there is a critical shear rate above which no alignment is observed, there should be a dark outer ring on the generated image, where the outer edge of the Maltese cross indicates the limiting shear rate.

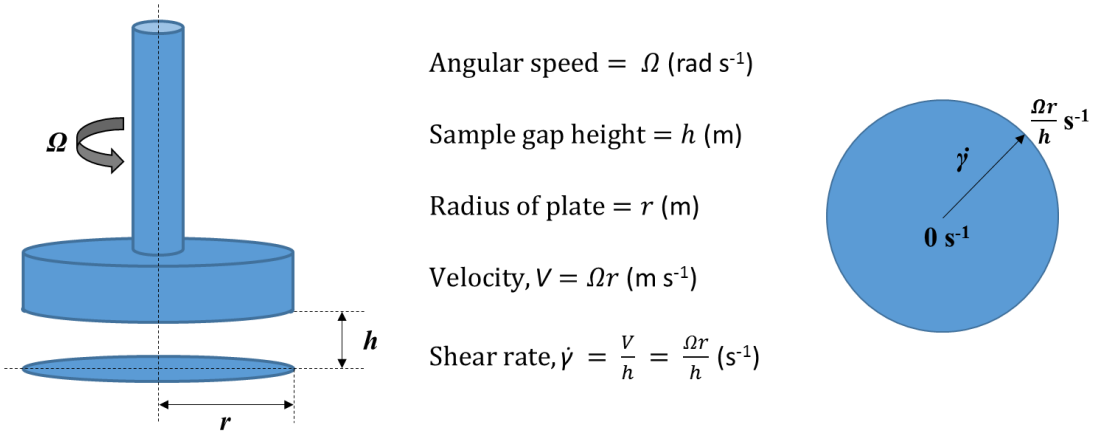

Figure 5.3. Schematic representation of the parallel plate geometry, demonstrating the linear dependence of shear rate ($\dot{\gamma}$) across the plate from the centre (0 s^{-1}) to the edge ($\Omega r/h$ s^{-1}).

Mykhaylyk et al.[23, 24] first developed this technique in combination with detailed SAXS studies to monitor the shear-induced crystallisation of thermoplastic polymers. Here birefringence was observed as a result of the alignment of stretched polymer chains at the onset of shear flow, followed by nucleation of oriented fibril species formed by the interaction of the individual polymer chains. SIPLI has since been used to observe shear alignment of native silk proteins,[25] as well as polystyrene-polyisoprene diblock copolymer lamellae.[26]

In this study, the rheological properties of $PSMA_{13}$-$PBzMA_x$ diblock copolymer worm gels synthesised at various copolymer concentrations in mineral oil are assessed. This enables important physical properties such as the critical gelation temperature (CGT) and the critical gelation concentration (CGC) to be determined. Such worms undergo

a thermo-reversible worm-to-sphere transition on heating as a result of surface plasticisation of the core-forming PBzMA block.[10] The shear-induced alignment of these worm gels is monitored using the SIPLI technique as a function of temperature, shear rate and copolymer concentration.

5.2. Experimental

5.2.1. Materials

Monomers were purchased from Sigma-Aldrich (UK) and passed through basic alumina prior to use to remove inhibitor. *Tert*-butyl peroxy-2-ethylhexanoate (T21s) initiator was purchased from AkzoNobel (The Netherlands). Cumyl dithiobenzoate (CDB), $CDCl_3$, and all other reagents were purchased from Sigma-Aldrich (UK) and were used as received, unless otherwise noted. THF and toluene were purchased from Fisher Scientific (UK), CD_2Cl_2 was purchased from Goss Scientific (UK) and industrial-grade mineral oil was provided by Lubrizol Corporation Ltd.

5.2.2. Synthesis of poly(stearyl methacrylate) (PSMA) macromolecular-chain transfer agent (macro-CTA)

The synthesis of the $PSMA_{13}$ macro-CTA was described earlier in this Thesis (Section 3.2.2.). The $PSMA_{13}$ macro-CTA was analysed using THF GPC (M_n = 5,700 g mol^{-1}; M_w/M_n = 1.17) and ^{1}H NMR spectroscopy as described earlier in this Thesis (mean DP = 13).

5.2.3. Synthesis of poly(stearyl methacrylate)-poly(benzyl methacrylate) (PSMA-PBzMA) diblock copolymer worms

A typical RAFT dispersion polymerisation synthesis of $PSMA_{13}$-$PBzMA_{65}$ diblock copolymer worms at 20% w/w solids in mineral oil was conducted as follows: A 10 mL round-bottomed flask was charged with benzyl methacrylate (BzMA; 0.368 g; 2.09 mmol), T21s initiator (1.39 mg; 6.42 μmol; dissolved at 10.0% v/v in mineral oil), $PSMA_{13}$ macro-CTA (0.15 g; 32.1 μmol; macro-CTA/initiator molar ratio = 5.0) and mineral oil (2.07 g). The reaction mixture was purged with nitrogen gas for 30 min and the deoxygenated solution was then placed in a pre-heated oil bath at 90 °C for 5 h (final BzMA conversion = 98 %; M_n = 12,700 g mol^{-1}, M_w/M_n = 1.15).

5.2.4. Gel permeation chromatography (GPC)

Molecular weight distributions (MWDs) were assessed by GPC using THF eluent at 30 °C. The THF GPC system was equipped with two 5 μm (30 cm) Mixed C columns and a WellChrom K-2301 refractive index detector operating at 950 ± 30 nm. The mobile phase contained 2.0% v/v triethylamine and 0.05% w/v butylhydroxytoluene (BHT) with a toluene flow rate marker and the flow rate was fixed at 1.0 mL min^{-1}. A series of ten near-monodisperse poly(methyl methacrylate) standards (M_p values ranging from 645 to 2,480,000 g mol^{-1}) were used for calibration.

5.2.5. ^{1}H Nuclear Magnetic Resonance (NMR) spectroscopy

^{1}H NMR spectra were recorded in either CD_2Cl_2 or $CDCl_3$ using a Bruker AV1-400 or AV1-250 MHz spectrometer. Typically 64 scans were averaged per spectrum.

5.2.6. Transmission electron microscopy (TEM)

TEM studies were conducted using a Philips CM 100 instrument operating at 100 kV and equipped with a Gatan 1 k CCD camera. Diluted block copolymer solutions (0.10% w/w) were placed on carbon-coated copper grids and exposed to ruthenium(VIII) oxide vapour for 7 min at 20 °C prior to analysis.[28] This heavy metal compound acted as a positive stain for the core-forming PBzMA block to improve contrast. The ruthenium(VIII) oxide was prepared as follows: ruthenium(IV) oxide (0.30 g) was added to water (50 g) to form a black slurry; subsequent addition of sodium periodate (2.0 g) with stirring produced a yellow solution of ruthenium(VIII) oxide within 1 min.

5.2.7. Small-angle X-ray scattering (SAXS)

SAXS patterns were recorded using a synchrotron source (Diamond Light Source, station I22, Didcot, UK). A monochromatic X-ray radiation (wavelength λ = 0.1001 nm) and a 2D Pilatus 2M detector (Dectris, Switzerland) were used for the experiments. The SAXS camera length set-up covered the q range from 0.02 nm^{-1} to 1.9 nm^{-1}, where $q = 4\pi \sin \theta / \lambda$ is the modulus of the scattering vector and θ is one half of the scattering angle. A 2.0 mm round glass capillary was used as a sample holder. X-ray scattering data were reduced using Dawn software version 1.7.1

(integration, normalisation)[29] and were further analysed using Irena SAS macros for Igor Pro (background subtraction, data modelling).[30] SAXS measurements were conducted on targeted $PSMA_{13}$-$PBzMA_{65}$ nanoparticles dispersed in mineral oil. The copolymer concentration was diluted to 1.0% w/w for all data collection.

5.2.8. Oscillatory rheology measurements

A TA Instruments AR-G2 rheometer equipped with a variable temperature Peltier plate and a 40 mm 2° aluminium cone was used for all experiments. The storage (*G*') and loss (*G*") moduli were measured as a function of temperature at a fixed strain of 1.0% and an angular frequency of 10 rad s^{-1} so as to assess the gel stiffness and critical gelation temperature (CGT). During temperature sweeps, the temperature was varied at 5 °C intervals, with an equilibration time of 5 min being allowed prior to each measurement. In all cases the gap between the cone and plate was 58 μm.

5.2.9. Shear-induced polarised light imaging (SIPLI)

A mechano-optical rheometer (Anton Paar Physica MCR301 with SIPLI attachment) was used for the shear-alignment experiments. The measurements were performed using a plate-plate geometry composed of a 25 mm polished steel plate and a fused quartz plate connected to a variable temperature Peltier system. The gap between plates was set at 1 mm for all experiments. An additional Peltier hood was used to achieve better control of the sample temperature. The viscosity was measured as a function of temperature at a cooling/heating rate of 2 °C min^{-1} at a constant angular speed. An Edmund Optics 150 W MI-150 high intensity fiber optic white light source was used for sample illumination. The polariser and analyser axes were crossed at 90° in order to obtain polarised light images (PLIs), which were recorded on a colour CCD camera (Lumenera Lu165c).

5.3. Results and Discussion

5.3.1. Synthesis of PSMA-PBzMA diblock copolymer worms

The $PSMA_{13}$ macro-CTA was chain-extended with BzMA monomer targeting $PSMA_{13}$-$PBzMA_{65}$ diblock copolymer worms via RAFT dispersion polymerisation (see Scheme 5.1). $PSMA_{13}$-$PBzMA_x$ worms were obtained over a range of copolymer

concentrations from 5.0 to 20% w/w solids and analysed using ^{1}H NMR spectroscopy, THF GPC and TEM (see Table 5.1).

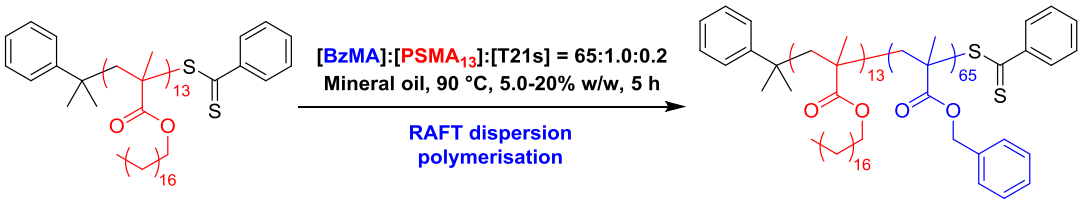

Scheme 5.1. Synthesis of targeted poly(stearyl methacrylate)$_{13}$-poly(benzyl methacrylate)$_{65}$ (PSMA$_{13}$-PBzMA$_{65}$) worms via RAFT dispersion polymerisation of BzMA in mineral oil at 90 °C and copolymer concentrations ranging from 5.0 to 20% w/w solids.

Table 5.1. Summary of total solids concentration, monomer conversion, GPC molecular weight data and assigned nanoparticle morphology for targeted PSMA$_{13}$-PBzMA$_{65}$ diblock copolymer worms prepared by RAFT dispersion polymerisation of BzMA in mineral oil at 90 °C using T21s and a PSMA$_{13}$ macro-CTA. [PSMA$_{13}$]/[T21s] molar ratio = 5.0. Relevant data for the PSMA$_{13}$ macro-CTA is displayed for reference.

% w/w	% BzMA[a]	Actual Composition[a]	M_n[b] / g mol^{-1}	M_w/M_n[b]	Morphology[c]
-	-	PSMA$_{13}$	4,900	1.17	-
5.0	98	PSMA$_{13}$-PBzMA$_{64}$	13,300	1.19	Worms
7.5	96	PSMA$_{13}$-PBzMA$_{62}$	12,200	1.19	Worms
10	97	PSMA$_{13}$-PBzMA$_{63}$	13,100	1.17	Worms
15	98	PSMA$_{13}$-PBzMA$_{64}$	12,800	1.16	Worms
20	98	PSMA$_{13}$-PBzMA$_{64}$	12,700	1.15	Worms

[a]Determined by ^{1}H NMR spectroscopy. [b]Determined by THF GPC against poly(methyl methacrylate) standards. [c]Morphologies were assigned using TEM.

Comparison of the molecular weight distributions (MWDs) for the targeted PSMA$_{13}$-PBzMA$_{65}$ diblock copolymers at each copolymer concentration (Figure 5.4) confirms the successful synthesis of PSMA-PBzMA diblock copolymers with comparable molecular weights. Moreover, a clear shift in the MWD from the initial PSMA$_{13}$ macro-CTA to the various PSMA$_{13}$-PBzMA$_x$ diblock copolymers indicates relatively high blocking efficiencies with minimal macro-CTA contamination.

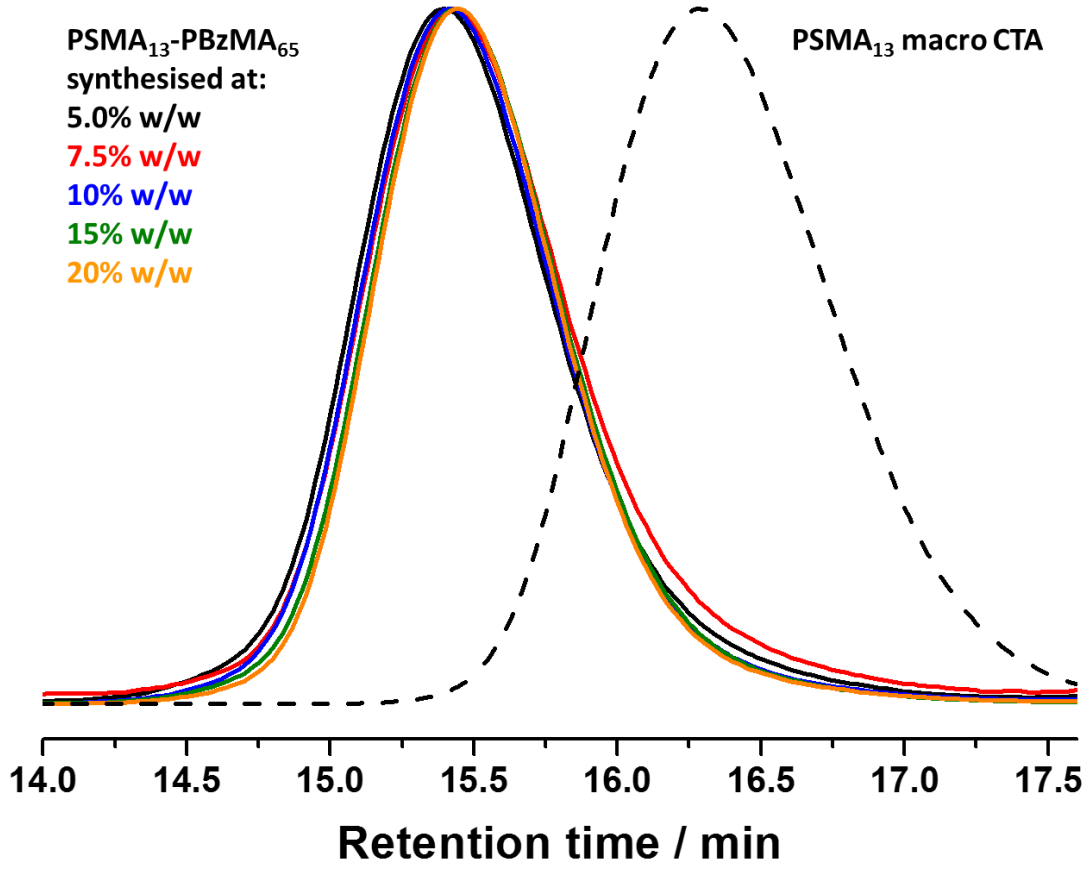

Figure 5.4. THF gel permeation chromatograms (vs. poly(methyl methacrylate) standards) obtained for targeted $PSMA_{13}$-$PBzMA_x$ diblock copolymer worms synthesised via RAFT dispersion polymerisation in mineral oil at various copolymer concentrations. The black dashed chromatogram represents the $PSMA_{13}$ macro-CTA and is displayed for reference.

TEM studies provide evidence that the targeted $PSMA_{13}$-$PBzMA_{65}$ diblock copolymers form worm-like nanoparticles, as stated in Table 5.1. The appearance of worms is confirmed by the representative TEM image shown in Figure 5.5, which was obtained for a 0.10% w/w dispersion of $PSMA_{13}$-$PBzMA_{63}$ nanoparticles synthesised at 10% w/w solids in mineral oil. The mean worm width (T_w) is estimated to be ~13 nm.

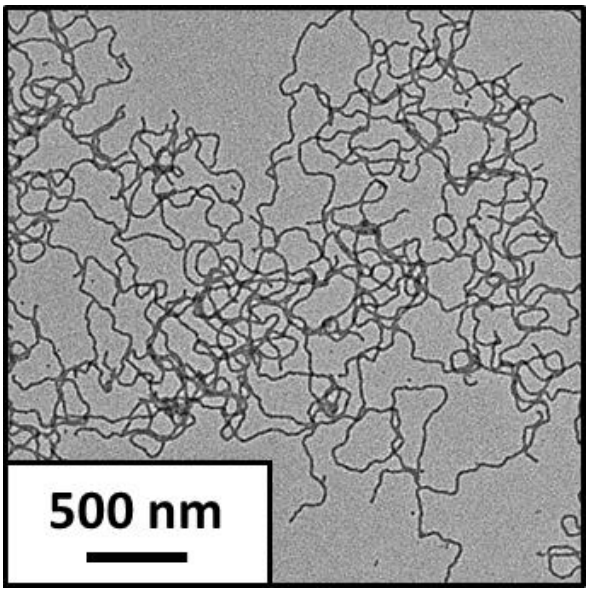

Figure 5.5. Transmission electron micrograph of a 0.10% w/w dispersion of $PSMA_{13}$-$PBzMA_{63}$ worms synthesised at 10% w/w in mineral oil.

SAXS analyses were also conducted in order to confirm the assigned worm morphology. This is because TEM only enables the dry morphology to be assessed for a few hundred nanoparticles, whereas SAXS is averaged over millions of nanoparticles and therefore is statistically more robust. Figure 5.6 shows representative SAXS patterns recorded for 1.0% w/w dispersions of $PSMA_{13}$-$PBzMA_x$ nanoparticles prepared at copolymer concentrations ranging from 5.0 to 20% w/w solids. All SAXS patterns confirmed a worm morphology as judged by the approximate -1 gradient at low *q*, which indicates highly anisotropic particles.[2, 10, 31] By fitting the data around the local minimum at high *q* (~0.5 nm^{-1}), mean worm thicknesses (T_w) were determined to be between 11.87 and 13.16 nm (see Table 5.2). It is evident that the SAXS patterns obtained for worms synthesised at 15% w/w (green data, Figure 5.6) and 20% w/w (orange data, Figure 5.6) deviate from the worm-like micelle model at low *q*. This may indicate the presence of branched worms, which is an important consideration later in this Chapter.

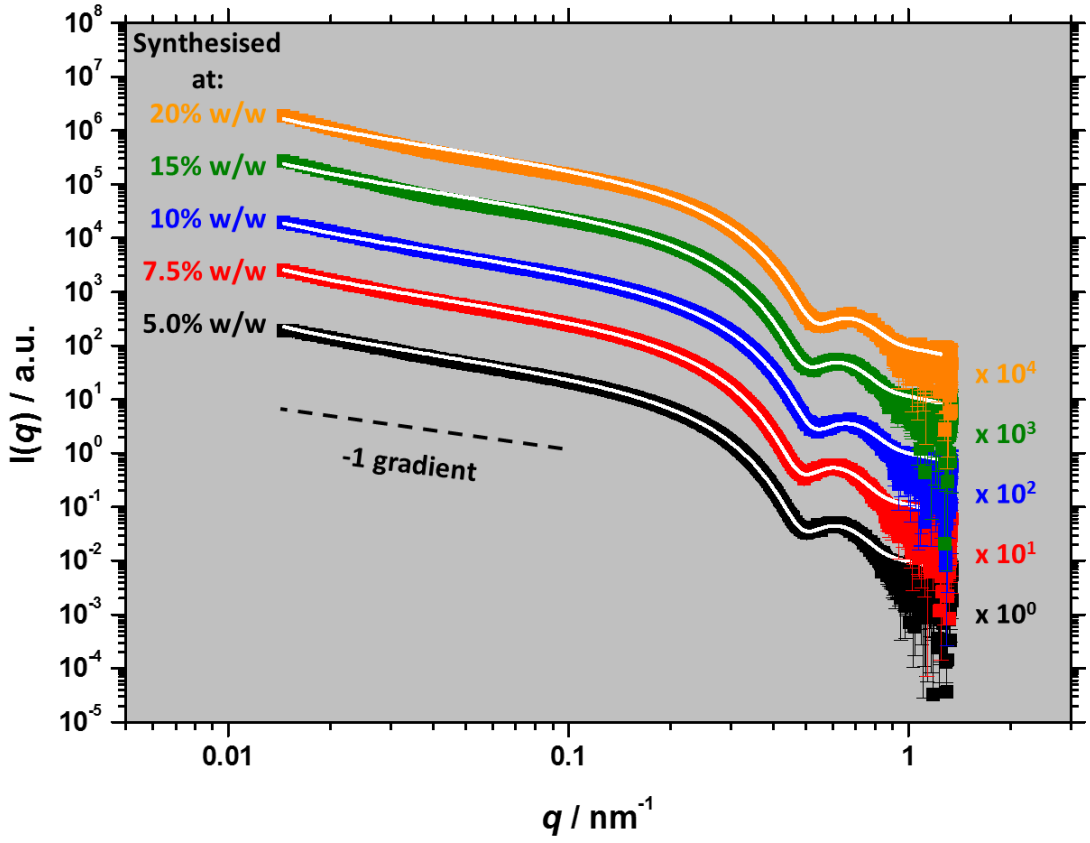

Figure 5.6. Representative small-angle X-ray scattering (SAXS) patterns recorded for 1.0% w/w dispersions of $PSMA_{13}$-$PBzMA_x$ worms synthesised in mineral oil at 5.0% w/w (black data), 7.5% w/w (red data), 10% w/w (blue data), 15% w/w (green data) and 20% w/w (orange data). White lines on each SAXS pattern indicates the data fit to a worm-like micelle model.[10, 32, 33]

These SAXS data were collected where the q range was limited to ~0.02-1.9 nm^{-1}. Thus it was not possible to determine the mean worm contour length (L_w), which is indicated by a subtle feature at $q < 0.01$ nm^{-1}. However, if sufficient branching exists this L_w feature may not be observed, as suggested by the SAXS patterns in Figure 5.6. For $PLMA_{16}$-$PBzMA_{37}$ worms synthesised via RAFT dispersion polymerisation in *n*-dodecane,[10] L_w was found to be 591 ± 9 nm when obtaining SAXS patterns over a wider q range (0.005 $nm^{-1} < q < 1.6$ nm^{-1}), which was achieved by combining data collected at short (for 0.08 $nm^{-1} < q < 1.6$ nm^{-1}) and long (for 0.005 $nm^{-1} < q < 0.12$ nm^{-1}) sample-to-detector lengths.[34] Similarly, the presence of potential branch points in the worms prepared at 5.0% w/w (black data, Figure 5.6), 7.5% w/w (red data, Figure 5.6) and 10% w/w solids (blue data, Figure 5.6) may not be observed due to the limited accessible q range for these SAXS experiments.

Table 5.2. Summary of the worm thickness (T_w) and corresponding standard deviation (σ) for $PSMA_{13}$-$PBzMA_x$ worms synthesised via RAFT dispersion polymerisation in mineral oil at various copolymer concentrations. SAXS data were recorded on 1.0% w/w dispersions in mineral oil.

Synthesised at / % w/w	Actual composition[a]	T_w[b] / nm	σ_{T_w}[b] / nm
5.0	$PSMA_{13}$-$PBzMA_{64}$	13.0	1.4
7.5	$PSMA_{13}$-$PBzMA_{62}$	13.1	1.4
10	$PSMA_{13}$-$PBzMA_{63}$	12.0	1.2
15	$PSMA_{13}$-$PBzMA_{64}$	12.6	1.4
20	$PSMA_{13}$-$PBzMA_{64}$	11.9	1.3

[a]Determined by ^{1}H NMR spectroscopy. [b]Determined by fitting representative SAXS patterns to an established worm-like micelle model.[10, 32, 33]

5.3.2. Rheological properties of $PSMA_{13}$-$PBzMA_x$ worm gels

Recent reports for closely-related PLMA-PBzMA diblock copolymers showed that pure diblock copolymer worms could be prepared only at copolymer concentrations of ≥ 17.5% w/w.[9, 10, 35] However, the current PSMA-PBzMA PISA formulation enables a pure worm phase to be accessed lower copolymer concentrations as low as 5.0% w/w as indicated in the phase diagram for $PSMA_{13}$-$PBzMA_x$ nanoparticles synthesised in mineral oil (see Chapter 3, Figure 3.14). Fielding and co-workers[10] found that a 20% w/w $PLMA_{16}$-$PBzMA_{37}$ diblock copolymer worm gel in *n*-dodecane exhibited thermo-responsive behaviour, transforming into a free-flowing fluid via a worm-to-sphere transition on heating to ~70 °C. Both SAXS and rheological studies indicated good thermo-reversibility for worm dispersions at (or above) 5.0% w/w solids. As previously discussed, this thermally-triggered worm-to-sphere transition arises as a result of surface plasticisation of the core-forming PBzMA block by ingress of hot solvent.[10] Similarly, $PSMA_{13}$-$PBzMA_x$ worm gels also display thermo-responsive behaviour: degelation occurs on heating up to 90 °C as judged by oscillatory rheology studies using a cone-and-plate geometry (see Figure 5.7). By definition, the worm dispersions are no longer a gel when the value of the storage modulus, *G*', is less than that for the loss modulus, *G*".[2, 3] Thus, the critical gelation temperature (CGT) can be defined as the temperature above which *G*' is less than *G*".

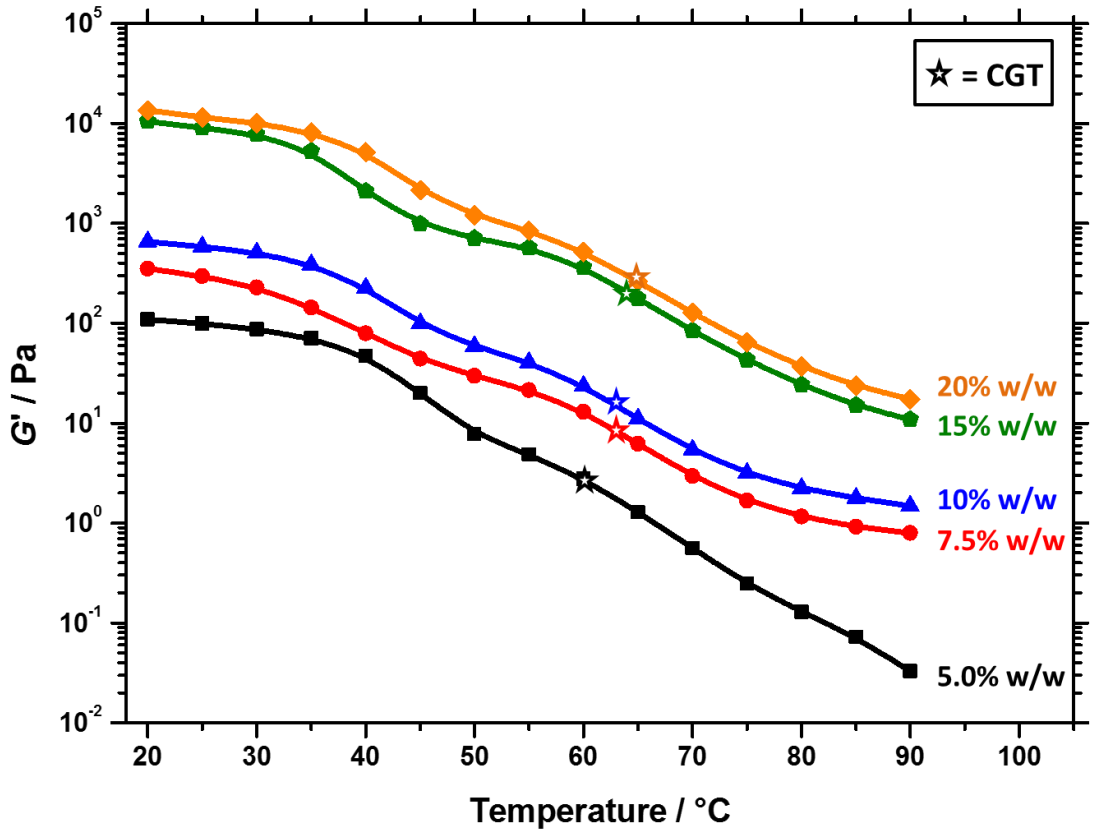

Figure 5.7. Variation of storage modulus (*G*') with temperature for $PSMA_{13}$-$PBzMA_x$ worm gels during a 20-90 °C thermal step. Conditions: 1.0% strain at an angular frequency of 10 rad s^{-1}. Data were recorded at 5 °C intervals, with an equilibration time of 5 min being allowed before each measurement. The critical gelation temperature (CGT) for each worm gel is indicated by a star symbol for each data set.

On lowering the copolymer concentration from 20 to 5.0% w/w, the CGT is reduced from 65 to 60 °C. Moreover, a systematic reduction in *G*' from ~10^4 to ~10^2 Pa is observed at 20 °C for worm gels on lowering the copolymer concentration from 20 to 5.0% w/w. This is because gelation is a macroscopic manifestation of multiple microscopic inter-worm contacts, which leads to restricted local diffusion and hence formation of a 3D network.[2-4, 6, 10, 35] Reducing the copolymer concentration from 20 to 5.0% w/w leads to significantly fewer inter-worm contacts and hence markedly weaker gels. This explanation also accounts for the subtle reduction in CGT observed when lowering the copolymer concentration. With fewer inter-worm contacts at lower copolymer concentrations, degelation may in fact occur earlier during the worm-to-sphere transformation (i.e. at lower temperatures). However, other parameters such as the L_w also affect the physical properties of worm gels.[36, 37]

It is evident that the worm-to-sphere transition is not complete at 90 °C, particularly at higher copolymer concentrations. This is because the *G*' at 90 °C is much greater than that expected for a free-flowing dispersion of purely spherical nanoparticles. In fact, a dispersion of spheres is expected to have a comparable viscosity to that of the solvent alone.[2, 3] This observation was confirmed for the closely-related $PLMA_{16}$-$PBzMA_{37}$ worms in *n*-dodecane, where SAXS studies indicated that the worm-to-sphere transition was only complete on heating to 160 °C.[10] In this case, L_w was reduced from ~600 nm at 20 °C to ~350 nm at 90 °C, hence the anisotropy (L_w/T_w) was approximately halved. For a 20% w/w dispersion of such $PLMA_{16}$-$PBzMA_{37}$ worms, the CGT was determined to be ~47 °C. Thus L_w at the CGT must lie between 600 nm and 350 nm, since a 'sequential budding of spheres' mechanism was identified.[10] The CGTs observed for $PSMA_{13}$-$PBzMA_x$ worm gels (see Figure 5.7) are higher than those reported for the $PLMA_{16}$-$PBzMA_{37}$ worm gel. One possible explanation is that the $PSMA_{13}$-$PBzMA_x$ worms are longer than the $PLMA_{16}$-$PBzMA_{37}$ worms, which suggests that a greater reduction in L_w would be required to reduce the number of inter-worm contacts sufficiently to cause degelation. However, this hypothesis was not examined due to the limited *q* range available when analysing these worms by SAXS. Alternatively, surface plasticisation of the core-forming PBzMA block may occur at higher temperatures for PSMA-PBzMA nanoparticles in mineral oil compared to PLMA-PBzMA nanoparticles in *n*-dodecane.

The critical gelation concentration (CGC) of the 20% w/w $PSMA_{13}$-$PBzMA_{64}$ worm gel was determined via systematic dilution. The CGC is defined as the lowest concentration at which the worm dispersion forms a free-standing gel at room temperature.[3] For $PSMA_{13}$-$PBzMA_{64}$ worms prepared at 20% w/w, the CGC was approximately 4.0% w/w (see Figure 5.8), which is significantly lower than that reported for various PLMA-PBzMA worms in *n*-dodecane,[10] mineral oil or a poly(*α*-olefin) (PAO) oil. The likely explanation for this observation is that the $PSMA_{13}$-$PBzMA_{64}$ worms are longer than the PLMA-PBzMA worms. This would lead to more efficient inter-worm interactions and thus afford free-standing gels at lower copolymer concentrations. Although these studies were only conducted on the 20% w/w dispersion of $PSMA_{13}$-$PBzMA_{64}$ worms, similar CGC values are expected for the $PSMA_{13}$-$PBzMA_x$ worms prepares at different copolymer concentrations in mineral

oil because the diblock copolymer chains are of similar molecular weight by GPC analysis (see Figure 5.4). Moreover, the $PSMA_{13}$-$PBzMA_{64}$ worms prepared at 5.0% w/w formed a free-standing gel, which is consistent with the observation of a CGC below this copolymer concentration.

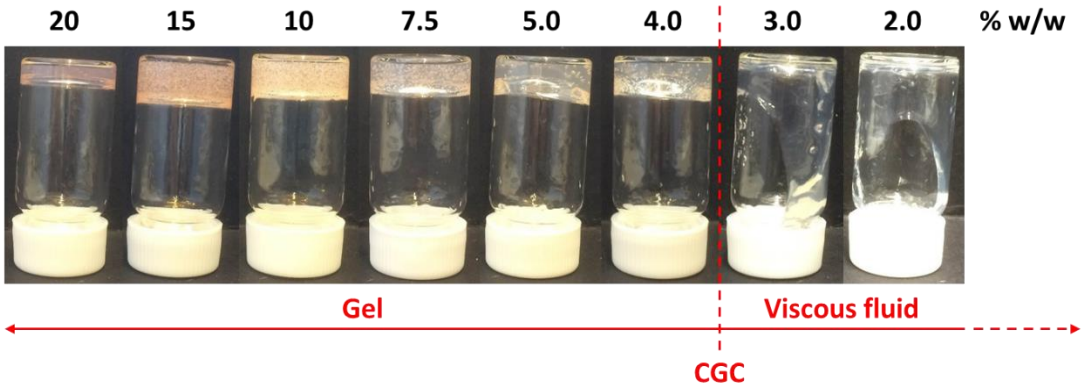

Figure 5.8. Digital images of $PSMA_{13}$-$PBzMA_{64}$ worm dispersions in mineral oil to determine the critical gelation concentration (CGC) via systematic dilution. The $PSMA_{13}$-$PBzMA_{64}$ worms used in this study were prepared at 20% w/w solids.

5.3.3. Shear-induced alignment of $PSMA_{13}$-$PBzMA_x$ diblock copolymer worms

5.3.3.1. Temperature-dependent shear-induced alignment

First, the $PSMA_{13}$-$PBzMA_{64}$ diblock copolymer worm gel synthesised at 20% w/w was analysed using the SIPLI technique. For all variable temperature measurements, the sample was loaded onto the fused quartz plate pre-heated to 150 °C in order to remove the thermal history of the gel (this is because the anisotropic worms form isotropic spheres at this temperature which are unable to form a gel network).[10] The apparent viscosity (η) was measured as a function of temperature at a maximum shear rate of 1, 10 or 100 s^{-1} and a cooling/heating rate of 2 °C min^{-1} from 150 °C to 20°C and from 20 °C to 150 °C. At a maximum shear rate of 1 s^{-1} (Figure 5.9), no birefringence was detected at 150 °C because only isotropic spherical nanoparticles exist at this temperature. This interpretation is consistent with η values of ~0.01 Pa s, which are characteristic of a free-flowing fluid. On cooling, the dispersion became progressively more viscous, indicating the formation of anisotropic worms from the fusion of multiple spheres.[10] The solution viscosity rapidly increased on cooling from 120 °C to 90 °C, suggesting that progressively longer worms are formed. The first

Maltese cross pattern is observed at 100 °C, suggesting that the worms present at this temperature are sufficiently aligned to cause birefringence at a shear rate at or below 1 s^{-1}. Interestingly, birefringence was observed throughout the dispersion, indicating a very low critical shear rate for alignment. Such alignment is observed on cooling from 100 °C to 60 °C. Between 90 °C and 65 °C, the dispersion viscosity continues to increase, albeit at a slower rate than between 120 °C and 90 °C. This again suggests that progressively longer worms are formed over this temperature range. Between 65 °C and 35 °C, the viscosity further increased and at a faster rate than between 90 °C and 65 °C. This implies further changes in the copolymer morphology and/or inter-worm interactions, which eventually cause gelation. For example, the presence of branched worms should increase the probability of inter-worm contacts, leading to more viscous dispersions. Greater worm clustering or entanglements could also increase the dispersion viscosity. Interestingly, the Maltese cross pattern is almost completely lost on cooling to 55 °C, which could also be attributed to the formation of branched worms or a worm network. Although alignment is not favoured over this temperature range, a modest degree of residual alignment is still visible in the optical images from 55 °C to 20 °C (see Figure 5.9). Given the high viscosity of the 20% w/w dispersion observed over this temperature range, it is feasible that a certain degree of alignment could become 'trapped', suggesting that the worms cannot relax to a completely disordered state.

Immediately after the temperature sweep from 150 °C to 20 °C shown in Figure 5.9, the same 20% w/w dispersion was heated from 20 °C to 150 °C at the same rate of 2 °C min^{-1} using the same constant maximum shear rate of 1 s^{-1} (see Figure 5.10).

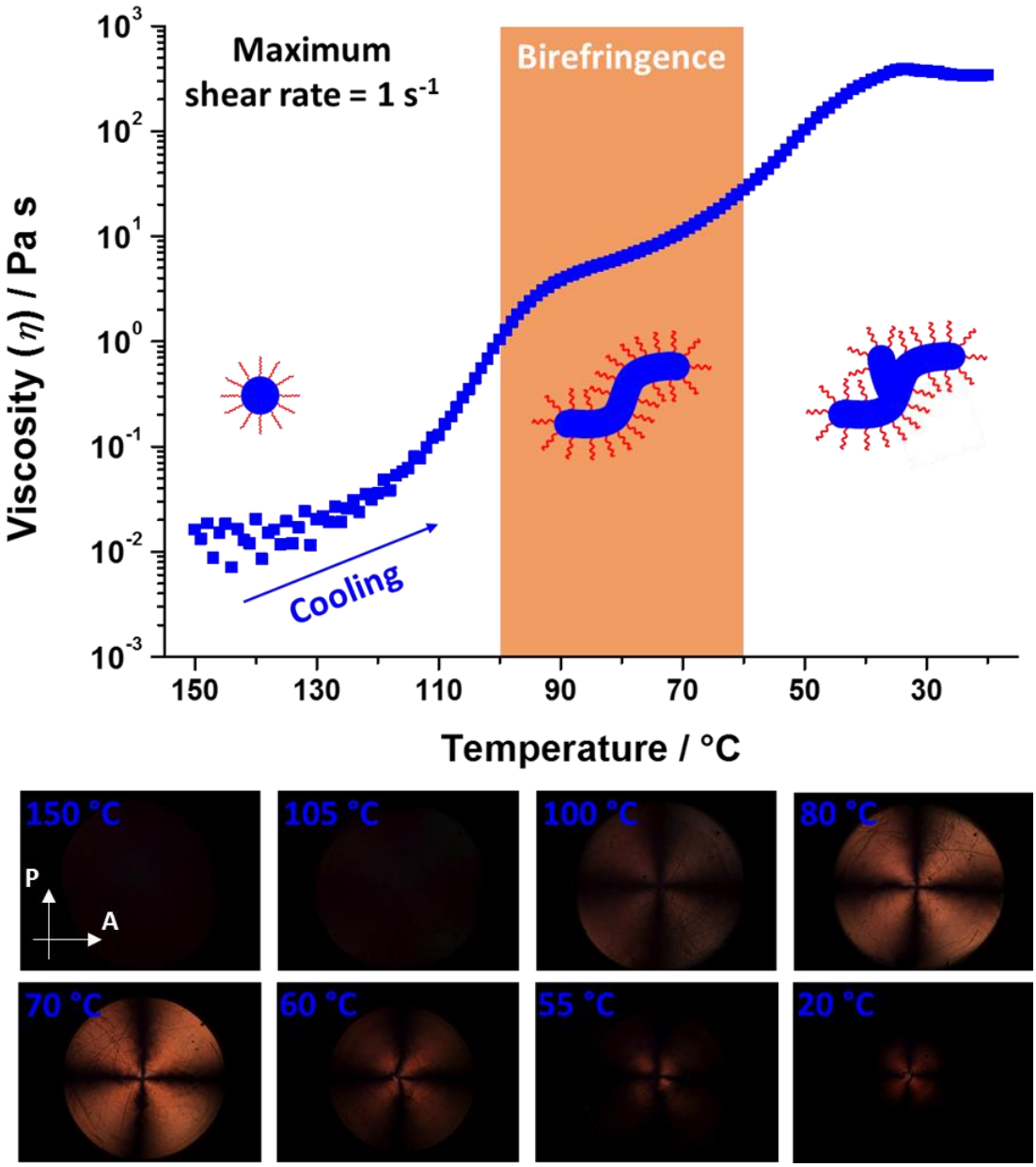

Figure 5.9. Viscosity-temperature profile and shear-induced polarised light imaging (SIPLI) of a 20% w/w dispersion of $PSMA_{13}$-$PBzMA_{64}$ diblock copolymer nanoparticles on cooling from 150 °C to 20 °C at a rate of 2 °C min^{-1} and a constant shear rate of 1 s^{-1}. Selected SIPLI images represent the birefringence observed at various temperatures. A Maltese cross pattern indicates shear-induced alignment, whereas the absence of such a pattern indicates no alignment.

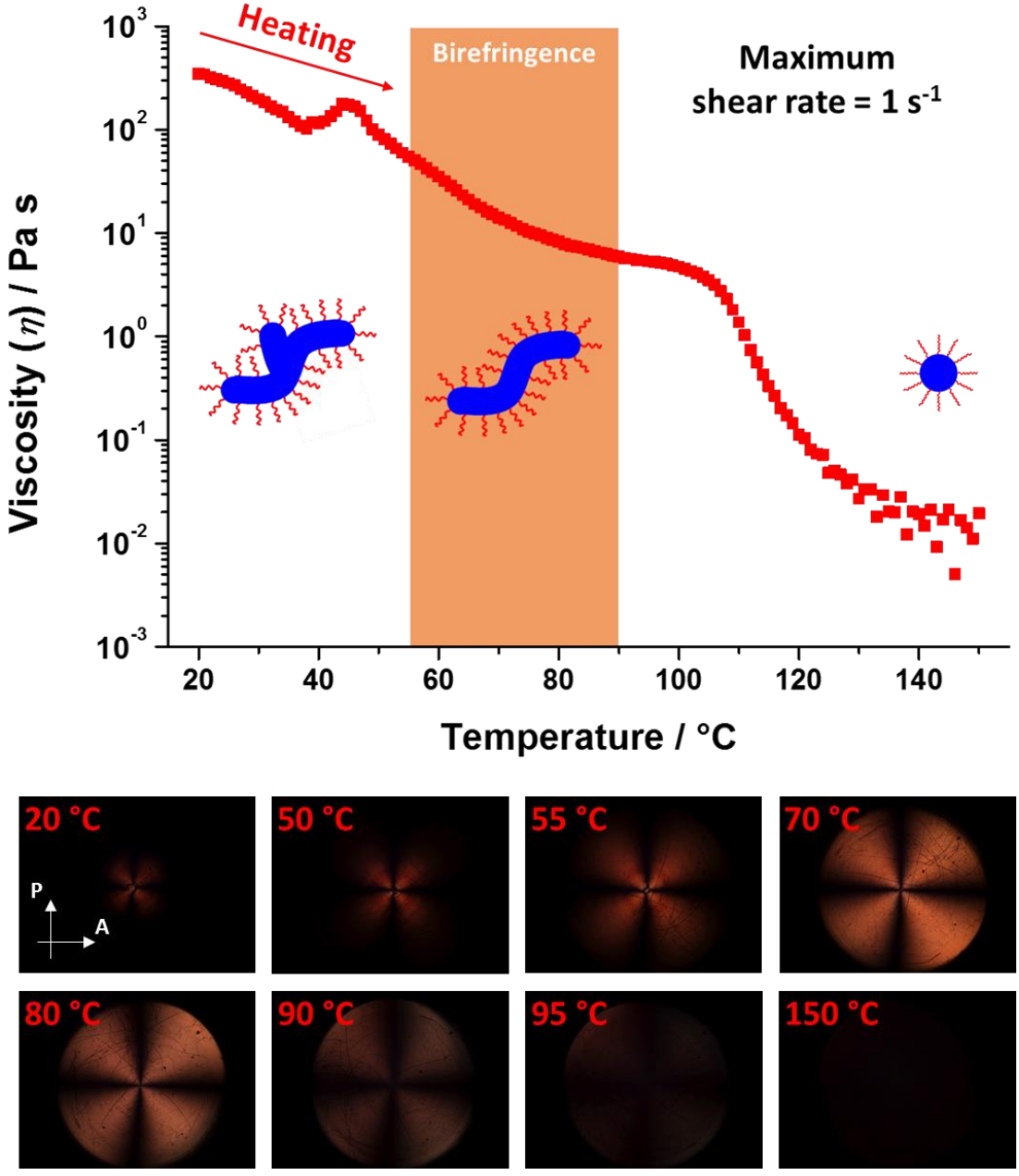

Figure 5.10. Viscosity-temperature profile and shear-induced polarised light imaging (SIPLI) of a 20% w/w dispersion of $PSMA_{13}$-$PBzMA_{64}$ diblock copolymer nanoparticles on heating from 20 °C to 150 °C at a rate of 2 °C min^{-1} and a constant shear rate of 1 s^{-1}. Selected SIPLI images represent the birefringence observed at various temperatures. A Maltese cross pattern indicates shear-induced alignment, whereas the absence of such a pattern indicates no alignment.

On initial inspection, the viscosity-temperature profile appears to mirror that for the cooling ramp, with the initial high-viscosity dispersion becoming less viscous at intermediate temperatures before a substantial reduction in viscosity at higher temperatures. However, the temperature ranges at which these changes in viscosity

occur are subtly different for the cooling and heating ramps. The first major difference to consider is the viscosity maximum at ~45 °C. This feature occurs before any evidence for shear alignment at 55 °C, indicating that it may correspond to the transition from branched/clustered worms to linear worms. The SIPLI images shown in Figure 5.10 indicate that shear alignment occurs between 55 °C and 90 °C, which differs from the temperature range for which shear alignment is observed on cooling from 100 °C to 60 °C. Similar hysteresis has been previously reported for $PLMA_{16}$-$PBzMA_{37}$ worms in *n*-dodecane.[10] On the other hand, the 'shoulder' in viscosity occurs at around 100 °C in both cases. This is presumably because the number of spherical nanoparticles increases relative to the number of worms to the point where they dictate the dispersion viscosity. The final viscosity of the 20% w/w dispersion at 150 °C was the same as that observed at the beginning of the variable-temperature SIPLI experiment (η ~ 0.01 Pa s). This indicates good thermo-reversibility for the sphere-to-worm-to-sphere transition on the experimental time scale. Figure 5.11 provides a more direct comparison between the data sets shown in Figure 5.9 and Figure 5.10.

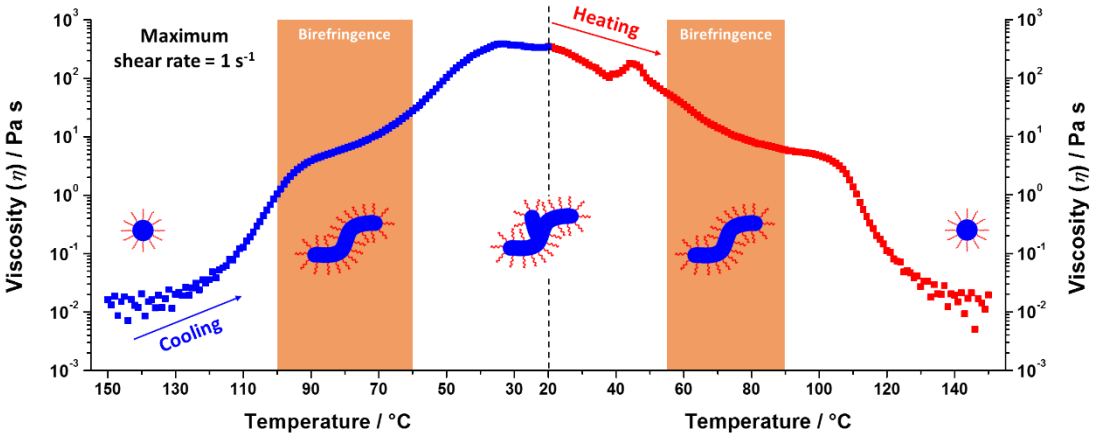

Figure 5.11. Combination of the viscosity-temperature profiles for the cooling (blue data) and heating (red data) ramps for a 20% w/w dispersion of $PSMA_{13}$-$PBzMA_{64}$ diblock copolymer nanoparticles on heating from 20 °C to 150 °C at a rate of 2 °C min^{-1} and a constant angular speed of 0.08 rad s^{-1} (maximum shear rate = 1 s^{-1}). Orange shaded regions represent the temperature ranges where shear-induced alignment (or birefringence) was observed.

5.3.3.2. Shear-rate dependence of shear-induced alignment and viscosity of $PSMA_{13}$-$PBzMA_x$ dispersions

Further investigation of the shear alignment and solution viscosity of $PSMA_{13}$-$PBzMA_x$ nanoparticles dispersed in mineral oil involved varying the shear rate. The same 20% w/w dispersion of $PSMA_{13}$-$PBzMA_{64}$ nanoparticles was used to conduct these variable-temperature SIPLI experiments at 10 and 100 s^{-1} and the data were compared to that obtained at 1 s^{-1} (see Figure 5.12). As expected, higher shear rates yielded lower-viscosity dispersions at 20 °C owing to their shear-thinning nature.[21, 22] This is particularly evident in Figure 5.12, where η ~ 345 Pa s at 20 °C for a maximum shear rate of 1 s^{-1}, while η ~ 40 Pa s at 10 s^{-1} and η ~ 4 Pa s at 100 s^{-1} at the same temperature. However, when free-flowing dispersions of spherical nanoparticles are formed at 150 °C, the dispersion viscosity is relatively independent of shear rate, indicating Newtonian behaviour.[38, 39] Interestingly, there are subtle differences for the temperature ranges over which shear alignment is observed for the same dispersion at maximum shear rates of 1, 10 and 100 s^{-1}. Nevertheless, birefringence is consistently observed between 95 °C and 75 °C during cooling and between 65 °C and 90 °C during heating . In principle, repeating these experiments using slower cooling/heating rates might provide more consistent temperature ranges over which shear alignment is observed.

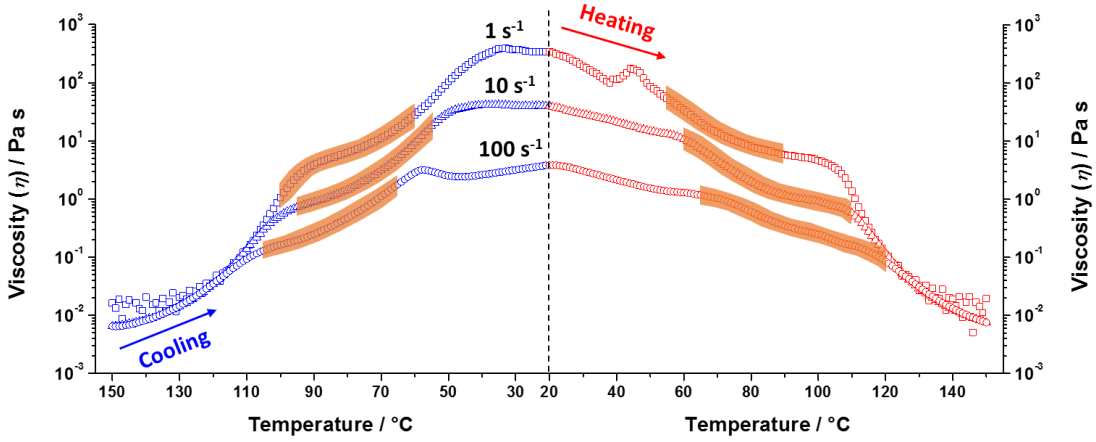

Figure 5.12. Combination of the viscosity-temperature profiles for the cooling (blue data) and heating (red data) ramps of a 20% w/w dispersion of $PSMA_{13}$-$PBzMA_{64}$ diblock copolymer nanoparticles on heating from 20 °C to 150 °C at a rate of 2 °C min^{-1} and constant angular speed of 0.08 rad s^{-1}(squares), 0.8 rad s^{-1} (triangles) and 8.0 rad s^{-1} (circles) (maximum shear rates of 1 s^{-1}, 10 s^{-1} and 100 s^{-1}, respectively). Orange shaded regions represent temperature ranges where birefringence is observed.

5.3.3.3. Concentration dependence on the shear-induced alignment and viscosity of $PSMA_{13}$-$PBzMA_x$ dispersions

Thus far, only $PSMA_{13}$-$PBzMA_{64}$ worms synthesised at 20% w/w have been analysed using the SIPLI technique. Hence $PSMA_{13}$-$PBzMA_x$ worm gels synthesised at 10 and 15% w/w were compared to that synthesised at 20% w/w. For this comparison, the same thermal cycle was used and the maximum shear rate was 100 s^{-1} for all measurements (see Figure 5.13). Clearly, the apparent viscosity at 20 °C is higher for more concentrated dispersions, as expected. The same features are observed in the viscosity-temperature profiles obtained for the 15 and 10% w/w dispersions as for those found for the 20% w/w dispersion. An initial low-viscosity fluid (η ~ 0.01 Pa s) at 150 °C became more viscous at lower temperature, indicating the formation of anisotropic worms. This higher viscosity is consistent with the observation of birefringence, as indicated by the characteristic Maltese cross pattern. A further increase in viscosity (η ~ 1-3 Pa s) suggests the formation of branched/clustered worms, which is supported by the loss of birefringence. There is significant overlap in the temperature ranges for which birefringence is observed for these dispersions, but there are subtle differences in the onset temperatures. In particular on cooling from 150 °C to 20 °C birefringence is observed sooner for the 20% w/w dispersion.

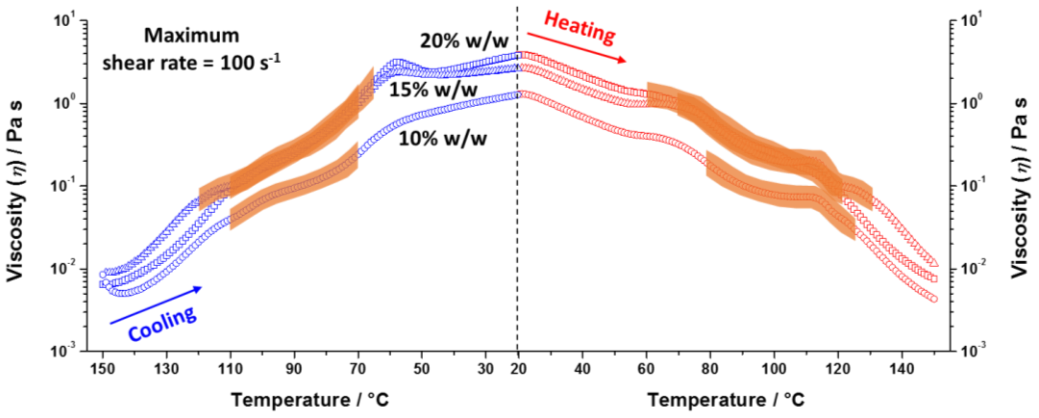

Figure 5.13. Combination of the viscosity-temperature profile for the cooling (blue data) and heating (red data) ramps of a 20% w/w (squares), 15% w/w (triangles) and 10% w/w (circles) dispersion of $PSMA_{13}$-$PBzMA_x$ diblock copolymer nanoparticles on heating from 20 °C to 150 °C at a rate of 2 °C min^{-1} and maximum shear rate of 100 s^{-1}. Orange shaded regions represent temperature ranges where birefringence is observed.

This may indicate more efficient sphere-sphere fusion at this higher copolymer concentration, as previously reported for the reformation of worms from their constituent spheres in related PISA formulations.[10]

5.4. Conclusions

In summary, $PSMA_{13}$-$PBzMA_{65}$ worms prepared at copolymer concentrations of 5.0 to 20% w/w in mineral oil form free-standing gels at 20 °C. All $PSMA_{13}$-$PBzMA_x$ block copolymers were of comparable molecular weight, as judged by THF GPC, and the worm morphology assignment was based on a combination of TEM studies and SAXS analyses performed on dilute dispersions. SAXS studies indicated that the mean worm thickness (T_w) of worms prepared at each copolymer concentration was approximately the same (T_w = 12.0-13.2 nm). Interestingly, some evidence for worm branching was obtained, but the degree of branching could not be determined using these experimental techniques. Each dispersion displayed thermo-reversible behaviour, with the initial free-standing worm gel at 20 °C forming a free-flowing fluid comprising spheres at 150 °C. The critical gelation temperature (CGT) only varied between 60 °C and 65 °C for $PSMA_{13}$-$PBzMA_x$ worm gels for various copolymer concentrations and the critical gelation concentration (CGC) was determined to be around 4.0% w/w as judged by the tube inversion test after serial dilution of a 20% w/w $PSMA_{13}$-$PBzMA_{64}$ worm gel. Shear-induced alignment of these worm gels could be observed within specific temperature ranges using the SIPLI technique. On cooling from 150 °C, isotropic spherical nanoparticles formed shear-aligned anisotropic worms. Further cooling resulted in the loss of birefringence. This suggests either the development of branched worms or worm clusters. Lower dispersion viscosities were observed at 20 °C for higher shear rates and lower copolymer concentrations. However, the dispersion viscosity at 150 °C, where spherical nanoparticles are present, exhibited little or no dependence on shear rate, indicating that such free-flowing dispersions act as Newtonian fluids.

Further work is clearly warranted in this area. In particular, the relaxation behaviour of various $PSMA_{13}$-$PBzMA_x$ worm gels for various applied shear rates should be studied over a range of copolymer concentrations and temperatures. However, this

constitutes many experimental variables and would require the synthesis of a large batch of $PSMA_{13}$-$PBzMA_x$ worms in order to analyse the effect of various parameters on the same dispersion. In addition, shear-alignment of worm gels should be monitored using a combination of rheology and *in situ* SAXS (so-called Rheo-SAXS). This can be achieved by applying shear to the worm gels within a Couette shear cell, while simultaneously collects SAXS data. Shear alignment should result in asymmetric 2D scattering patterns, which can be used to gain structural information and perhaps distinguish between the formation of branched worms and worm clusters.

5.5. References

1. S. Sugihara, A. Blanazs, S. P. Armes, A. J. Ryan and A. L. Lewis, *Journal of the American Chemical Society*, 2011, **133**, 15707-15713.
2. A. Blanazs, R. Verber, O. O. Mykhaylyk, A. J. Ryan, J. Z. Heath, C. W. I. Douglas and S. P. Armes, *Journal of the American Chemical Society*, 2012, **134**, 9741-9748.
3. R. Verber, A. Blanazs and S. P. Armes, *Soft Matter*, 2012, **8**, 9915-9922.
4. V. J. Cunningham, L. P. D. Ratcliffe, A. Blanazs, N. J. Warren, A. J. Smith, O. O. Mykhaylyk and S. P. Armes, *Polymer Chemistry*, 2014, **5**, 6307-6317.
5. M. K. Kocik, O. O. Mykhaylyk and S. P. Armes, *Soft Matter*, 2014, **10**, 3984-3992.
6. J. R. Lovett, N. J. Warren, L. P. D. Ratcliffe, M. K. Kocik and S. P. Armes, *Angewandte Chemie International Edition*, 2015, **54**, 1279-1283.
7. D. Zehm, L. P. D. Ratcliffe and S. P. Armes, *Macromolecules*, 2013, **46**, 128-139.
8. Y. W. Pei, N. C. Dharsana, J. A. Van Hensbergen, R. P. Burford, P. J. Roth and A. B. Lowe, *Soft Matter*, 2014, **10**, 5787-5796.
9. L. A. Fielding, M. J. Derry, V. Ladmiral, J. Rosselgong, A. M. Rodrigues, L. P. D. Ratcliffe, S. Sugihara and S. P. Armes, *Chemical Science*, 2013, **4**, 2081-2087.
10. L. A. Fielding, J. A. Lane, M. J. Derry, O. O. Mykhaylyk and S. P. Armes, *Journal of the American Chemical Society*, 2014, **136**, 5790-5798.
11. A. P. Lopez-Oliva, N. J. Warren, A. Rajkumar, O. O. Mykhaylyk, M. J. Derry, K. E. B. Doncom, M. J. Rymaruk and S. P. Armes, *Macromolecules*, 2015, **48**, 3547-3555.
12. Y. Pei, L. Thurairajah, O. R. Sugita and A. B. Lowe, *Macromolecules*, 2015, **48**, 236-244.
13. Y. Pei, O. R. Sugita, L. Thurairajah and A. B. Lowe, *RSC Advances*, 2015, **5**, 17636-17646.
14. M. Y. Lin, H. J. M. Hanley, G. C. Straty, D. G. Peiffer, M. W. Kim and S. K. Sinha, *Int J Thermophys*, 1994, **15**, 1169-1178.
15. V. Croce, T. Cosgrove, C. A. Dreiss, S. King, G. Maitland and T. Hughes, *Langmuir*, 2005, **21**, 6762-6768.
16. B. D. Frounfelker, G. C. Kalur, B. H. Cipriano, D. Danino and S. R. Raghavan, *Langmuir*, 2009, **25**, 167-172.

17. M. Y. Lin, H. J. M. Hanley, S. K. Sinha, G. C. Straty, D. G. Peiffer and M. W. Kim, *Physica B: Condensed Matter*, 1995, **213–214**, 613-615.
18. V. Castelletto and I. W. Hamley, *Polymers for Advanced Technologies*, 2006, **17**, 137-144.
19. V. Castelletto, P. Parras, I. W. Hamley, P. Bäverbäck, J. S. Pedersen and P. Panine, *Langmuir*, 2007, **23**, 6896-6902.
20. H. Schnablegger and Y. Singh, *The SAXS Guide: Getting Acquainted with the Principles, 2nd Edition*, Anton Paar GmbH, Graz, 2011.
21. S. R. Raghavan and E. W. Kaler, *Langmuir*, 2001, **17**, 300-306.
22. V. Croce, T. Cosgrove, G. Maitland, T. Hughes and G. Karlsson, *Langmuir*, 2003, **19**, 8536-8541.
23. O. O. Mykhaylyk, *Soft Matter*, 2010, **6**, 4430-4440.
24. O. O. Mykhaylyk, P. Chambon, C. Impradice, J. P. A. Fairclough, N. J. Terrill and A. J. Ryan, *Macromolecules*, 2010, **43**, 2389-2405.
25. C. Holland, F. Vollrath, A. J. Ryan and O. O. Mykhaylyk, *Advanced Materials*, 2012, **24**, 105-109.
26. O. O. Mykhaylyk, A. J. Parnell, A. Pryke and J. P. A. Fairclough, *Macromolecules*, 2012, **45**, 5260-5272.
27. *The Theory of Birefringence*, Cambridge Polymer Group, Inc., Boston, 2004.
28. J. S. Trent, *Macromolecules*, 1984, **17**, 2930-2931.
29. M. Basham, J. Filik, M. T. Wharmby, P. C. Y. Chang, B. El Kassaby, M. Gerring, J. Aishima, K. Levik, B. C. A. Pulford, I. Sikharulidze, D. Sneddon, M. Webber, S. S. Dhesi, F. Maccherozzi, O. Svensson, S. Brockhauser, G. Naray and A. W. Ashton, *Journal of Synchrotron Radiation*, 2015, **22**, 853-858.
30. J. Ilavsky and P. R. Jemian, *Journal of Applied Crystallography*, 2009, **42**, 347-353.
31. O. Glatter and O. Kratky, *Small-angle X-ray Scattering*, Academic Press: London, 1982.
32. J. S. Pedersen and P. Schurtenberger, *Macromolecules*, 1996, **29**, 7602-7612.
33. J. S. Pedersen, *Journal of Applied Crystallography*, 2000, **33**, 637-640.
34. K. L. Thompson, L. A. Fielding, O. O. Mykhaylyk, J. A. Lane, M. J. Derry and S. P. Armes, *Chemical Science*, 2015, **6**, 4207-4214.
35. M. J. Derry, L. A. Fielding and S. P. Armes, *Polymer Chemistry*, 2015, **6**, 3054-3062.
36. A. P. Chatterjee, *Journal of Chemical Physics*, 2010, **132**.
37. R. H. J. Otten and P. van der Schoot, *Journal of Chemical Physics*, 2011, **134**.
38. G. M. Kavanagh and S. B. Ross-Murphy, *Progress in Polymer Science*, 1998, **23**, 533-562.
39. H. A. Barnes, *A Handbook of Elementary Rheology*, The University of Wales Institute of Non-Newtonian Fluid Mechanics, Aberystwyth, 2000.

6. Applications of Diblock Copolymer Nanoparticles as Additives for Engine Base Oils and Crude Oil

6.1. Introduction

In 2010 Zheng et al.[1] reported that block copolymer micelles exhibit friction reduction properties in lubricant base oil. Specifically, all-acrylic poly[(2-ethylhexyl acrylate)-*stat*-(*tert*-butyl acrylate)]-poly(2-hydroxyethyl acrylate) (P[EHA-tBA]-PHEA) block copolymer spheres were synthesised via atom transfer radical polymerisation (ATRP) in cyclohexane prior to transfer to base oil. Crosslinking of such spheres was achieved via the addition of cinnamoyl chloride, which reacts with the 2-hydroxyethyl acrylate (EHA) residues to form pendant vinyl groups that enable crosslinking on exposure to UV light. In addition to crosslinking groups, acid functionality was added to the block copolymer spheres in varying amounts via the statistical copolymerisation of acrylic acid (AA) with EHA and *tert*-butyl acrylate (tBA), before chain-extending with 2-hydroxyethyl acrylate (HEA) to yield poly[(2-ethylhexyl acrylate)-*stat*-(*tert*-butyl acrylate)-*stat*-(acrylic acid)]-poly(2-hydroxyethyl acrylate) (P[EHA-tBA-AA]-PHEA, see Figure 6.1a).

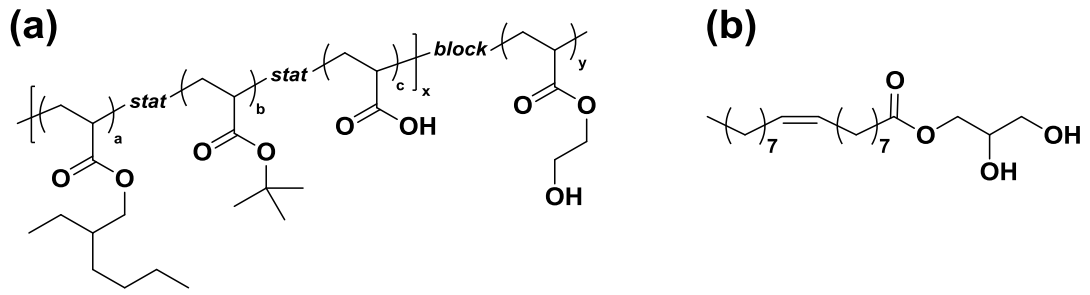

Figure 6.1. (a) Chemical structure of poly[(2-ethylhexyl acrylate)-*stat*-(*tert*-butyl acrylate)-*stat*-(acrylic acid)]-poly(2-hydroxyethyl acrylate) (P[EHA-tBA-AA]-PHEA) block copolymers synthesised via ATRP for use as lubricity improvement additives in lubricant base oil. (b) Chemical structures of glyceryl monooleate (GMO), an industry-standard friction modifier.

A series of block copolymer spherical micelles with the general structure shown in Figure 6.1a were assessed for their lubricity improvement of a lubricant oil comprising 95% saturated hydrocarbon content, high viscosity (36.3 cSt at 22 °C) and low volatility, provided by Exxon Mobil.[1] Addition of 0.5% w/w crosslinked P[EHA-tBA-AA]-PHEA spheres of 35 nm diameter reduced the friction coefficient of the base oil more than the addition of 1.0% w/w of an industry standard friction modifier, glyceryl monooleate (GMO, Figure 6.1b), in the boundary lubrication regime. This regime is particularly important considering the current trend towards lower-viscosity oils.

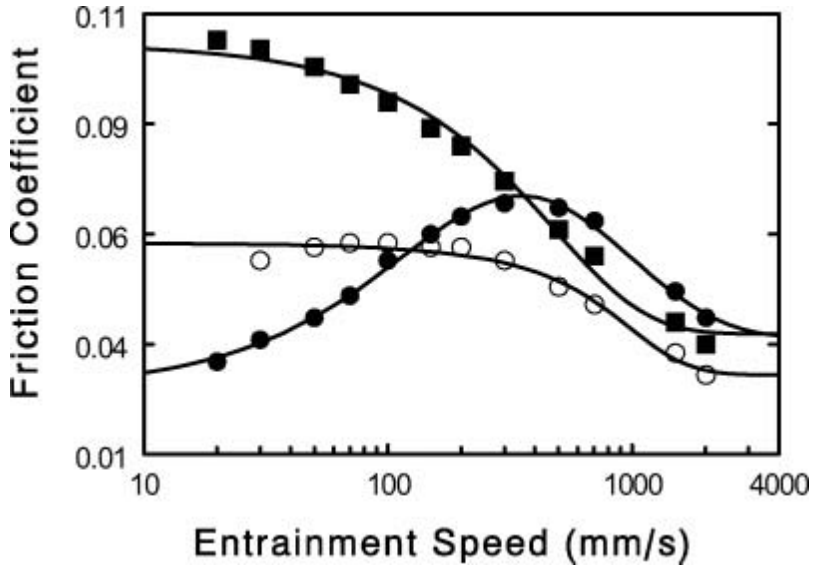

Figure 6.2. Friction coefficient vs. entrainment speed for a lubricating base oil alone (black squares), with 1.0% w/w glyceryl monooleate (open circles) and with 0.5% w/w 35 nm crosslinked P[EHA-tBA-AA]-PHEA spheres (filled circles).[1]

Similar observations were made when varying the extent of crosslinking and amount of acid functionality, suggesting that such block copolymer micelles offer great promise for friction reduction in lubricating base oils. However, there are a number of problems with the synthetic protocol utilised by Zheng et al. for preparing the spherical micelles.[2] Most notably, the use of ATRP invariably leads to copper contamination. Although the presence of copper in the lubricant base oil may not actually adversely affect the lubricity performance, it could potentially lead to the failure of industry tests, which must be passed prior to commercialisation. Also, the use of photo-induced crosslinking led to discolouration of the lubricating base oil. This is unlikely to be commercially attractive, because customers would be unlikely to welcome an 'off-colour' oil.

Clearly, the methacrylic spherical nanoparticles discussed in this Thesis offer a much more attractive route to the acrylic block copolymer micelles studied by Zheng et al.[1] Perhaps the most notable advantage of the synthesis protocol reported in this Thesis is the use of RAFT chemistry, which has been successfully scaled up for the production of commercial star polymers for viscosity modification by Lubrizol Corporation Ltd. Unlike ATRP, RAFT polymerisation requires no copper catalyst, so the problem of

residual copper in lubricating base oils is eliminated. Also, chemical crosslinking can be achieved simply by the addition of ethylene glycol dimethacrylate (EGDMA) to a RAFT dispersion formulation, which does not discolour the base oil. Therefore, this Chapter discusses the potential advantages for diblock copolymer nanoparticles synthesised by RAFT dispersion polymerisation *directly* in an industrially-relevant 4 cSt API Group III mineral oil. The lubricity improvement of spherical nanoparticles, as observed by Zhang et al.,[1] is examined, along with the viscosity modification performance of spherical and worm-like nanoparticles and the wax inhibition properties of spherical nanoparticles.

Polymeric additives are also commonly used as viscosity modifiers (VMs) for lubricating base oils.[3-10] Examples of VMs include crosslinked high molecular weight polyethylene,[3] hydrogenated polystyrene-polyisoprene-polybutadiene statistical block copolymers,[4] poly(alkyl acrylates)[5-7] and poly(alkyl methacrylates).[7-10] Although such additives are typically utilised at low copolymer concentrations (~1% w/w), the effect on the viscosity modification of the lubricating oil can significantly broaden the operational temperature range oil the oil.[3-5] Ideally, a VM should provide a temperature-independent oil viscosity. Such perfect behaviour cannot be achieved in practice, but VMs can modify the rate at which the oil viscosity is reduced at higher temperatures.[6] Additionally, VMs exhibiting high shear stability are deemed particularly desirable when high shear stresses are applied.[3, 4] This is a significant technical challenge, since high molecular weight polymers often provide better thickening performance but are usually more susceptible to shear degradation. This problem can be addressed by using complex architectures such as star-shaped or hyperbranched copolymers.[3]

Similarly, it is well-known that polymers with pendant alkyl groups can be used to improve the flow properties of crude oil by inhibiting wax crystal formation.[11-15] Such additives are known as pour point depressants (PPDs): the temperature at which the crude oil becomes too viscous to pour is reduced because the polymer interacts with growing wax crystals due to their similar chemical strucures.[14] The mechanism of wax inhibition is an example of co-crystallisation, whereby the PPD interacts with the growing wax crystal surface, thus retarding growth and also providing steric

stabilisation, hence reducing the extent of aggregation between precipitating wax crystals.[14] PPDs are important in the oil industry since wax deposits on the walls of crude oil pipelines can lead to blocked lines,[13] which lead to high maintenance costs.

Another important technical problem for the oil industry involves the dispersion of asphaltenes,[16] because deposition of such material can also contribute to the blockage of crude oil pipelines. Asphaltenes are the most polar fraction of crude oil, being soluble in aromatic solvents but insoluble in *n*-alkanes.[16] They comprise polyaromatic and polycyclic rings, with short alkyl chains and heteroatoms (most commonly nitrogen, oxygen and sulfur), as shown in Figure 6.3a.[17, 18] A range of additives have been used as asphaltene dispersants, including alkyl benzene-derived amphiphiles (see Figure 6.3b).[19]

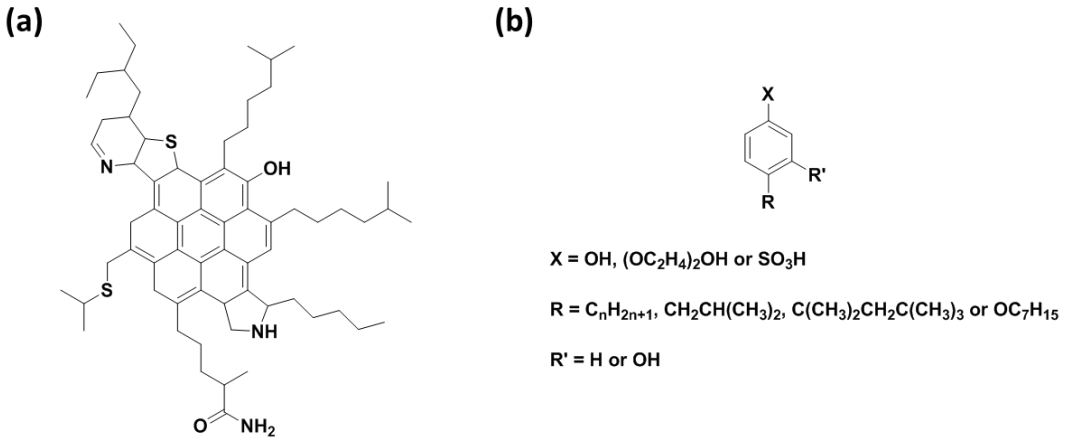

Figure 6.3. Typical chemical structures of (a) an asphaltene and (b) asphaltene dispersants.[17-19]

Lubricity improvers, viscosity modifiers, wax inhibitors and asphaltene dispersants are just a few of many classes of additives used within the oil industry. The broad range of applications for such species and the industry-wide trend towards thinner oils, as well as oils with a higher bio-derived fatty acid methyl ester (FAME) content, suggests new opportunities for the development of a new generation of additives.

6.2. Experimental

6.2.1. Materials

A 4 cSt API Group III mineral oil, a fully-formulated automotive gear oil (AGO) and behenyl methacrylate (BhMA) monomer were provided by Lubrizol Corporation Ltd. 4-Cyano-4-(2-phenylethane sulfanylthiocarbonyl)sulfanylpentanoic acid (PETTC) was synthesised according to the literature[20] by Nicholas Penfold, for which he is thanked.

6.2.2. Synthesis of diblock copolymer nanoparticles

The synthesis of various methacrylic diblock copolymer nanoparticles has been described in earlier sections in this Thesis (Sections 2.2.3 and 3.2.3), other than those described in Section 6.2.3 below.

6.2.3. Synthesis of poly(behenyl methacrylate)-poly(benzyl methacrylate) (PBhMA-PBzMA) diblock copolymer spheres

Firstly, a $PBhMA_{37}$ macro-CTA was synthesised as follows: A 250 mL round-bottomed flask was charged with behenyl methacrylate (BhMA; 23.8 g, 60.3 mmol), 4-cyano-4-(2-phenylethane sulfanylthiocarbonyl)sulfanylpentanoic acid (PETTC; 410 mg, 1.21 mmol), 2,2'-azobisisobutyronitrile (AIBN; 39.6 mg, 241 μmol; [PETTC]/[AIBN] molar ratio = 5.0) and toluene (28.0 g). The reaction vessel was purged with nitrogen and place in a pre-heated oil bath at 70 °C for 3 h. The resulting PBhMA (BhMA conversion = 57 %; M_n = 12,400 g mol^{-1}, M_w/M_n = 1.18) was purified by precipitation into excess 2-propanol. The mean degree of polymerisation (DP) of this macro-CTA was calculated to be 37 using ^{1}H NMR spectroscopy by comparing the integrated signals corresponding to the PETTC aromatic protons at 7.0-7.5 ppm with that assigned to the two oxymethylene protons of PBhMA at 3.4-4.2 ppm. Secondly, this macro-CTA was utilised during the RAFT non-polar dispersion polymerisation of benzyl methacrylate (BzMA) at 20% w/w solids in mineral oil. A typical synthesis protocol is described: Benzyl methacrylate (BzMA; 2.34 g, 13.3 mmol), T21s initiatior (5.8 mg; 26.8 μmol; dissolved at 10% v/v in mineral oil) and $PBhMA_{37}$ macro-CTA (2 g; 134 μmol; [macro-CTA]/[initiator] molar ratio = 5.0) were dissolve in mineral oil (6.54 g). The reaction mixture was purged with nitrogen

for 30 min and the deoxygenated solution was then place in a pre-heated oil bath at 90 °C for 5 h (final BzMA conversion = 99 %; M_n = 22,700 g mol^{-1}; M_w/M_n = 1.15).

6.2.4. Gel permeation chromatography (GPC)

Molecular weight distributions (MWDs) were assessed by GPC using THF eluent at 30 °C. The THF GPC system was equipped with two 5 μm (30 cm) Mixed C columns and a WellChrom K-2301 refractive index detector operating at 950 ± 30 nm. The mobile phase contained 2.0% v/v triethylamine and 0.05% w/v butylhydroxytoluene (BHT) with a toluene flow rate marker and the flow rate was fixed at 1.0 mL min^{-1}. A series of ten near-monodisperse poly(methyl methacrylate) standards (M_p values ranging from 645 to 2,480,000 g mol^{-1}) were used for calibration.

6.2.5. Dynamic light scattering (DLS)

DLS studies were performed at 50 °C using a Zetasizer Nano-ZS instrument (Malvern Instruments, UK) at a fixed scattering angle of 173°. Copolymer dispersions were diluted in *n*-dodecane (0.1% w/w) prior to DLS studies. The intensity-average diameter and polydispersity of the diblock copolymer particles were calculated by cumulants analysis of the experimental correlation function using Dispersion Technology Software version 6.20. Data were averaged over three sets of thirteen runs with each run of thirty seconds duration.

6.2.6. Transmission electron microscopy (TEM)

TEM studies were conducted using a Philips CM 100 instrument operating at 100 kV and equipped with a Gatan 1 k CCD camera. Diluted block copolymer solutions (0.10% w/w) were placed on carbon-coated copper grids and exposed to ruthenium(VIII) oxide vapour for 7 min at 20 °C prior to analysis.[21] This heavy metal compound acted as a positive stain for the core-forming PBzMA block to improve contrast. The ruthenium(VIII) oxide was prepared as follows: ruthenium(IV) oxide (0.30 g) was added to water (50 g) to form a black slurry; subsequent addition of sodium periodate (2.0 g) with stirring produced a yellow solution of ruthenium(VIII) oxide within 1 min.

6.2.7. Turbidimetry

Turbimetry measurements were performed using a Shimadzu UV-1800 spectrophotometer equipped with a DBS instruments twin Peltier temperature controller. A 1.0% w/w solution of $PBhMA_{37}$ in mineral oil was first heated to 50 °C and equilibrated for 5 min. Data were recorded at 650 nm during cooling (50 °C to 20 °C) and heating (20 °C to 50 °C) steps, with 5 min equilibration at each temperature.

6.2.8. Evaluation of lubricity performance

Stribeck curves were obtained using a PCS Instruments mini-traction machine (MTM) consisting of a 19.05 mm diameter steel ball and a 46 mm diameter steel disc. The steel ball and disc are driven independently to create a rolling/sliding contact ratio, or slide-to-roll ratio (SRR), of 50% or 20% with a constant load of 35 N. Tribology measurements were conducted using on either a 4 cSt API Group III mineral oil or fully-formulated automotive gear oil (AGO) with and without 0.5% w/w additive at 100 °C, at entrainment speeds ranging from 10 to 3000 mm s^{-1}. These studies were conducted by Zahra Hussain (Lubrizol Corporation Ltd.), for which she is thanked.

6.2.9. Evaluation of viscosity modification

A TA Instruments AR 2000 rheometer equipped with a variable temperature Peltier plate and a 40 mm 2° steel cone was used for all experiments. Viscosity-temperature profiles were obtained during a 25-100-25 °C heating/cooling ramp at a heating/cooling rate of 1 °C min^{-1} and a constant shear rate of 100 s^{-1}. Viscosity-shear rate profiles were obtained during a linear 10-1000 s^{-1} shear rate ramp over 20 min at 25 °C, before a linear 1000-10 s^{-1} shear rate ramp over 10 min at 25 °C. Prior to each rheological measurement, samples were pre-sheared at a shear stress of 3 Pa for 30 s and then equilibrated at 25 °C for 2 min. These studies were conducted by Dr. Kieran Trickett (Lubrizol Corporation Ltd.), for which he is thanked.

6.2.10. Evaluation of wax inhibition

A TA Instruments AR 2000 rheometer equipped with a variable temperature Peltier plate and a 40 mm 2° steel cone was used for all experiments. Viscosity-temperature profiles were obtained during a 60 °C to 10 °C cooling ramp at a cooling rate of 1 °C

min^{-1} and a constant shear rate of 30 s^{-1}. Prior to each rheological measurement, samples were pre-sheared at a shear stress of 3 Pa for 30 s and then equilibrated at 60 °C for 2 min. These studies were conducted by Dr. David Growney (Lubrizol Corporation Ltd.), for which he is thanked.

6.2.11. Evaluation of asphaltene dispersion

Asphaltene dispersion efficiency was analysed via dynamic turbidimetry. 150 μL of crude oil was added to 10 mL of *n*-heptane precipitant and stirred using a vortex mixer at 2,000 rpm for 30 seconds. A Formulaction Turbiscan MA2000 instrument was used to monitor the transmittance of the solution, which was measured at 1 min intervals for 15 min at 25 °C. Data were recorded in duplicate and the mean transmittance (%) was reported for each of the time intervals. These studies were conducted by Dr. David Growney (Lubrizol Corporation Ltd.), for which he is thanked.

6.3. Results and Discussion

6.3.1. Diblock copolymer spheres as lubricity improvers

Informed by the studies of Zheng et al.,[1] various block copolymer spheres synthesised via RAFT-mediated PISA were assessed for their friction modification performance. Specifically, PLMA-PBzMA and PSMA-PBzMA spheres synthesised directly in an industrially-relevant 4 cSt API Group III mineral oil were assessed, see Table 6.1. The fact that such spheres can be synthesised directly in an industrially-relevant oil offers a more attractive synthetic protocol compared to that described by Zheng et al.[2] Moreover, using RAFT polymerisation, a technology which has been successfully commercialised by Lubrizol Corporation Ltd., rather than ATRP offers a commercially viable route to block copolymer spheres.

The performance of each sample of block copolymer spheres was assessed by measuring the friction coefficient (μ_f) using the mini-traction machine (MTM). Friction generated between the rotating steel ball and disk in the MTM set-up is manifested as the amount of force which can be applied before the system slips. The friction coefficient (μ_f) relates the friction force (F_f) to the force exerted on the system (or the normal force, F_n), as shown in below:

$$F_f = \mu_f \times F_n \quad 6.1$$

Table 6.1. Summary of block copolymer spheres for assessment as lubricity improvers. All spheres were synthesised via RAFT dispersion polymerisation in mineral oil (see Sections 2.2.3 and 3.2.3).

Sample ID	Block Composition	DLS diameter (PDI)	THF GPC (vs. PMMA)	
			M_n / g mol^{-1}	M_w/M_n
L_{47}-B_{46}	$PLMA_{47}$-$PBzMA_{46}$	42 nm (0.06)[a]	15,800	1.55
[L_{49}-M_1]-B_{47}	P[LMA_{49}-*stat*-MAA_1]-$PBzMA_{47}$	41 nm (0.03)[a]	15,500	1.44
L_{47}-B_{297}	$PLMA_{47}$-$PBzMA_{297}$	116 nm (0.03)[a]	53,400	1.68
S_{31}-[B_{200}-E_{20}]	$PSMA_{31}$-P[$BzMA_{200}$-$EGDMA_{20}$]	46 nm (0.04)[a] 73 nm (0.06)[b]	28,000[c]	1.22[c]

[a]DLS data obtained on 0.1% w/w dispersions in *n*-dodecane. [b]DLS data obtained on a 0.1% w/w dispersion in THF in order to demonstrate successful crosslinking. [c]Molecular weight data obtained on a small sample of linear PSMA-PBzMA withdrawn from the reaction vessel prior to the addition of EGDMA (E) crosslinker.

6.3.1.1. Lubricity improvement in base oil

Firstly, the lubricity performance of various PLMA-PBzMA spheres shown in Table 6.1 (L_{47}-B_{46}, [L_{49}-M_1]-B_{47} and L_{47}-B_{297}) was assessed in base oil alone (see Figure 6.4). At slide-to-roll ratios (SRRs) of 20% or 50%, the base oil had a friction coefficient of ~0.015-0.020 at high entrainment speeds (1000-3000 mm s^{-1}), rising up to ~0.15 at low entrainment speeds (10 mm s^{-1}). Figure 6.4 clearly shows that the addition of 0.5% w/w 116 nm L_{47}-B_{297} spheres (red data) had an adverse effect on the lubrication performance of the oil, since higher friction coefficients are observed at intermediate entrainment speeds (~25-100 mm s^{-1}) at a 20% SRR and throughout the whole range of speeds at 50% SRR. In contrast, addition of 0.5% w/w 42 nm L_{47}-B_{46} spheres (purple data, Figure 6.4) reduced the friction coefficient of the base oil at

entrainment speeds of ~200 mm s^{-1} and below at both 20% and 50% SRR, suggesting that these smaller spheres offer a lubricity benefit in the mixed/boundary lubrication regime. However, using the same amount of similar-sized spheres containing acid functionality in the stabiliser block (41 nm $[L_{49}\text{-}M_1]\text{-}B_{47}$ spheres, blue data, Figure 6.4) produced much lower friction coefficients over all entrainment speeds, with values of ~0.075 being observed at 10 mm s^{-1} at both 20% and 50% SRR. Comparing these data to those obtained for 0.5% w/w glyceryl monooleate (GMO, green data, Figure 6.4), it is clear that the 41 nm $[L_{49}\text{-}M_1]\text{-}B_{47}$ spheres offered slightly better performance in the mixed lubrication regime at both 20% and 50% SRR, but GMO produced lower friction coefficients at 10 mm s^{-1}. Ultimately, Figure 6.4 suggests that smaller, acid-functional spheres offer enhanced lubricity, with comparable performance to the industry-standard GMO additive in the mixed lubrication regime.

Zheng et al.[1] also reported that the addition of core-crosslinked spheres could enhance the lubricant performance of a base oil. However, the method of crosslinking in this example involved the use of UV light, which has the unwanted side effect of oil discolouration. In the present work, chemical crosslinking of the PBzMA core-forming chains should not discolour the base oil. Thus, 10 mol% (vs. BzMA monomer) of ethylene glycol dimethacrylate (EGDMA) was added to the RAFT dispersion polymerisation formulation at relatively high (> 90%) BzMA conversion. This is an important experimental detail, since adding the EGDMA crosslinker too early during the BzMA polymerisation can lead to ill-defined nanoparticles and possibly inter-nanoparticle crosslinking.[22]

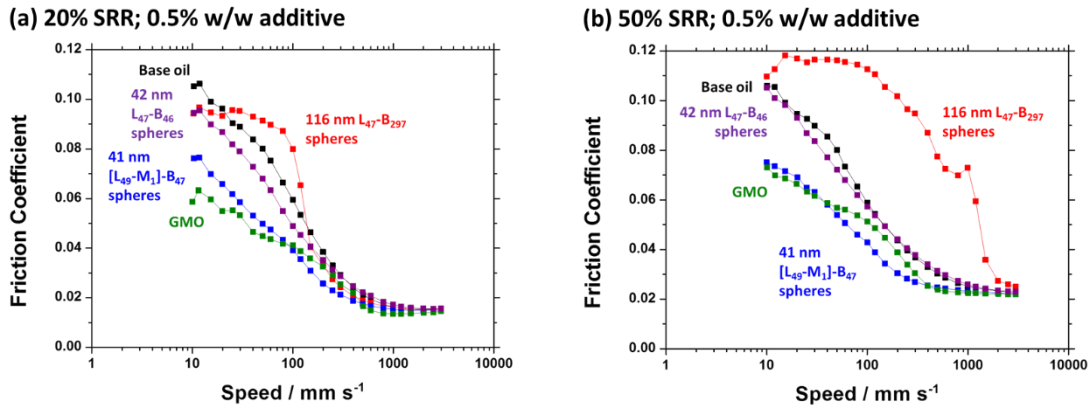

Figure 6.4. Friction coefficient vs. entrainment speed for a lubricating base oil alone (black data), with L_{47}-B_{297} 116 nm spheres (red data), L_{47}-B_{46} 42 nm spheres (purple data), [L_{49}-M_1]-B_{47} 41 nm spheres (blue data) and glyceryl monooleate (GMO, green data) for experiments conducted at (a) 20% and (b) 50% slide-to-roll ratio (SRR). Data were collected at 0.5% w/w additive concentration and under a load of 35 N at 100 °C.

Considering the data shown in Figure 6.4, crosslinked spheres of similar diameter to the 41 nm [L_{49}-M_1]-B_{47} spheres (blue data, Figure 6.4) were assessed for their lubricity performance. Successful crosslinking was confirmed by DLS studies. The intensity-average diameter of the S_{31}-[B_{200}-E_{20}] spheres was determined to be 46 nm in *n*-dodecane. On diluting this dispersion in THF, a good solvent for the PSMA and PBzMA blocks, the spheres swelled to 73 nm diameter, but remained intact. The crosslinked 46 nm S_{31}-[B_{200}-E_{20}] spheres were evaluated for their lubricity performance under the same conditions employed for Figure 6.4a (see Figure 6.5a). Data from Figure 6.4a for the base oil (black data), 0.5% w/w 41 nm [L_{49}-M_1]-B_{47} spheres (blue data) and 0.5% w/w GMO (green data) are shown for reference. Core-crosslinking using EGDMA clearly lowers the friction coefficient at low entrainment speeds (< 50 mm s^{-1}) compared to 41 nm [L_{49}-M_1]-B_{47} spheres. Moreover, the 46 nm S_{31}-[B_{200}-E_{20}] spheres reduce the friction coefficient of the base oil significantly more than GMO at low entrainment speeds (< 40 mm s^{-1}). In fact, the Stribeck curve is rather similar to that obtained by Zheng et al.[1] when using 0.5% w/w 35 nm crosslinked P[EHA-tBA-AA]-PHEA spheres under the same conditions. The friction coefficient observed for 0.5% w/w 46 nm S_{31}-[B_{200}-E_{20}] spheres is approximately 0.02, which is lower than that reported for 0.5% w/w 35 nm crosslinked P[EHA-tBA-AA]-PHEA spheres. This suggests that there may be a performance benefit for the block copolymer spheres synthesised via RAFT-mediated PISA in addition to the various

synthetic advantages. However, it is difficult to directly compare the degree of crosslinking within spherical cores for each type of spheres.

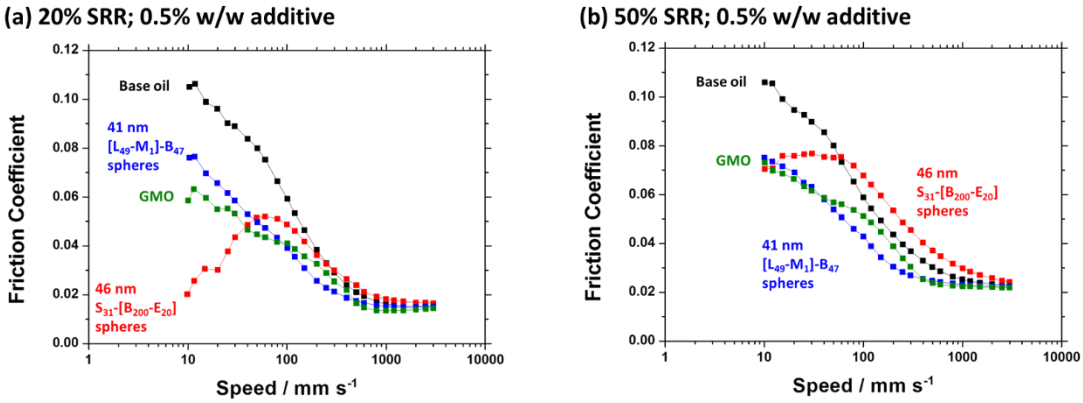

Figure 6.5. Friction coefficient vs. entrainment speed for a lubricating base oil alone (black data), with 41 nm $[L_{49}\text{-}M_1]\text{-}B_{47}$ spheres (blue data), 46 nm $S_{31}\text{-}[B_{200}\text{-}E_{20}]$ spheres (red data) and glyceryl monooleate (GMO, green data) for experiments conducted at (a) 20% and (b) 50% slide-to-roll ratio (SRR). Data were collected at 0.5% w/w additive concentration under a load of 35 N at 100 °C.

Despite the promising lubricant performance of crosslinked 46 nm $S_{31}\text{-}[B_{200}\text{-}E_{20}]$ spheres in base oil at 20% SRR (Figure 6.5a, red data), rather different behaviour is observed when conducting the same experiment at 50% SRR (see Figure 6.5b). Under these conditions, the acid-functional, non-crosslinked 41 nm $[L_{49}\text{-}M_1]\text{-}B_{47}$ spheres (Figure 6.5b, blue data) produced lower friction coefficients throughout the entire range of entrainment speeds compared to the crosslinked 41 nm $S_{31}\text{-}[B_{200}\text{-}E_{20}]$ spheres (Figure 6.5b, red data). Interestingly, the acid-functional 41 nm $[L_{49}\text{-}M_1]\text{-}B_{47}$ spheres offer comparable lubricity improvement to that conferred by GMO (Figure 6.5b, green data) under these conditions, with slightly enhanced performance in the mixed lubrication regime.

6.3.1.2. Lubricity improvement in automotive gear oil

Although the data shown in the previous Section suggest that various block copolymer spheres in base oil alone are promising lubricant additives, their performance must also be assessed in a fully-formulated automotive gear oil (AGO). In this Section, the 41 nm $[L_{49}\text{-}M_1]\text{-}B_{47}$ and 46 nm $S_{31}\text{-}[B_{200}\text{-}E_{20}]$ spheres (see Table 6.1) were assessed in a fully-formulated automotive gear oil (AGO) at 50% SRR (see Figure 6.6).

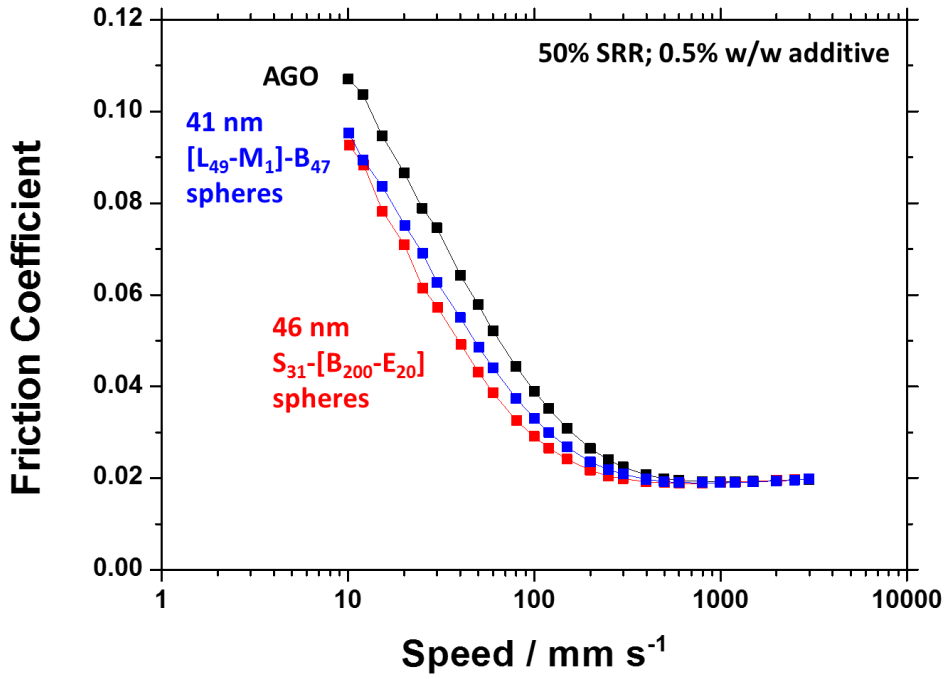

Figure 6.6. Friction coefficient vs. entrainment speed for an automotive gear oil (AGO, black data), with 41 nm $[L_{49}\text{-}M_1]\text{-}B_{47}$ spheres (blue data) and 46 nm $S_{31}\text{-}[B_{200}\text{-}E_{20}]$ spheres (red data) for experiments conducted at 50% slide-to-roll ratio (SRR). Data were collected at 0.5% w/w additive concentration under a load of 35 N at 100 °C.

On the addition of 0.5% w/w 41 nm $[L_{49}\text{-}M_1]\text{-}B_{47}$ and 46 nm $S_{31}\text{-}[B_{200}\text{-}E_{20}]$ spheres, the friction coefficients observed for the AGO were reduced from ~0.11 to ~0.095 at low entrainment speeds (10 mm s^{-1}), see Figure 6.6. Although this friction reduction is not as significant as that observed for base oil alone (see Figure 6.5), these data provide the first indication that these diblock copolymer spheres offer genuine potential for lubricity improvement in *fully formulated* oils. The competing chemistries and additives within the AGO may explain the less pronounced reduction in friction coefficient compared to base oil alone. The similarity between the Stribeck curves for AGO compared to either set of spheres suggests that, for similar-sized spheres, the nature of the stabiliser block (with or without acid functionality, whether C_{12} or C_{18} side chains) and the core-forming block (with or without crosslinking) has relatively little effect on lubricity performance in AGO. This suggests that, in a fully formulated oil, the presence of suitably-sized spherical nanoparticles, regardless of their surface and core chemistries, may provide sufficient friction modification. This hypothesis warrants further research, since similar or even better lubricity performance using spheres synthesised using cheaper starting materials (e.g. MMA

instead of BzMA) has the potential for significant impact within the automotive additive industry.

6.3.2. Viscosity modification of base oil

6.3.2.1. Diblock copolymer spheres as viscosity modifiers

PLMA-PBzMA spheres of similar size to those identified as useful lubricant additives in the previous Section were assessed for their viscosity modification properties. Specifically, 40 nm $PLMA_{39}$-$PBzMA_{99}$ (L_{39}-B_{99}; M_n = 20,100 g mol^{-1}; M_w/M_n = 1.15) block copolymer spheres were used in this study. These linear spheres were synthesised via RAFT dispersion polymerisation in mineral oil at 50% w/w and were subsequently diluted to various desired concentrations prior to analysis.

Firstly, a suitable industrially-relevant reference material was required in order to compare the viscosity modification properties of the 40 nm L_{39}-B_{99} spheres. A commercial linear oil-soluble alkyl-rich poly(methacrylate) (PMA) viscosity modifier (VM) was selected in view of its functionality to these spheres. In order to compare the linear PMA control, which does not self-assemble in base oil, to the L_{39}-B_{99} spheres, both additives were blended to produce the same oil viscosity at 100 °C. A 10% w/w dispersion of 40 nm L_{39}-B_{99} spheres and a 12% w/w solution of the linear PMA reference additive each gave viscosities of ~0.005 Pa s at 100 °C. The fact that a lower concentration of 40 nm L_{39}-B_{99} spheres than the linear PMA reference additive is required to deliver the same viscosity at 100 °C suggests the potential benefit of using the former additive rather than the latter. Comparison of the viscosity-temperature profiles of these two additives (see Figure 6.7) highlights another advantage of the block copolymer spheres. Both the 12% w/w solution of the linear PMA reference material (blue data, Figure 6.7) and the 10% w/w dispersion of L_{39}-B_{99} 40 nm spheres (red data, Figure 6.7) produced higher viscosities compared to the base oil alone (black data, Figure 6.7) throughout the temperature range studied. The benefit of using the spheres over the linear PMA becomes evident when considering the viscosity at 25 °C. A base oil should provide higher viscosity at elevated (e.g. 100 °C) temperature, but not increase the base oil viscosity at ambient (e.g. 25 °C) temperatures. In this context, the 10% w/w dispersion of 40 nm L_{39}-B_{99} spheres

exhibits viscosities of ~0.030-0.033 Pa s at 25 °C compared to ~0.041 Pa s for the 12% w/w solution of the linear PMA reference additive. It was highlighted in Chapter 2 (Figure 2.10a) that RAFT-mediated PISA offers a convenient route for the synthesis of block copolymer spheres at high solids content (≤ 50% w/w), whereas soluble polymers synthesised at such high concentrations suffer from inherently high viscosities. This explains why the 10% w/w dispersion of 40 nm L_{39}-B_{99} spheres exhibited a much lower viscosity at 25 °C than the 12% w/w solution of the linear PMA reference.

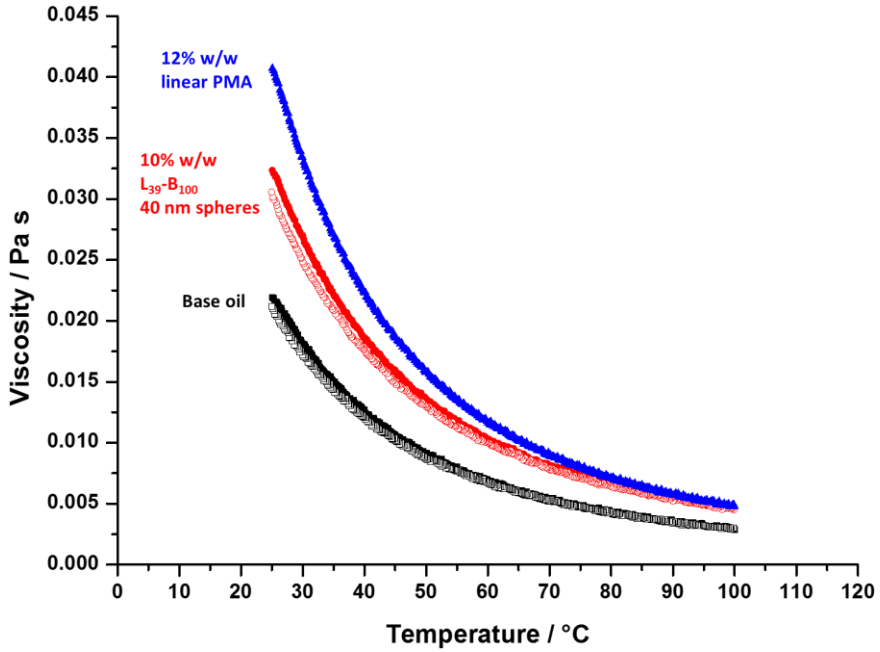

Figure 6.7. Viscosity-temperature profiles of base oil alone (black data), 10% w/w 40 nm L_{39}-B_{99} spheres (red data) and 12% w/w linear PMA reference (blue data) during heating (filled symbols) and cooling (open symbols) ramps. Data were collected during a 25-100-25 °C thermal cycle at a heating/cooling rate of 1 °C min^{-1}.

The specific viscosity (η_{sp}) is a useful parameter when considering the contribution of polymeric additives to the overall viscosity of the oil, and is calculated using:

$$\eta_{sp} = \frac{\eta - \eta_0}{\eta_0} \qquad 6.2$$

where η is the viscosity of the solution and η_0 is the viscosity of the base oil. Figure 6.8 shows the variation of the specific viscosity with temperature for both the 10%

w/w dispersion of L_{39}-B_{99} spheres (red data) and the 12% w/w solution of the linear PMA reference (blue data). The linear PMA contributed less towards the overall viscosity of the base oil, as indicated by the lowering specific viscosity upon heating from 25 °C to 100 °C. Conversely, the 40 nm L_{39}-B_{99} spheres enhance the overall oil viscosity over the same temperature range. This is a desirable property of a VM, since this indicates that the oil viscosity is effectively modified at high temperatures, whereas the oil is not too viscous at lower temperatures.

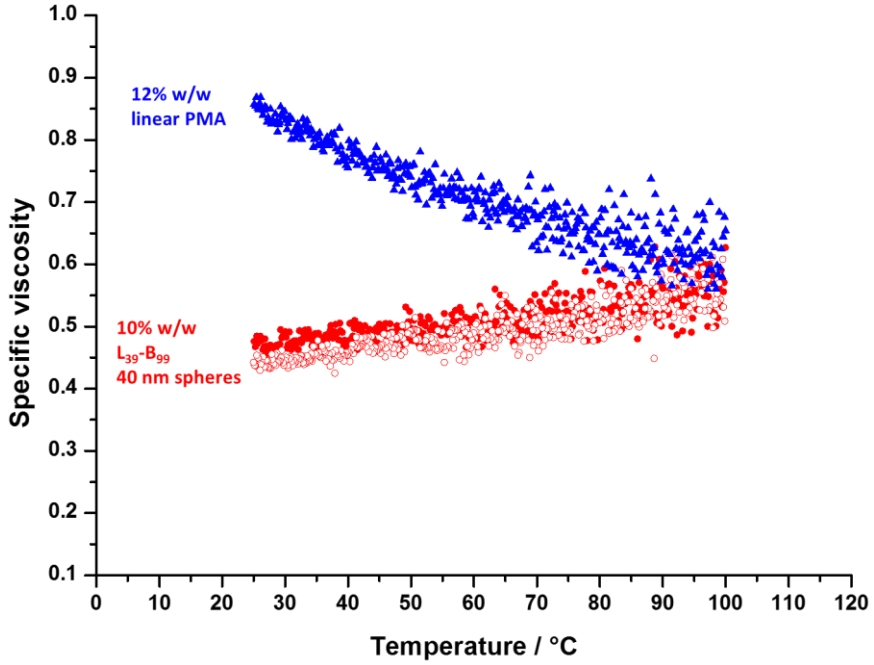

Figure 6.8. Specific viscosity vs. temperature for 10% w/w 40 nm L_{39}-B_{99} spheres (red data) and 12% w/w linear PMA reference additive (blue data) in base oil. Data were collected during a 25-100 °C heating ramp (filled symbols) and a 100-25 °C cooling ramp (empty symbols) at a heating/cooling rate of 1 °C min^{-1}.

The shear stability of various dispersions of 40 nm L_{39}-B_{99} spheres was also studied (see Figure 6.9). These are important experiments, since the data displayed in Figure 6.7 and Figure 6.8 were collected at a constant shear rate of 100 s^{-1}. However, this nominal shear rate does not represent the relatively harsh conditions within an automotive engine. Therefore, the viscosity of dispersions at various copolymer concentrations over shear rates ranging from 10 to 1000 s^{-1} were measured at 25 °C (see Figure 6.9). It was observed that dispersions of 40 nm L_{39}-B_{99} spheres in base oil exhibited Newtonian-type behaviour, since the viscosity of each dispersion remained

independent of shear rate within this range. This indicates that the spheres are in fact stable up to shear rates of 1000 s^{-1} and at copolymer concentrations of up to 40% w/w solids, suggesting that such spheres may offer genuine potential for viscosity modification in base oil. As expected, the higher dispersion viscosities were obtained on increasing the copolymer concentration. At 25 °C, a 5% w/w copolymer dispersion (Figure 6.9, purple data) had a viscosity of ~0.025 Pa s, a 10% w/w dispersion (Figure 6.9, red data) had a viscosity of ~0.030 Pa s and a 20% w/w dispersion (Figure 6.9, green data) had a viscosity of ~0.050 Pa s. It is noteworthy that copolymer dispersions up to 20% w/w solids exhibited viscosities lower than the 12% w/w linear PMA reference shown in Figure 6.7. In fact, only on increasing the dispersion concentration up to 40% w/w (Figure 6.9, orange data) were higher viscosities (~0.40 Pa s) observed. This 40% w/w dispersion also showed Newtonian-type behaviour.

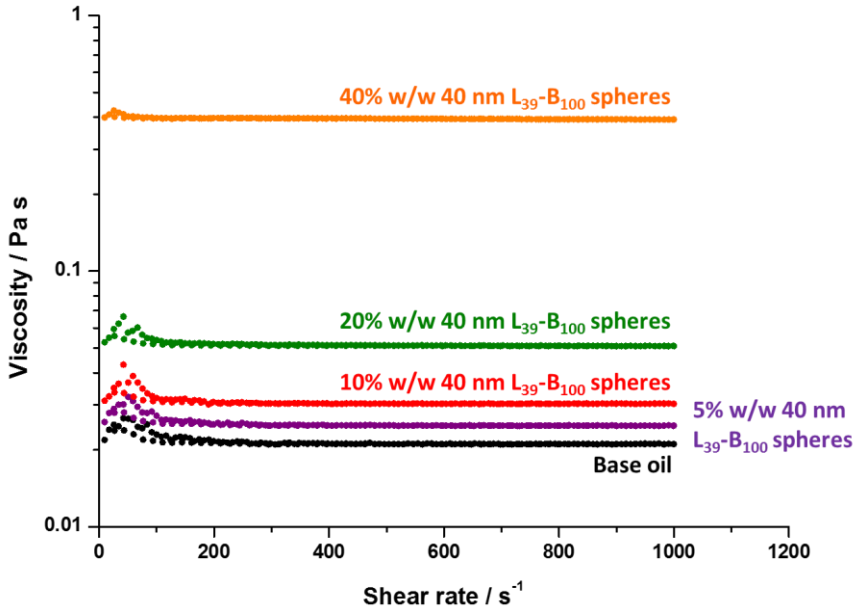

Figure 6.9. Shear rate vs. viscosity for base oil alone (black data), 5% w/w (purple data), 10% w/w (red data), 20% w/w (green data) and 40% w/w (orange data) 40 nm L_{39}-B_{99} spheres in base oil. Data were collected at 25 °C during a linear 10-1000-10 s^{-1} shear rate ramp over a 30 min time period.

6.3.2.2. Diblock copolymer worms as viscosity modifiers

Considering the promising viscosity modification properties exhibited by the 40 nm L_{39}-B_{99} spheres discussed in the previous Section, diblock copolymer worms were also assessed. It has been shown that block copolymer worms synthesised by RAFT-

mediated PISA form free-standing gels at sufficiently high copolymer concentrations.[23-32] Clearly, it would not be beneficial to add diblock copolymer worms at concentrations greater than the critical gelation concentration (CGC), but the potential for enhanced viscosities at lower concentrations was assessed. More specifically, $PLMA_{18}$-$PBzMA_{40}$ (L_{18}-B_{40}; M_n = 8,000 g mol^{-1}; M_w/M_n = 1.28) diblock copolymer worms were added to base oil and analysed for their viscosity modification using the same experimental protocol as described in the previous Section. In order to directly compare their viscosity modification performance, the L_{18}-B_{40} worms and the linear (PMA) reference polymer were added in turn to a base oil at concentrations corresponding to equal viscosity at 100 °C (4.0% w/w and 1.25% w/w, respectively). Figure 6.10 shows the viscosity-temperature profiles for these potential VM additives.

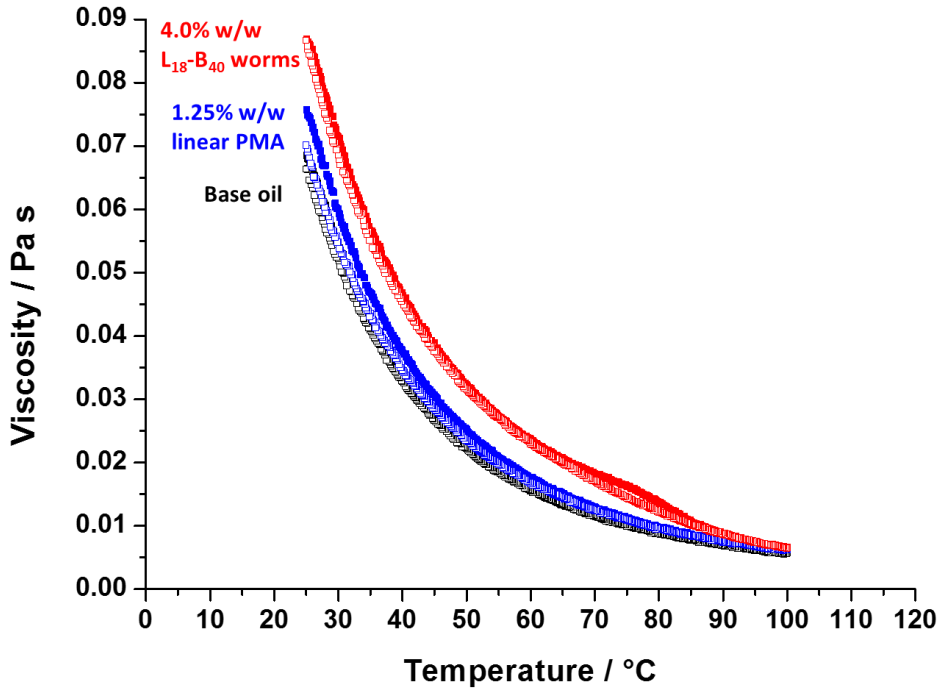

Figure 6.10. Viscosity-temperature profiles of base oil alone (black data), 1.25% w/w linear PMA reference additive (blue data) and 4.0% w/w L_{18}-B_{40} worms (red data) during heating (filled symbols) and cooling (open symbols) ramps. Data were collected during a 25-100-25 °C thermal cycle at a heating/cooling rate of 1 °C min^{-1}.

Clearly, the L_{18}-B_{40} worms (red data) provide much higher viscosities at lower temperatures than the PMA reference (blue data). This is not unexpected, since anisotropic worm-like nanoparticles are known to form free-standing gels via multiple inter-worm contacts at concentrations above the CGC, with viscous free-flowing

dispersions being observed below the CGC.[24] However, given that the optimal performance for a VM additive is high-temperature thickening with minimal thickening at ambient temperature, such worm-like nanoparticles do not offer appropriate VM performance. Nevertheless, the specific viscosity (as defined in Equation 6.2) of the base oil plus 4.0% w/w L_{18}-B_{40} worms or 1.25% w/w linear PMA over the same temperature range was calculated (see Figure 6.11).

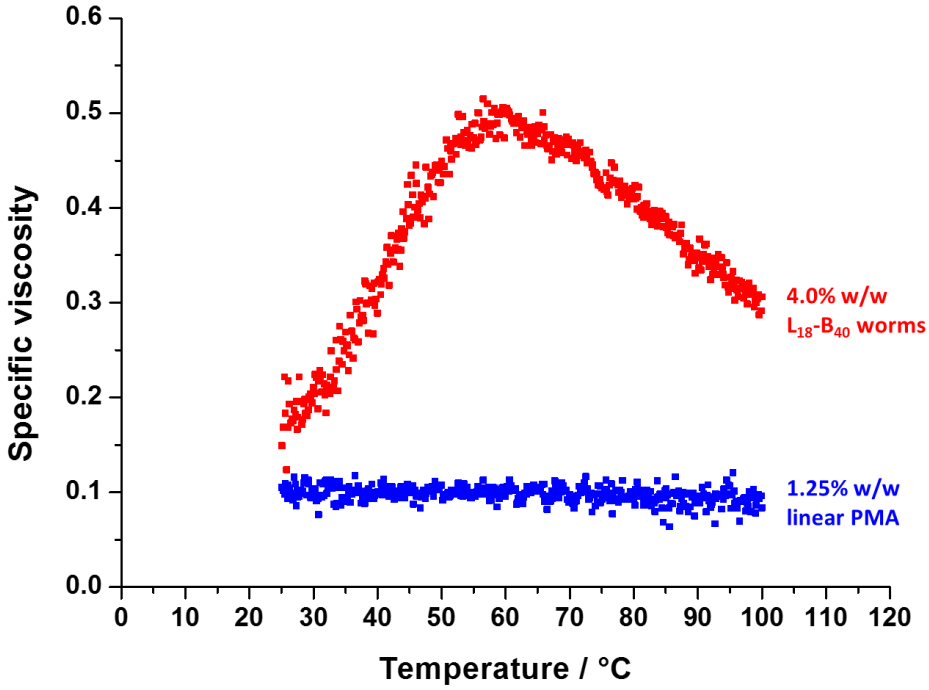

Figure 6.11. Specific viscosity vs. temperature for 4.0% w/w L_{18}-B_{40} worms (red data) and 1.25% w/w linear PMA reference additive (blue data) in base oil. Data were collected during a 25-100 °C heating ramp at a rate of 1 °C min^{-1}.

The specific viscosity of the base oil containing 1.25% w/w linear PMA (blue data) remains relatively constant between 25 °C and 100 °C. In contrast, the specific viscosity for the base oil containing 4.0% w/w L_{18}-B_{40} worms increases on heating from 25 °C to ~55 °C, before decreasing from 55 °C to 100 °C. This behaviour can be explained by considering the worm-to-sphere transition observed for PLMA-PBzMA diblock copolymer worms in various oils, which leads to a characteristic critical gelation temperature (CGT) of ~45-50 °C (see Section 2.3.3). This suggests that, above the CGT, the mixture of short worms and spheres present in the dispersion do not provide sufficient inter-particle interactions so a gel is no longer formed. This

explains the maximum in specific viscosity observed at a temperature that is comparable to the CGT observed for similar PLMA-PBzMA worms. This unusual behaviour, coupled with the undesirably high viscosity at ambient temperature suggests that such worm-like nanoparticles are not viable VMs for engine oils. In addition, the worm phase identified for the PISA formulations described in this Thesis is very narrow (~10 BzMA units), which is likely to make reproducible syntheses difficult to achieve on an industrial scale.

Considering the problems associated with the use of worm-like nanoparticles as VMs, an alternative solution to high-temperature thickening could be provided by exploiting the vesicle-to-worm transition described in Chapter 4. For example, a low-viscosity 10% w/w dispersion of $PSMA_{13}$-$PBzMA_{96}$ vesicles in mineral oil formed a very weak gel ($G' \approx 1$ Pa; $G'' \approx 0.5$ Pa) upon heating above 135 °C due to the *in situ* formation of worms. However, this vesicle-to-worm transition suffers from two significant disadvantages as a potential route to high-temperature thickening. Firstly, the initial $PSMA_{13}$-$PBzMA_{96}$ vesicles scatter light, which makes the oil turbid. Although this optical property is not necessarily a disadvantage in terms of performance, it is highly unlikely that the formulated oil consumers would accept such a turbid oil compared to the current transparent oils on the market. More importantly, the vesicle-to-worm transition is not fully reversible, meaning that thicker oils are likely to be formed at ambient temperature after just one thermal cycle. Nevertheless, this new mechanism for viscosity modification warrants further research to see whether such problems can be overcome. For example, in principle the turbidity could be addressed by utilising a copolymer that is contrast-matched to the engine oil. There are examples of such an approach in the PISA literature.[33]

6.3.3. Diblock copolymer spheres as wax inhibitors

6.3.3.1. Synthesis of poly(behenyl methacrylate)-poly(benzyl methacrylate) diblock copolymer spheres

Thus far, the potential applications of PLMA-PBzMA and PSMA-PBzMA diblock copolymer spheres and worms have been discussed. Extending the alkyl side chains of the stabiliser block from $C_{12}H_{25}$ or $C_{18}H_{37}$ to $C_{22}H_{45}$ by using a poly(behenyl

methacrylate) (PBhMA) macro-CTA for the RAFT dispersion polymerisation of BzMA suggests the possibility of wax inhibition applications. Firstly, a $PBhMA_{37}$ macro-CTA was synthesised via RAFT solution polymerisation in toluene as previously described for PLMA and PSMA macro-CTAs (see Chapters 2 and 3). However, in this case, the PETTC trithiocarbonate CTA (see Figure 1.18a) was utilised for the preparation of the $PBhMA_{37}$ macro-CTA (see Scheme 6.1) rather than the dithiobenzoate-based CTA (CDB) previously used for the preparation of PLMA and PSMA macro-CTAs.

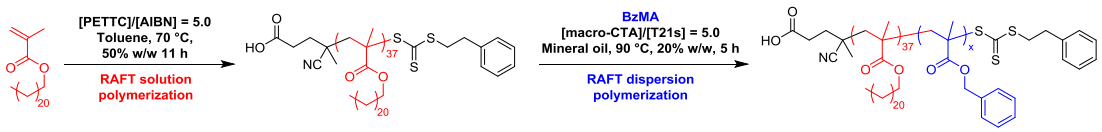

Scheme 6.1. Synthesis of a poly(behenyl methacrylate)$_{37}$ ($PBhMA_{37}$) macro-CTA via RAFT solution polymerisation in toluene, followed by the RAFT dispersion polymerisation of benzyl methacrylate (BzMA) in mineral oil.

Subsequent chain extension using BzMA yielded a series of $PBhMA_{37}$-$PBzMA_x$ (x = 50-1000) spheres whose size increased systematically with x (see Table 6.2) as described in the PISA literature upon when other relatively long stabiliser blocks.[20, 25, 34]

Table 6.2. Summary of particle diameters and molecular weight data for poly(behenyl methacrylate) (PBhMA) homopolymer and poly(behenyl methacrylate)-poly(benzyl methacrylate) (PBhMA-PBzMA) block copolymer spheres synthesised via RAFT dispersion polymerisation in mineral oil at 90 °C.

Composition	DLS diameter[a] / nm (PDI)	THF GPC (vs. PMMA)	
		M_n / g mol^{-1}	M_w/M_n
$PBhMA_{37}$	-	12,400	1.18
$PBhMA_{37}$-$PBzMA_{50}$	21 nm (0.08)	16,200	1.15
$PBhMA_{37}$-$PBzMA_{100}$	32 nm (0.01)	22,700	1.15
$PBhMA_{37}$-$PBzMA_{150}$	37 nm (0.02)	28,100	1.18
$PBhMA_{37}$-$PBzMA_{200}$	55 nm (0.01)	33,800	1.24
$PBhMA_{37}$-$PBzMA_{300}$	67 nm (0.01)	43,900	1.38
$PBhMA_{37}$-$PBzMA_{400}$	103 nm (0.07)	56,100	1.68
$PBhMA_{37}$-$PBzMA_{500}$	115 nm (0.08)	61,000	1.88
$PBhMA_{37}$-$PBzMA_{1000}$	167 nm (0.09)	105,800	2.87

[a] As determined for a 0.10% w/w dispersion in *n*-dodecane at 50 °C.

DLS studies indicated that the $PBhMA_{37}$-$PBzMA_x$ diblock copolymer spheres shown in Table 6.2 displayed narrow size distributions for spheres ranging from 21 nm (x = 50) to 167 nm (x = 1000) in diameter (see Figure 6.12), which is similar to the PSMA-PBzMA spheres discussed in Chapter 3. GPC analysis (Figure 6.13a) confirmed relatively good control over the MWD when targeting PBzMA DPs up to 200, since $M_w/M_n < 1.30$. However, gradual loss of control is observed when targeting DPs of 300 to 1000, with M_w/M_n increasing from 1.38 up to 2.87. Despite this problem, the M_n values for all $PBhMA_{37}$-$PBzMA_x$ diblock copolymers in Table 6.2 increased linearly when targeting higher PBzMA DPs as expected (see Figure 6.13b). Blocking efficiencies are estimated to be around 90% for this formulation, with unreacted macro-CTA being evident when targeting $PBhMA_{37}$-$PBzMA_{1000}$.

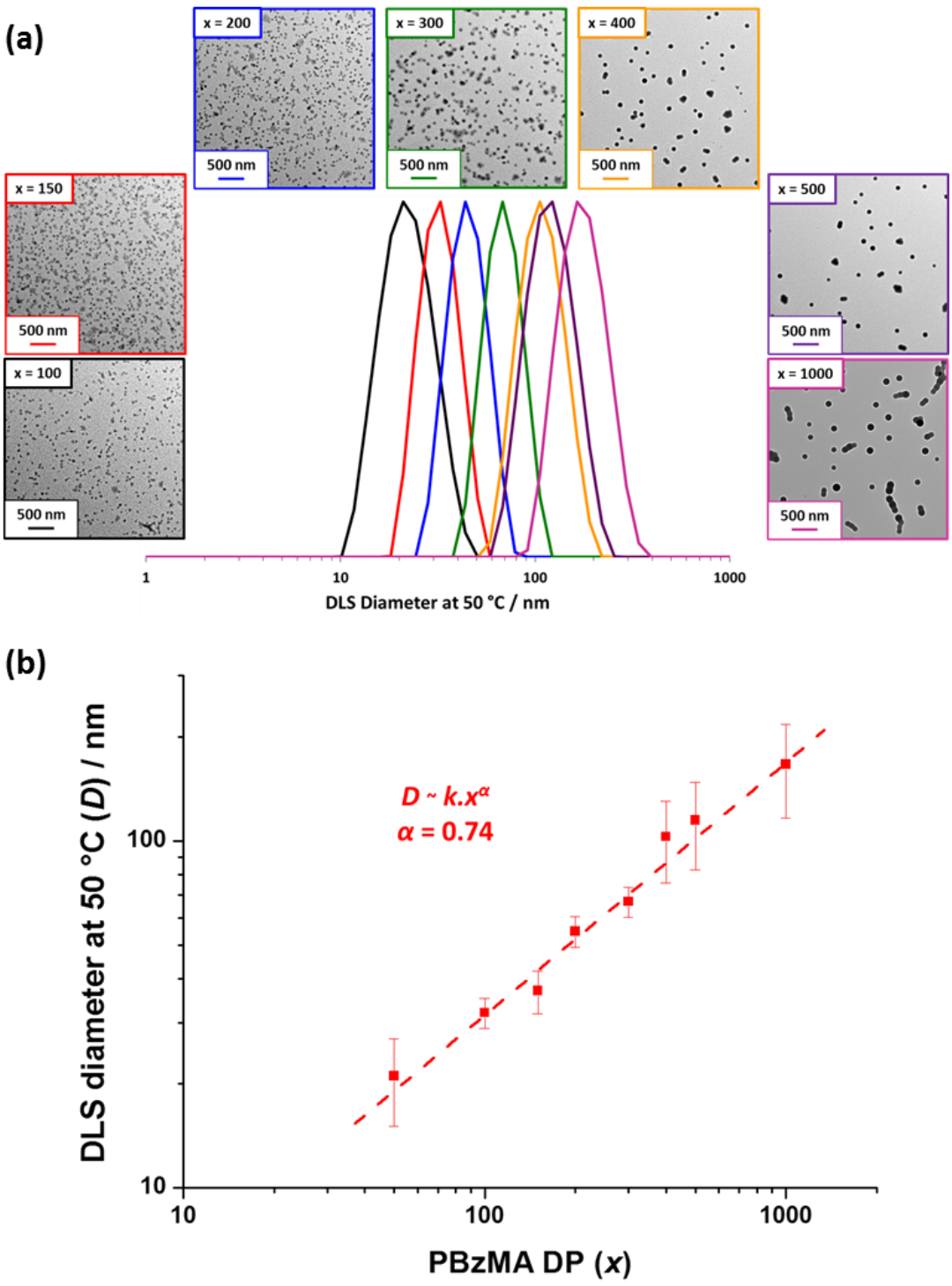

Figure 6.12. (a) Transmission electron micrographs and dynamic light scattering (DLS) size distributions for 0.10% w/w dispersions of $PBhMA_{37}$-$PBzMA_x$ (x = 50-1000) diblock copolymer spheres. Samples were prepared at 50 °C. (b) DLS diameter at 50 °C (*D*) vs. PBzMA DP (*x*) plot indicates an α scaling exponent of 0.74.

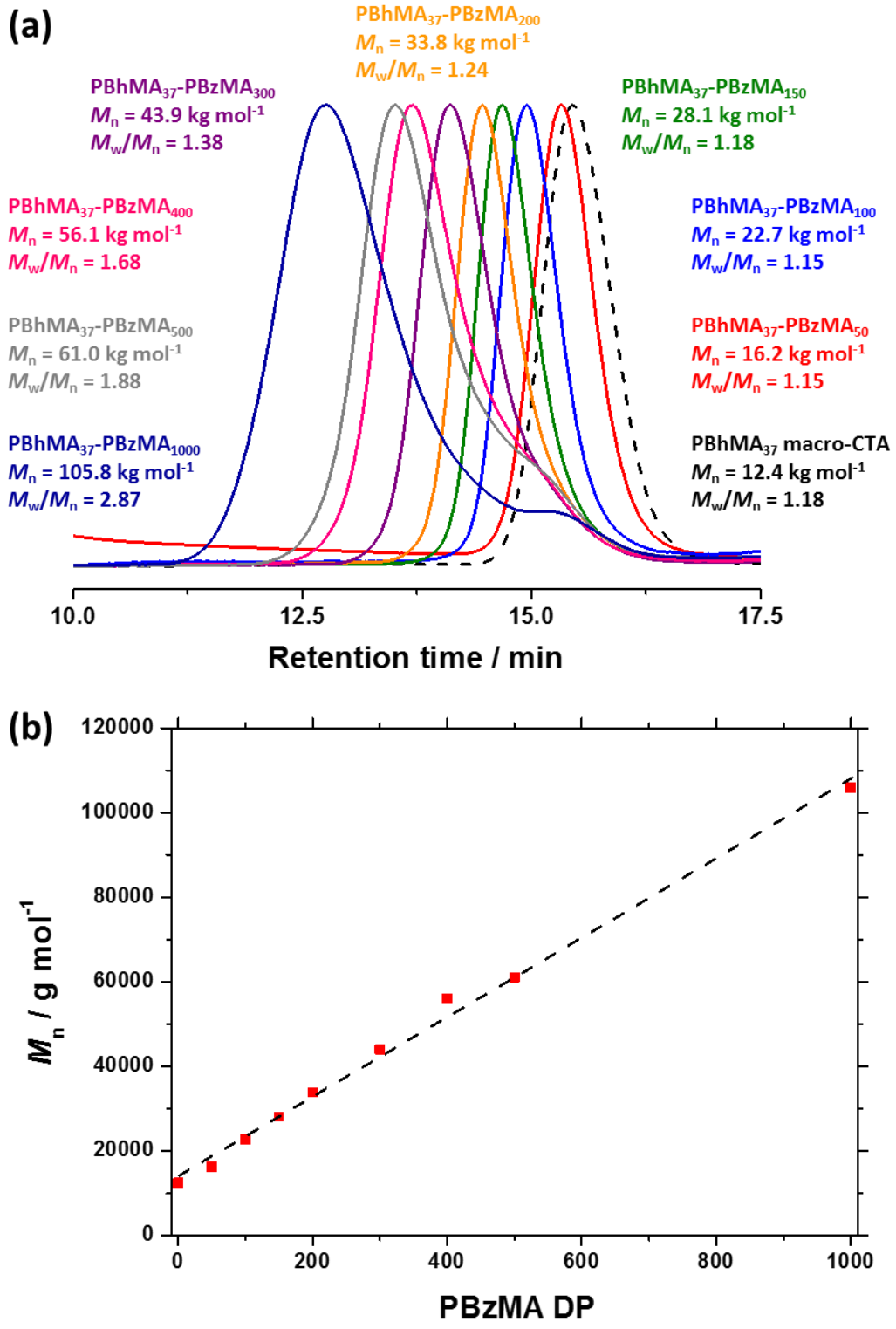

Figure 6.13. (a) THF gel permeation chromatograms (vs. poly(methyl methacrylate) standards) obtained for the series of $PBhMA_{39}$-$PBzMA_x$ diblock copolymer spheres synthesised via RAFT dispersion polymerisation of BzMA in mineral oil at 90 °C and 20% w/w solids. The precursor $PBhMA_{39}$ macro-CTA (prepared in toluene at 70 °C and 40% w/w solids; black dashed curve) is also shown as a reference. (b) M_n vs. PBzMA DP plot for the same $PBhMA_{39}$-$PBzMA_x$ series, where x = 0 represents the $PBhMA_{37}$ macro-CTA.

Interestingly, the $PBhMA_{37}$ stabiliser block exhibits UCST-type behaviour in mineral oil (see Figure 6.14), with ~100% transmittance at 50 °C and ~0% transmittance at 20 °C. On cooling, the UCST appears to be ~31.5 °C, however this critical temperature increases to ~44.5 °C on heating, which could be due to C_{22} side chain crystallisation.

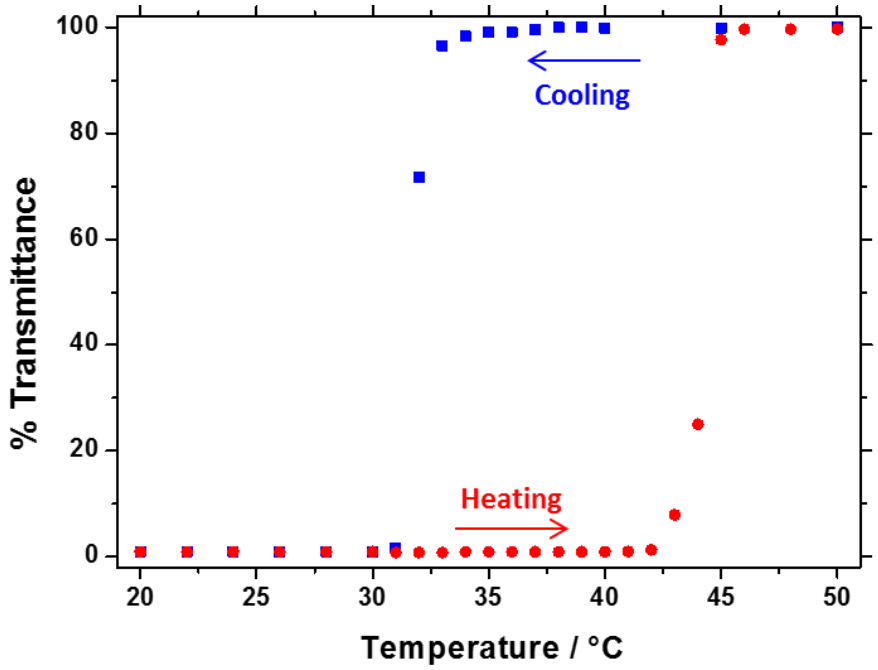

Figure 6.14. % Transmittance vs. temperature plot for a 1.0% w/w solution of $PBhMA_{37}$ in mineral oil during cooling (blue squares) and heating (red circles) steps. Data were collected at 650 nm after 5 min equilibration at each temperature.

This thermal transition causes the dispersions of $PBhMA_{37}$-$PBzMA_x$ spheres to form turbid free-standing gels on cooling to room temperature, which is fully reversible; heating the flocculated dispersions up to 50 °C produces a range of free-flowing dispersions of increasing turbidity (see Figure 6.15.), as expected for dispersions containing larger nanoparticles. Thus, the DLS data reported in Table 6.2 were obtained at 50 °C in order to ensure that the spherical nanoparticles were well dispersed, rather than flocculated.

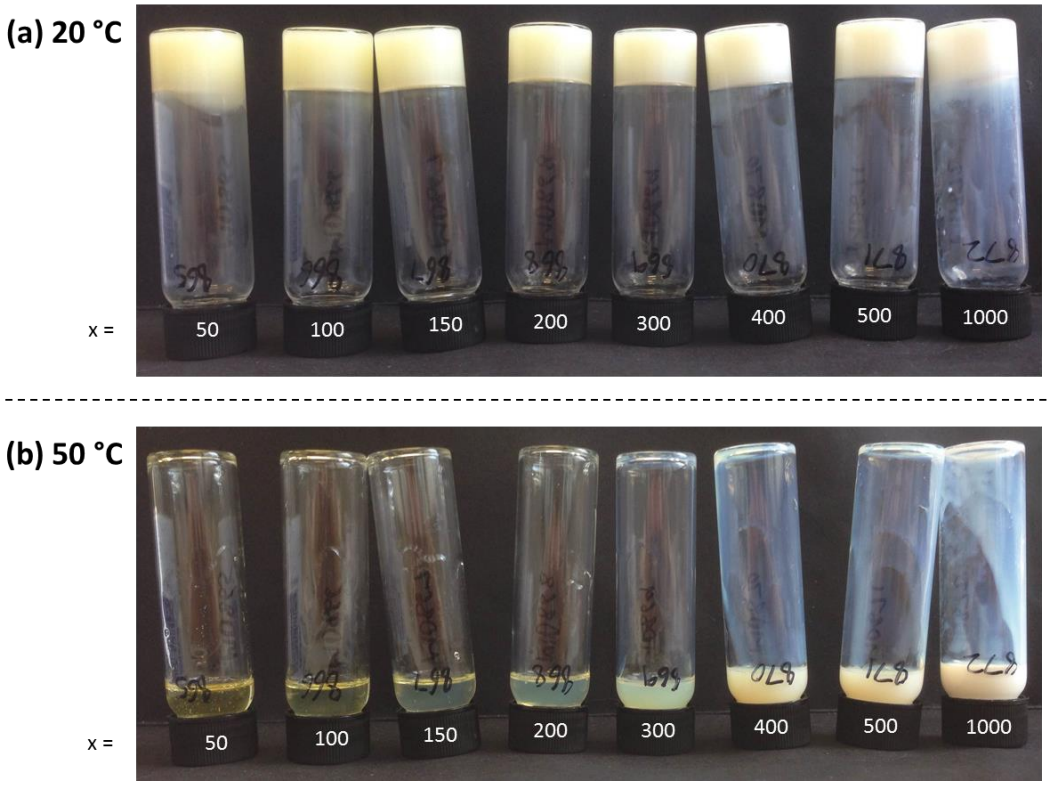

Figure 6.15. Digital images recorded for 20% w/w dispersions of $PBhMA_{37}$-$PBzMA_x$ diblock copolymer spheres in mineral oil at (a) 20 °C and (b) 50 °C. Turbid free-standing gels are obtained at 20 °C due to the UCST behaviour of the $PBhMA_{37}$ stabiliser block, whereas free-flowing dispersions of varying turbidity are obtained on heating to 50 °C, which is above the UCST of 31.5 °C or 44.5 °C. This thermal transition is fully reversible.

6.3.3.2. Wax inhibition testing

It has already been shown that ~40 nm diameter spheres offer better lubricity performance, and that spheres of a similar size also show promising viscosity modification behaviour. Therefore, the 37 nm spheres $PBhMA_{37}$-$PBzMA_{150}$ (see Table 6.2) were selected in order to assess for their wax inhibition performance in crude oil. Retarding the growth of wax crystals in crude oil is important in the oil industry, since this helps prevent the blockage of crude oil pipelines in many parts of the world.[15] If the crude oil solidifies, the pipelines may even be rendered useless.[12] Prior research suggests that polymeric additives, particularly poly(alkyl methacrylates) with pendant alkyl chains comprising 20-30 carbon atoms,[12] offer significant potential for wax inhibition. The mechanism of wax inhibition is believed to involve such polymers adsorbing onto the growing wax crystals, leading to retarded crystal growth and such additives are known as pour point depressants (PPDs). Thus, the performance of both PBhMA homopolymer and PBhMA-stabilised spheres as wax

inhibitors in crude oil was assessed and compared to an industry-leading commercial PPD (see Figure 6.16).

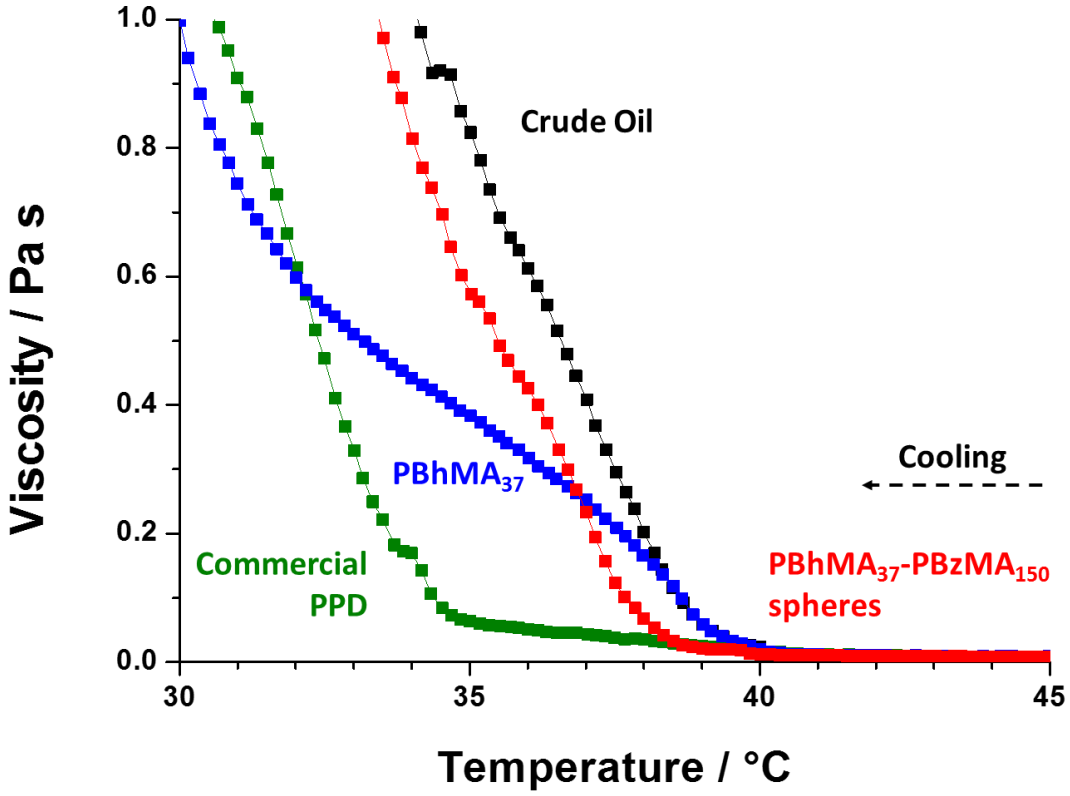

Figure 6.16. Viscosity-temperature profiles obtained on cooling at 1 °C min^{-1} for crude oil alone (black data), 0.1% w/w $PBhMA_{37}$ homopolymer (blue data), 0.1% w/w $PBhMA_{37}$-$PBzMA_{150}$ spheres (red data) and 0.1% w/w commercial pour point depressant (PPD, green data) at a constant applied shear rate of 30 s^{-1}.

The crude oil used in this study showed an onset in viscosity increase of ~40 °C (black data, Figure 6.16). On addition of 0.1% w/w $PBhMA_{37}$ homopolymer, this onset in viscosity increase remained unchanged (blue data, Figure 6.16), which indicates that $PBhMA_{37}$ alone does not act as an efficient PPD. Conversely, 0.1% w/w 37 nm $PBhMA_{37}$-$PBzMA_{150}$ spheres reduced thin onset by ~1.5 °C (red data, Figure 6.16). This suggests that the pendant alkyl chains on the $PBhMA_{37}$ chains can more effectively interact with the growing wax crystals when present in the form of nanoparticles. However, this performance was clearly inferior compared to the same concentration of the commercial PPD used in this study (green data, Figure 6.16), which reduced the onset of viscosity increase by ~5 °C. It is therefore evident that, at least for this particular crude oil, 0.1% w/w 37 nm $PBhMA_{37}$-$PBzMA_{150}$ spheres are

not effective PPDs. In order to further investigate the potential wax inhibition performance of PBhMA-stabilised nanoparticles, a range of spheres of varying mean diameter should be assessed for a range of crude oils. This is particularly important since the solubility of a given PPD will vary in different crude oils, and this PPD solubility is known to play a major role in the performance of a PPD.[15]

6.3.4. Diblock copolymer spheres as asphaltene dispersants

The dispersion of asphaltenes in crude oil is another method employed to prevent the blockage of crude oil pipelines.[16] Dynamic turbidimetry is a laboratory technique which is commonly employed to analyse the performance of asphaltene dispersants, whereby the mean transmittance of a solution of crude oil containing an asphaltene dispersant in *n*-heptane is measured over time. The role of the *n*-heptane is to precipitate the asphaltene component of the crude oil, since asphaltenes are insoluble in *n*-alkanes.[16] Thus the ability of the additive to disperse the asphaltenes under such conditions can be assessed. At the beginning of the experiment, the mean transmittance is 0% since the asphaltenes are well dispersed. As the precipitating asphaltenes gradually sediment over time, the mean transmittance of the dispersion increases. Thus, the ideal performance for an asphaltene dispersant corresponds to a mean transmittance of 0% regardless of the ageing time. In practice, such performance is unlikely, but the challenge for the oil industry is to prolong the stability of the crude oil for as long as possible. A range of diblock copolymer spheres, prepared by RAFT dispersion polymerisation in mineral oil, and a $PBhMA_{37}$ homopolymer, prepared by RAFT solution polymerisation in toluene, were assessed as putative asphaltene dispersants (Figure 6.17).

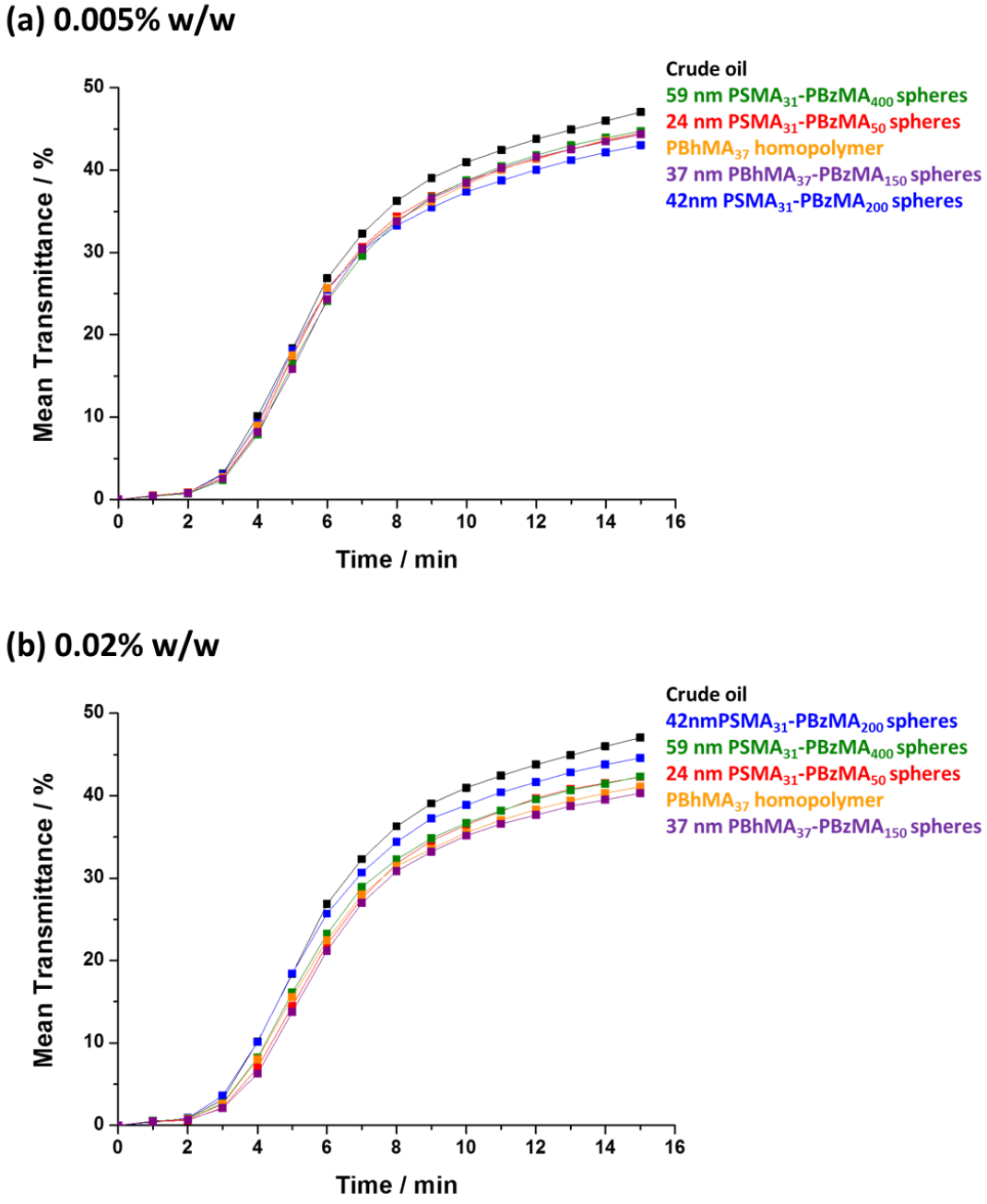

Figure 6.17. (a) Mean transmittance vs. time curves obtained for a mixture of crude oil and *n*-heptane (added as an asphaltene precipitant) containing no polymeric additive (black data) with 0.005% w/w 24 nm $PSMA_{31}$-$PBzMA_{50}$ spheres (red data), 42 nm $PSMA_{31}$-$PBzMA_{200}$ spheres (blue data), 59 nm $PSMA_{31}$-$PBzMA_{400}$ spheres (green data), $PBhMA_{37}$ homopolymer (orange data) and 37 nm $PBhMA_{37}$-$PBzMA_{150}$ spheres (purple data). (b) The same experiment repeated using 0.02% w/w (co)polymer additive.

Firstly, solutions where the total polymer concentration was 0.005% w/w were analysed (Figure 6.17a). After 15 minutes, the mean transmittance of the solutions were reduced relative to the crude oil in *n*-heptane alone (black data). However, this

reduction in transmittance was modest compared to that provided by commercial asphaltene dispersants. The performance of these potential dispersants was compared using the following equation:

$$\%\ Dispersion = \frac{T_{\text{crude}} - T_{\text{disp}}}{T_{\text{crude}}} \times 100 \qquad 6.3$$

where T_{crude} is the final mean transmittance of the crude oil in *n*-heptane alone and T_{disp} is the final mean transmittance of the same solution containing the potential asphaltene dispersant. Comparing % dispersion values allows direct comparison of each of the potential asphaltene dispersants (see Table 6.3). According to this data set, 42 nm $PSMA_{31}$-$PBzMA_{200}$ spheres (Figure 6.17a, blue data) was the best performing dispersant at 0.005% w/w.

Table 6.3. % Dispersion (as calculated using Equation 6.3) for asphaltenes in a crude oil in the presence of a range of polymeric additives at 0.005% w/w and 0.02% w/w.

Polymeric additive	**% Dispersion**	
	0.005% w/w	**0.02% w/w**
24 nm $PSMA_{31}$-$PBzMA_{50}$ spheres	5.4	10.2
42 nm $PSMA_{31}$-$PBzMA_{200}$ spheres	8.5	5.3
59 nm $PSMA_{31}$-$PBzMA_{400}$ spheres	4.9	10.0
$PBhMA_{37}$ homopolymer	5.7	12.7
37 nm $PBhMA_{37}$-$PBzMA_{150}$ spheres	5.7	14.3

The same asphaltene dispersants were assessed at a total polymer concentration of 0.02% w/w (Figure 6.17b). As expected, a higher dispersant concentration generally provided better performance. However, the best performing dispersant at 0.005% w/w (42 nm $PSMA_{31}$-$PBzMA_{200}$ spheres) actually provided a lower % dispersion value at 0.02% w/w, and was the worst performing dispersant at this concentration (Figure 6.17b, blue data). In fact, the 37 nm $PBhMA_{37}$-$PBzMA_{150}$ spheres provided the best performance here. Ultimately, at least for this data set, it is not possible to determine an optimum sphere size or even stabiliser block type for effective asphaltene

dispersion. Furthermore, the performance of sterically-stabilised diblock copolymer spheres cannot be distinguished from that of the stabiliser block alone.

6.4. Conclusions

Poly(lauryl methacrylate)-poly(benzyl methacrylate) (PLMA-PBzMA) diblock copolymer spheres are promising lubricant additives for base oil. Specifically, 42 nm $PLMA_{47}$-$PBzMA_{46}$ spheres reduced the friction coefficient of a base oil and provided significantly better performance than 116 nm $PLMA_{47}$-$PBzMA_{297}$ spheres. The presence of just one methacrylic acid (MAA) residue per stabilising chain further reduced the friction coefficient of the base oil, with 41 nm P[LMA_{49}-MAA_{1}]-$PBzMA_{47}$ spheres offering comparable performance to glyceryl monooleate (GMO). The use of 46 nm poly(stearyl methacrylate)$_{31}$-poly[(benzyl methacrylate)$_{200}$-*stat*-(ethylene glycol dimethacrylate)$_{20}$] ($PSMA_{31}$-P[$BzMA_{200}$-$EGDMA_{20}$]) spheres highlights the potential for obtaining significantly lower friction coefficients in the boundary lubrication regime. However, only moderate performance was observed on adding the same diblock copolymer spheres to a fully-formulated automotive gear oil (AGO), although some lubricity improvement was observed under these conditions.

Similar 40 nm $PLMA_{39}$-$PBzMA_{100}$ spheres exhibited very promising viscosity modification properties in a base oil. The oil viscosity was higher at 100 °C with less thickening at 25 °C than when using a linear poly(methacrylate) (PMA) reference additive. In fact, the specific viscosity (η_{sp}) of the base oil plus 40 nm $PLMA_{39}$-$PBzMA_{100}$ spheres increased at higher temperature, indicating a greater contribution to the oil viscosity from these nanoparticles. Although providing high-temperature thickening, $PLMA_{18}$-$PBzMA_{40}$ worms are not viable VMs because the oil viscosity at 25 °C was too high. Also, the narrow phase space occupied by worm-like nanoparticles would most likely make reproducible PISA syntheses difficult to achieve on an industrial scale.

Introducing longer alkyl side chains in the stabiliser block enabled the potential wax inhibition properties of poly(behenyl methacrylate)-poly(benzyl methacrylate) (PBhMA-PBzMA) spheres to be evaluated. Specifically, 37 nm $PBhMA_{37}$-$PBzMA_{150}$ spheres reduced the onset of viscosity increase of a crude oil as a result of retarded

wax crystal growth, but not as effectively as an industry-leading pour point depressant (PPD). Additionally, $PSMA_{31}$-$PBzMA_x$ and $PBhMA_{37}$-$PBzMA_x$ spheres, as well as the $PBhMA_{37}$ homopolymer, do not appear to offer significant benefit as asphaltene dispersants.

6.5. References

1. R. Zheng, G. Liu, M. Devlin, K. Hux and T.-C. Jao, *Tribology Transactions*, 2010, **53**, 97-107.
2. R. Zheng, G. Liu and T.-C. Jao, *Polymer*, 2007, **48**, 7049-7057.
3. S. Morgan, Z. Ye, R. Subramanian and S. Zhu, *Polymer Engineering & Science*, 2010, **50**, 911-918.
4. W. Li, Y. Li, Y. Hu and Y. Wang, *Lubrication Science*, 2012, **24**, 188-197.
5. S. A. Mohamad, N. S. Ahmed, S. M. Hassanein and A. M. Rashad, *Journal of Petroleum Science and Engineering*, 2012, **100**, 173-177.
6. A. M. Nassar, N. S. Ahmed, R. S. Kamal, A.-A. A. Abdel Azim and E. I. El-Nagdy, *Petroleum Science and Technology*, 2005, **23**, 537-546.
7. M. J. Souza de Carvalho, P. Rudolf Seidl, C. R. Pereira Belchior and J. Ricardo Sodré, *Tribology International*, 2010, **43**, 2298-2302.
8. Z. Janovic, K. Saric and K. Sertic-Bionda, *Chemical and Biochemical Engineering Quarterly*, 1998, **12**, 19-24.
9. A. Jukic, E. Vidovic and Z. Janovic, *Chemistry and Technology of Fuels and Oils*, 2007, **43**, 386-394.
10. R. L. Stambaugh and B. G. Kinker, *Viscosity Index Improvers and Thickeners*, Springer-Verlag Berlin, Berlin, 2010.
11. M. d. C. García, *Energy & Fuels*, 2000, **14**, 1043-1048.
12. K. S. Pedersen and H. P. Rønningsen, *Energy & Fuels*, 2003, **17**, 321-328.
13. A. Aiyejina, D. P. Chakrabarti, A. Pilgrim and M. K. S. Sastry, *International Journal of Multiphase Flow*, 2011, **37**, 671-694.
14. B. Wei, *Journal of Petroleum Exploration and Production Technology*, 2014, **5**, 391-401.
15. B. P. Binks, P. D. I. Fletcher, N. A. Roberts, J. Dunkerley, H. Greenfield, A. Mastrangelo and K. Trickett, *Physical Chemistry Chemical Physics*, 2015, **17**, 4107-4117.
16. K. Kraiwattanawong, H. S. Fogler, S. G. Gharfeh, P. Singh, W. H. Thomason and S. Chavadej, *Energy & Fuels*, 2009, **23**, 1575-1582.
17. O. P. Strausz, T. W. Mojelsky and E. M. Lown, *Fuel*, 1992, **71**, 1355-1363.
18. H. Groenzin and O. C. Mullins, *Energy & Fuels*, 2000, **14**, 677-684.
19. C.-L. Chang and H. S. Fogler, *Langmuir*, 1994, **10**, 1749-1757.
20. E. R. Jones, M. Semsarilar, A. Blanazs and S. P. Armes, *Macromolecules*, 2012, **45**, 5091-5098.
21. J. S. Trent, *Macromolecules*, 1984, **17**, 2930-2931.
22. S. Sugihara, S. P. Armes, A. Blanazs and A. L. Lewis, *Soft Matter*, 2011, **7**, 10787-10793.
23. A. Blanazs, R. Verber, O. O. Mykhaylyk, A. J. Ryan, J. Z. Heath, C. W. I. Douglas and S. P. Armes, *Journal of the American Chemical Society*, 2012, **134**, 9741-9748.

24. R. Verber, A. Blanazs and S. P. Armes, *Soft Matter*, 2012, **8**, 9915-9922.
25. L. A. Fielding, M. J. Derry, V. Ladmiral, J. Rosselgong, A. M. Rodrigues, L. P. D. Ratcliffe, S. Sugihara and S. P. Armes, *Chemical Science*, 2013, **4**, 2081-2087.
26. L. A. Fielding, J. A. Lane, M. J. Derry, O. O. Mykhaylyk and S. P. Armes, *Journal of the American Chemical Society*, 2014, **136**, 5790-5798.
27. V. J. Cunningham, L. P. D. Ratcliffe, A. Blanazs, N. J. Warren, A. J. Smith, O. O. Mykhaylyk and S. P. Armes, *Polymer Chemistry*, 2014, **5**, 6307-6317.
28. N. J. Warren and S. P. Armes, *Journal of the American Chemical Society*, 2014, **136**, 10174-10185.
29. Y. W. Pei, N. C. Dharsana, J. A. Van Hensbergen, R. P. Burford, P. J. Roth and A. B. Lowe, *Soft Matter*, 2014, **10**, 5787-5796.
30. Y. Pei, O. R. Sugita, L. Thurairajah and A. B. Lowe, *RSC Advances*, 2015, **5**, 17636-17646.
31. Y. Pei, L. Thurairajah, O. R. Sugita and A. B. Lowe, *Macromolecules*, 2015, **48**, 236-244.
32. A. P. Lopez-Oliva, N. J. Warren, A. Rajkumar, O. O. Mykhaylyk, M. J. Derry, K. E. B. Doncom, M. J. Rymaruk and S. P. Armes, *Macromolecules*, 2015, **48**, 3547-3555.
33. M. Semsarilar, E. R. Jones and S. P. Armes, *Polymer Chemistry*, 2014, **5**, 195-203.
34. Y. Li and S. P. Armes, *Angewandte Chemie-International Edition*, 2010, **49**, 4042-4046.

7. Conclusions and Future Work

Conclusions and Future Work

Various non-polar PISA formulations were explored in this Thesis. The RAFT dispersion polymerisation of BzMA at 90 °C was examined in industrially relevant mineral and poly(α-olefin) oils using PLMA, PSMA or PBhMA stabiliser macro-CTAs comprising varying *n*-alkyl side chain lengths (C_{12}, C_{18} and C_{22}, respectively). Good control over the RAFT polymerisation (final diblock copolymers with $M_w/M_n \leq 1.30$) was achieved when targeting PBzMA DPs up to 500 using a $PSMA_{31}$ macro-CTA. However, similar control was only achieved when targeting PBzMA DPs up to around 200-300 using $PLMA_{47}$ and $PBhMA_{37}$ macro-CTAs. This significant difference is not yet understood and further work is required to rationalise these unexpected results. Empirically, it is clear that PSMA macro-CTAs are preferred for academic studies.

In all PISA formulations, stabiliser block DP is an important parameter when targeting a specific copolymer morphology. When using sufficiently long stabilisers (e.g. $PLMA_{39}$, $PSMA_{18}$ or $PBhMA_{37}$), only kinetically-trapped spherical nanoparticles are accessible due to inefficient sphere-sphere fusions which are a prerequisite for the formation of so-called higher order morphologies (i.e. worms or vesicles). This constraint is actually useful when spherical nanoparticles are required (e.g. for lubricity applications) and the mean sphere diameter can be readily tuned by systematically varying the core-forming PBzMA DP. Additionally, it was found that spheres synthesised using macro-CTAs with different DPs (e.g. $PSMA_{31}$ and $PSMA_{18}$) exhibited different scaling relationships between spherical diameter (D) and PBzMA DP (x), where $D = k.x^{\alpha}$. An α scaling factor of 0.50 was obtained for $PSMA_{31}$-$PBzMA_x$ spheres, which indicates unperturbed PBzMA chains, whereas $\alpha = 0.61$ for $PSMA_{18}$-$PBzMA_x$ spheres, indicating more stretched/solvated PBzMA chains. Importantly, a highly convenient 'one-pot' synthetic protocol has been developed, whereby targeted 39 nm $PLMA_{50}$-$PBzMA_{100}$ spheres can be synthesised from their monomer building blocks via successive RAFT solution and dispersion polymerisations conducted in mineral oil at 70% w/w and 30% w/w solids respectively within 9 h. It was also demonstrated that $PLMA_{47}$-$PBzMA_{100}$ spheres can be synthesised at copolymer concentrations up to 50% w/w solids. Evaluating various diblock copolymer spheres for their lubricity performance highlighted that the optimum diameter is approximately

40 nm. More specifically, 41 nm P[LMA_{49}-MAA_1]-$PBzMA_{47}$ spheres offer comparable lubricity performance compared to the industry standard, GMO. Similar 40 nm $PLMA_{39}$-$PBzMA_{100}$ spheres also provide promising viscosity modification properties compared to a linear soluble PMA reference. Additionally, 37 nm $PBhMA_{37}$-$PBzMA_{150}$ spheres offered modest wax inhibition and asphaltene dispersion properties.

Using shorter stabiliser macro-CTAs (e.g. $PLMA_{18}$ or $PSMA_{13}$) allows access to the full range of copolymer morphologies: spheres, worms and vesicles. Phase diagrams for PLMA-PBzMA diblock copolymer nanoparticles in mineral oil and a poly(*α*-olefin) indicated that changing the solvent leads to subtle differences in the phase space occupied by pure spheres, worms and vesicles. Interestingly, $PSMA_{13}$-$PBzMA_x$ nanoparticles synthesised in mineral oil exhibited little dependence on the copolymer concentration, with pure sphere, worm and vesicle phases all being accessible at 5% w/w solids. Conversely, various PLMA-PBzMA phase diagrams in *n*-heptane, *n*-dodecane, as well mineral and the poly(*α*-olefin) reported in this Thesis show that copolymer concentrations of at least 12.5% w/w are required to access such pure phase spaces. This is not yet understood and again warrants further research.

The evolution of nanoparticle morphology when targeting $PSMA_{31}$-$PBzMA_{2000}$ spheres and $PSMA_{13}$-$PBzMA_{150}$ vesicles was monitored using *in situ* synchrotron SAXS. When targeting $PSMA_{31}$-$PBzMA_{2000}$ spheres, the PBzMA core diameter increases monotonically during the polymerisation, with increasing aggregation numbers (N_s) also being observed (final PBzMA core diameter: D_{co} = 117 nm; N_s = 1688). The volume fraction of BzMA monomer within these cores is relatively high just after nucleation occurs, with this local monomer concentration leading to the observed increase in polymerisation rate. The average distance between adjacent copolymer chains at the core-shell interface increases during the polymerisation until a limiting value of 5.0 nm is reached. When targeting $PSMA_{13}$-$PBzMA_{150}$ vesicles, the full range of copolymer morphologies is observed, from soluble copolymer chains to the final vesicular morphology via intermediate spheres and worms. Detailed TEM studies of a laboratory-scale synthesis of such vesicles confirmed that the final vesicles are formed from worms via transient octopi and jellyfish morphologies, as first reported by Blanazs et al. for an aqueous PISA formulation. This suggests that the

mechanism of vesicle formation is universal for all PISA formulations. Within vesicle phase space, the membrane thickness (T_m) increases monotonically with increasing PBzMA DP. Subsequent *post mortem* SAXS analyses for $PSMA_{13}$-$PBzMA_x$ vesicles (when x = 150-400) shows that T_m varies with PBzMA DP (x) according to $T_m = k.x^{0.86}$. Importantly, the overall vesicle dimensions remain relatively constant within this DP range, which supports the 'inward growth' mechanism previously reported by Warren et al. for an aqueous PISA formulation. Thus, such an 'inward growth' mechanism for diblock copolymer vesicles synthesised by PISA is likely to be universal. The development of such robust *in situ* SAXS protocols provides the opportunity to investigate morphological transformations for a wide range of PISA formulations (i.e. aqueous or alcoholic, plus more exotic solvents such as supercritical CO_2 or ionic liquids).

In addition to *in situ* observations, post-polymerisation morphological transitions are observed for various poly(*n*-alkyl methacrylate)-PBzMA diblock copolymer nanoparticles. As suggested for closely related formulations, such transformations are the result of surface plasticisation of the PBzMA core-forming block at elevated temperatures, which is caused by the ingress of hot solvent. Such surface plasticisation was invoked to explain the observed morphology transformations in relation to the packing parameter (P) and are supported by SAXS and NMR observations. On heating certain diblock copolymer nano-objects, either worm-to-sphere and vesicle-to-worm transitions can be observed. In both cases, a reduction in the packing parameter must occur, thus suggesting that the volume of the core-forming block (V) is also reduced. If *uniform* plasticisation of the core-forming PBzMA block occurred, V would actually increase and lead to a larger value of P. Only *surface* plasticisation, where the BzMA residues closest to the block junction become solvated by the hot solvent, results in a reduction in V and therefore a reduction in P.

The worm-to-sphere transition results in degelation of initial free-standing worm gels to form free-flowing dispersions of spheres. These structural and physical transformations have been characterised using TEM, DLS and both oscillatory and rotational rheology. Birefringence was observed for $PSMA_{13}$-$PBzMA_{65}$ worms in mineral oil using shear-induced polarised light imaging (SIPLI). For spheres at 150 °C, no birefringence was observed because such nanoparticles are isotropic. On

cooling, a classic Maltese cross pattern is observed when anisotropic worms are present, but loss of this birefringence occurred on cooling further to 20 °C, which is attributed to the formation of branched/clustered worms. Such SIPLI studies should be supplemented by *in situ* SAXS studies in future work, since this should provide additional structural insights.

Similarly, $PSMA_{13}$-$PBzMA_{96}$ vesicles form worms on heating to 150 °C as judged by TEM and SAXS studies. Interestingly, this morphological transition results in a dramatic increase in viscosity for a 10% w/w dispersion of $PSMA_{13}$-$PBzMA_{96}$ nanoparticles in mineral oil when heating above 130 °C due to the formation of inter-worm contacts. This provides a potential route to high temperature thickening of engine oils, which could in principle have a significant impact within the automotive industry. However, the vesicle-to-worm transition reported in this Thesis is not fully reversible and the initial turbidity of the $PSMA_{13}$-$PBzMA_{96}$ vesicles is likely to be problematic for the consumer market. Therefore, further research is required to obtain a formulation which offers such high temperature thickening without the associated disadvantages. One possibility in this regard may be to design transparent PISA formulations using contrast-matched vesicles.

Clearly, there is much promise for the use of diblock copolymer nanoparticles, particularly spheres, over a range of applications in the automotive industry. Ideally, new protocols for the synthesis of such diblock copolymer spheres using cheaper starting materials should also be developed. For example, MMA is a cheap oil-soluble monomer which could be used to chain extend an oil-soluble macro-CTA to form an oil-insoluble PMMA block. Moreover, cheap monomer stocks containing mixtures of C_{12}-C_{15} methacrylates are widely used in industry and are likely to stabilise such PMMA nanoparticles. Ultimately, a comprehensive matrix of diblock copolymer nanoparticles with various sizes, chemical compositions and functionalities should be prepared and examined for their performance in a wide range of applications. Initial studies by the industrial sponsor of this PhD Thesis (Lubrizol Corporation Ltd.) have confirmed that the 'one-pot' PISA syntheses described herein can be performed on an 18 kg scale.

8. Appendix

8.1. Structural Models for Small-Angle X-ray Scattering (SAXS) Analysis

The following SAXS models were used and modified from various literature sources where indicated. The models described herein were initially applied by Dr. Oleksandr Mykhaylyk, for which he is thanked.

In general, the X-ray intensity scattered by a dispersion of nano-objects [usually represented by the scattering cross section per unit sample volume, $\frac{d\Sigma}{d\Omega}(q)$] can be expressed as:

$$\frac{d\Sigma}{d\Omega}(q) = N.S(q)\int_0^\infty \dots \int_0^\infty F\left(q, r_{1,} \dots, r_{\mathrm{k}}\right)^2 \Psi\left(r_{1,} \dots, r_{\mathrm{k}}\right) dr_1 \dots dr_{\mathrm{k}} \qquad A1$$

where $F(q, r_1, \dots, r_{\mathrm{k}})$ is their form factor, $r_1, \dots, r_{\mathrm{k}}$ is a set of *k* parameters describing the structural morphology, $\Psi\left(r_{1,} \dots, r_{\mathrm{k}}\right)$ is the distribution function, S(q) is the structure factor and *N* is the nano-object number density per unit volume expressed as:

$$N = \frac{\varphi}{\int_0^\infty \dots \int_0^\infty V\left(r_{1,} \dots, r_{\mathrm{k}}\right) \Psi\left(r_{1,} \dots, r_{\mathrm{k}}\right) dr_1 \dots dr_{\mathrm{k}}} \qquad A2$$

where $V\left(r_{1,} \dots, r_{\mathrm{k}}\right)$ is volume of the nano-object and φ is their volume fraction in the dispersion.

8.1.1. Spherical micelle model

The spherical micelle form factor for Equation A1 is given by:[1]

$$F_{\mathrm{s\_mic}}(q) = {N_{\mathrm{s}}}^2 {\beta_{\mathrm{s}}}^2 {A_{\mathrm{s}}}^2(q, R_{\mathrm{s}}) + N_{\mathrm{s}} {\beta_{\mathrm{c}}}^2 F_{\mathrm{c}}\left(q, R_{\mathrm{g}}\right) + N_{\mathrm{s}}(N_{\mathrm{s}} - 1){\beta_{\mathrm{c}}}^2 {A_{\mathrm{c}}}^2(q) + 2{N_{\mathrm{s}}}^2 \beta_{\mathrm{s}} \beta_{\mathrm{c}} A_{\mathrm{s}}(q, R_{\mathrm{s}}) A_{\mathrm{c}}(q) \qquad A3$$

where R_s is the radius of the spherical micelle core, R_g is the radius of gyration of the PSMA coronal block, the core block and the corona block X-ray scattering length contrast is given by $\beta_s = V_s(\xi_s - \xi_{sol})$ and $\beta_c = V_c(\xi_c - \xi_{sol})$, respectively. Here ξ_s, ξ_c and ξ_{sol} are the X-ray scattering length densities of the core block (ξ_{PBzMA} = 10.38 × 10^{10} cm^{-2}), the corona block (ξ_{PSMA} = 9.24 × 10^{10} cm^{-2}) and the solvent (ξ_{sol} = 7.63 × 10^{10} cm^{-2}), respectively. V_s and V_c are volumes of the core block (V_{PBzMA}) and the corona block (V_{PSMA31}), respectively. The volumes were obtained from $V = \frac{M_{n,pol}}{N_A \rho}$ using the density of PBzMA (ρ_{PBzMA} = 1.15 g cm^{-3})[2] and the solid-state homopolymer density of PSMA determined by helium pycnometry (ρ_{PSMA} = 0.97 g cm^{-3}), where $M_{n,pol}$ corresponds to the number-average molecular weight of the block determined by ^{1}H NMR spectroscopy. The sphere form factor amplitude is used for the amplitude of the core self-term:

$$A_c(q, R_s) = \Phi(qR_s)\exp\left(-\frac{q^2\sigma^2}{2}\right) \qquad A4$$

where $\Phi(qR_s) = \frac{3[\sin(qR_s) - qR_s\cos(qR_s)]}{(qR_s)^3}$. A sigmoidal interface between the two blocks was assumed for the spherical micelle form factor [Equation A]. This is described by the exponent term with a width σ accounting for a decaying scattering length density at the membrane surface. This σ value was fixed at 2.5 during fitting.

The form factor amplitude of the spherical micelle corona is:

$$A_c(q) = \frac{\int_{R_s}^{R_s+2s} \mu_c(r)\frac{\sin(qr)}{qr} r^2 dr}{\int_{R_s}^{R_s+2s} \mu_c(r) r^2 dr} \exp\left(-\frac{q^2\sigma^2}{2}\right) \qquad A5$$

The radial profile, $\mu_c(r)$, can be expressed by a linear combination of two cubic b splines, with two fitting parameters *s* and *a* corresponding to the width of the profile and the weight coefficient, respectively. This information can be found elsewhere,[3, 4] as can the approximate integrated form of Equation A5. The self-correlation term for the corona block is given by the Debye function:

$$F_{\mathrm{c}}(q, R_{\mathrm{g}}) = \frac{2\left[\exp\left(-q^2 {R_{\mathrm{g}}}^2\right) - 1 + q^2 {R_{\mathrm{g}}}^2\right]}{q^4 {R_{\mathrm{g}}}^4} \qquad A6$$

where R_{g} is the radius of gyration of the PSMA coronal block. The aggregation number of the spherical micelle is:

$$N_{\mathrm{s}} = (1 - x_{\mathrm{sol}}) \frac{\frac{4}{3}\pi {R_{\mathrm{s}}}^3}{V_{\mathrm{s}}} \qquad A7$$

where x_{sol} is the volume fraction of solvent in the PBzMA micelle core. An effective structure factor expression proposed for interacting spherical micelles[5] has been used in Equation A1:

$$S_{\mathrm{s}}(q) = 1 + \frac{A^{\mathrm{av}}_{\mathrm{s\_mic}}(q)^2 [S_{\mathrm{PY}}(q, R_{\mathrm{PY}}, f_{\mathrm{PY}}) - 1]}{F_{\mathrm{s\_mic}}(q)} \qquad A8$$

Herein the form factor of the average radial scattering length density distribution of micelles is used as $A^{\mathrm{av}}_{\mathrm{s\_mic}}(q) = N_{\mathrm{s}}[\beta_{\mathrm{s}} A_{\mathrm{s}}(q, R_{\mathrm{s}}) + \beta_{\mathrm{c}} A_{\mathrm{c}}(q)]$ and $S_{\mathrm{PY}}(q, R_{\mathrm{PY}}, f_{\mathrm{PY}})$ is a hard-sphere interaction structure factor based on the Percus-Yevick approximation,[6] where R_{PY} is the interaction radius and f_{PY} is the hard-sphere volume fraction. A polydispersity for one parameter (R_{s}) is assumed for the micelle model which is described by a Gaussian distribution. Thus, the polydispersity function in Equation A can be represented as:

$$\Psi(r_1) = \frac{1}{\sqrt{2\pi {\sigma_{R\mathrm{s}}}^2}} \exp\left(-\frac{(r_1 - R_{\mathrm{s}})^2}{2{\sigma_{R\mathrm{s}}}^2}\right) \qquad A9$$

where σ_{Rs} is the standard deviation for R_{s}. In accordance with Equation A2 the number density per unit volume for the micelle model is expressed as:

$$N = \frac{\varphi}{\int_0^\infty V(r_1)\Psi(r_1)dr_1} \qquad A10$$

where φ is the total volume fraction of copolymer in the spherical micelles and $V(r_1)$ is the total *volume* of copolymer in a spherical micelle $[V(r_1) = (V_s + V_c)N_s(r_1)]$.

The model fitting to the final SAXS pattern of $PSMA_{31}$-$PBzMA_{2000}$ spheres indicated φ = 0.063, R_{PY} = 62.8 nm and f_{PY} = 0.073, which is consistent with the expected volume fraction of polymer (0.075) in this system after synthesis at full conversion. The experimental R_g obtained from this fitting for the corona PSMA block (1.5 nm) is also physically reasonable, since it is close to the estimated parameter. Assuming that the projected contour length of a PSMA monomer is 0.255 nm (two C-C bonds in *all-trans* conformation), the total contour length of a $PSMA_{31}$ block, L_{PSMA31} = 31 × 0.255 nm = 7.905 nm. Given a mean Kuhn length of 1.53 nm [based on the known literature value for PMMA[7]] an estimated unperturbed radius of gyration, R_g = $(7.905 \times 1.53/6)^{0.5}$, or 1.42 nm is determined.

8.1.2. Worm-like micelle model

The worm-like micelle form factor for Equation A1 is given by:[1]

$$F_{w\_mic}(q) = N_w{}^2\beta_s{}^2F_{sw}(q) + N_w\beta_c{}^2F_c(q, R_g) + N_w(N_w - 1)\beta_c{}^2S_{cc}(q) + 2N_w{}^2\beta_s\beta_cS_{sc}(q) \quad A11$$

where the core block and the corona block X-ray scattering length contrast is given by $\beta_s = V_s(\xi_s - \xi_{sol})$ and $\beta_c = V_c(\xi_c - \xi_{sol})$, respectively. Here ξ_s, ξ_c and ξ_{sol} are the X-ray scattering length densities of the core block (ξ_{PBzMA} = 10.38 × 10^{10} cm^{-2}), the corona block (ξ_{PSMA} = 9.24 × 10^{10} cm^{-2}) and the solvent (ξ_{sol} = 7.63 × 10^{10} cm^{-2}), respectively. V_s and V_c are volumes of the core block (V_{PBzMA}) and the corona block (V_{PSMA}), respectively. The volumes were obtained from $V = \frac{M_{n,pol}}{N_A\rho}$ using the density of PBzMA (ρ_{PBzMA} = 1.15 g cm^{-3})[2] and the solid-state homopolymer density of PSMA determined by helium pycnometry (ρ_{PSMA} = 0.97 g cm^{-3}), where $M_{n,pol}$ corresponds to the number-average molecular weight of the block determined by ^{1}H NMR spectroscopy. The self-correlation term for the worm-like micelle core or radius R_{sw} is:

$$F_{\mathrm{sw}}(q) = F_{\mathrm{worm}}(q, L_{\mathrm{w}}, b_{\mathrm{w}}) {A_{\mathrm{cs}_{\mathrm{worm}}}}^2(q, R_{\mathrm{sw}}) \qquad A12$$

which is a product of a core cross-section term:

$$F_{\mathrm{cs}_{\mathrm{worm}}}(q, R_{\mathrm{g}}) = {A_{\mathrm{cs}_{\mathrm{worm}}}}^2(q, R_{\mathrm{sw}}) = \left[2\frac{J_1(qR_{\mathrm{sw}})}{qR_{\mathrm{sw}}}\right]^2 \qquad A13$$

where J_1 is the first-order Bessel function of the first kind, and a form factor $F_{\mathrm{worm}}(q, L_{\mathrm{w}}, b_{\mathrm{w}})$ for self-avoiding semi-flexible chains represents the worm-like micelle, where b_{w} is the worm Kuhn length and L_{w} is the mean worm contour length. A complete expression for the chain form factor can be found elsewhere.[8] The self-correlation term for the corona block is given by the Debye function shown in Equation A6. The interference cross-term between the worm micelle core and the corona chain is given by:

$$S_{\mathrm{sc}}(q) = \Psi^2(qR_{\mathrm{g}}) {J_0}^2\left[q\left(R_{\mathrm{sw}} + R_{\mathrm{g}}\right)\right] F_{\mathrm{worm}}(q, L_{\mathrm{w}}, b_{\mathrm{w}}) \qquad A14$$

where $\Psi\left(qR_{\mathrm{g}}\right) = \frac{1-\exp\left(-q^2{R_{\mathrm{g}}}^2\right)}{\left(qR_{\mathrm{g}}\right)^2}$ is the form factor amplitude of the corona chain, R_{g} is the radius of gyration of the PSMA corona block and J_0 is the zero-order Bessel function of the first kind. The interference term between the worm corona chains is:

$$S_{\mathrm{cc}}(q) = \Psi\left(qR_{\mathrm{g}}\right) A_{\mathrm{cs\_worm}} J_0\left[q\left(R_{\mathrm{sw}} + R_{\mathrm{g}}\right)\right] F_{\mathrm{worm}}(q, L_{\mathrm{w}}, b_{\mathrm{w}}) \qquad A15$$

The mean aggregation number of the worm-like micelle is given by:

$$N_{\mathrm{w}} = (1 - x_{\mathrm{sol}}) \frac{\pi {R_{\mathrm{sw}}}^2 L_{\mathrm{w}}}{V_{\mathrm{s}}} \qquad A16$$

where x_{sol} is the volume fraction of solvent within the worm-like micelle core. Possible semi-spherical caps at the ends of each worm are not considered in this form factor. It is also assumed that $S(q) = 1$ at sufficiently low copolymer concentrations (e.g. 1.0% w/w).

8.1.3. Vesicle model

The vesicle form factor in Equation A1 is expressed as:[9]

$$F_{\mathrm{ves}}(q) = N_{\mathrm{v}}{}^2\beta_{\mathrm{m}}{}^2A_{\mathrm{m}}{}^2(q) + N_{\mathrm{v}}\beta_{\mathrm{vc}}{}^2F_{\mathrm{c}}\left(q, R_{\mathrm{g}}\right) + N_{\mathrm{v}}(N_{\mathrm{v}} - 1)\beta_{\mathrm{vc}}{}^2A_{\mathrm{vc}}{}^2(q) + 2N_{\mathrm{v}}{}^2\beta_{\mathrm{m}}\beta_{\mathrm{vc}}A_{\mathrm{m}}(q)A_{\mathrm{vc}}(q) \qquad \textit{A17}$$

The X-ray scattering length contrast for the membrane-forming block (PBzMA) and the coronal stabiliser block (PSMA) is given by $\beta_{\mathrm{m}} = V_{\mathrm{m}}(\xi_{\mathrm{m}} - \xi_{\mathrm{sol}})$ and $\beta_{\mathrm{vc}} = V_{\mathrm{vc}}(\xi_{\mathrm{vc}} - \xi_{\mathrm{sol}})$, respectively, where ξ_{m}, ξ_{vc} and ξ_{sol} are the X-ray scattering length densities of the membrane-forming block (ξ_{PBzMA} = 10.38 × 10^{10} cm^{-2}), the coronal stabiliser block (ξ_{PSMA} = 9.24 × 10^{10} cm^{-2}) and the solvent (ξ_{sol} = 7.63 × 10^{10} cm^{-2}). V_{m} and V_{vc} are the volumes of the membrane-forming block and the coronal stabiliser block, respectively. Using the molecular weights of the PBzMA and PSMA blocks and their respective mass densities: ρ_{PBzMA} = 1.15 g cm^{-3} and ρ_{PSMA} = 0.97 g cm^{-3}, the individual block volumes can be calculated from $V = \frac{M_{\mathrm{n,pol}}}{N_{\mathrm{A}}\rho}$, where $M_{\mathrm{n,pol}}$ corresponds to the number-average molecular weight of the block determined by ^{1}H NMR spectroscopy. The amplitude of the membrane self-term is:

$$A_{\mathrm{m}}(q) = \frac{V_{\mathrm{out}}\varphi(qR_{\mathrm{out}}) - V_{\mathrm{in}}\varphi(qR_{\mathrm{in}})}{V_{\mathrm{out}} - V_{\mathrm{in}}}\exp\left(-\frac{q^2{\sigma_{\mathrm{in}}}^2}{2}\right) \qquad \textit{A18}$$

where $R_{\mathrm{in}} = R_{\mathrm{m}} - \frac{1}{2}T_{\mathrm{m}}$ is the inner radius of the membrane, $R_{\mathrm{out}} = R_{\mathrm{m}} + \frac{1}{2}T_{\mathrm{m}}$ is the outer radius of the membrane, $V_{\mathrm{in}} = \frac{4}{3}\pi{R_{\mathrm{in}}}^3$, $V_{\mathrm{out}} = \frac{4}{3}\pi{R_{\mathrm{out}}}^3$. It should be noted that Equation A17 differs from the original work in which they were first described.[9] The exponent term in Equation A18 represents a sigmoidal interface between the blocks,

with a width σ_{in} accounting for a decaying scattering length density at the membrane surface. The value of σ_{in} was fixed at 2.5. The mean vesicle aggregation number, N_v, is given by:

$$N_v = (1 - x_{sol})\frac{V_{out} - V_{in}}{V_m} \qquad A19$$

where x_{sol} is the solvent (i.e. mineral oil) volume fraction within the vesicle membrane.

A simpler expression for the corona self-term of the vesicle model than for the spherical micelle corona self-term was used due to the fact that the contribution to the scattering intensity from the corona block in this case was much less than the contribution from the membrane block. Assuming that there is no penetration of the solvophilic coronal blocks into the solvophobic membrane, the amplitude of the vesicle corona self-term is expressed as:

$$A_{vc}(q) = \Psi(qR_g)\frac{1}{2}\left[\frac{\sin[q(R_{out} + R_g)]}{q(R_{out} + R_g)} + \frac{\sin[q(R_{in} - R_g)]}{q(R_{in} - R_g)}\right] \qquad A20$$

where the term outside the square brackets is the factor amplitude of the corona block polymer chain such that:

$$\Psi(qR_g) = \frac{1 - \exp(-qR_g)}{(qR_g)^2} \qquad A21$$

Again, the obtained R_g of the $PSMA_{13}$ coronal block of ~1.21 nm is comparable to the estimated value. The latter can be calculated from the total contour length of the $PSMA_{13}$ block, L_{PSMA13} = 13 × 0.255 nm = 3.315 nm (since the projected contour length per SMA monomer repeat unit is defined by two carbon bonds in an all-*trans* conformation, or 0.255 nm) and the Kuhn length of 1.53 nm [based on the known literature value for PMMA[7]] result in an approximate R_g of $(3.315 \times 1.53/6)^{1/2}$ = 0.92 nm.

It was assumed for the vesicle model that two parameters are polydisperse: the overall radius of the vesicles and the membrane thickness (R_m and T_m, respectively). They are considered to have a Gaussian distribution and, therefore, the polydispersity function in Equation A1 can be expressed as:

$$\Psi(r_1, r_2) = \frac{1}{\sqrt{2\pi\sigma_{R\mathrm{m}}{}^2}} \exp\left(-\frac{(r_1 - R_\mathrm{m})^2}{2\sigma_{R\mathrm{m}}{}^2}\right) \frac{1}{\sqrt{2\pi\sigma_{T\mathrm{m}}{}^2}} \exp\left(-\frac{(r_1 - T_\mathrm{m})^2}{2\sigma_{T\mathrm{m}}{}^2}\right) \quad A22$$

where $\sigma_{R\mathrm{m}}$ and $\sigma_{T\mathrm{m}}$ are the standard deviations for R_m and T_m, respectively. Following Equation A2 the number density per unit volume for the vesicle model is expressed as:

$$N = \frac{\varphi}{\int_0^\infty \int_0^\infty V(r_1, r_2)\Psi(r_1, r_2) dr_1 dr_2} \quad A0.1$$

where φ is the total *volume fraction* of copolymer in the vesicles and $V(r_1, r_2)$ is the total *volume* of copolymers in a vesicle [$V(r_1, r_2) = (V_\mathrm{m} + V_\mathrm{vc})N_\mathrm{v}(r_1, r_2)$]. The region of the SAXS patterns which would be affected by the structure factor of concentrated vesicle dispersions were not well resolved in the performed SAXS measurements and, therefore, were excluded from the fitted pattern [i.e. only SAXS data for q > 0.06 nm^{-1} were used for the fitting and the structure factor in Equation A1 was set to unity, $S(q) = 1$]. Programming tools within the Irena SAS Igor Pro macros[10] were used to implement the scattering models.

8.2. References

1. J. S. Pedersen, *Journal of Applied Crystallography*, 2000, **33**, 637-640.
2. L. A. Fielding, J. A. Lane, M. J. Derry, O. O. Mykhaylyk and S. P. Armes, *Journal of the American Chemical Society*, 2014, **136**, 5790-5798.
3. J. S. Pedersen and M. C. Gerstenberg, *Colloids and Surfaces a-Physicochemical and Engineering Aspects*, 2003, **213**, 175-187.
4. J. S. Pedersen, C. Svaneborg, K. Almdal, I. W. Hamley and R. N. Young, *Macromolecules*, 2003, **36**, 416-433.
5. J. S. Pedersen, *Journal of Chemical Physics*, 2001, **114**, 2839-2846.
6. D. J. Kinning and E. L. Thomas, *Macromolecules*, 1984, **17**, 1712-1718.
7. L. J. Fetters, D. J. Lohsey and R. H. Colby, in *Physical Properties of Polymers Handbook*, ed. J. E. Mark, Springer, New York, 2nd edn., 2007, ch. 25, pp. 447-454.
8. J. S. Pedersen and P. Schurtenberger, *Macromolecules*, 1996, **29**, 7602-7612.

9. J. Bang, S. M. Jain, Z. B. Li, T. P. Lodge, J. S. Pedersen, E. Kesselman and Y. Talmon, *Macromolecules*, 2006, **39**, 1199-1208.
10. J. Ilavsky and P. R. Jemian, *Journal of Applied Crystallography*, 2009, **42**, 347-353.